Université de Strasbourg

UNIVERSITÉ DE STRASBOURG

École doctorale Mathématiques, sciences de l'information et de l'ingénieur | ED 269 Université de Strasbourg

ÉCOLE DOCTORALE MATHEMATIQUES, SCIENCES DE L'INFORMATION ET DE L'INGENIEUR – ED269

LABORATOIRE ICUBE (UMR7357)

THÈSE:

Présenté par:

Milad AKRAMI

Soutenue le : **20 décembre 2023**

Pour obtenir le grade de: **Docteur de l'Université de Strasbourg**

Discipline/ Spécialité: Circuits et Systèmes

Design and Implementation of Electric Motor Drive for Automotive Cooling Water Pump

DIRECTEURS DE THÈSE:

M. FRICK Vincent	Professeur, Université de Strasbourg, Laboratoire ICube
M. JAMSHIDPOUR Ehsan	Maître de conférences, Université de Lorraine, Laboratoire GREEN

RAPPORTEURS:

Mme. ORLOWSKA-KOWALSKA Teresa	Professeur, Wroclaw University of Science and Technology
M. GAO Fei	Professeur, Université Technologique de Belfort Montbéliard (UTBM), Institut FEMTO-ST

EXAMINATEURS:

M. MEIBODY-TABAR Farid	Professeur, ENSEM Nancy, Laboratoire LEMTA
M. PIERFEDERICI Serge	Professeur, ENSEM Nancy, Laboratoire LEMTA
M. KAMMERER Jean-Baptiste	Maître de conférences HDR, Université de Strasbourg, Laboratoire ICube
M. NAHID-MOBARAKEH Babak	Professeur, McMaster University, Canada

Abstract

Recently, a great deal of effort has been put into replacing conventional internal combustion engine vehicles with electric vehicles (EVs). Whatever the type of motorization (internal combustion engine, electric or hybrid), the cooling system plays a critical role during the vehicle operation. The cooling requirements for standard commercial and passenger vehicles has remained unchanged over the last century. In a conventional vehicle powered with an internal combustion engine, a mechanical coolant pump linked to a valve able to regulate the flow usually suffices to roughly control the operating temperature of the engine.

Nowadays, owing to the increasing awareness of environmental pollution and energy depletion around the world, this traditional solution needs to be replaced by more efficient ones like a dedicated electric motor for the water pump. Also, this solution is preferred for EVs since they have many heat-regulated components (engines, batteries, power electronic converters) that require dedicated cooling circuits. To meet these needs, the mechanical cooling pump will be replaced by an electric motor pump in this thesis. Motors in EVs are usually required to operate in severe environments, including high temperatures and vibrations. The aim of the thesis is to design and implement a new and compatible drive for the electric motor (that has been designed with the frame of another thesis related to the same project) of the water pump in EV application.

There has been a rapid increase of variable-speed drives based on hybrid drives in the automotive industry. This growth is also influencing the industry demand for variable-speed permanent magnet (PM) drives. Therefore, permanent magnet synchronous motors (PMSMs) and brushless DC (BLDC) motors have become a popular choice for automotive applications including EVs and hybrid electric vehicles (HEVs) over the past decades due to several features including high torque density, high efficiency, and high power density.

Traditionally, PMSM drives are controlled by field-oriented control (FOC) using Proportional-Integral (PI) controllers for speed and torque regulation. Designing controller parameters based on linear methods requires linear approximation, which is dependent on the operating point of the system. Model-based nonlinear control strategies

including differential flatness control have been proposed as a solution to the nonlinear nature of the PMSM drive system. In this alternate representation, nonlinear controller design and trajectory planning are clearly shown. Using differential flatness, it is possible to estimate the trajectory of the system directly from the trajectory of a flat output and its derivatives without integrating differential equations.

In comparison to classic FOC control, flatness-based control of PMSMs offers several advantages. Firstly, it eliminates the need for regulators if all parameters are known, allowing for open-loop control. Secondly, it can achieve high dynamic performance even in the presence of model errors and external disturbances. Additionally, the trajectory planning method used in flatness-based control outperforms cascaded linear controllers in both transient and disturbed conditions. Lastly, it has been demonstrated that flatness-based control consistently delivers competitive performance compared to conventional field-oriented control techniques.

Trajectory planning affects the response of indirectly controlled states. As the maximum allowable motor currents are determined by the motor and driver's electrical ratings, and also limits of the switching voltages depend on the DC-bus voltage (and in some cases, on the state of charge of the DC battery), the flatness condition of the system can fail and it may result in system instability. A trajectory planning method for flatness-based control of PMSM drives for EV water pump application is proposed in this thesis. This approach is primarily intended to ensure PMSM motor current remains within permissible limits through indirect flatness-based control while still having the advantages of one-loop control. Furthermore, the constraint on switching voltage has been taken into account in the proposed trajectory planning method to maintain the proper operation of the PMSM drive system in steady-state mode as well as during transients. A window-based trajectory planning function is used for the PMSM drive in this method. The trajectory function is calculated using an optimization algorithm considering the speed overshoot, motor current, and switching voltage constraints. Unlike conventional trajectory planning, which is a second-order function, this method takes controller limits into account while using one-loop flatness-based control.

Résumé

Récemment, de nombreux efforts ont été déployés pour remplacer les véhicules conventionnels à moteur thermiques par des véhicules électriques (VE). Quel que soit le type de motorisation (moteur à combustion interne, électrique ou hybride), le système de refroidissement joue un rôle essentiel dans le fonctionnement du véhicule. Les exigences en matière de refroidissement pour les véhicules utilitaires et de tourisme sont restées inchangées au cours du siècle dernier. Dans un véhicule conventionnel équipé d'un moteur thermique, une pompe à liquide de refroidissement mécanique reliée à une vanne capable de réguler le débit suffit généralement à contrôler grossièrement la température de fonctionnement du moteur.

Aujourd'hui, en raison de la prise de conscience croissante de la pollution environnementale et de l'épuisement des ressources énergétiques dans le monde, cette solution traditionnelle doit être remplacée par des solutions plus efficaces, comme un moteur électrique dédié à la pompe à eau. Cette solution est également privilégiée pour les véhicules électriques, car ils comportent de nombreux composants thermorégulés (moteurs, batteries, convertisseurs électroniques de puissance) qui nécessitent des circuits de refroidissement dédiés. Pour répondre à ces besoins, la pompe de refroidissement mécanique sera remplacée par une pompe à moteur électrique dans cette thèse. Les moteurs des véhicules électriques doivent généralement fonctionner dans des environnements difficiles, avec des températures élevées et des vibrations. L'objectif de cette thèse est de concevoir et de mettre en œuvre une nouvelle commande compatible avec un moteur électrique (développé dans le cadre d'une autre thèse liée à ce projet) de la pompe à eau véhicules électriques.

L'industrie automobile a connu une augmentation rapide des variateurs de vitesse basés sur des entraînements hybrides. Cette croissance influe également sur la demande de variateurs de vitesse à aimant permanent (PM). Par conséquent, les moteurs synchrones à aimant permanent (PMSM) et les moteurs à courant continu sans balais (BLDC) sont devenus un choix populaire pour les applications automobiles, y compris les véhicules électriques (VE) et les véhicules électriques hybrides (VEH), au cours des dernières décennies, en raison de plusieurs caractéristiques, notamment une densité de couple élevée, un rendement élevé et une densité de puissance élevée.

Traditionnellement, les variateurs PMSM sont commandés par un contrôle orienté

champ (FOC) utilisant des contrôleurs proportionnels et intégraux (PI) pour la régulation de la vitesse et du couple. La détermination des paramètres du contrôleur basée sur des méthodes linéaires nécessite une approximation linéaire qui dépend du point de fonctionnement du système. Des stratégies de contrôle non linéaire basées sur des modèles, y compris le contrôle différentiel de la platitude, ont été proposées comme solution à la nature non linéaire du système d'entraînement PMSM. Dans cette approche alternative, la conception de contrôleurs non linéaires et la planification de trajectoires sont clairement abordées. En utilisant la platitude différentielle, il est possible d'estimer la trajectoire du système directement à partir de la trajectoire d'une sortie plane et de ses dérivées sans intégrer d'équations différentielles.

Par rapport à la commande FOC classique, la commande des PMSM basée sur la platitude offre plusieurs avantages. Tout d'abord, elle élimine le besoin de régulateurs si tous les paramètres sont connus, ce qui permet un contrôle en boucle ouverte. Deuxièmement, elle permet d'obtenir des performances dynamiques élevées même en présence d'erreurs de modélisation et de perturbations externes. En plus, la méthode de planification de trajectoire utilisée dans le contrôle basé sur la platitude surpasse les contrôleurs linéaires en cascade dans les conditions transitoires et perturbées. Enfin, il a été démontré que le contrôle basé sur la platitude offre systématiquement des performances compétitives par rapport aux techniques de contrôle conventionnelles axées sur le champ.

La planification de la trajectoire affecte la réponse des états contrôlés indirectement. Étant donné que les courants maximaux admissibles du moteur sont déterminés par les caractéristiques électriques du moteur et du pilote, et que les tensions de commutation dépendent de la tension du bus continu (et, dans certains cas, de l'état de charge de la batterie à courant continu), la condition de platitude du système peut s'avérer insuffisante et entraîner l'instabilité du système. Cette thèse propose une méthode de planification de trajectoire pour le contrôle basé sur la platitude des entraînements PMSM pour les pompes à eau des véhicules électriques. Cette approche vise principalement à garantir que le courant du moteur PMSM reste dans les limites permises grâce à un contrôle indirect basé sur la platitude, tout en conservant les avantages du contrôle en boucle unique. En outre, la contrainte de la tension de commutation a été prise en compte dans la méthode de planification de trajectoire proposée pour maintenir le bon fonctionnement du système d'entraînement du PMSM en régime permanent ainsi que

pendant les phases transitoires. Une fonction de planification de trajectoire basée sur une fenêtre est utilisée pour l'entraînement PMSM dans cette méthode. La fonction de trajectoire est calculée à l'aide d'un algorithme d'optimisation prenant en compte les contraintes de dépassement de vitesse, de courant moteur et de tension de commutation. Contrairement à la planification conventionnelle de la trajectoire, qui est une fonction de second ordre, cette méthode prend en compte les limites du contrôleur tout en utilisant un contrôle basé sur la platitude en boucle unique.

Acknowledgments

I would like to express my sincere gratitude to my respected supervisors, Prof. Vincent Frick and Prof. Ehsan Jamshidpour, for their consistent support and guidance throughout my Ph.D. journey. Their patience, motivation, and vast knowledge have been instrumental in shaping my research work, and I am truly indebted to them for their mentorship.

I am also deeply appreciative of Prof. Serge Pierfederici for his invaluable assistance, guidance, and consultation during the research project. His expert advice significantly contributed to the success of our research.

Furthermore, I extend my thanks to Prof. Farid Meibody-Tabar and Prof. Wilfried Uhring for their insightful suggestions and guidance during the monitoring committees. Their feedback played a pivotal role in refining our ideas and research.

I am also grateful to Prof. Julien Fontchastagner and Prof. Noureddine Takorabet for their support in implementing the testbench, which was crucial for our research.

My appreciation also extends to the members of the ICube team and GREEN Team, with special mentions to Dr. Peyman Haghgooyi and Mr. Paisak Poolphaka for their assistance and contributions to our work.

Additionally, I would like to express my thanks to Sogefi Company for their funding of this project, which enabled its successful completion.

I must express my gratitude to my parents and my sister, for their continuous moral support and motivation that sustained me throughout this academic journey.

Last but certainly not least, I owe a debt of gratitude to my beloved wife, Sima, who stood by me at every step of this research work and in life. Her support has been my rock, and I am deeply thankful for her presence in my life.

Contents

Symbols

B	viscous damping of the rotor
$F_{ab/bc}, F_{bc/ca}, F_{ca/ab}$	flux linkage functions
G_{inv}	inverter gain model
I_{dc}	DC-bus current
$I_{q,max}$	maximum limit of q-axis current
J	moment of inertia of a motor
L	phase stator inductance of a motor
L_d	stator inductance in d-axis
L_{nom}	nominal phase inductance of a motor
L_q	stator inductance in q-axis
L_s	stator self-inductance of a motor
M	mutual inductance between two phases of a motor
R	phase stator impedance of a BLDC motor
R_s	phase stator impedance of a PMSM
T_{cal}	maximum computation time of the optimization function
T_e	virtual sampling interval of the optimization function
T_L	load torque of a motor
T_w	trajectory planning window interval
U_{d-h}	high-frequency voltage components in d-axis
U_{pul-h}	injected pulsating sinusoidal high-frequency voltage amplitude
U_{q-h}	high-frequency voltage components in q-axis
U_{rot-h}	injected rotating high-frequency voltage amplitude

V	motor phase terminal voltage
V_a, V_b, V_c	terminal voltages for phases a, b, and c
V_{ab}, V_{bc}, V_{ca}	line-to-line terminal voltages
V_d	d-axis terminal voltage
V_{dc}	DC-bus voltage of the inverter
V_q	q-axis terminal voltage
V_{td}	voltage drop on d-axis
V_{tq}	voltage drop on q-axis
e	motor phase back-EMF
e_a, e_b, e_c	back-EMF voltages for phases a, b, and c
e_{ab}, e_{bc}, e_{ca}	line-to-line back-EMF voltages
e_d	d-axis back-EMF voltage
e_q	q-axis back-EMF voltage
f	friction coefficient of the motor
i	motor phase current
i_a, i_b, i_c	stator currents for phases a, b, and c
i_{ab}, i_{bc}, i_{ca}	line-to-line stator currents
i_d	d-axis current
i_{d-h}	high-frequency current components in d-axis
i_q	q-axis current
i_{q-h}	high-frequency current components in q-axis
$i_{q,expected}$	expected q-axis current using the novel trajectory planning
k_{ic}	integral coefficients of the current PI-controller
k_{pd}	proportional coefficients of the d-axis current PI-controller
k_{pq}	proportional coefficients of the q-axis current PI-controller
$k_{i\Omega}$	integral coefficients of the speed current PI-controller
$k_{p\Omega}$	proportional coefficients of the speed current PI-controller
p	number of pole pairs

t	time
y_{inf}	trajectory planning block input
y_{ref}	trajectory planning block output
Ω	mechanical speed of a motor
ζ_d	damping ratio of poles of the d-axis flatness regulator
ζ_f	damping coefficient of the second-order trajectory function
ζ_Ω	damping ratio of poles of the speed flatness regulator
θ	rotor phase angle
$\lambda_{ab}, \lambda_{bc}, \lambda_{ca}$	line-to-line PM flux linkage of a motor
λ_M	flux caused by permanent magnets
τ_d	time constant of the first-order d-axis current response
τ_{id}	time constant of the d-axis current PI-controller
τ_{iq}	time constant of the q-axis current PI-controller
τ_m	mechanical time constant of the rotor
τ_q	time constant of the first-order q-axis current response
τ_Ω	time constant of the speed current PI-controller
ψ_d	magnetic flux in d-axis
$\psi_d(i_d, i_q)$	magnetic flux in d-axis considering saturation effect
ψ_f	constant magnet flux
ψ_q	magnetic flux in q-axis
$\psi_q(i_d, i_q)$	magnetic flux in q-axis considering saturation effect
ω	rotor angular velocity
ω_d	natural frequency of poles of the d-axis flatness regulator
ω_f	Cutoff frequency of the second-order trajectory function
ω_h	high-frequency angular frequency
ω_Ω	natural frequency of poles of the speed flatness regulator

Chapter 1

Introduction

1.1 Motivation

Over the last decade, the automotive industry has undergone a remarkable transition with a surge in the production of EVs and HEVs [1]. Consequently, these vehicles are crucial to lowering greenhouse gas emissions and mitigating climate change. As a result, the demand for efficient and reliable cooling systems in these vehicles has intensified [2, 3].

Electric and hybrid vehicles require efficient cooling due to the heavy reliance on battery and power electronic components, all of which generate considerable heat while in operation. Managing this heat is crucial not only to maintaining vehicle performance, but also to extend the lifespan of critical components. Electric motors play a pivotal role in EV water pump applications, as they are responsible for the cooling process [4, 5].

Induction motors have been the predominant choice for residential and industrial water pump applications for several decades due to their low maintenance requirements, cost-effectiveness, and ease of use. Induction motors, however, do not offer a long-term solution in terms of energy efficiency due to their inherent inefficiencies. Alternatively, PMs motors including PMSMs and BLDC motors offer considerably higher efficiency within a more compact design, making them ideal for loads with similar characteristics. PMSMs, in particular, have gained recognition for their high power density, high torque-to-weight ratio, and uncomplicated design, making them ideal for various applications [6–8]. A comparison of the five most used electric motor types in EV and HEV

applications is conducted in [9], which is summarized in Table 1.1.

Table 1.1: Comparison of most used electric motors for EV/HEV application [9].

Motor	**BLDC**	**DC Series Motor**	**PMSM**	**Switched Reluctance**	**Induction Motor**
Overall cost	High	Low	High	Medium	Medium
Weight	Low	Heavy	Medium	Medium	Medium
Maintenance	Negligible	Brushed wear	Negligible	Negligible	Negligible
Pros	Fast response, Long lifespan, Higher starting torque	Not expensive, Higher starting torque	Good dynamic performance, Good efficiency, Less noise, High starting torque	Low inertia, Can be tailored for specific applications	Cost-effective, Ease of use
Cons	Torque ripple, Less efficiency	Requires maintenance, Bulky, Limited rotation speed, Requires large windings	Complex control system	Requires position sensor	Complex control system
% Efficiency with electric motor	80	80	97	94	90
% Efficiency with electric motor and drive	78	78	90	84	83

1.2 Structure of PM motors

A rotating electrical machine is a two-way electromechanical system that can convert electrical energy into mechanical energy (as a motor) and convert mechanical energy into electrical energy (as a generator). These electrical machines are composed of two main components: the stationary part known as the stator and the rotating part known as the rotor. These two parts are separated by a small gap. In general, electrical machines can be categorized based on three key factors:

- Stator power source: direct current (DC) or alternating current (AC).
- Rotor structure: whether it uses permanent magnets, has a short-circuited winding, or employs an excited winding, among other possibilities.
- Air gap structure.

Figure 6.1 presents the 3D model and construction structure, while Figure 1.2 illustrates the general configuration of frameless brushless PM motors. These motors have a three-phase stator winding, which is constructed similarly to that of an AC induction

motor. A three-phase stator winding is wound to produce a trapezoidal or sinusoidal distribution of air-gap flux depending on whether the motor is a BLDC motor or a PMSM one. The rotor of these motors is made up of high-performance permanent magnets firmly attached to the core. There are a variety of motor characteristics that can be achieved by adjusting the arrangement, shapes, and positioning of these magnets [10].

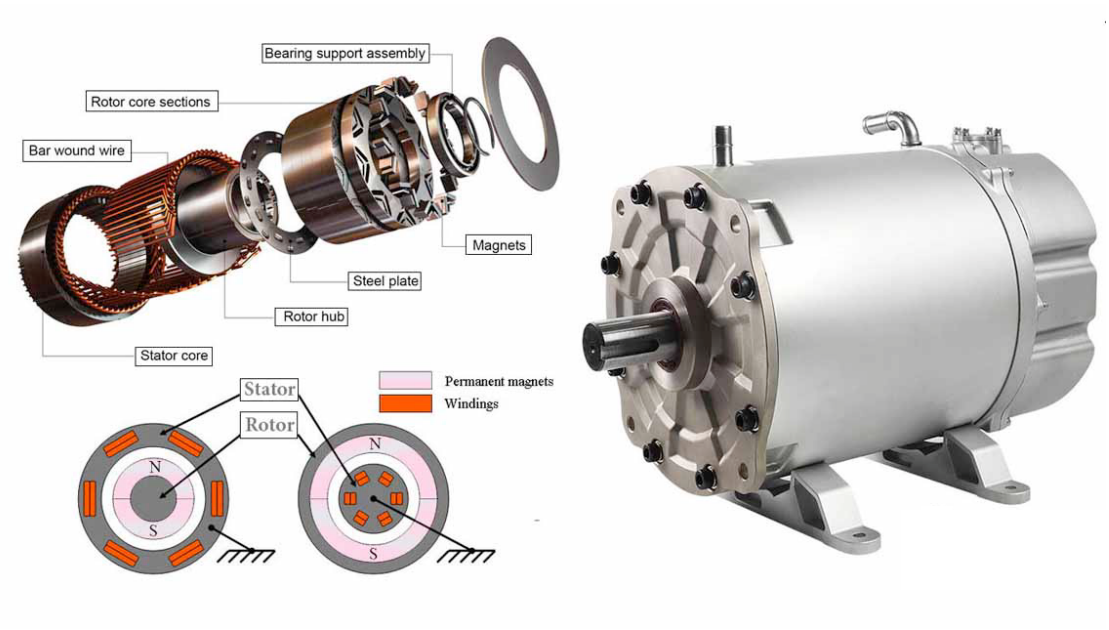

Figure 1.1: PM motor construction [11].

1.3 Application of PM motors in EV water pump

Automotive water pump systems today are dominated by PMSMs and BLDC motors. As outlined in [12], there has been an effort to optimize BLDC motor designs for water pump applications in EVs, balancing cost, performance, and lifespan.

A different perspective is presented in [13] which examines the process of designing and analyzing electrical machines, with a special focus on PMSMs for automotive applications. In addition to providing an overview of the design process, the paper offers insights into two primary design approaches: analytical design and computer-aided design (CAD).

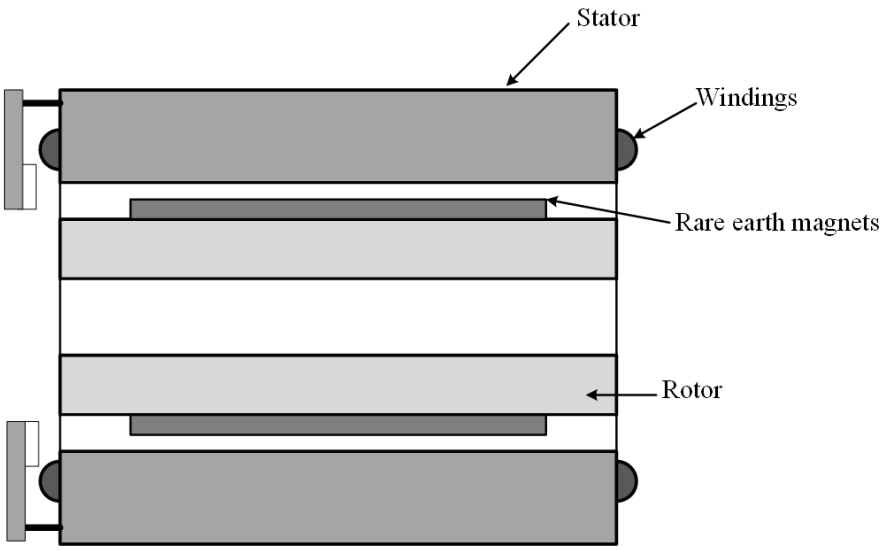

Figure 1.2: Cross section of a frameless brushless PM motor [10].

Accordingly, [14] explores how axial flux motors could replace traditional radial flux motors in electrical pumps taking advantage of high pressure and low flow transmissions. The purpose of this approach is to decrease bearing friction, achieve levitation, and thus increase the efficiency and lifespan of the pump.

Among the control methods employed for PMSMs, FOC method has long been a standard method for regulating speed and torque. One of the most popular control schemes is the Proportional-Integral-Derivative (PID) controller, which is especially simple to configure and implement. However, the fixed gain characteristics of this system pose a challenge in dynamic EV systems with frequently changing operating conditions [15].

In the absence of a position sensor, observer-based controls are usually used in motor control, making it possible to perform sensorless control and optimize efficiency. Various techniques, such as the Extended Kalman filter (EKF), model reference adaptive system (MRAS) method, high-frequency signal injection (HFSI), sliding-mode observer (SMO), and flux observer, have been proposed to estimate rotor speed and position accurately [16–20].

In the automotive industry, achieving sensorless control that is cost-effective and efficient is challenging due to feedback signal noise on the motor side. Due to torque ripples, motor stalling, and cogging caused by signal noise when position sensors are

unavailable, extensive studies are necessary to make a balance between cost-efficiency and performance [12].

1.4 Thesis structure

Taking into account the points discussed earlier, PM brushless motors, specifically PMSMs, have been selected as the ideal choice for the water pump application. This thesis focuses on the flatness-based control method among the various methods available for PMSMs. This particular control approach excels in the precise tracking of reference signals and superior dynamic performance.

Moreover, traditional linear controllers may have difficulties controlling PMSM systems, given their inherent nonlinearity. There can be problems when the system's operational conditions change frequently, or when saturation effects cannot be ignored. It is especially important when the motor is designed to operate in a nonlinear mode to minimize costs.

Traditional flatness-based control methods can generally be divided into two categories. The first category consists of cascaded controllers, which sacrifice rapid dynamic performance. In the second category, you can find one-loop controllers, which often compromise motor current protection.

The objective of this research is to introduce a novel control method based on flatness-based control for driving PMSM motors. With the one-loop control structure, it is possible to predict the motor current through the system's model. With the help of trajectory function planning, the prediction is then used to control the motor providing fast dynamic performance and motor current protection.

Following is the structure of the thesis manuscript:

A detailed discussion of BLDC motors is presented in Chapter 2. This chapter introduces BLDC motors by describing their structure, essential characteristics, and modeling. Subsequently, it provides an overview of the general drive principles for BLDC motors, as well as an examination of various drive strategies. Hall-position sensor-based approaches and sensorless techniques are also discussed in the chapter for controlling BLDC motors.

BLDC motors have been controlled with several sensorless control methods, including methods based on terminal voltage sensing, third-harmonic techniques, back-EMF

voltage analysis, fuzzy control, neural network, PM flux linkage utilization, and stochastic filters. Additionally, this thesis addresses recent research developments concerning the control of BLDC motors in the presence of nonideal and asymmetric back-EMFs. Lastly, simulation results are presented in Chapter 2.

It's worth noting that during the second year of the project, the motor used in the parallel thesis (which focused on designing a water pump motor) transitioned from BLDC to PMSM. This transition was guided by the superior features of PMSM when considering the trade-off between cost, efficiency, and motor performance. As a result, no further testing or analysis has been conducted on BLDC motors, and the subsequent chapters of this thesis will center on the study of PMSM drives.

Chapter 3 explores the operation of PMSMs. The first section of the chapter provides an overview of the PMSM drive system, emphasizing the model and equations in the dq-frame. The chapter then examines sensorless control techniques as well as other control strategies. It also discusses in detail how different control methods for low-speed and high-speed applications can be employed.

Furthermore, the chapter introduces the PMSM testbench setup and outlines the parameter identification tests. It also presents simulation and experimental results for FOC, as well as a theoretical approach to tuning the controller coefficients.

In Chapter 4, flatness-based control is extensively explored for PMSMs. The chapter begins with a review of flatness control theory, which shows that the PMSM drive system exhibits flatness characteristics. There will be a survey of the existing literature on flatness-based control. Research developments in flatness-based controllers, trajectory planning, and state observers will be presented as well. Then, a comparison is made between conventional flatness-based control and FOC method.

Moreover, in order to address the controller limits of flatness control in a one-loop structure, a novel trajectory planning method is proposed, with an in-depth analysis of how it is implemented. The chapter also discusses the use of load torque and resistance observers to enhance the dynamic performance and robustness of flatness-based control. The efficacy of the proposed method is verified through simulation studies and experimental tests, which highlight its advantages over conventional methods.

As the concluding chapter of the thesis, Chapter 5 summarizes the key findings and insights drawn from the preceding chapters. It highlights potential steps for further research and development, paving the way for further exploration.

Chapter 2

Drive of BLDC Motors

Contents

2.1 Introduction

As mentioned in the previous chapter, PM motors, including BLDC motors, have been employed in various industries, particularly in EV applications. In this chapter, a comprehensive review of BLDC motor drives has been conducted. This chapter starts with the exploration of BLDC motor drives, providing an in-depth understanding of their operation, models, and system equations in Section 2.2. Section 2.3 outlines the general drive mechanisms used for BLDC motors, emphasizing their operational characteristics and challenges.

Section 2.4 presents a comprehensive review of sensorless control methods for BLDC motors. Several sensorless control methods, including those based on terminal voltage measurement, third harmonic back-EMF signals, back-EMF integration, fuzzy control, and neural networks, as well as those based on PM flux linkage, stochastic filters, and observers, have been investigated and compared based on their advantages and

drawbacks.

Sections 2.5 and 2.6 are dedicated to recent research, which deal with issues regarding the nonideal back-EMF and asymmetric back-EMF characteristics in BLDC motor control. These methodologies provide innovative solutions to real-world challenges, ensuring optimal motor performance.

Section 2.7 presents simulation results for driving BLDC motors using Hall position sensors and a sensorless method. Finally, in Section 2.8, the conclusion and key points of this chapter are provided.

2.2 BLDC motor

The stator structure of a BLDC motor closely resembles that of a typical synchronous or induction motor. In this type of winding, one- or multiphase windings are wound within a core of iron, and they are connected in either a "Y" or "Δ" configuration. As a result of both cost and performance factors, Y-type connections are most frequently used. In contrast to brushed DC motors where the armature winding is located within the rotor, BLDC motors have the armature winding located on the stator side. In addition to reducing heating, this placement contributes to the motor's efficiency and longevity [21].

Figure 2.1 shows a simple two-pole motor with a 180-degree magnetic pole arc. Each phase of the three-phase stator winding in this motor consists of two slots. Figure 2.2 illustrates how a BLDC motor behaves when there is no fringing within the air gap. The rotation of the rotor induces a voltage within the stator windings, and the position of the rotor affects the magnetic field's strength linearly. There are maximum strengths of positive and negative magnetic fields at 0 degrees and 180 degrees, respectively. Furthermore, in each switching period of a BLDC motor, only two phases of a star-connected motor conduct electricity, while the third phase remains unexcited [10].

2.2.1 BLDC motor model

BLDC motors have similar torque and voltage equations to DC brushed motors [22]. Figure 2.3 illustrates a block diagram of the general drive system used for a BLDC

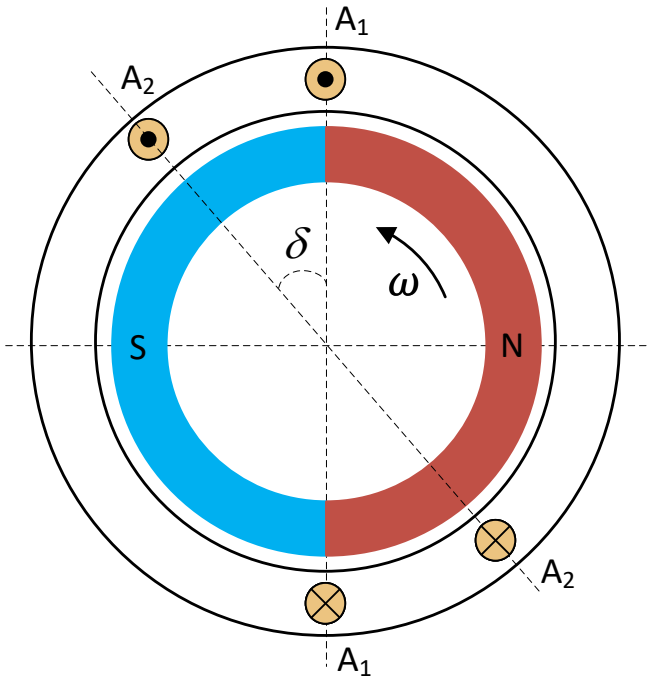

Figure 2.1: Cross-section of an ideal BLDC motor with two coils in one phase (A_1 and A_2), δ is equal to 30° in this case [10].

motor. From an electrical point of view, BLDC motors can be represented as follows:

$$V = Ri + \frac{d}{dt}[L(\theta)i + \lambda_M] = Ri + L(\theta)\frac{di}{dt} + i\omega\frac{d}{d\theta}L(\theta) + e \tag{2.1}$$

Where V, i, and e represent the motor phase terminal voltage, current, and back-EMF, respectively. In addition, stator impedance and inductance are represented by R and L, respectively. Parameters θ and ω are rotor phase angle and angular velocity.

It is important to note that $i\omega\frac{d}{d\theta}L(\theta)$ is zero since inductance does not change with position. As a result, the model can be simplified as follows:

$$\begin{bmatrix} V_a \\ V_b \\ V_c \end{bmatrix} = \begin{bmatrix} R & 0 & 0 \\ 0 & R & 0 \\ 0 & 0 & R \end{bmatrix} \begin{bmatrix} i_a \\ i_b \\ i_c \end{bmatrix} + \begin{bmatrix} L & 0 & 0 \\ 0 & L & 0 \\ 0 & 0 & L \end{bmatrix} \frac{d}{dt} \begin{bmatrix} i_a \\ i_b \\ i_c \end{bmatrix} + \begin{bmatrix} e_a \\ e_b \\ e_c \end{bmatrix} \tag{2.2}$$

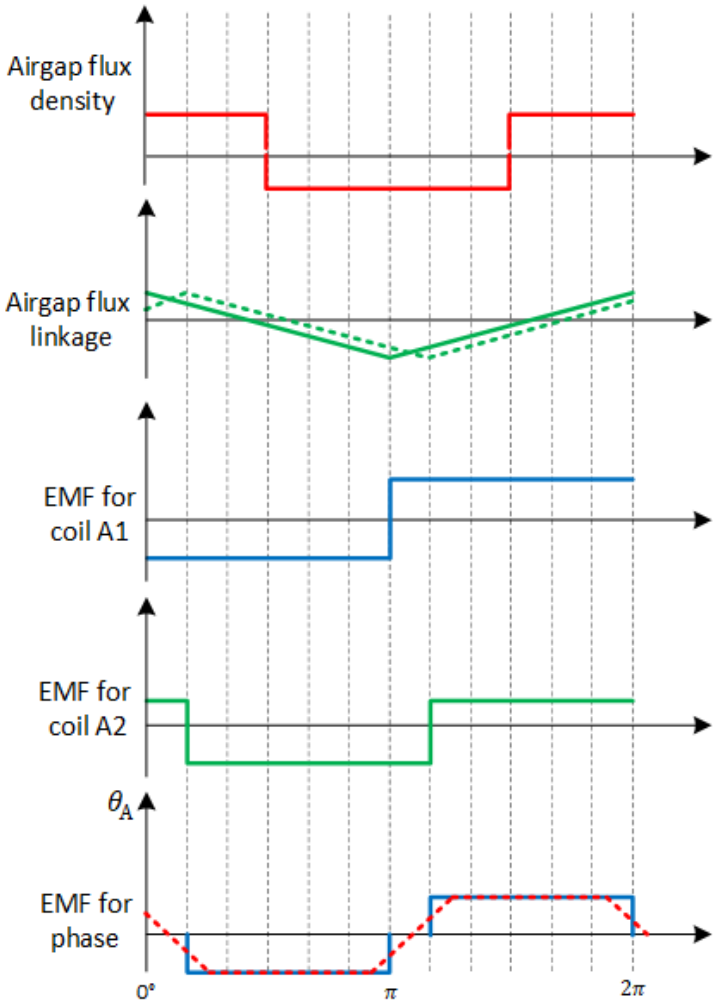

Figure 2.2: Waveforms for an ideal BLDC motor including airgap flux density, airgap flux linkage, and EMF for each coil and one phase; the actual phase back-EMF (red dotted curve) is trapezoidal due to magnetic fringing and motor construction [10].

where i_a, i_b, and i_c are phase currents, V_a, V_b, and V_c are phase voltages, and e_a, e_b, and e_c are phase back-EMF voltages. It should be mentioned that $L = L_s - M$, that L_s is the stator self-inductance and M is the mutual inductance between two phases. As $i_a + i_b + i_c = 0$, the inductance matrix is simplified as described in (2.3).

$$\begin{bmatrix} L_s & M & M \\ M & L_s & M \\ M & M & L_s \end{bmatrix} \frac{d}{dt} \begin{bmatrix} i_a \\ i_b \\ i_c \end{bmatrix} = \begin{bmatrix} L & 0 & 0 \\ 0 & L & 0 \\ 0 & 0 & L \end{bmatrix} \frac{d}{dt} \begin{bmatrix} i_a \\ i_b \\ i_c \end{bmatrix} \tag{2.3}$$

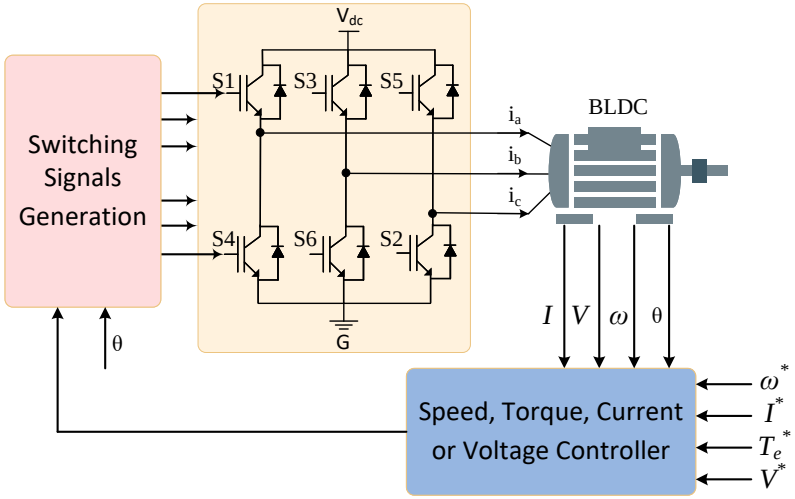

Figure 2.3: Structure of the general BLDC motor drive featuring a three-phase inverter, including a controller block for parameter regulation based on the control strategy, and a switching signals generation block for switch pair determination [23].

The electromagnetic torque of the BLDC motor can be expressed as follows:

$$T_e = \frac{1}{\omega}(e_a i_a + e_b i_b + e_c i_c) \tag{2.4}$$

When there is no phase difference between the back-EMF and the current, then the electromagnetic torque can be calculated as:

$$T_e = \frac{2EI}{\omega} \tag{2.5}$$

where E and I are back-EMF voltage peak amplitude and DC-link current amplitude.

In addition electromagnetic torque can be expressed as:

$$T_e = T_L + J\frac{d\omega}{dt} + B\omega \tag{2.6}$$

where, T_L is load torque, J is inertia, and B is the viscous damping.

Figure 2.4 illustrates the waveforms of the back-EMF and phase currents in an ideal three-phase BLDC motor. As mentioned earlier, the motor demonstrates a trapezoidal

back-EMF voltage pattern and square-wave phase currents due to the fact that one of the three phases remains inactive during each conduction period.

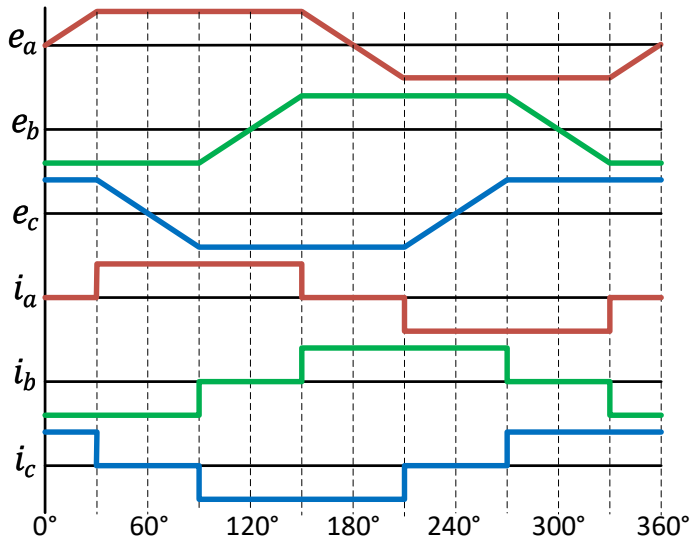

Figure 2.4: Back-EMF and phase current waveforms of an ideal BLDC motor.

2.3 BLDC motor drive

Control strategies play a crucial role in regulating desired motor parameters such as speed, torque, and current. These strategies are implemented by the drive system as described and reviewed in [23]. The sensorless control strategies generate switching signals based on the rotor's position within every 60 degrees of electrical rotation that determine which switch pair should be selected for the three-phase inverter.

To effectively control a BLDC motor, information about the rotor's position and speed is essential. Various mechanical position sensor methods, including Hall sensors, photoelectric encoders, and rotary transformers, are commonly employed for this purpose, as discussed in [24,25]. However, traditional position sensors have some drawbacks. They not only increase the motor's size and inertia but also reduce its power density, add complexity to the system, and makes the system more expensive. Additionally,

these sensors are sensitive to temperature variations and electromagnetic interference. The accuracy of sensor installation can affect the motor performance, especially in motors with a higher number of poles, as highlighted in [26]. Consequently, sensorless control methods have received considerable attention in recent literature as effective solutions to address these issues [23, 27].

2.4 Sensorless control methods for BLDC motors

Sensorless control is a method employed to control BLDC motors without the need for external position sensors [28]. Instead of relying on conventional position and speed sensors, sensorless control methods employ various techniques to estimate the rotor's position and commutation timing [29]. These techniques typically involve monitoring motor current, voltage, or back-EMF signals to determine the rotor's position [30, 31]. Sensorless control systems alleviate complexity, improve reliability, and reduce costs by eliminating external position sensors. Several industries such as automotive, robotics, and home appliances have adopted sensorless techniques for controlling PM motors [32, 33].

A review of BLDC motors including their structure, design, modeling, and drive can be found in [34]. However, this review does not provide a comprehensive overview of sensorless control methods for BLDC motors. Another review focusing on sensorless control for BLDC motors is presented in [35]. Nevertheless, it does not address the latest advancements in this field, especially concerning issues associated with BLDC motors with nonideal and asymmetrical back-EMFs.

2.4.1 Sensorless control methods based on zero-crossing point (ZCP) approach (terminal voltage sensing)

Model-based techniques are commonly employed in medium- and high-speed applications [36–38]. A sensorless control method for an automotive fuel pump BLDC motor is presented in [39, 40]. In this method, the back-EMF signal is acquired by measuring the voltage of the unexcited motor phase, as depicted in Figure 2.5. The voltage expressions when phase C is unexcited and current flows through phases A and B in the converter can be determined by neglecting the forward voltage of switches and diodes:

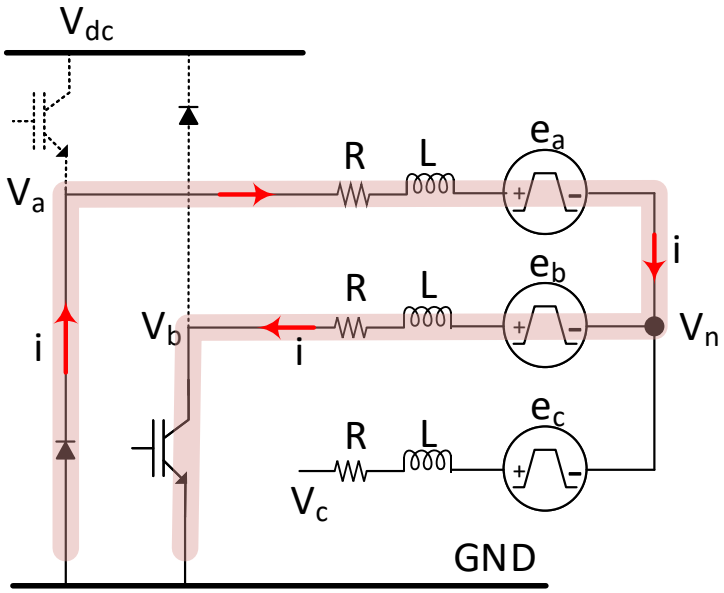

Figure 2.5: Back-EMF detection in the PWM off-time moment, in this example, phase C is unexcited [40].

$$\begin{cases} V_n = -Ri - L\dfrac{di}{dt} - e_a \\ V_n = +Ri + L\dfrac{di}{dt} - e_b, \end{cases} \tag{2.7}$$

where parameter V_n is the neutral point voltage. Equation (2.7) leads to:

$$V_n = -\frac{e_a + e_b}{2} \tag{2.8}$$

Assuming the motor phases to be balanced ($e_a + e_b + e_c = 0$), the terminal voltage V_c is equal to:

$$V_c = e_c + V_n = \frac{3}{2}e_c \tag{2.9}$$

Therefore, the measured terminal voltage for an unexcited phase is proportional to the back-EMF voltage for the phase. Commutation signals can be derived from the

ZCPs of the back-EMF voltage, and these ZCPs are equivalent to those found in the terminal voltage of the unexcited phase [40–44].

There have been numerous sensorless methods for detecting commutation points in BLDC motors. For this purpose, [45] utilized the symmetric terminal voltages of the unexcited phase. There is also an approach described in [46] that involves a four-switch position sensorless method for BLDC motor drives. Researchers in [47] have investigated BLDC motor safety operations controlled with sensorless techniques using line-to-line voltage measurement to detect ZCPs. Additionally, this study highlights the influence of PWM patterns on sensorless control performance. The paper evaluates whether the motor is theoretically capable of running at predetermined speeds and torques based on the parameters provided.

However, it is important to note that sensorless methods relying on terminal voltage measurements may yield unreliable results when motor speeds are close to zero, since the back-EMF is extremely low at low speeds [48, 49]. In order to minimize line-to-line voltage disturbances and improve BLDC motor performance, a LPF incorporating a variable cut-off frequency is proposed in [50]. In Figure 2.6, an overview of the compensation approach is presented, which includes an open-loop method to address phase delays and a closed-loop approach to address uncertainty related to commutation errors. In high-speed applications, the LPF introduces a phase lag, which must be compensated, as discussed in [51, 52].

An alternative sensorless method for detecting ZCPs in BLDC motors is to use virtual line voltage [53]. In [54], a hybrid sensorless driving method incorporating virtual neutral voltage is proposed for high-speed BLDC motors, although high-speed performance remains unaddressed. Similarly, [55] introduces the concept of virtual neutral voltage as another sensorless hybrid control method for BLDC motors. However, it is worth noting that generating commutation signals from voltage signals in these methods can be challenging due to commutation notches and electromagnetic interference. Therefore, a LPF is required in this method.

To address the phase delay introduced by LPFs, [51] presents a sensorless control technique for PMSMs illustrated in Figure 2.7. The method relies on transitioning between two commutation modes: "90 - α" and "150 - α," where α represents the commutation retarding angle.

When α falls below 90 electrical degrees, it causes Z_1 to shift to Q_1 before M_1. To

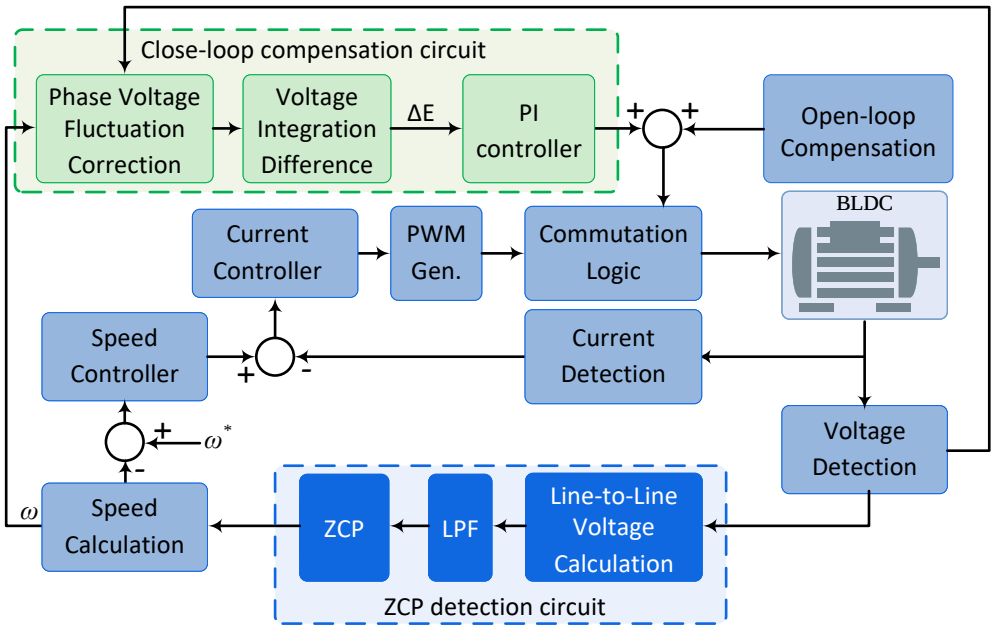

Figure 2.6: Sensorless control method proposing open-loop and close-loop compensation blocks [50].

ensure precise commutation signaling, Q_1 should be advanced by 90 – α degrees (where 90 – α > 0 must be met) to align with the exact commutation point M_1. In medium- and high-speed applications, the LPF introduces a phase lag greater than 90 electrical degrees. Consequently, utilizing the "90 – α" commutation mode may make the system unstable. To implement the "150 – α" mode, Q_1 must be adjusted by 150 – α degrees (where 150 – α > 0) to align precisely with the commutation point N_1. It's essential to recognize, however, that this method is subject to a conductivity error, as discussed in [51].

In [56], an approach is presented to mitigate the commutation torque ripple in BLDC motor drives utilized in air conditioners. However, this method does not include stator current control.

Figure 2.8 illustrates a position sensorless control scheme proposed [57, 58], designed for BLDC motors employed in Photovoltaics (PV)-based water pump applications. In this approach, a LPF is used to detect back-EMF signals by measuring line

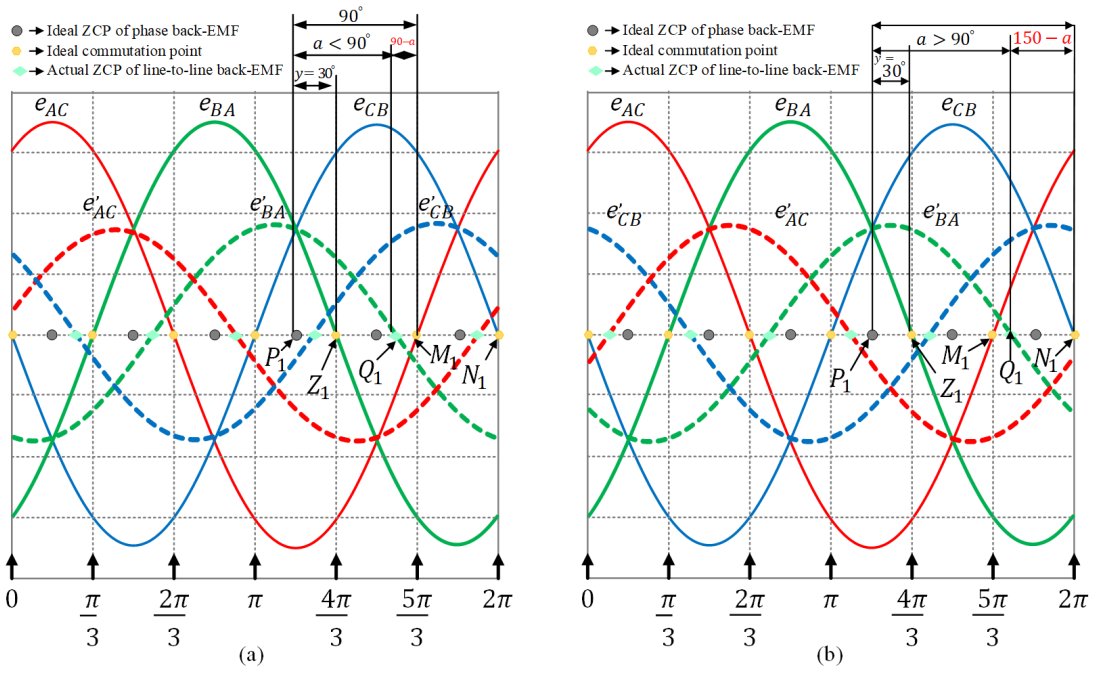

Figure 2.7: Schematic diagram of the "$90-\alpha$" commutation mode and the "$150-\alpha$" commutation mode [51]. (a) "$90-\alpha$" mode. (b) "$150-\alpha$" mode.

voltages.

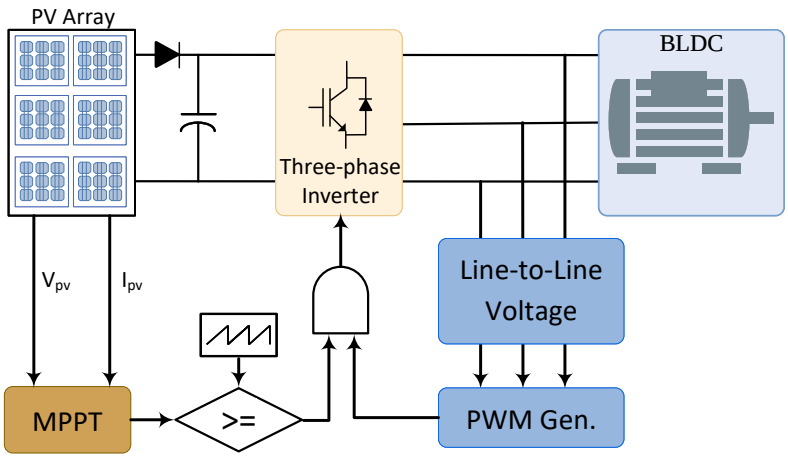

Figure 2.8: Sensorless control method for a PV-based water pump [57].

As a part of the BLDC motor applications, a sensorless control system is presented for a fuel pump in [59]. In this system, a hysteresis comparator is used in conjunction with a high-torque starting mechanism to implement a sensorless approach. Figure 2.9 shows how the hysteresis comparator operates to avoid phase delays caused by LPFs. As well as mitigating noise and transient output transitions, it attenuates voltage ripples caused by external noise. Furthermore, [60] uses a specially designed inverter circuit in order to demonstrate a Fourier-series-based method to minimize phase delays in ZCP detection.

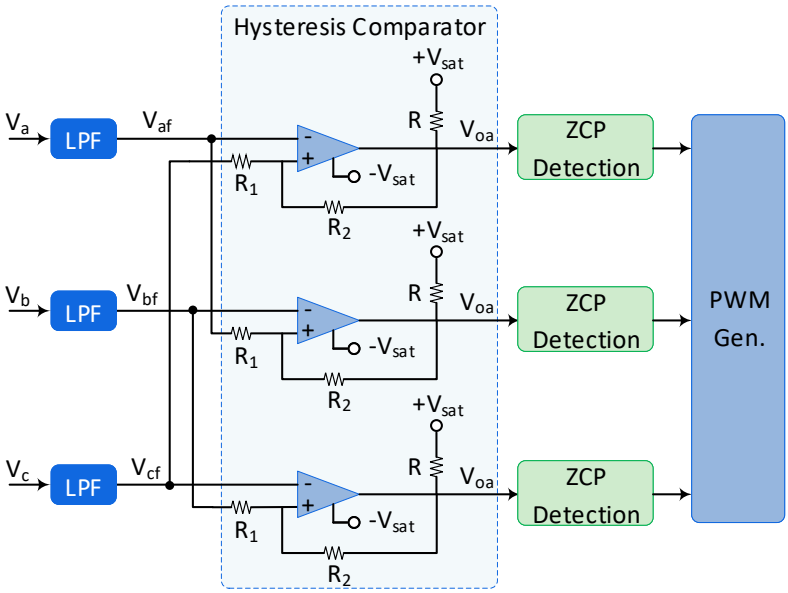

Figure 2.9: Block diagram of sensorless control by using a hysteresis comparator [59].

Back-EMF measurement and terminal voltage measurement have certain limitations. Because of the low magnitude of the back-EMF at low speeds, these methods are challenged to deal with speed fluctuations induced by the LPF, and produce discrete estimates of speed. As a result, achieving effective closed-loop speed control becomes difficult, particularly at low and medium speeds with substantial steady-state variations.

2.4.2 Sensorless control methods based on third harmonic approach

Third harmonic of the back-EMF voltages have been used for sensorless motor control of BLDC motors, which addresses the issues associated with ZCP detection approach based on terminal voltage measurement [61–63]. In contrast to the back-EMF voltage, the third harmonic is not affected by PWM noise. Therefore, higher cut-off frequencies can be achieved for LPFs. Sensorless commutation control systems maintain consistent phase relationships regardless of motor speed using the third harmonic of the back-EMF [61]. However, this method is not applicable at low speeds because of significant noise interference and integral errors.

The third harmonic back-EMF is combined with PLLs in [63] for sensorless control of PM brushless motors. Furthermore, [64] presents an alternative strategy to correct deviations in PLL-based commutation. A sensorless drive method using the third harmonic of the back-EMF is presented in [65] for driving both BLDC motors and PMSMs in flux-weakening mode.

Figure 2.10 illustrates the block diagram of a BLDC motor drive system employing a control method based on the virtual third harmonic of back-EMF signals. By comparing the voltage between the motor's neutral point 'N' and the virtual neutral point 'S', it is possible to determine the rotor's position. However, in some applications the access to the neutral wire is not possible. To overcome this limitation, control methods based on virtual third harmonic back-EMF have been presented in [61, 66, 67]. In these methods, the position signal is determined by measuring the voltage between the virtual neutral point 'S' and the midpoint of the DC-link 'P' (u_{SP}), where V_{dc} is the DC-bus voltage.

As shown in [66], during the conduction periods of S_3 and S_4, u_{SP} derives as follows:

$$u_{SP} = \frac{1}{3}(e_c - \frac{e_a + e_b}{2}) \tag{2.10}$$

Signal u_{SP} operates at three times of fundamental phase back-EMF frequency, which coincides with its third harmonic frequency. Consequently, both u_{SP} and the back-EMF third harmonic have the same ZCPs, as illustrated in Figure 2.11. To determine the rotor position of BLDC motors, a synchronization-frequency filter based on the u_{SP} signal utilizing a second-order generalized integrator-based phase-locked loop

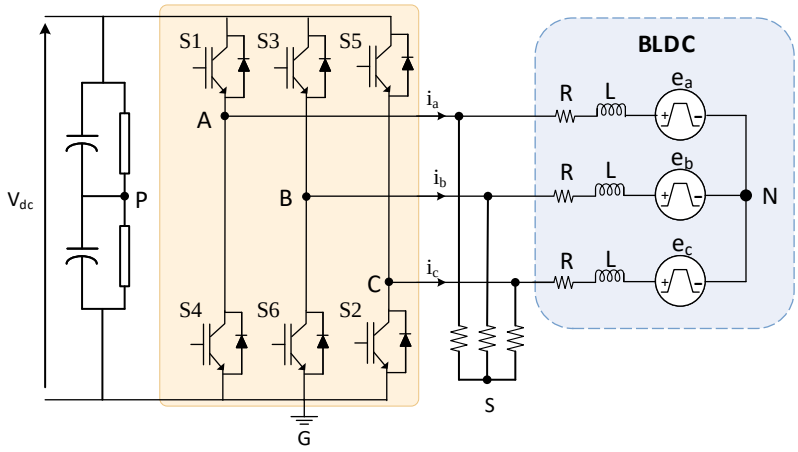

Figure 2.10: Diagram of the drive system using a sensorless method based on virtual third harmonic voltage [66].

(SFF-SOGI-PLL) is proposed in [66].

A sensorless control method based on third harmonic flux linkage was discussed in [68] as an alternative sensorless drive method. As shown in Figure 2.12, the flux linkages are generated through the integration of the third harmonic back-EMFs (u_{sn}). Instead of relying on zero crossings of the third harmonic flux linkage, an alternative approach utilizes a continuous sinusoidal signal (ψ_{sn}) as a reference [68].

2.4.3 Sensorless control method based on back-EMF integration

Several studies have proposed back-EMF integration as a method for detecting the position of BLDC motors [69–73]. This method integrates the back-EMF of the unexcited phase. However, the method has issues when it is applied to low-speed motors, due to the accumulation of errors.

Alternative sensorless methods include back-EMF integration and PLLs. The PLL is used to keep the integral result at zero. There are, however, limitations to this method, particularly when dealing with heavy loads and high-speed commutation errors that can result in voltage distortions at terminals. It has been demonstrated that commutation errors can be compensated by integrating over adjacent 60-degree intervals before and after a commutation event [74].

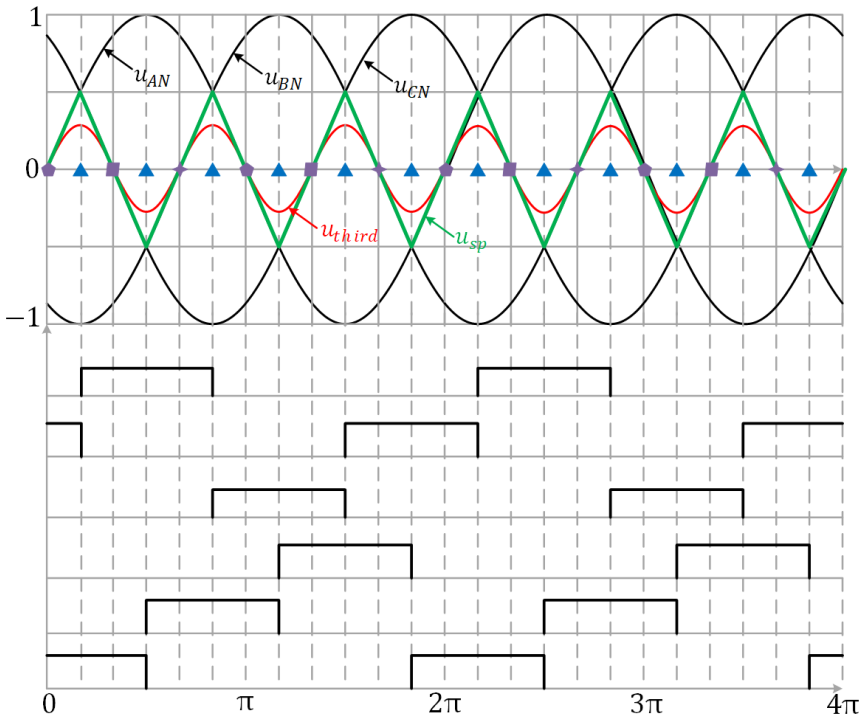

Figure 2.11: Relationships between the phase back-EMFs, the third harmonic back-EMF, voltage u_{SP}, and the commutation points [66].

A second method based on back-EMF integration is introduced in [75], which improves commutation accuracy by two significant factors. At first, integral thresholds are dynamically adjusted to take into account LPFs and system delays. Secondly, an integral prediction method is used to estimate the commutation points to reduce errors caused by inadequate sampling during commutation [75].

2.4.4 Sensorless control method based on fuzzy control and neural network

Sensorless control of BLDC motors has been investigated using fuzzy logic controllers, as outlined in [76, 77]. Despite offering a superior dynamic response to linear PI controllers, this approach is more challenging to design and implement.

It is also possible to estimate the rotor position using the freewheeling current in the unexcited phase [78]. The implementation of this approach poses a challenge due to the

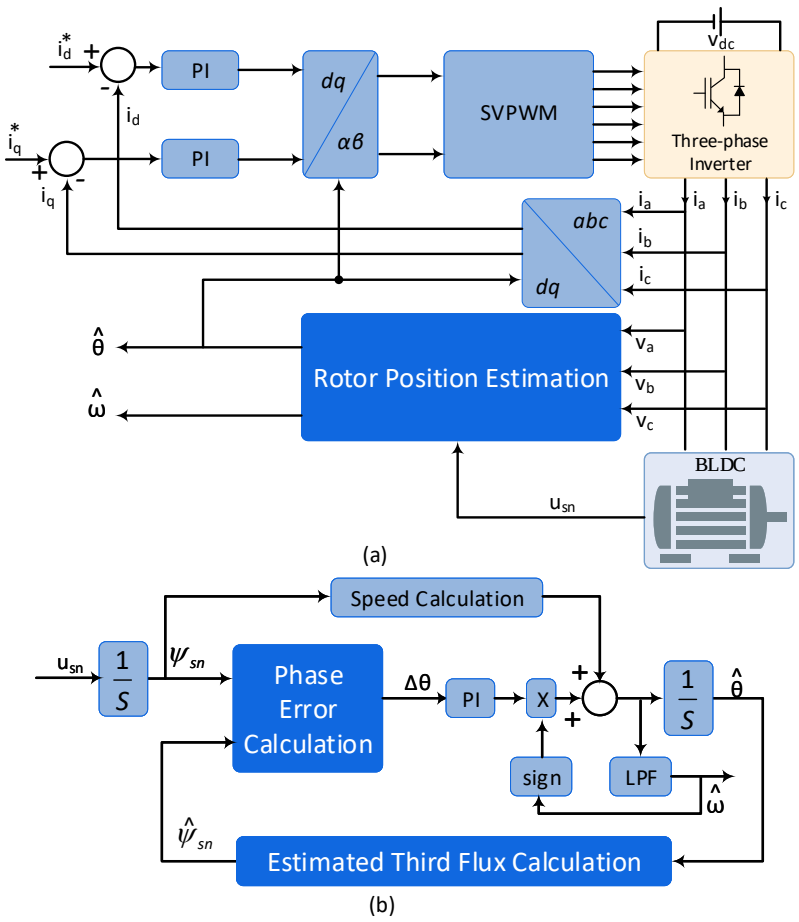

Figure 2.12: Schematic of the control method using back-EMF third harmonic in [68] (a) Overall scheme (b) Rotor position estimator.

complexity of the hardware required. The authors in [79] have introduced a fuzzy model to estimate and compensate for the error in the motor's estimated position. However, high-speed motor control schemes can be quite complex to estimate. A sensorless fuzzy logic commutation control scheme using equal area criteria is presented in [80].

Sensorless methods are being developed with neural networks in order to enhance detection accuracy [81, 82]. An alternative approach involves the use of a sensorless neuro-fuzzy inference system (ANFIS) based on a multisector space vector PWM method (MS-SVPWM), as detailed in [83]. This method not only reduces DC-bus voltage ripple, torque ripple, and total harmonic distortion but also minimizes switching

losses, leading to increased system efficiency. Additionally, [84] presents a sensorless method utilizing a phase-error correction algorithm based on a neuro-fuzzy controller for BLDC motors. Authors in [85] propose a sensorless start-up current control method based on adaptive neural network inverse for high-speed BLDC motors, although its complexity results in implementation challenges.

2.4.5 Sensorless control method based on PM flux linkage

The application of flux-linkage (the linkage of magnetic flux produced by the stator windings with the rotor, or more precisely, with the PMs on the rotor) estimation method to sensorless control of PM motors was presented in [86–88]. However, as a result of its complexity, sensitivity to motor parameters, and error accumulation at low speeds, this method may not be appropriate for certain applications. To address these limitations, an alternative method is presented in [89]. This method employs a speed-independent flux linkage function to estimate the commutation points of BLDC motors, utilizing the G-function method outlined in [90], as illustrated in Figure 2.13.

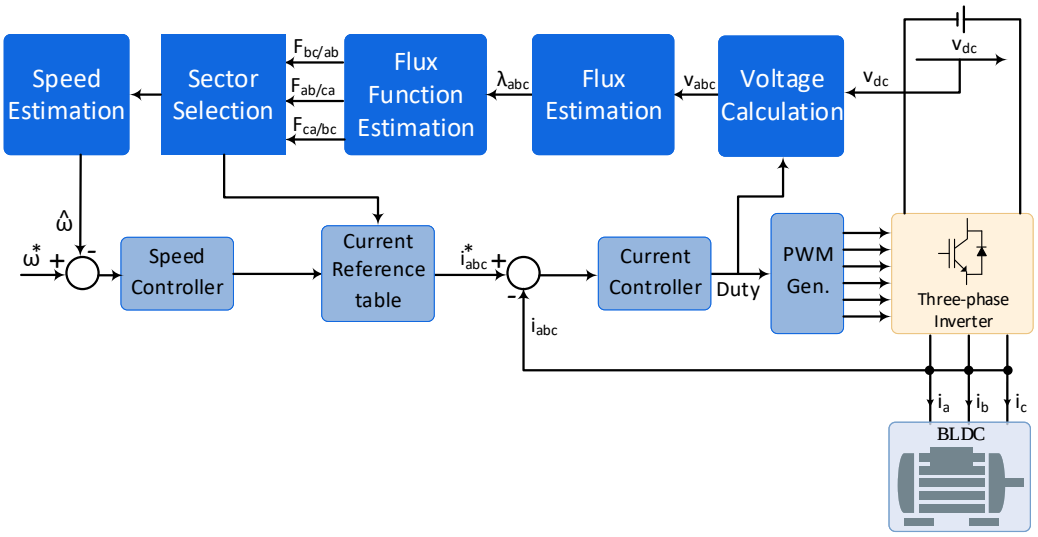

Figure 2.13: Sensorless control method for the BLDC motor using flux-linkage function [89].

Considering the equations of BLDC motors, the line-to-line PM flux linkage for

these motors (λ_{ab}, λ_{bc}, and λ_{ca}) can be expressed as follows:

$$\begin{cases} \lambda_{ab} = \int_0^t [(V_a - V_b) - R(i_a - i_b)]\, dt - L(i_a - i_b) \\ \lambda_{bc} = \int_0^t [(V_b - V_c) - R(i_b - i_c)]\, dt - L(i_b - i_c) \\ \lambda_{ca} = \int_0^t [(V_c - V_a) - R(i_c - i_a)]\, dt - L(i_c - i_a) \end{cases} \tag{2.11}$$

In order to determine the commutation point for phase a, it is necessary to introduce a 30-degree electrical delay to the ZCPs of the line-to-line flux linkage λ_{bc}. The ratio of line-to-line flux linkage is suggested as the flux linkage function in this approach. For example,

$$F_{ab/bc} = \frac{\lambda_{ab}}{\lambda_{bc}} \tag{2.12}$$

By using flux-linkage functions, it is possible to detect commutation points, which are usually small, except at extreme points, when they increase significantly. As illustrated in Figure 2.14, the rapid change in the flux-linkage function coincides with the ZCPs of the line-to-line flux linkage. It is therefore possible to determine the commutation points by delaying these jumping edges by 30 electrical degrees.

2.4.6 Sensorless control methods using stochastic filters and estimation approaches

Observer controllers and estimation techniques have been the focus of sensorless control methods [91–100]. The integration of stochastic filters into control systems has been proposed to address system uncertainties and external noise.

In [93], a sensorless method based on back-EMF mapping is discussed, while in [94], torque constants serve as a reference for a sensorless approach. For sensorless control of brushless motors, a SMO scheme is highlighted in [95, 96]. It has been suggested to replace the LPF with a more advanced Second Order Generalized Integrator (SOGI) in [101]. To enhance position estimation accuracy, [102] utilizes an SMO in conjunction with Dual SOGIs and a Frequency Locked Loop (FLL).

Due to insufficient filtering, conventional SMOs suffer from chattering and distorted estimated back-EMF [103, 104]. Consequently, high-order SMOs are preferred for reducing chattering and enhancing convergence time [105]. Furthermore, [106] introduces

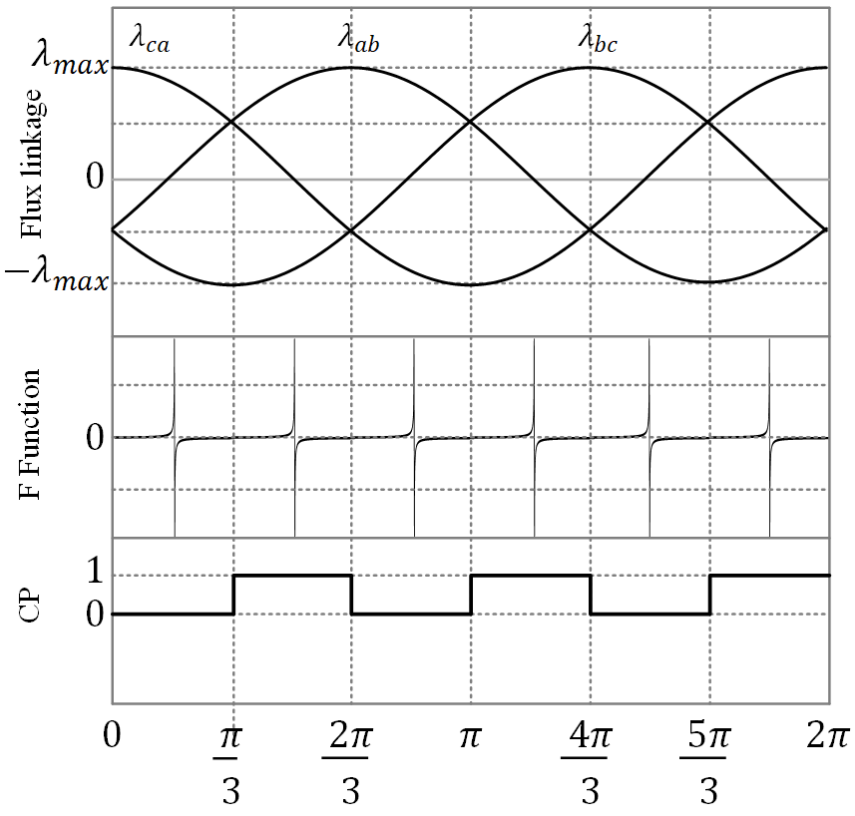

Figure 2.14: Relation between line-to-line flux linkage signals, flux-linkage function, and commutation points [89].

a second-order SMO with online parameter estimation that accounts for variations in stator resistance due to temperature, resulting in improved stability. To compensate for commutation errors during operation, a dual PLL control system is integrated with a SMO approach presented in [107].

There is also the use of observer-based sensorless control methods, such as Kalman Filters (KF), for controlling BLDC motors [97, 98]. Despite successfully achieving speed control, an inherent error persists in the estimated rotor position derived from this method.

A sensorless direct torque control method for BLDC motors using KF is described in [108]. According to this method, the KF is responsible for estimating the state variable "x_k":

$$\begin{cases} x_k = Ax_{k-1} + Bu_k + \omega_k \\ z_k = Hx_{k-1} + v_k \end{cases} \tag{2.13}$$

Where A represents the state matrix, B stands for the control matrix, H is the output matrix, $x_k = \begin{bmatrix} i_a(k) & i_b(k) & \Omega(k) & \theta(k) & T_e \end{bmatrix}^t$ and x_{k-1} are the current and previous state matrix, and $u_k = \begin{bmatrix} v_a(k) & v_b(k) \end{bmatrix}^t$ is the input state matrix. Also, z_k represents the output state matrix, and ω_k and v_k are process and measurement variables.

It should be noted that the estimated torque using this method can be highly inaccurate due to the limited applicability of the conventional KF model to linear systems. To address this issue, alternative KF control methods, such as the Extended Kalman Filter (EKF) [100, 109, 110], Unscented Kalman Filter (UKF) [111], and Cubature Kalman Filter (CKF) [112], have been developed. In EKF, UKF, and CKF methods, the state vector is typically represented as $x_k = \begin{bmatrix} i_a(k) & i_b(k) & i_c(k) & \Omega(k) & \theta(k) \end{bmatrix}^t$, while u_k is a vector derived from phase or line-to-line terminal voltages and torque load.

In [113], a nonlinear Model Predictive Control (MPC) strategy for BLDC motors is proposed, incorporating online state estimation techniques. This study evaluates three methods: EKF, UKF, and Nonlinear Moving Horizon Estimation (NMHE). According to the findings in [113], the combination of NMHE with nonlinear MPC offers superior performance compared to other estimation methods. However, it comes at the cost of increased computational complexity compared to EKF and UKF.

Furthermore, in [114], a sensorless method based on back-EMF observers is presented. Trapezoidal back-EMFs are considered as unknown inputs, and an unknown input observer is proposed for real-time estimation of line-to-line back-EMFs, as illustrated in Figure 2.15.

The different sensorless control methods for BLDC motor drive application presented in this section are summarized in Table 2.1.

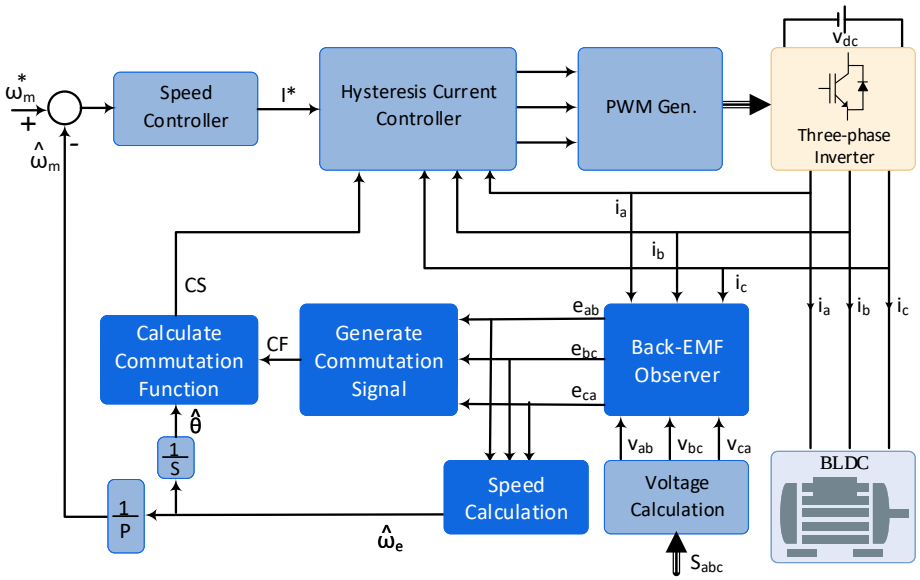

Figure 2.15: Sensorless control based on back-EMF observer [114].

Table 2.1: Comparison of different sensorless control methods for BLDC motor drive.

Method	Technique	Advantages	Disadvantages
Terminal voltage sensing	ZCP detection based, phase shift compensation	Easy to implement	Difficult ZCP detection at low speed, Phase lag error at high speed
Third harmonic approach	Virtual third harmonic measuring, Third harmonic integration	Not affected by PWM noise, Higher cut-off frequency for LPF	Integral errors at low speed
Back-EMF integration	Integrating the back-EMF of the unexcited phase	Can be used for wider range of speed	Accumulation of errors at low speed, Terminal voltage distortions at high speed
Fuzzy control and neural network	Fuzzy logic controllers, Artificial neural network	Higher accuracy, Superior dynamic performance	Complex algorithms
PM flux-linkage function	Estimation of PM flux linkage, G-function method	Not affected by noise, Speed-independent flux linkage function	Sensitivity to motor parameters, Error accumulation at low speeds
Stochastic filters	Different type of Kalman Filters, Model Predictive Control, Nonlinear Moving Horizon Estimation	Dealing with system uncertainties and external noise, Dealing with nonlinear systems	Computational complexity, Tuning challenge
Observers	Back-EMF observers, Sliding mode observers	Can be used for wider range of speed	Sensitivity to motor parameters

2.5 Sensorless control for BLDC motors with nonideal back-EMF

In many applications, especially those involving high-speed BLDC motors with low inductance, the back-EMF signals deviate from an ideal trapezoidal form, as shown in Figure 2.16 [115, 116].

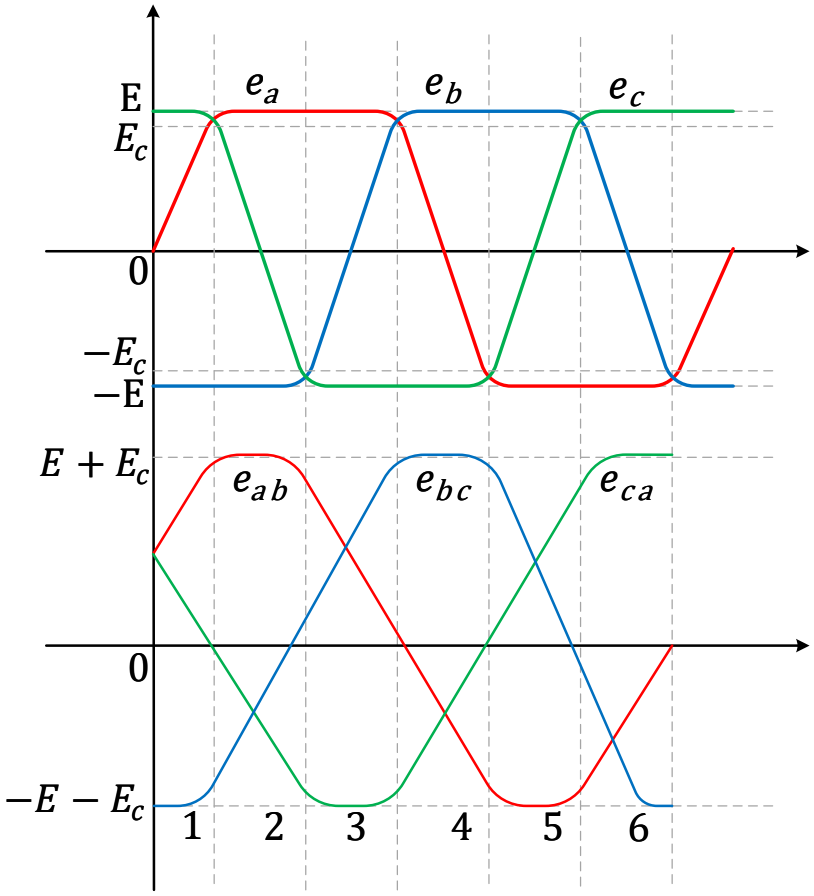

Figure 2.16: Nonideal back-EMF voltages of a high-speed BLDC motor.

The shape of the back-EMF signals is influenced by the commutation process [117]. For instance, when the current transitions from phase a to phase b, phase a's current does not drop directly to zero; it decreases gradually. Some of this current flows through the freewheeling diode during commutation. The voltage values at that point are $V_a = 0$,

$V_b = V_{dc}$, $V_c = 0$, $e_a = e_b = E_c$, and $e_c = E$. Where, "E" represents the absolute magnitude of the phase back-EMF voltage, while "E_c" is the magnitude at the point where two phase back-EMF voltages intersect. Therefore, the differential equations for stator currents are as follows:

$$\begin{cases} Ri_a + L\dfrac{di_a}{dt} = -\dfrac{V_{dc} + E + E_c}{3} = v_{a,com} \\ Ri_b + L\dfrac{di_b}{dt} = \dfrac{2V_{dc} - E - E_c}{3} = v_{b,com} \\ Ri_c + L\dfrac{di_c}{dt} = -\dfrac{V_{dc} - 2E - 2E_c}{3} = v_{c,com} \end{cases} \tag{2.14}$$

Taking the initial conditions for phase currents into account, i.e. $i_{a,0} = I_{dc}$, $i_{b,0} = 0$, $i_{c,0} = -I_{dc}$, the phase currents during the commutation period will be the following:

$$\begin{cases} i_a = \dfrac{v_{a,com}}{R} + (I_{dc} - \dfrac{v_{a,com}}{R})e^{-\dfrac{R}{L}t} \\ i_b = \dfrac{v_{b,com}}{R} - \dfrac{v_{b,com}}{R}e^{-\dfrac{R}{L}t} \\ i_c = \dfrac{v_{c,com}}{R} - (I_{dc} + \dfrac{v_{c,com}}{R})e^{-\dfrac{R}{L}t} \end{cases} \tag{2.15}$$

The duration for the current in phase a to decrease from I_{dc} to zero and for the current in phase b to increase from zero to I_{dc} can be computed as follows:

$$\begin{cases} t_a = \dfrac{3LI_{dc}}{3RI_{dc} + V_{dc} + E + E_c} \\ t_b = \dfrac{3LI_{dc}}{2V_{dc} - E - E_c} \end{cases} \tag{2.16}$$

In low-speed range, $V_{dc} \geq 3RI_{dc} + 2E + 2E_c$. Therefore, $t_a \geq t_b$ and $t_a \leq \dfrac{LI_{dc}}{2RI_{dc} + E + E_c}$. In medium and high-speed range, $V_{dc} \leq 3RI_{dc} + 2E + 2E_c$. Therefore, $t_a < t_b$ and $t_b \leq \dfrac{LI_{dc}}{2RI_{dc} + E + E_c}$. It has been shown in [115] that the commutation interval decreases when the motor speed increases.

Commutation points obtained by (2.16) are not accurate and require compensation, especially in the medium- and high-speed range [117]. The position error is composed of the error due to the voltage drop on the stator resistance, phase delay of LPF, system

delay, and error due to abnormal conduction of the freewheeling diode in the unexcited phase [118]. In [119], an Extended State Observer (ESO) method is introduced for estimating the BLDC motor's back-EMF signals. The commutation error is calculated based on the estimated back-EMF. Unlike the conventional closed-loop correction method, which relies on back-EMF symmetry, the ESO-based approach for compensating commutation errors excels at determining errors within a single commutation cycle.

2.6 BLDC motor drive in presence of asymmetric back-EMF

It is possible for sensorless switching signals to be affected by asymmetric motor parameters such as stator resistance and inductance. As well as motors with asymmetric parameters, DC-link voltage drops and DC-link offset voltages can also cause unbalanced ZCP detection. The ZCPs deviate from their ideal positions when motors have asymmetric parameters, as illustrated in Figure 2.17. As a result, the commutation system produces signals that are inaccurate, posing challenges for the control system. Furthermore, it can lead to increased fluctuations in torque and current. Therefore, conventional sensorless control of BLDC motors with unbalanced ZCP detection may lead to instability [115, 120, 121].

The authors in [120] have introduced a sensorless drive system for BLDC motors that relies on third harmonic back-EMF signals. In contrast to conventional approaches, this method eliminates the use of LPFs in analog-to-digital converters, resulting in no phase lag. To reduce sampling delays in ZCP detection in high-speed regions, a dynamic oversampling technique is employed in this approach. Additionally, it also presents a method to compensate for commutation errors arising from asymmetric back-EMF, as shown in Figure 2.18.

There is an input-output feedback-based linearization approach presented in [122]. The linearized model of the system is used to develop a sensorless optimal commutation control method for steady-state operations. This method aims to rectify commutation errors using only one current sensor, while also accounting for the presence of asymmetric back-EMF, as discussed in [123].

The authors in [124] have introduced the Dual Improved Second-Order Generalized

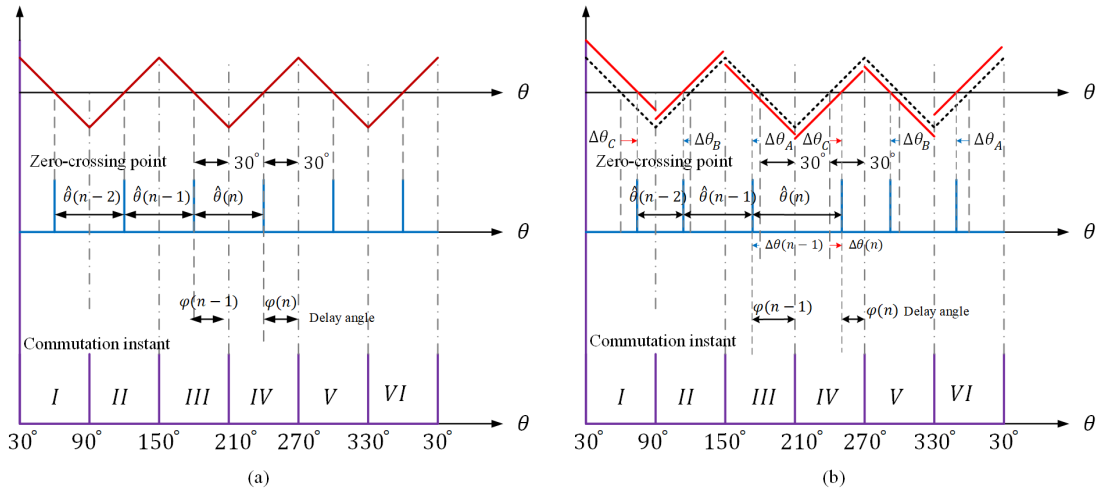

Figure 2.17: Comparison of ZCP interval $\hat{\theta}(n)$, ZCP error $\Delta\theta(n)$, and commutation delay angle $\varphi(n)$ for symmetrical and asymmetric back-EMF signals [120]. (a) Symmetrical impedances. (b) Asymmetric impedances.

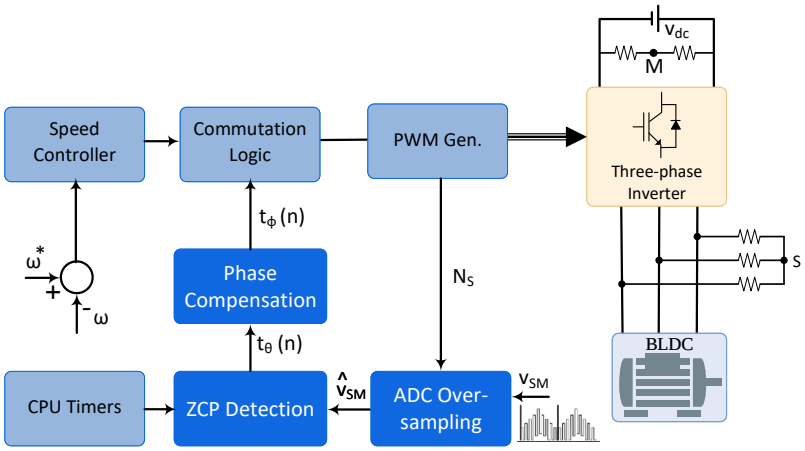

Figure 2.18: Sensorless control of BLDC motor with commutation phase compensation using analog to digital converter [120].

Integrator with Positive Sequence Component Extractor (DISOGI-PSCE). The purpose of this approach is to correct deviations in BLDC motors while taking into consideration the back-EMF asymmetry. Additionally, in [125], an integral method is proposed to mitigate the challenges associated with asymmetric back-EMFs and to improve system robustness.

2.7 Simulation and experimental results

In this section, we perform simulations of two distinct control methods for a BLDC motor using Matlab Simulink. The first method relies on sensor-based control, utilizing low-resolution Hall-position sensors to regulate the motor's speed. The second method is sensorless, employing the back-EMF observer method described in [114] for speed control. The parameters of the studied BLDC motor is given in Table 2.2.

Sensorless control is compared and validated through simulation, with the sensor-based method serving as the benchmark due to its fundamental nature in driving BLDC motors. Sensorless control systems provide an advantage by reducing drive system costs through the elimination of position sensors. It utilizes a back-EMF observer in conjunction with commutation functions, enabling its operation in both low-speed and high-speed ranges.

Table 2.2: BLDC motor parameters

Nominal speed	4000 rpm
Number of poles	8
Battery voltage	24 V
Motor equivalent resistance	0.9 Ω
Motor series inductance	1.115 mH
Motor inertia	240 $g.cm^2$

2.7.1 Control method using Hall sensors

In this method, a PI controller is employed to control the mechanical speed of the BLDC motor. Within the framework of this approach, a notable feature is that during each conduction mode of the motor, one of the motor's phases remains unexcited.

Under typical operating conditions where no faults are present, the method utilizes Hall signals as a critical element in determining the current conduction mode and subsequently the pair of switches. The back-EMF sign for each phase will be selected based on the Hall signals with a look-up table presented in Table 2.3.

The polarity of the back-EMF signals can then be evaluated to determine the type of active conducting switch to use, as demonstrated in Table 2.4.

Table 2.3: Back-EMF voltage polarity determination based on Hall signals

$Hall_A$	$Hall_B$	$Hall_C$	e_a	e_b	e_c
0	0	1	0	-	+
0	1	0	-	+	0
0	1	1	-	0	+
1	0	0	+	0	-
1	0	1	+	-	0
1	1	0	0	+	-

Table 2.4: Back-EMF polarity-driven switch pair selection

e_a	e_b	e_c	S_1	S_2	S_3	S_4	S_5	S_6
0	0	0	0	0	0	0	0	0
0	-	+	0	0	0	0	1	1
-	+	0	0	0	1	1	0	0
-	0	+	0	0	0	1	1	0
+	0	-	1	1	0	0	0	0
+	-	0	1	0	0	0	0	1
0	+	-	0	1	1	0	0	0

The Figure 2.19 shows the mechanical speed of the BLDC motor for the following scenario:

- At t = 1.2 s, the speed reference changes from 2000 to 4000 rpm.
- At t = 2 s, the load torque changes from 0 to 0.06 N.m.

2.7.2 Sensorless control method based on back-EMF observer

The sensorless control method relies on a back-EMF observer. The design of the back-EMF observer involves a set of equations that can be expressed as follows:

$$\begin{cases} \dfrac{di_{ab}}{dt} = -\dfrac{2R}{2L}i_{ab} + \dfrac{1}{2L}v_{ab} - \dfrac{1}{2L}e_{ab} \\ \dfrac{di_{bc}}{dt} = -\dfrac{2R}{2L}i_{bc} + \dfrac{1}{2L}v_{bc} - \dfrac{1}{2L}e_{bc} \\ \dfrac{di_{ca}}{dt} = -\dfrac{2R}{2L}i_{ca} + \dfrac{1}{2L}v_{ca} - \dfrac{1}{2L}e_{ca} \end{cases} \tag{2.17}$$

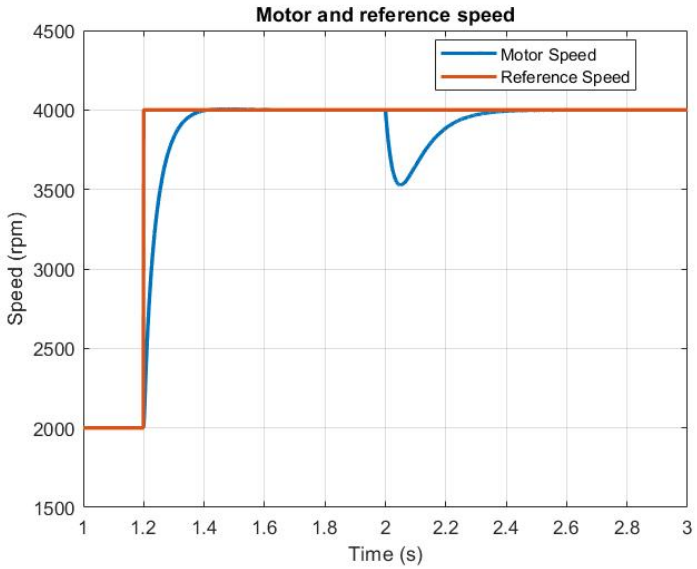

Figure 2.19: The motor speed and its reference signal for a BLDC motor controlled based on Hall position sensors.

where, v_{ab}, v_{bc}, and v_{ca} are the line-to-line terminal voltages. Similarly, e_{ab}, e_{bc}, and e_{ca} are the line-to-line back-EMF voltages. Also $i_{ab} = i_a - i_b$, $i_{bc} = i_b - i_c$, and $i_{ca} = i_c - i_a$.

Considering $\mathbf{x}_{ab} = \begin{bmatrix} i_{ab} & e_{ab} \end{bmatrix}^t$, $\mathbf{u}_{ab} = \begin{bmatrix} v_{ab} \end{bmatrix}$, and $\mathbf{y}_{ab} = \begin{bmatrix} i_{ab} \end{bmatrix}$, the differential equations for designing the back-EMF observer can be described as:

$$\dot{\hat{\mathbf{x}}}_{ab} = \mathbf{A}_{ab}\hat{\mathbf{x}}_{ab} + \mathbf{B}_{ab}\mathbf{u}_{ab} + \mathbf{K}_{ab}(\mathbf{y}_{ab} - \hat{\mathbf{y}}_{ab}) \tag{2.18}$$

Where $\mathbf{K}_{ab}$ is the gain matrix of the observer and $\mathbf{A}_{ab}$ and $\mathbf{B}_{ab}$ are calculated based on (2.19).

$$\begin{cases} \mathbf{A}_{ab} = \begin{bmatrix} -\dfrac{2R}{2L} & -\dfrac{1}{2L} \\ 0 & 0 \end{bmatrix} \\ \mathbf{B}_{ab} = \begin{bmatrix} \dfrac{1}{2L} \\ 0 \end{bmatrix} \end{cases} \tag{2.19}$$

The block diagram of the back-EMF observer is illustrated in Figure 2.20. Based on the estimated back-EMF signals and the commutation functions presented in (2.20), it is

possible to determine the conduction mode of the BLDC motor, as explained in Section 2.4.5.

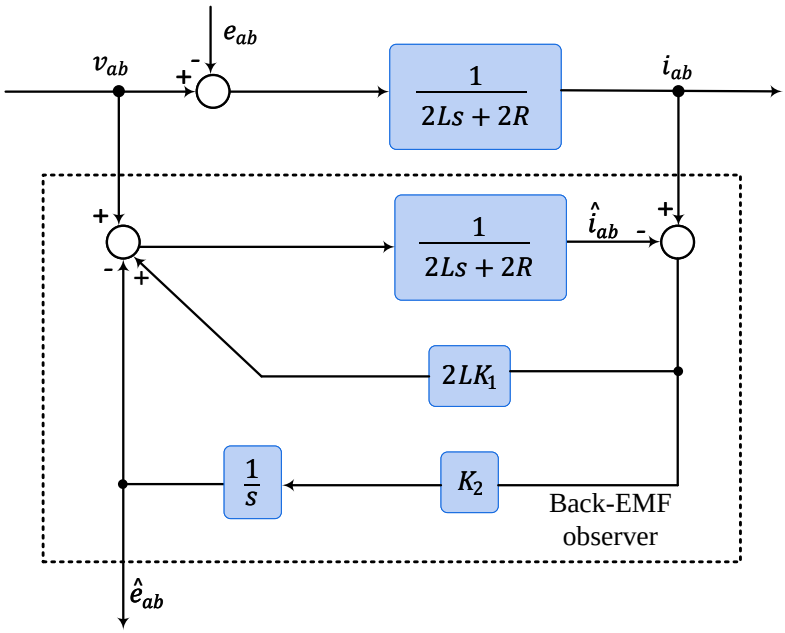

Figure 2.20: Schematic of the back-EMF observer for the BLDC motor.

$$\begin{cases} CF_{ab/bc} = \dfrac{\hat{e}_{ab}}{\hat{e}_{bc}} \\ CF_{bc/ca} = \dfrac{\hat{e}_{bc}}{\hat{e}_{ca}} \\ CF_{ca/ab} = \dfrac{\hat{e}_{ca}}{\hat{e}_{ab}} \end{cases} \tag{2.20}$$

By employing a PI controller to regulate the mechanical speed of the motor and utilizing its output as the reference for motor current, we can effectively manage the current flowing through the conducting switches. This control is complemented by a hysteresis mechanism, which offers current protection to the system. Figure 2.21 depicts the motor speed and its reference signal when the speed reference changes from 2000 to 4000 rpm at t = 1.2 s and load torque changes from 0 to 0.06 N.m at t = 2 s.

Both methods effectively control and track the reference speed in both steady-state

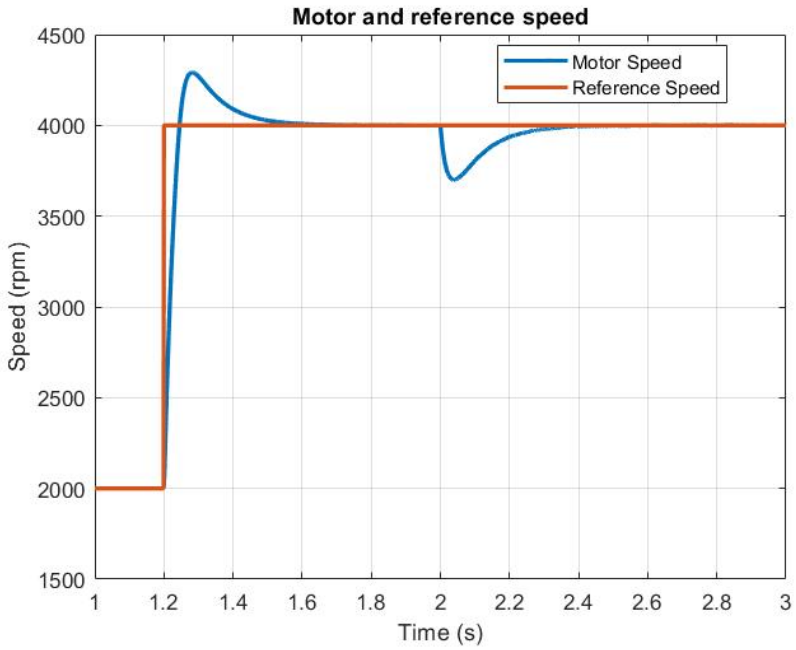

Figure 2.21: The motor speed and its reference signal for a BLDC motor controlled based on back-EMF observer.

and transient events. The two methods are capable of controlling the method and tracking the reference speed at steady-state and during transient events. Sensor-based methods are easy to implement and straightforward. Sensorless controllers, however, are more complex and less robust against motor parameter variation despite reducing system cost.

2.8 Conclusion

This chapter presented an in-depth exploration of BLDC drive systems, including a comprehensive examination of various aspects. The chapter began by reviewing the fundamental model and equations of the BLDC drive system. Subsequently, it discussed the general structure of the drive system and explored the most prevalent control methods for BLDC motors.

Sensorless control methods, in particular, have received considerable attention in the current literature. We conducted a thorough review of multiple sensorless methods.

We classified and compared these diverse sensorless control methods based on their operational principles.

Moreover, this chapter also covered the recent research focused on enhancing the control of BLDC motors. It paid particular attention to scenarios where nonideal and asymmetric back-EMF signals need to be considered, contributing to a more comprehensive understanding of real-world applications. In addition to theoretical insights, this chapter included simulation results of the control of BLDC motors using Hall position sensors and a sensorless approach based on a back-EMF observer.

Chapter 3

Drive of PMSMs

Contents

3.1 Introduction

In the context of the automotive industry, PM motors have received significant attention, primarily owing to their advantages, as thoroughly examined in the previous chapters. A detailed explanation of PMSMs and their drive systems is provided in this chapter.

Section 3.2 describes the structural elements and operational principles of PMSMs. Section 3.3 introduces the modeling and equations that describe PMSM behavior. The dq-frame model is explored here specifically, which simplifies the motor's 3-phase time-varying parameters into a two-phase linear model for controller design.

In section 3.4, a review of PMSM drives is conducted. This includes a discussion of prominent control strategies, such as vector control and Direct Torque Control (DTC). Several speed control methodologies are also explored, including FOC method, Fuzzy controllers, and Neural Networks. They are evaluated and compared according to their respective merits and demerits.

Section 3.5 focuses on sensorless control strategies for PMSMs. A number of sensorless techniques are examined here, namely low-speed methods such as HFSI and medium-to-high-speed techniques, which are model-based methods. Additionally, control of PMSMs using low-resolution Hall position sensors are discussed in this section. It should be mentioned that the application of Hall-position sensors in control of PMSMs has comprehensively been reviewed by the author et al. in [126].

Section 3.6 covers conventional measurements methods for parameter identification of PMSMs. An overview of simulation results obtained using the FOC control method can be found in Section 3.7. Lastly, section 3.8 summarizes this chapter's key conclusions and insights.

3.2 Structure of PMSMs

A three-phase PMSM with one coil per phase and two rotor poles is shown in Figure 3.1. As a result of electrical displacement, windings are spaced at 120° intervals. By

taking derivatives of the mutual flux linkages, it is possible to calculate the induced electromotive forces (EMFs), which are three balanced sinusoidal voltages for a ideal three-phase PMSM [127].

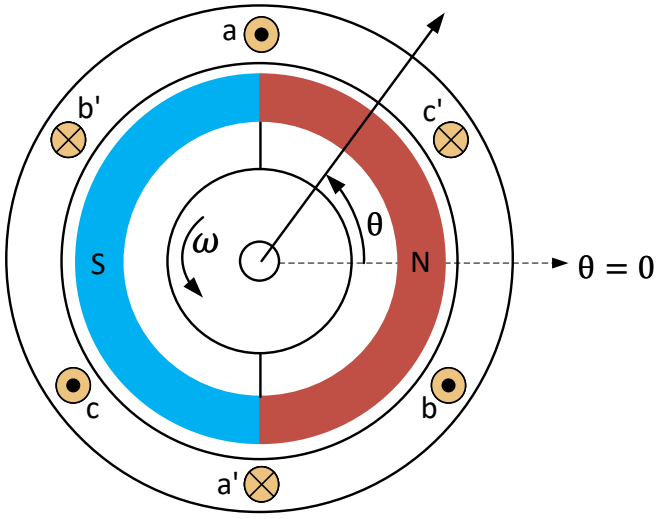

Figure 3.1: Simple three-phase machine with sinusoidal flux density [127].

3.3 Model of PMSMs

As mentioned in the previous chapter the electrical model of the brushless motors including PMSMs can be expressed as follows:

$$\begin{bmatrix} V_a \\ V_b \\ V_c \end{bmatrix} = \begin{bmatrix} R_s & 0 & 0 \\ 0 & R_s & 0 \\ 0 & 0 & R_s \end{bmatrix} \begin{bmatrix} i_a \\ i_b \\ i_c \end{bmatrix} + \begin{bmatrix} L & 0 & 0 \\ 0 & L & 0 \\ 0 & 0 & L \end{bmatrix} \frac{d}{dt} \begin{bmatrix} i_a \\ i_b \\ i_c \end{bmatrix} + \begin{bmatrix} e_a \\ e_b \\ e_c \end{bmatrix} \tag{3.1}$$

where R_s and L are stator impedance and inductance; i_a, i_b, and i_c are phase currents; V_a, V_b, and V_c are phase voltages; and e_a, e_b, and e_c are phase back-EMF voltages.

It is quite challenging to analyze the behavior of the motor with the time-variant sinusoidal equations, particularly during transient operation, despite simplifying assump-

tions regarding the system model. As a means of simplifying this analysis, the Park transformation is used to express the variables in a rotating dq-frame. Also, to ensure this zero-sum condition for stator currents, it is possible to express the stator variables (current, voltage, and flux) in an αβ reference frame. In this frame, the current vector lies in the αβ-frame, and the homopolar component of the current, which is proportional to the sum of phase currents, would be zero. Thus, a homopolar component of voltage or total flux does not play a role in electromechanical energy conversion, especially when expressing electromagnetic torque. As a result, the behavior of the PMSM can be represented by the αβ components of stator variables. The transformation can be divided into two stages:

- Concordia transformation: Three-phase (abc-frame) to two-phase transformation in the stationary frame (αβ-frame).
- Park transformation: Stationary frame (αβ-frame) to rotating frame transformation (dq-frame).

Concordia transformation can be expressed as:

$$\begin{bmatrix} x_\alpha \\ x_\beta \end{bmatrix} = T_{32}^t \begin{bmatrix} x_a \\ x_b \\ x_c \end{bmatrix} \ , \ T_{32} = \sqrt{\frac{2}{3}} \begin{bmatrix} 1 & 0 \\ -\frac{1}{2} & \frac{\sqrt{3}}{2} \\ -\frac{1}{2} & -\frac{\sqrt{3}}{2} \end{bmatrix} . \tag{3.2}$$

where x_α and x_β are the components of the variable x in α- and β-axis in stationary frame (αβ-frame). Also, the matrix T_{32} is the Concordia transformation matrix.

Different variables can be expressed in terms of their components in a rotating reference frame (dq-frame) linked to the rotor, in order to ensure that their components are independent of the rotor position. In the second step, the Park transformation is applied to the model of the system. When applying the Park transformation, the dq components of the stator voltage are expressed as follows:

$$\begin{bmatrix} x_d \\ x_q \end{bmatrix} = P(-\theta) \begin{bmatrix} x_\alpha \\ x_\beta \end{bmatrix} \ , \ P(\theta) = \begin{bmatrix} cos(\theta) & -sin(\theta) \\ sin(\theta) & cos(\theta) \end{bmatrix} . \tag{3.3}$$

Figure 6.2 illustrates the model of PMSM in dq-frame. Its windings are offset by

90 degrees electrically, and the rotor winding is positioned at an angle of θ relative to the stator's d-axis winding. It is assumed that the q-axis leads the d-axis, causing the rotor to rotate counterclockwise. For PMSMs with more poles, it is possible to calculate electrical angle of the rotor by multiplying the mechanical position of the rotor by number of pair poles.

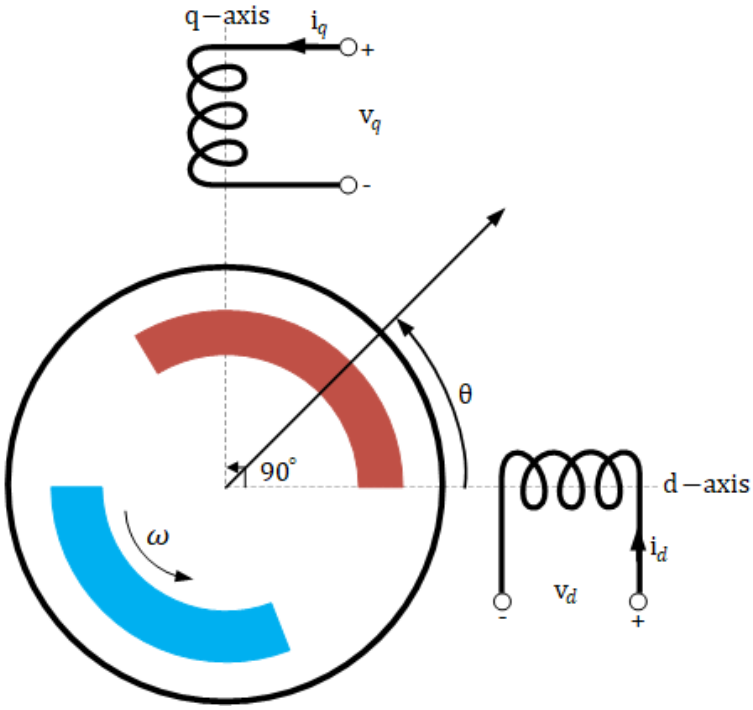

Figure 3.2: Two-phase PMSM model in dq-frame [127].

Therefore the model of the PMSM drive system in dq-frame can be described as:

$$\begin{bmatrix} V_d \\ V_q \end{bmatrix} = R \begin{bmatrix} i_d \\ i_q \end{bmatrix} + \frac{d}{dt} \begin{bmatrix} \psi_d \\ \psi_q \end{bmatrix} + \dot{\theta} P(\pi/2) \begin{bmatrix} \psi_d \\ \psi_q \end{bmatrix} \tag{3.4}$$

where V_d, V_q, i_d, and i_q are terminal voltage and stator current in dq-frame, respectively. Parameters ψ_d and ψ_q are magnetic flux in dq-frame. Considering the fact that $\dot{\theta} = \omega_e$

is the electrical speed of motor and motor is in unsaturated mode, (3.4) simplifies to:

$$\begin{cases} V_d = Ri_d + L_d \dfrac{di_d}{dt} - p\Omega L_q i_q \\ V_q = Ri_q + L_q \dfrac{di_q}{dt} + p\Omega L_d i_d + p\psi_f \Omega \end{cases} \tag{3.5}$$

where direct and quadrature currents are indicated by i_d and i_q, respectively. Parameter ψ_f is the constant magnet flux of the motor. Also, L_d and L_q refer to the d-axis inductance and q-axis inductance, respectively. Parametr p is the number of pole pairs and Ω refers to the mechanical speed of the motor.

When the stator and rotor flux interact, they generate an electromagnetic torque within the air gap. If this torque reaches a sufficient magnitude, it initiates rotor rotation. In the context of a rotating electrical machine, the torque equation is defined as follows:

$$J\frac{d\Omega}{dt} = T_e - f\Omega - T_L. \tag{3.6}$$

where J is the moment of inertia of the rotor, T_L and T_e refers to the load torque and electromagnetic torque, respectively. Parameter f indicates the friction coefficient. The electromagnetic torque developed by synchronous machines with sinusoidal back-EMF can be expressed as:

$$T_e = p[\psi_f + (L_d - L_q)i_d]i_q. \tag{3.7}$$

Therefore, the PMSM model can be described using (6.2) and (6.4).

3.3.1 Saturation effect

The previous section introduced a model for a unsaturated synchronous machine, which does not account for the saturation effect. Figure 3.3 illustrates the saturation effect, depicting how the flux (ψ) changes concerning the current. In an unsaturated motor (linear zone of the flux-current curve), $\dfrac{d\psi_d(i_d, i_q)}{di_d}$ is a constant value, represented by L_d in (6.2), while this assumption is not correct anymore when the saturation effect is considered. Therefore, (6.2) changes to [128]:

$$\begin{bmatrix} V_d \\ V_q \end{bmatrix} = R \begin{bmatrix} i_d \\ i_q \end{bmatrix} + \frac{d}{dt} \begin{bmatrix} \psi_d(i_d, i_q) \\ \psi_q(i_d, i_q) \end{bmatrix} + \dot{\theta} P(\pi/2) \begin{bmatrix} \psi_d(i_d, i_q) \\ \psi_q(i_d, i_q) \end{bmatrix}. \tag{3.8}$$

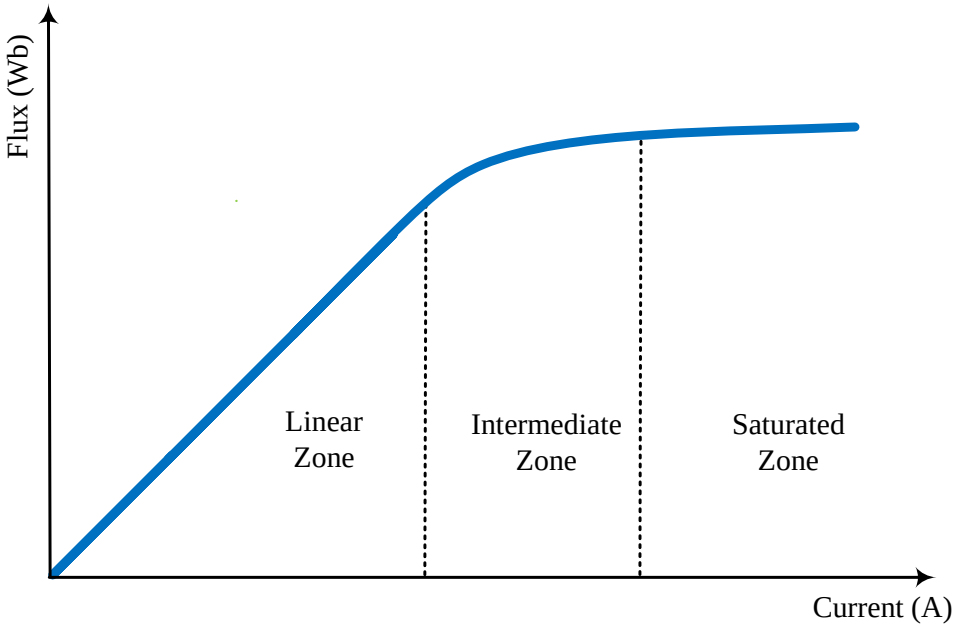

Figure 3.3: Flux-current curve considering the saturation effect.

Also the electromagnetic torque of the motor can be describes as:

$$T_e = p[\psi_d(i_d, i_q)i_q - \psi_q(i_d, i_q)i_d]. \tag{3.9}$$

3.4 PMSM drive

Previous sections about PMSM operation, principles, and model, particularly the electrical model of the system in dq-frame, enables us to examine the various drive methods of these motors in the current literature. Throughout this section, we will examine the various strategies and techniques employed to drive PMSMs, as well as their advantages and drawbacks.

3.4.1 Control strategies of PMSM drive

Different control techniques have been developed to regulate the speed, torque, and position of the rotor in order to achieve the highest level of performance and efficiency. Among these control strategies, two prominent approaches are DTC and Vector Control, both extensively used in drive of PMSMs [129, 130].

Vector Control: This technique uses FOC method to regulate the motor current, flux, or voltage based on a space vector control model. Generally, these vectors can be divided into components responsible for generating torque and those responsible for shaping electromagnetic fields. A vector control motor design is similar to drive of DC motors which makes it easy to implement [130].

Direct Torque Control (DTC): This control strategy is based on controlling the flux linkage and torque of the PMSM. In most cases, it uses a feedback system to detect and adjust motor speed based on rotor position data. In advanced DTC systems, three-phase voltages at the input terminals of PMSMs are measured to estimate flux and torque. Stator voltage vectors are used in DTC to minimize torque and flux errors within the hysteresis band, in response to varying reference values and torque variations. Compared to Vector Control, digital implementation of DTC method consumes relatively low amount of power [130–132].

3.4.2 PMSM speed control techniques

3.4.2.1 Field-oriented control (FOC)

The separate control of excitation current and armature current in PMSMs is a challenging task. In mathematical decoupling, the stator current is split into two components, the direct component (i_d), which creates the motor field and the quadrature component (i_q), which generates the motor torque within a rotating dq-frame. Figure 6.3 illustrates the concept of FOC method. PMSMs can be controlled on the same basis as DC motors using PI current controllers and PWM inverters. In this approach, the stator currents and voltages are converted to dq-frame using the Park transform, which enables independent control of motor flux and torque. The individual control of the d-axis current (i_d) and q-axis current (i_q) is accomplished through the implementation of decoupling feed-forward compensation in the d-q axes. This technique is used to make the control

design simpler and also to enhance the overall performance of the motor drive. As part of FOC, a rotor position sensor, such as an encoder, or a sensorless position estimator method must be used to determine the rotor position for speed control. The rotor position is required not only for speed control but also for Park transformation. The FOC system offers several advantages, including the ability to convert a complex dual AC system into a general linear system, high torque at low current during startup, and high efficiency [130].

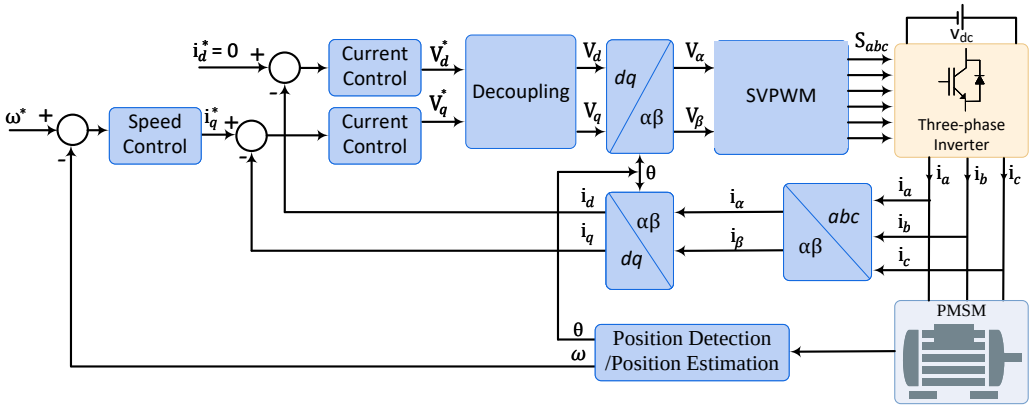

Figure 3.4: Schematic of the FOC control of PMSM.

3.4.2.2 Fuzzy Logic Control (FLC)

Logic controllers such as FLCs are well-defined sets of logical rules used to address the electrical limitations of linear control methods of PMSMs. Linear controllers such as PID controllers are typically not able to adapt to changes in system parameter values due to their relatively limited tuning flexibility. It is common to use adaptive controllers in AC electrical drive applications, but they perform best when tracking linear systems. The fuzzy logic-based controllers, on the other hand, provide more precise and faster solutions, as they are capable of handling intricate nonlinear characteristics [133–135].

3.4.2.3 Neural network control

Artificial Neural Network (ANN) methods provides several advantages over conventional methods including robustness, parallel structure, and nonlinearity adaptation. A

major advantage of this approach is the elimination of the need for an analytical model of the system. ANNs are also capable of handling tasks that linear processes cannot, which makes them useful in many applications. A key challenge faced by ANN-based systems is establishing a clear relationship between the structure of the neural network and the physical processes of the motor, and there are no established guidelines regarding the number of hidden nodes and layers to use for this control method [136, 137].

3.4.2.4 Flatness-based control

Among these control methods, FOC has gained popularity in the today's industry. However, the PMSM drive system is nonlinear, and the dynamic performance of the system using FOC method is affected by system operating points. To deal with issues resulting from system nonlinearity, flatness-based control has been suggested as an alternative to FOC during the last decade. Due to its inherent decoupling, it allows the design of controllers for individual variables (e.g., speed or angle). The method can provide robust control even in the presence of parameter variations and disturbances. A high-performance control system can achieve precise tracking of reference values by directly controlling key variables [138].

3.5 Sensorless control methods for PMSMs

As discussed in the previous chapter, sensorless control technique is used to control the motor without the use of external position sensors. A sensorless control method estimates the rotor's position and commutation timing through various techniques, rather than using conventional position and speed sensors. Most of these techniques involve monitoring motor current, voltage, or back-EMF signals. These methods increase the system reliability and minimize costs by eliminating external position sensors [139, 140]. Figure 3.5 illustrates the sensorless control techniques were developed for PMSM drives for a wide range of applications from low- to high-speed range.

3.5.1 Saliency-based sensorless control methods

The saliency-based sensorless control methods have been developed in response to the limitation that model-based sensorless methods are not suitable for low-speed applica-

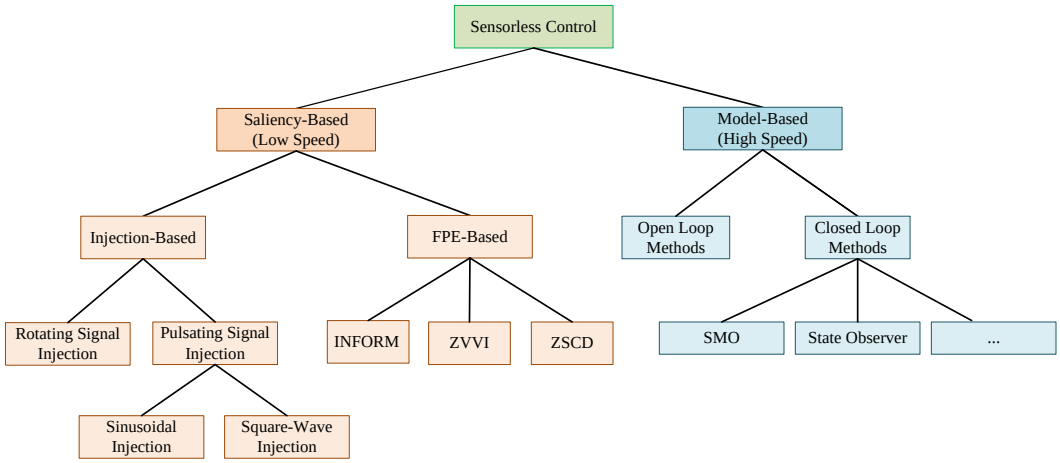

Figure 3.5: Different categories for position sensorless drives of PMSMs [141].

tions in PMSM motors. A saliency-based sensorless control method can be divided into two categories: Injection-based control methods and fundamental pulse width modulation (PWM) excitation (FPE)-based control methods. Among the most well-known FPE techniques are indirect flux detection by online reactance measurement (INFORM), zero sequence current derivatives (ZSCD), and zero voltage vector injection (ZVVI) [141].

3.5.1.1 Signal injection-based sensorless control method

Injection-based control methods are more common in low-speed applications. The position information is computed by utilizing a HFSI and motor reluctance. These methods of control can be divided into rotating signal injection methods and pulsating signal injection methods [142–151]. It is important to note that in this method, the injection frequency is much higher than the operation frequency. As a result, assuming no voltage drops on stator resistances in low-speed applications, the equations in dq-frame can be expressed as follows:

$$\begin{bmatrix} u_{d-h} \\ u_{q-h} \end{bmatrix} = \begin{bmatrix} L_d & 0 \\ 0 & L_q \end{bmatrix} \frac{d}{dt} \begin{bmatrix} i_{d-h} \\ i_{q-h} \end{bmatrix} \tag{3.10}$$

where “h” indicates the high-frequency component, L_d and L_q are the dq-axis inductance, u_{d-h}, u_{q-h}, i_{d-h}, and i_{q-h} are the high-frequency voltage and current components

in dq-frame, respectively. The equation in αβ-frame is:

$$\begin{bmatrix} u_{\alpha-h} \\ u_{\beta-h} \end{bmatrix} = \begin{bmatrix} L_0 + \Delta L cos(2\theta) & \Delta L sin(2\theta) \\ \Delta L sin(2\theta) & L_0 - \Delta L cos(2\theta) \end{bmatrix} \frac{d}{dt} \begin{bmatrix} i_{\alpha-h} \\ i_{\beta-h} \end{bmatrix} \tag{3.11}$$

where θ is the rotor position, $L_0 = (L_d + L_q)/2$, and $\Delta L = (L_d - L_q)/2$. Also, L_d and L_q are the d- and q-axis inductances, p is the number of pair poles, $u_{\alpha-h}$, $u_{\beta-h}$, $i_{\alpha-h}$, and $i_{\beta-h}$ are the high-frequency voltage and current components in αβ-frame, respectively [141].

An example of sensorless control of a PMSM using rotating signal injection can be seen in Figure 3.6. This approach involves injecting a high-frequency (ω_h) rotating voltage space vector into the αβ-frame. Sensorless control can then be achieved by using either the negative sequence current method [152] or the zero sequence voltage method [153], both of which are based on (3.10)-(3.12).

$$\begin{bmatrix} u_{\alpha-h} \\ u_{\beta-h} \end{bmatrix} = U_{rot-h} \begin{bmatrix} cos(\omega_h) \\ sin(\omega_h) \end{bmatrix} \tag{3.12}$$

where U_{rot-h} is the injected rotating HF voltage amplitude.

Using a pulsating signal injection method is another sensorless method for PMSMs. In contrast to the previous method, this approach requires knowledge of the initial rotor position, since the high-frequency signal is injected into the dq-frame. The pulsed signals can be classified into two types based on the type of pulsating injection used: pulsating sinusoidal injection and pulsating square-wave injection [141]. The block diagram of a pulsating sinusoidal injection-based sensorless control method is depicted in Figure 3.7. The high-frequency pulsating sinusoidal signal method can be expressed as:

$$\begin{bmatrix} u_{d-h} \\ u_{q-h} \end{bmatrix} = U_{pul-h} \begin{bmatrix} sin(\omega_h t) \\ 0 \end{bmatrix} \tag{3.13}$$

where U_{pul-h} is the amplitude of the injected pulsating sinusoidal HF voltages.

The structure of sensorless control schemes that use pulsating square-wave injection is similar to that of control schemes based on pulsating sinusoidal injection. Injection frequencies in this case can be considerably higher than rotating injection and

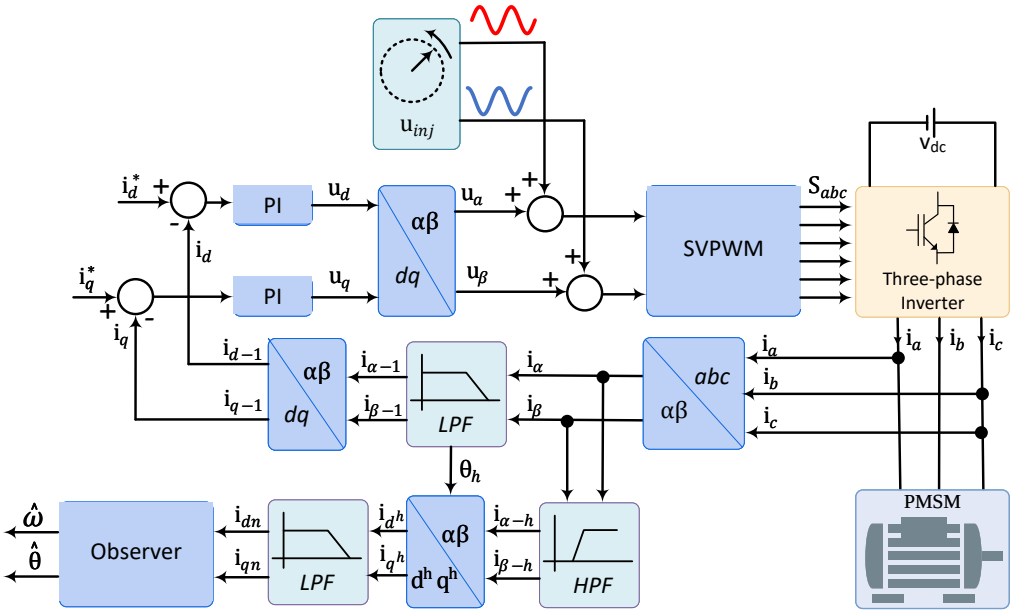

Figure 3.6: Block diagram of rotating signal injection [141].

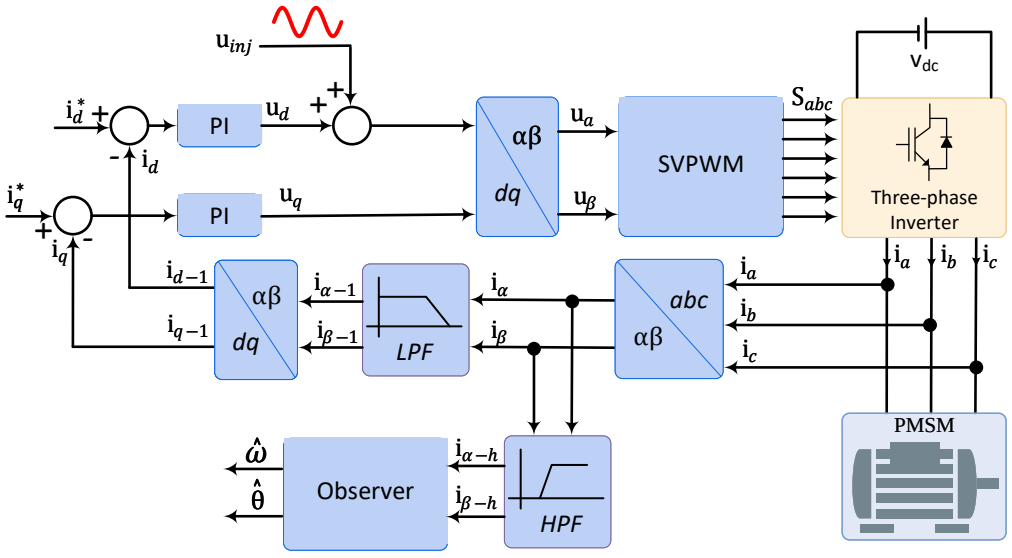

Figure 3.7: Block diagram of pulsating sinusoidal injection [141].

pulsating sinusoidal injection, which is advantageous for separating and extracting high-frequency signals [154].

3.5.1.2 Fundamental PWM excitation-based sensorless control

As HFSI methods require additional signal processing and observers, FPE-based sensorless control methods were developed to simplify this process. Basically, FPE-based methods can be categorized into three main groups: INFORM, ZSCD, and ZVVI [141].

In INFORM method, space vector voltages are applied from various directions and their responses are measured. Through this process, variations in inductance are calculated, which ultimately determines the rotor's position. In contrast to methods that use back-EMF, INFORM can work at low-speed applications and at standstills. Additionally, it does not depend on motor equations. Therefore, it is robust against variations in motor parameters. Nevertheless, any distortion in the motor flux distribution can lead to errors in estimating speed and rotor position. Also this method may cause ripples in the motor current [139, 155, 156].

The ZSCD method involves injecting test vectors into the machine, which allows the instantaneous values of the dq-axis inductances to be used to calculate zero sequence current derivatives. As a result of this derivation, the position of the rotor can be determined. Voltage test vectors corresponding to six non-zero switching states of the voltage source inverter (VSI) are obtained with this method and can be performed in the gap between PWM cycles quickly. As mentioned, this method is most useful in the low- and zero-speed range, when EMF variations and resistive voltage drops are less significant. Despite its simplicity and high performance, ZSCD requires access to the neutral point in order to excite the zero sequence components. As a result, it may not be suitable for use in certain industrial applications [141, 157].

ZVVI addresses the issue of noise and torque generated by high-frequency signals in motors. A zero voltage vector injection solution was developed by comparing FPE-based and HFSI-based methods. This technique combines current calculations with zero voltage injection, which makes it suitable for sensorless drive of PMSMs at low-speed range applications. This method has several advantages including being quiet, not requiring extra signal, being straightforward, and robustness against motor parameter variations. This method depends on the accuracy of the current measurement and

their derivatives. It is discussed in some papers how to detect or calculate these derivatives using special current detectors or high-resolution sensors. In this method, the current sampling is slower and can't continuously sample during zero vectors. Therefore, they have used current oversampling technology and FPGA chips to improve derivative accuracy [141, 158, 159].

3.5.2 Model-based sensorless control methods

It has been shown that the saliency-based sensorless control methods are effective at low- and zero-speed ranges. However, these methods have certain drawbacks including increased losses, torque ripples, and acoustic noises. In addition, the maximum output voltage of the inverter at high operating speeds may limit the additional injected signal. Thus, when using sensorless control, it is recommended to use saliency-based methods with signal injection only in low and zero speed ranges and switch seamlessly to model-based methods above a threshold speed [160].

In situations with medium to high-speed operations, model-based methods are used to estimate position information. The SMO method is suggested in [95], but it suffers from signal chattering during dynamic operations. A general PLL position tracker is another method proposed for estimating position and speed information of the motor [161], but tuning the proper gains for this method can be challenging. Several other model-based methods including extended back-EMF observer [162] and MARS method [163] have been proposed in the last decades.

Model-based sensorless control methods are categorized into two main groups: open-loop control methods and closed-loop control methods. Open-loop control methods can be classified as follows:

- Direct calculation [164].
- Stator inductance calculation [165].
- Back-EMF integration [166].

Even though these methods have simple dynamic, fast response, and straightforward implementations, they suffer from sensitivity to parameter variation and low accuracy in speed estimation.

Several sensorless closed-loop control methods have been proposed in the current literature to solve the problems of open-loop control, including:

- Extended kalman filter (EKF) [167, 168].
- Sliding mode observer (SMO) [169, 170].
- Model reference adaptive system (MRAS) [171, 172].

Field-oriented sensorless control relies on accurate estimation of position and speed, particularly in high-performance applications. The lack of appropriate estimation can lead to issues, such as instability in closed-loop speed control. A high observer bandwidth can, on the other hand, amplify measurement noise, resulting in increased torque losses. Therefore, a PMSM sensorless control system must be designed meticulously in order to optimize performance [173].

The open-loop and closed-loop methods of model-based sensorless control may be used for calculating EMF and flux of the motor. Generally, closed-loop estimations are more accurate and robust than open-loop estimations. Various factors can affect the estimation of EMF or flux for position or speed estimation, including the reference frame used, mathematical models, and error convergence methods [174, 175].

Despite advances in EMF estimation, current research aims to improve performance, robustness, and low-frequency operation. Spatial flux harmonics and inverter nonlinearities are important factors that have been considered as the key elements in the recent works. In addition, low-frequency ratios pose critical challenges in terms of stability and reliability. It is possible to estimate the position of the stator by integrating the flux model, taking into account the stator current and voltage of the motor [176].

As the PMSM drive system is a nonlinear system, methods such as nonlinear observers have been proposed to deal with the issues resulted from its nonlinear characteristic [177–179]. However, the system stability especially against parameter variations is a challenge in this method.

Estimation techniques have recently been refined in order to achieve a well-balanced adjustment of observer feedback gains. Over the past decade, many papers have aimed to formulate closed-form solutions for synthesizing these gains in a way that is broadly applicable to diverse PMSM configurations. Moreover, significant attention has been

paid to increasing the observer's robustness under nonideal conditions, including addressing factors such as PMSM parameter variations, online parameter estimation, and designing position observers that are robust to distortions. Additionally, there has been an effort to explore sensorless applications operating at high speeds with low-sampling frequencies, contributing to the expanding field of sensorless control of PMSMs [173].

3.5.3 Rotor position and speed estimation method using Hall-position sensor

The acquisition of rotor position and speed is critical to the performance of PMSMs in many applications. As mentioned previously, there are two major categories of position-measuring methods for PMSMs' control systems. One method is to use high-precision mechanical position sensors, such as resolvers or photoelectric encoders, to determine motor speed and rotor position. However, they are more expensive and require larger volumes, and they are easily restricted by the conditions in the room, despite providing precise control of the motor. The reliability of mechanical position sensors is also affected by their potential failure during motor operation [180].

It is also possible to determine rotor position and motor speed without using sensorless methods. It is challenging, however, to achieve accurate speed and position estimates, especially in applications that operate at a wide speed range, since these methods are sensitive to variations in motor parameters, temperature, and inverter characteristics [181]. Hall position sensors have emerged as a solution for these challenges as they balance performance and cost considerations [182–185].

Figure 3.8(a) shows a three-phase Hall sensor setup for a one-pole PMSM. The $Hall_A$, $Hall_B$, and $Hall_C$ sensors in this configuration serve as three-phase position sensors. Rotation of the rotor causes the Hall position sensor to generate a rectangular wave with a variable frequency. A complete rotor cycle generates three rectangular waves of 180° pulse width and 120° phase difference. Consequently, each Hall section represents one state of the three-phase Hall signal, and the 360° electrical cycle is divided into six Hall sections. Figure 3.8(b) illustrates the relationship between the phase Hall signal and back-EMFs. For precise control of the PMSM as specified, it is essential to acquire rotor position information based on the motor's Hall signals [186].

In [185], it's highlighted that there are generally three distinct approaches for speed

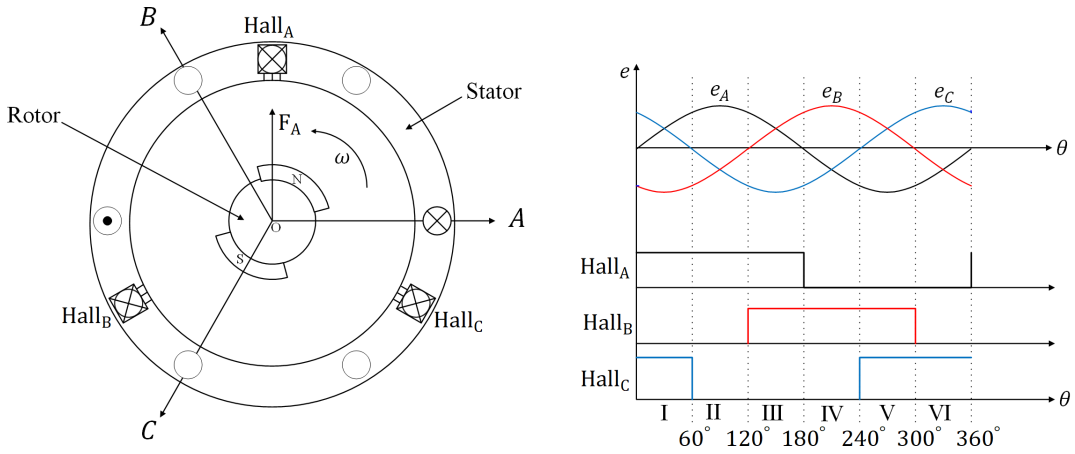

(a) (b)

Figure 3.8: (a) The Hall position sensors for a one-pole PMSM. (b) Correspondence diagram of Hall position signals and motor back-EMF voltages [126].

and position estimation using Hall position sensors: the interpolation method [187], the observer method [188], and the filter method [189]. Interpolation and filtering methods are relatively easy to implement, but they introduce phase lag and noise into closed-loop speed control systems, limiting performance in various PMSM applications. On the other hand, the observer method can provide more accurate rotor position and speed estimates based on the motor system's model parameters. It's important to note, however, that the observer method can be sensitive to motor parameters [185]. In addition, some nonlinear position control algorithms based on Hall-position sensors have been introduced in order to improve the stability of standstills [190, 191].

3.5.3.1 Interpolation method

An interpolation method estimates the speed and position of a rotor using a discrete function approximation. According to the states of Hall signals, the entire rotational space is divided into six sectors. Based on this method, continuous rotor position information can be determined within a sector assuming a constant rotor speed [187, 192]. Several Hall signal interpolation methods have been proposed so far, which the average speed method, the average acceleration method, and the least square method are among the most conspicuous ones.

Based on the average velocity observed in the previous Hall sector, the average speed method predicts the rotor's position in the next Hall sector. A constant sector speed is assumed with this approach, regardless of the difference in speeds between sectors. However, Hall sensor placement deviations limit its accuracy, resulting in large fluctuations in motor speed, which affect rotor position estimation. To overcome this problem, motor acceleration and moving average interpolation have been developed. According to the average acceleration method, angular acceleration remains the same within each Hall sector, thus ensuring smoother transitions between sectors [193, 194].

If a motor's speed fluctuates significantly, the average acceleration method may cause rotor pulsations, hampering the motor's normal operation. As a result of its potential limitations in such scenarios, it may not be suitable for applications requiring high dynamic performance. Although Taylor series expansion can mitigate estimation errors, it simultaneously increases the complexity of software implementation, causing significant delays in estimation results [195].

Alternatively, the least squares method takes into account the mechanical installation error of Hall position sensors [196]. A least-squares method combined with Taylor linear interpolation can be employed to deal with misplaced Hall sensors in some instances [197]. According to [198], an control method based on combining integrating non-model-based least square algorithms with model-based SMOs in order to estimate both position and speed.

3.5.3.2 Filter method

Filter method has become an alternative to interpolation, because it does not require a function derived from the motion equation of the PMSM. The Hall signals are converted into Hall rotation vectors using coordinate transformations, which contain vital information about rotor position. In the discrete signal model, sinusoidal waves are decomposed into Fourier coefficients, and filtering is used to isolate fundamental signals from Hall vectors derived via coordinate transformations [199, 200].

In [189], an enhanced orthogonal PLL is proposed to mitigate speed ripple, enabling reduced position error and enhanced dynamic performance. Nevertheless, variable electrical frequency poses challenges, leading to fluctuations in LPF cutoff frequency and the need to adjust controller parameters. In [201], fundamental signals are extracted

using synchronous frequency tracking filters (SFTFs) to handle Hall sensor installation errors in PMSM control, as shown in Figure 3.9.

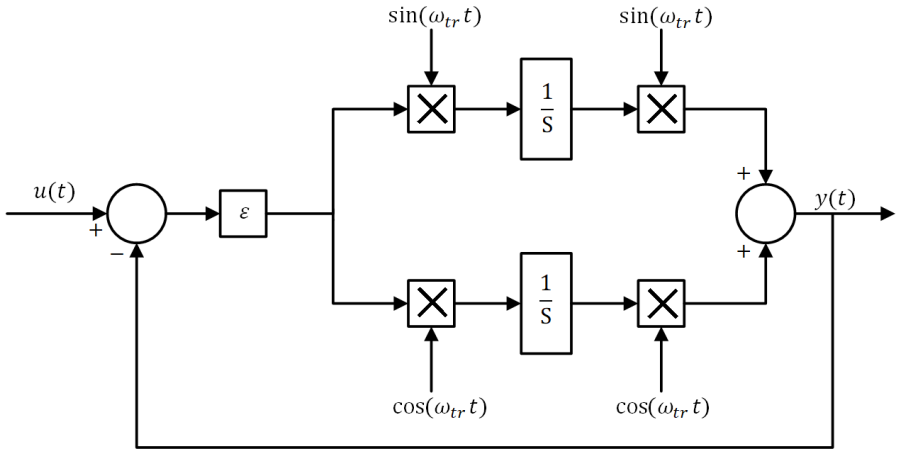

Figure 3.9: Block diagram of SFTF [201].

3.5.3.3 Observer method

Even though signal processing-based methods are relatively straightforward, they suffer from inherent time delays in speed estimation, resulting in inefficiency and possible instability. On the other hand, model-based approaches such as state observers [200, 202], Kalman filters [203], and state observers require comprehensive motor information. A Luenberger state observer was introduced in [199], based on the motor's mechanical parameters.

The authors of [204] have proposed a method for calculating rotor position by integrating low-resolution Hall position signals as the back-EMF observer. This approach is robust against changes in mechanical parameters and remains relatively unaffected by changes in the moment of inertia and torque discrepancies. Due to the relatively low amplitude and frequency of back-EMF voltages during low-speed applications, it faces challenges in determining the actual rotor position. In addition, the signal-to-noise ratio and accuracy of current sampling significantly affect observer performance, particularly during light load operations [205].

Position vector tracking observers were introduced in [193] for controlling PMSM using Hall sensors. This observer offers two advantages: it facilitates smooth motor

starts at low speeds, and it exhibits minimal sensitivity to Hall sensor installation errors. Nevertheless, configuring the observer system's parameters can be rather complicated. When the controller bandwidth settings are too high, it can cause significant fluctuations in instantaneous speed observations and estimated positions. On the other hand, setting the bandwidth too low may compromise the stability of the observer [206].

As proposed in [207], another approach involves tracking Hall signals using Fourier decoupling feedback. With this approach, the position vector can be divided into fundamental and high-order harmonic components. Figure 3.10 illustrates an overall block diagram of the observer with Hall signal feedback decoupling. Choosing the most appropriate terms for the discrete Fourier series expansion is the key challenge here. Although this technique allows the motor to operate at its full speed range, it has difficulty extending its speed loop bandwidth at low speeds [207, 208].

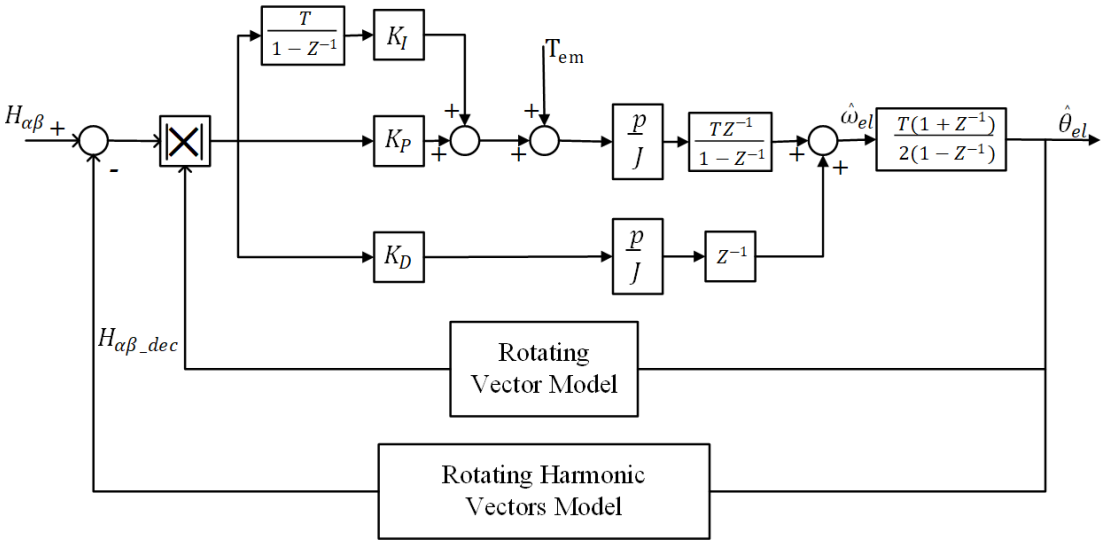

Figure 3.10: Block diagram of rotor position estimation of vector tracking observer [207].

In some studies, researchers have proposed cascaded observer approaches to improve estimation accuracy and decrease rotor speed and position lag [209]. This can be accomplished with the dual observer method described in [210], because two successive observers are used. In this scheme, one observer estimates rotor speed, while the other estimates rotor position. This method offers superior frequency characteristics compared to the filter method. Its application in current industries is limited by the

intricate coordination required among observer parameters, motor specifications, and control system parameters [211, 212].

The presented methods for driving PMSMs using low-resolution Hall position sensors are summarized and compared in Table 3.1.

Table 3.1: Comparison of different control methods of PMSMs using low-resolution Hall position sensors.

Method	Technique	Advantages	Disadvantages
Interpolation method	Average speed method	- Easy to implement	- Assuming constant speed in each sector, - Affected by Hall sensor misplacement
	Average acceleration method	- Better accuracy than Average speed method	- Rotor pulsation when speed fluctuates greatly, - Not suitable in applications with high dynamic performance requirements
	Least Square method	- Considers Hall sensor misplacement	- Not enough information at the start-up, - Trade-off between accuracy and efficiency
Filter method	PLL-based methods	- Not requiring a function based on the motion equation of the PMSM, - Superior dynamic performance than Interpolation methods	- Variation of the LPF cutoff frequency
	SFTF-based methods	- Not requiring a function based on the motion equation of the PMSM, - Superior dynamic performance than Interpolation methods, - Eliminates the high-frequency interference	- Vulnerability to noise, - Sensitivity to parameter changes
Observer method	Back-EMF observer	- Good robustness to mechanical parameters	- Bad performance at low speed applications, - Affected by the current sampling accuracy, and the signal-to-noise ratio
	Vector Tracking observer	- Smooth start at low speed, - Not affected by Hall sensor misplacement	- Complicated parameter setting
	Cascaded observer	- High accuracy, - Reduces the lag of the rotor speed and position estimation, - Superior frequency characteristics	- Complex parameter design, - Sensitive to motor parameters

3.6 Conventional measurement of motor parameters

This section introduces the traditional approaches for parameter identification in PMSMs. Stator resistance and inductance can be calculated using (6.2). It is possible to calculate these parameters by applying a step voltage to the motor and measuring the motor current. For measuring stator resistance (R) and stator inductance (L), the rotor

is held stationary, therefore, the speed (Ω) will be zero and consequently the back-EMF of the motor will be zero, too. Hence, (6.2) will be simplified to:

$$\begin{cases} V_d = Ri_d + L_d \dfrac{di_d}{dt} \\ V_q = Ri_q + L_q \dfrac{di_q}{dt} \end{cases} \tag{3.14}$$

First, different steps of V_d voltage has been applied to the motor and i_d is measured for each step respectively. Based on (3.14), the stator current signal has a first-order response to the step voltage, as shown in Figure 3.11.

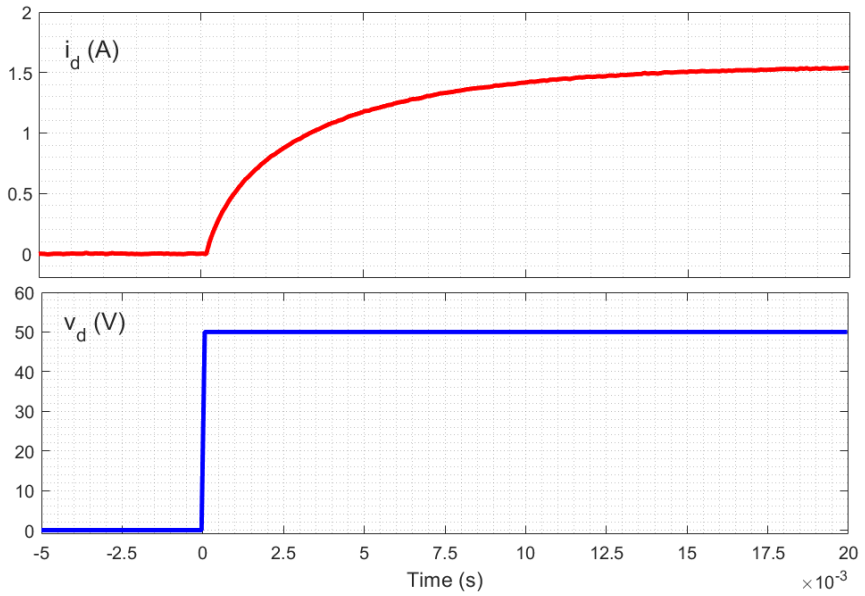

Figure 3.11: Experimental result of the d-axis current (i_d) response to a step change in voltage V_d.

Therefore, based on the step voltage (V_d) and measured current (i_d), it is possible to calculate stator resistance using the following equation:

$$R = \frac{\Delta V_d}{\Delta i_d} \simeq 30\Omega \tag{3.15}$$

After calculating R using (3.15), it is possible to calculate L using the time constant

(τ_d) of the first-order current response. Therefore,

$$\tau_d = \frac{L_d}{R} = 2.1\ ms. \tag{3.16}$$

Therefore, $L_d \simeq 65\ mH$.

The same test should be conducted by applying a voltage step (V_q) while V_d remains zero. According to the same process of calculating the stator resistance and d-axis inductance, the q-axis current can be used to calculate the q-axis inductance. As Figure 3.12 shows, i_q has a first-order response to this voltage step, similar to i_d. Therefore,

$$\tau_q = \frac{L_q}{R} = 4.3\ ms. \tag{3.17}$$

Therefore, $L_q \simeq 130\ mH$.

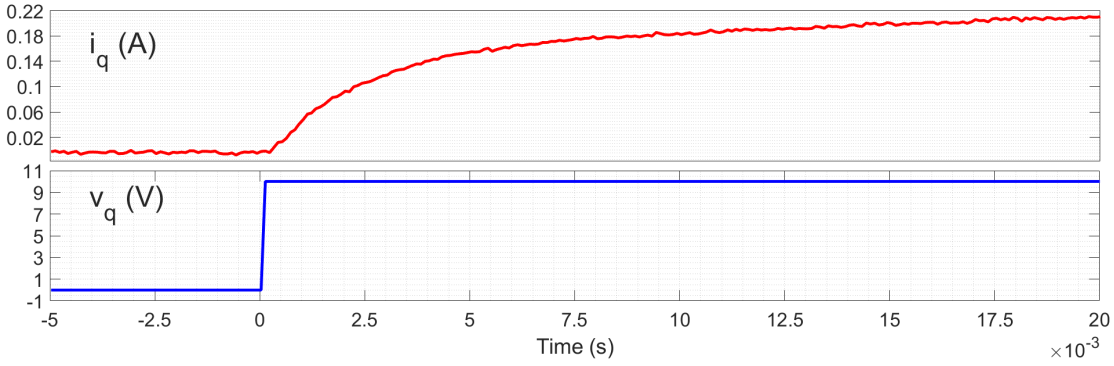

Figure 3.12: Experimental result of the q-axis current (i_q) response to a step change in voltage V_q.

Following are the tests that can be used to calculate the rest of the motor parameters for the dq-frame model. Nevertheless, these tests will be performed when the motor current is controlled by FOC. To ensure that Park transformation is correct and the control system is functioning properly, it is necessary to determine the initial position offset of the rotor. In order to determine the position offset, the i_q reference will be maintained at zero, while a substantial i_d reference value is applied to the control system. If the position offset is not accurate, the rotor will initiate rotation. Adjustments to the position offset value are necessary to ensure that the motor remains stationary when any i_d values are applied.

The magnetic flux of the motor can be calculated using (6.2) and controlling the motor in a closed-loop current control mode. In this test, a step of q-axis reference current is applied to the motor, i_d remains zero and switching voltage in dq-frame (V_d and V_q) are monitored. Considering the steady-state equations:

$$\Delta V_q = R\Delta i_q + p\psi_f \Delta\Omega \tag{3.18}$$

As ΔV_q, Δi_q, and $\Delta\Omega$ can be measured in steady-state situation, ψ_f can be calculated using (3.18). Therefore, magnetic flux can be calculated based on the response of the system variables to a step change in reference of q-axis current ($i_{q,ref}$ change from 0.5 A to 1 A), as depicted in Figure 3.13.

$$\psi_f = \frac{\Delta V_q - R\Delta i_q}{p\Delta\Omega} = \frac{97.5 - 30 \times 0.5}{2 \times 37} = 1.1\ Wb. \tag{3.19}$$

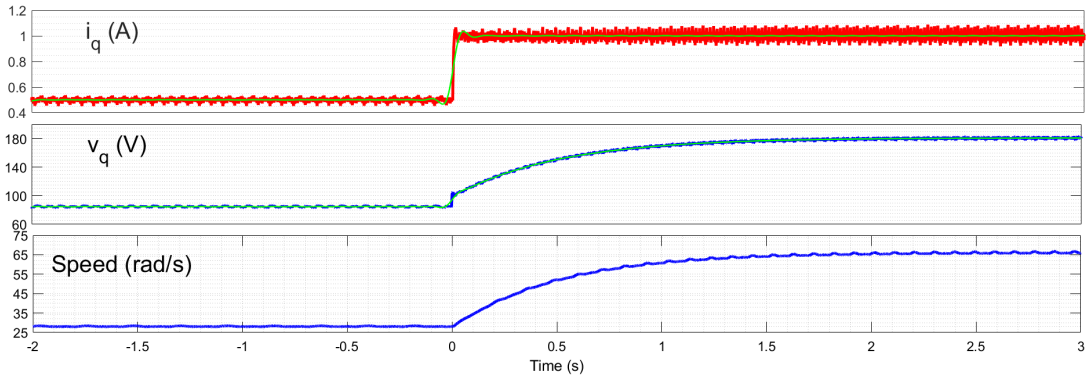

Figure 3.13: Experimental result of the q-axis voltage (V_q) and motor speed (Ω) responses to a step change in reference of i_q current.

The calculated electrical parameters of the motor are similar to those in [213] as the studied motor is the same.

To determine the mechanical parameters of the PMSM, it is assumed that the current dynamics are significantly faster than the mechanical dynamics of the motor. Therefore, it is assumed that the current follows its reference instantly when the system works in closed-loop current control mode. Considering this assumption, (6.3) can be used to calculate mechanical parameters of the motor. In this approach, a step of q-axis current (i_q) as is applied as the reference signal to the FOC control system. It should be

mentioned that i_d remains zero in this case. Therefore (6.3) will be simplified to:

$$J\frac{d\Omega}{dt} = p\psi_f i_q - f\Omega - T_L. \tag{3.20}$$

Assuming constant load torque, (3.20) for initial and final value of the (Ω) in response to step signal of (i_q) can be rewritten as:

$$\begin{cases} J\dfrac{d\Omega_i}{dt} = p\psi_f i_{q,i} - f\Omega_i - T_L \\ J\dfrac{d\Omega_f}{dt} = p\psi_f i_{q,f} - f\Omega_f - T_L \end{cases} \tag{3.21}$$

Equation (3.21) can be rewritten as:

$$J\frac{d\Delta\Omega}{dt} = p\psi_f \Delta i_q - f\Delta\Omega. \tag{3.22}$$

Therefore,

$$\frac{\Delta\Omega}{\Delta i_q} = \frac{\frac{p\psi_f}{f}}{1+\tau_m s} \tag{3.23}$$

where $\tau_m = \frac{J}{f}$ is the mechanical time constant of the motor. Hence, the speed of the motor has a first-order response to the step of q-axis reference current, as depicted in Figure 3.13.

Considering the steady-state situation and calculating ψ_f based on (3.18), friction coefficient of the motor f can be determined as $f = p\psi_f \frac{\Delta i_q}{\Delta\Omega}$. Therefore, $f = 2 \times 1.1 \times \frac{0.5}{37} = 0.029\ Nms$.

Finally the moment of inertia J of the rotor can be calculated using the time constant (τ_m) of the first-order motor speed response based on (3.23). In this case, the time constant (τ_m) is 0.5 s. Therefore, J is equal to 0.0145 kgm^2.

This section presented the tests that can be used to calculate all the motor parameters for the PMSM model in dq-frame. The model is required for designing model-based control methods such as FOC and flatness-based control.

3.7 Simulation and experimental results

In this section, the simulation of the FOC method for PMSMs is conducted in Matlab Simulink ®. The FOC method, which is one of the most prevalent control methods in PMSM drives, uses the dq-model to control the system. The simulations will be used as a reference for comparison in the subsequent chapter, which introduces a novel method.

Additionally, this section provides experimental results gathered from tests conducted on the dedicated testbench shown in Figure 3.14.

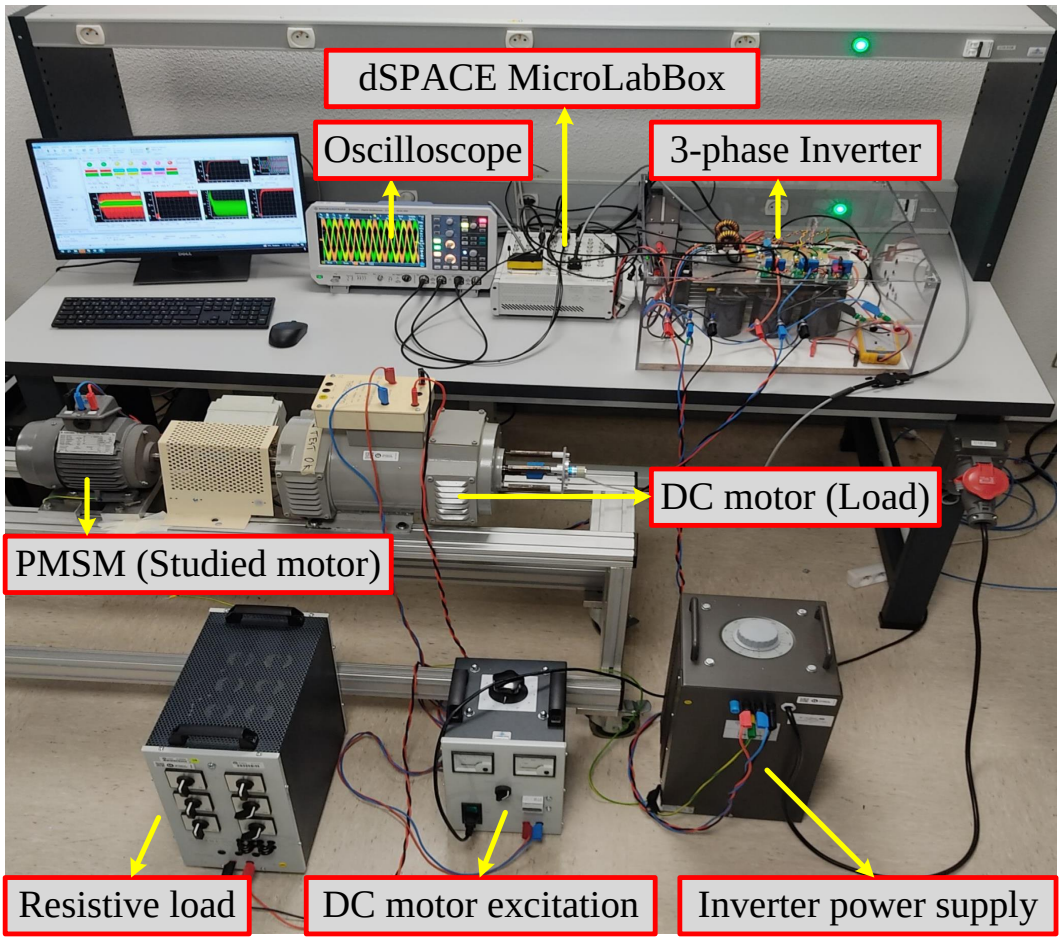

Figure 3.14: Testbench for the studied PMSM drive system.

As the original testbench for the water pump PMSM encountered mechanical problem during the final month of the thesis, we had to set up a this PMSM testbench for

experimental validation. We utilized the testbench described in Table 3.2 to conduct our experimental validation.

Table 3.2: PMSM parameters for the new testbench

Nominal speed	600 rpm
Number of poles	4
DC bus voltage	600 V
Equivalent resistance	30 Ω
Motor d-axis inductance	65 mH
Motor q-axis inductance	130 mH
Constant magnet flux	1.1 Wb
Motor inertia	0.0145 $kg.m^2$

The control system operates with a switching frequency of 10 kHz, and the control algorithm is executed on the dSpace MicroLabBox platform. As mentioned earlier, the drive system utilizes a three-phase IGBT inverter, with SEMiX251GD126HD IGBT modules, and employs SKHI23/12R drivers for gate control of the switches.

In the experimental setup, the PMSM under study is mechanically coupled to a DC motor acting as the load. This configuration allows for detailed investigation and performance evaluation of the PMSM under various operating conditions. It's noteworthy that the DC motor, acting as the load for the PMSM, is connected to a resistive load. This connection ensures to provide the required load torque during the tests, offering a controlled environment to analyze the response and efficiency of the PMSM under different load scenarios.

3.7.1 Current controller

Figure 3.15 shows the schematic of the control system using FOC method. The current control loop is designed based on (6.2). Therefore, the transfer function of system model for designing the control loop can be expressed as:

$$\frac{i_d}{V_d} = \frac{1}{R + L_d s} = \frac{\frac{1}{R}}{1 + \frac{L_d}{R} s} \tag{3.24}$$

The PWM inverter is modeled using a simple unit gain, $G_{inv} = \dfrac{V_{dc}}{2V_p}$, where V_{dc}

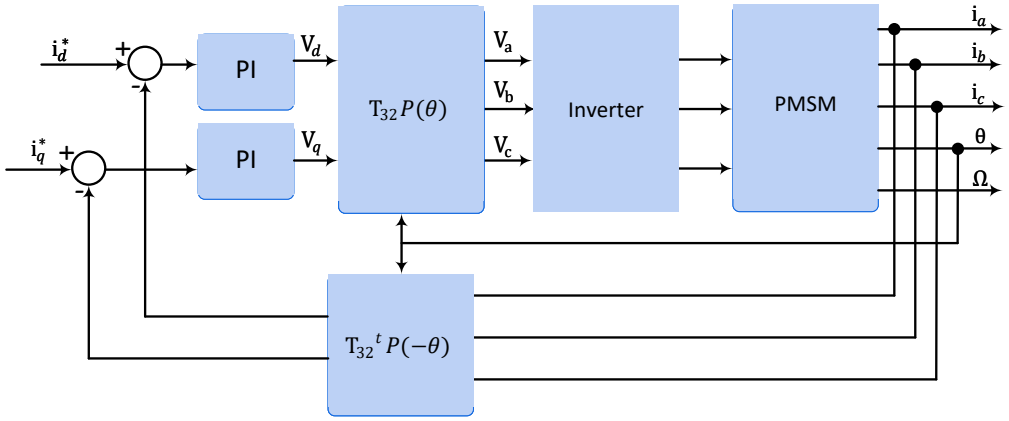

Figure 3.15: Schematic of the PMSM control system using FOC method.

represents the voltage of the DC-bus of the inverter, and V_p is the amplitude of the carrier wave in of the PWM switching method. As depicted in Figure 3.16, for each dq-axis currents, a PI-controller can be expressed as:

$$\begin{cases} C_d(s) = k_{pd}\dfrac{1+\tau_{id}s}{\tau_{id}s} \\ C_q(s) = k_{pq}\dfrac{1+\tau_{iq}s}{\tau_{iq}s} \end{cases} \tag{3.25}$$

where k_{pd} and k_{pq} are the proportional coefficients, and τ_{id} and τ_{iq} are the time constants of the PI-controllers for d-axis and q-axis current, respectively.

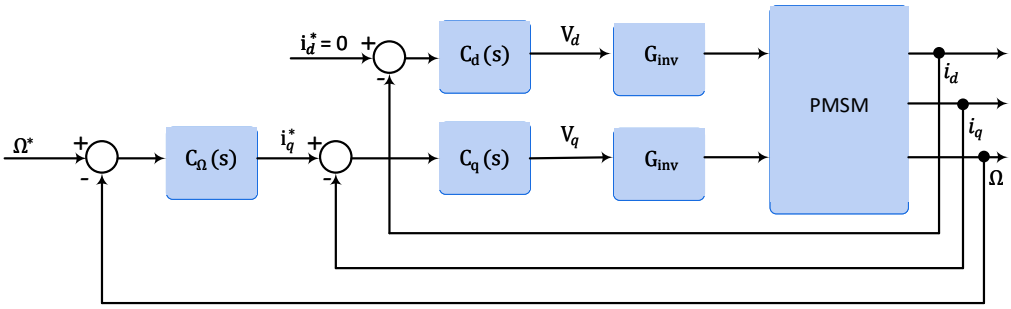

Figure 3.16: Schematic of the current and speed controllers.

The current controller's design aims to achieve the following characteristics in response to a step input:

- Elimination of steady-state error.
- A settling time of approximately 10 ms.
- Absence of overshoot.

Therefore, the open-loop transfer function of the current controller can be expressed as:

$$H_{oc} = k_{pq}\frac{1+\tau_{iq}s}{\tau_{iq}s}.G_{inv}.\frac{\frac{1}{R}}{1+\frac{L_q}{R}s} \tag{3.26}$$

Therefore, by choosing $\tau_{iq} = \frac{L_q}{R}$, (3.26) will be simplified to:

$$H_{oc} = k_{pq}\frac{G_{inv}}{R\tau_{iq}s} \tag{3.27}$$

Hence, the closed-loop transfer function is equal to:

$$H_{cc} = \frac{1}{1+\frac{R\tau_{iq}}{k_{pq}G_{inv}}s} \tag{3.28}$$

Hence, based on the required settling time (t_{set}) the proportional gain of the current PI-controller can be calculated as follows:

$$k_{pq} = \frac{3R\tau_{iq}}{t_{set}G_{inv}} \tag{3.29}$$

3.7.2 Speed controller

The speed control loop is designed based on (6.3) Therefore, the transfer function of system model for designing the control loop can be expressed as:

$$\frac{\Omega}{i_q} = \frac{\frac{p\psi_f}{f}}{1+\frac{J}{f}s} \tag{3.30}$$

For designing the speed control loop, it is considered that the current loop is much faster than the speed control loop. Therefore, it is assumed that the q-axis current fol-

lows its reference value much faster the dynamic of the speed control loop ($i_q{}^* = i_q$). The PI-controller can be expressed as:

$$C_\Omega(s) = k_{p\Omega}\frac{1+\tau_\Omega s}{\tau_\Omega s} \tag{3.31}$$

where $k_{p\Omega}$ and τ_Ω are proportional gain and time constant of the PI-controller for the motor speed.

The speed controller's design aims to achieve the following characteristics in response to a step input:

- Elimination of steady-state error.
- A settling time of approximately 100 ms.
- Less than 10% overshoot.

Therefore, the open-loop transfer function of the speed controller can be expressed as:

$$H_{o\Omega} = k_{p\Omega}\frac{1+\tau_\Omega s}{\tau_\Omega s}\frac{\frac{p\psi_f}{f}}{1+\frac{J}{f}s} \tag{3.32}$$

Therefore, by choosing $\tau_\Omega = \frac{J}{f}$, (3.32) simplifies to:

$$H_{o\Omega} = k_{p\Omega}\frac{\frac{p\psi_f}{f}}{\tau_\Omega s} \tag{3.33}$$

Hence, the closed-loop transfer function is equal to:

$$H_{c\Omega} = \frac{1}{1+\frac{f\tau_\Omega}{k_{p\Omega}p\psi_f}s} \tag{3.34}$$

Hence, based on the required settling time (t_{set}) the proportional gain of the speed PI-controller can be calculated as follows:

$$k_{p\Omega} = \frac{3R\tau_\Omega f}{t_{set}p\psi_f} \tag{3.35}$$

3.7.3 Results

Figures 3.17 and 3.18 illustrate the system's response to a step change in speed reference, based on simulation and experimental data, respectively. The speed reference shifts from 0 to 600 rpm, with both simulation and experimental scenarios considering a maximum I_q value of 5 A. The results affirm the system's efficient control of motor speed, meeting the desired response time.

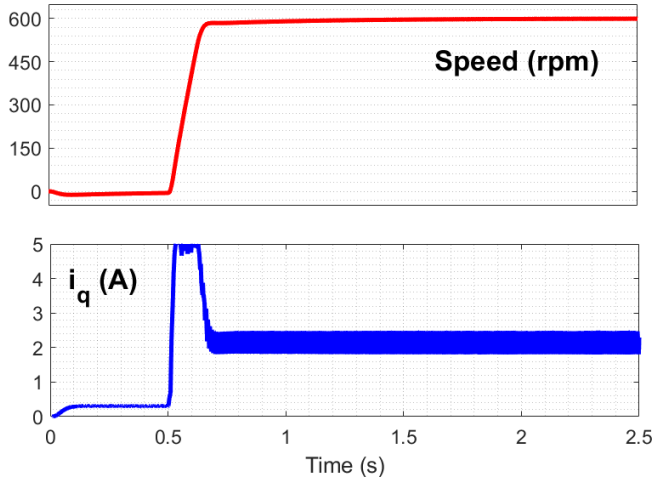

Figure 3.17: Simulation of the responses of motor speed and q-axis current (i_q) to a step change in speed reference (Ω_{ref} changes from 0 to 600 rpm at t = 0.5 s).

In another scenario, the motor's speed reference undergoes stepwise changes, as shown in Figure 3.19 for simulation and Figure 3.20 for experimental studies. The speed reference changes at specific time points: from 0 to 150 rpm at t = 2 s, 150 rpm to 300 rpm at t = 7 s, 300 rpm to 450 rpm at t = 12 s, and finally, 450 rpm to 600 rpm at t = 17 s. As the DC motor's speed, linked to the PMSM under study, increases, the load torque is estimated using a nonlinear state observer.

In another scenario, we analyzed the system's response to load variations. With the motor speed set at 600 rpm, we introduced load torque changes by altering the load connected to the DC motor. Figures 3.21 and 3.22 show the results for simulation and experimentation, respectively. The torque load increased from 3 Nm to 5.5 Nm at t = 2 s and returned to 3 Nm at t = 5 s. The control system effectively regulated the motor speed, although the response time was somewhat slow due to the cascaded structure of the control system.

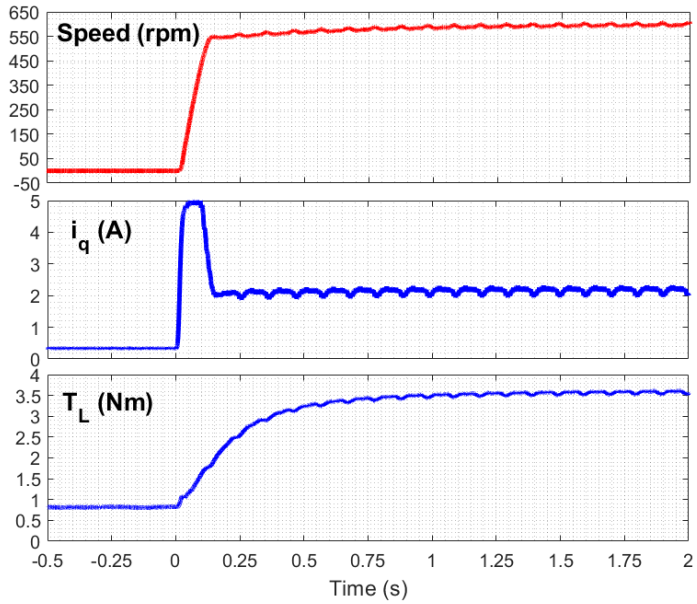

Figure 3.18: Experimental results of the variation of load torque (T_L) and responses of motor speed and q-axis current (i_q) to a step change in speed reference (Ω_{ref} changes from 0 to 600 rpm at t = 0 s).

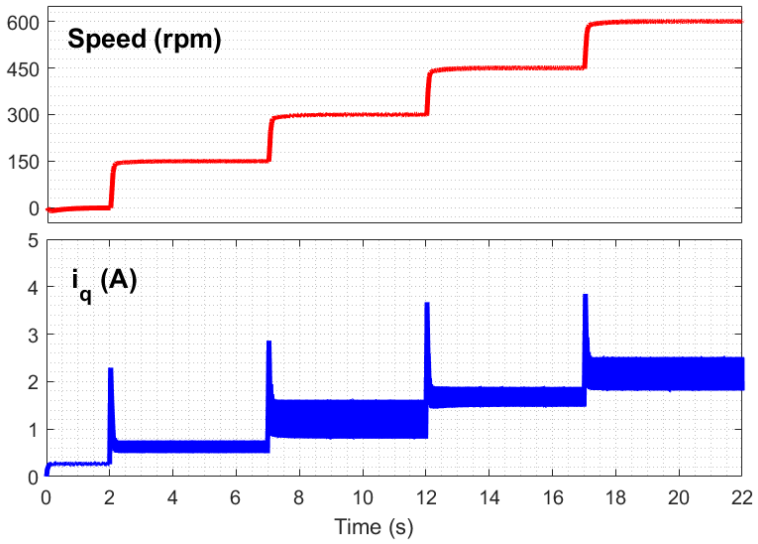

Figure 3.19: Simulation of the responses of motor speed and q-axis current (i_q) to step-wise changes of speed reference (Ω_{ref}) using FOC method.

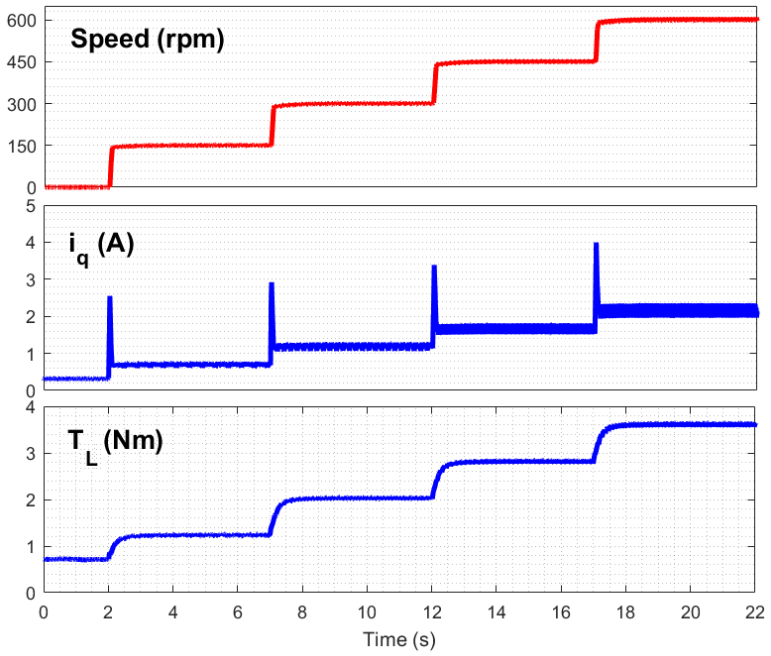

Figure 3.20: Experimental results of the variation of load torque (T_L) and responses of motor speed and q-axis current (i_q) to step-wise changes of speed reference (Ω_{ref}) using FOC method.

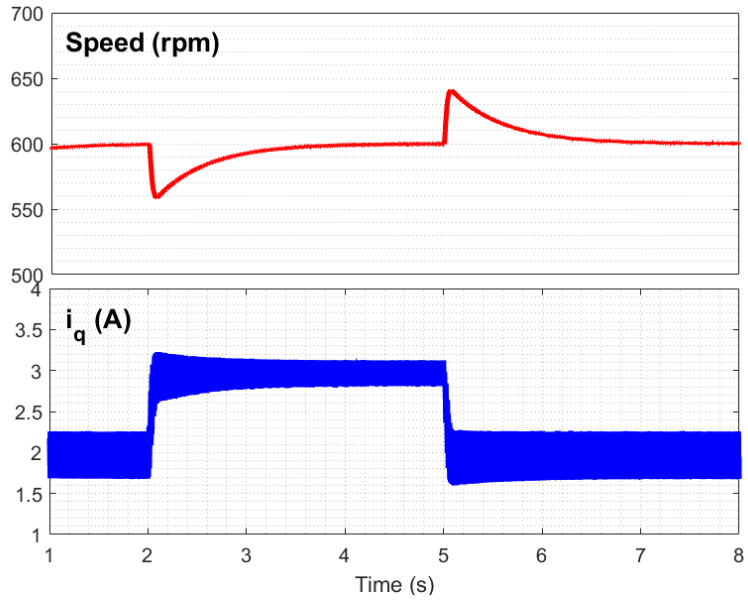

Figure 3.21: Simulation of the responses of motor speed (Ω) and q-axis current (i_q) to changes of the load torque (T_L) using FOC method.

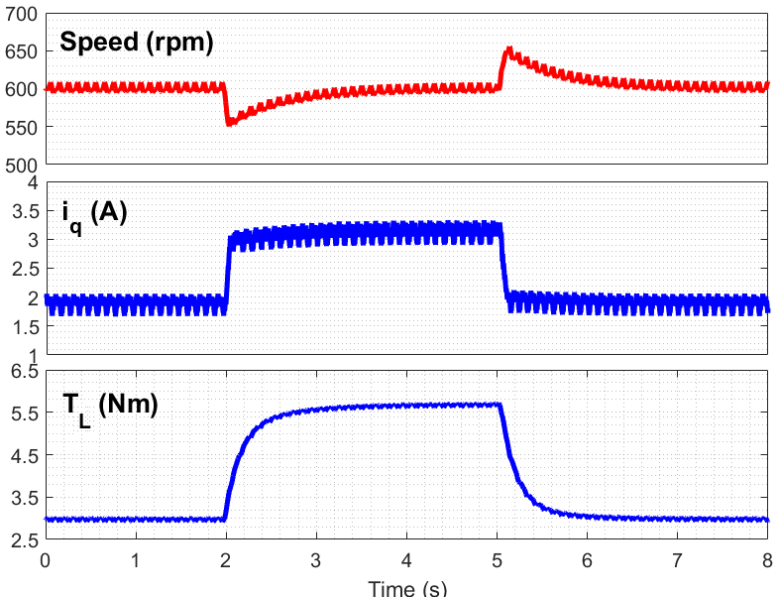

Figure 3.22: Experimental results of the responses of motor speed (Ω) and q-axis current (i_q) to changes of the load torque (T_L) using FOC method.

3.8 Conclusion

This chapter presented a detailed analysis of PMSMs. It began by delving into the structure and model of three-phase PMSMs within the dq-model framework. There was a thorough review of various control strategies and drive methods, as well as their advantages and disadvantages. Particularly, the chapter emphasizes the suitability of HFSI methods and FPE-based approaches for low-speed applications, whereas model-based methods find prominence in applications with medium- to high-speed ranges. As a compromise between sensorless and sensor-based approaches, low-resolution Hall-position sensors can also be considered as a cost-performance option.

Additionally, this chapter outlined the essential tests required for the identification of system parameters using the testbench utilized in this thesis. It also discussed the theoretical approach to tuning both current and speed controllers using the FOC method, followed by simulation results using Matlab Simulink. A testbench was then used to validate the simulation results, providing a crucial reference point for comparing the novel method to be described in the next chapter.

Furthermore, the chapter briefly introduced flatness-based control as a potential solution to address the issued of FOC method resulted from nonlinearity of the PMSM system. There will be a more comprehensive exploration of this method in the following chapter, where a novel approach for trajectory planning to address controller limits will be discussed thoroughly.

Chapter 4

Flatness-based control of PMSMs

Contents

4.1 Introduction

The PMSM drive system is recognized as a nonlinear system. Although the FOC method is the most common control method in today's industry, it is essentially a linear controller whose performance is determined by the system's operating point. In an attempt to overcome issues associated with the inherent nonlinearity of PMSM systems, flatness-based control methods have been proposed.

Trajectory planning significantly impacts the response of the flatness-based control system. As a result, current literature predominantly uses a second-order trajectory with a cascaded flatness-based control structure that has current saturation. Therefore, flatness-based control loses one of its core features, the ability to quickly track references even during transient events as a result of this cascaded structure. Alternatively, using a second-order trajectory function forces a trade-off between overcurrent protection and employing a single-loop control structure. The application of flatness-based motor drive control is therefore restricted by controller limit constraints.

A window-based function trajectory planning method is introduced in this thesis to address the aforementioned challenge. The method utilizes online optimization to minimize the control system's response time while adhering to the constraints imposed by the controller, such as motor current and switching voltage.

There is a detailed analysis of the PMSM model and flatness-based control in Section 4.2, which concludes that the PMSM drive system inherently possesses flatness characteristics. A comprehensive bibliography review of flatness-based control in PMSMs is provided in Section 4.3, providing an insight into the current state of the art for flatness-based control and trajectory planning. In Section 4.4, a comprehensive examination of flatness-based control approaches and guidelines for controller coefficient tuning is provided. The FOC method and conventional flatness-based control are compared in Section 4.5, which includes a robustness assessment using the Jacobian matrix of the closed-loop system model. A detailed explanation of the proposed trajectory planning methodology is provided in Section 4.6, which includes the underlying idea, the mathematical foundation, as well as optimization algorithms. In Section 4.7, torque

and voltage drop observers are examined as a means of improving the robustness and dynamic performance of flatness-based control. In this section, two types of observers are examined: nonlinear state observers and Extended Luenberger observers (ELOs). Simulation and experimental results are presented in Section 4.8, providing support for the proposed methodologies. A summary of the key findings and contributions of this chapter is presented in Section 4.9.

4.2 Flatness-based control of the PMSM

Traditional PMSM drive control approaches use FOC in conjunction with PI controllers to regulate torque and speed of the motor [130, 140, 141]. Nevertheless, linear methods such as FOC require linear approximations of system models when designing controller parameters. Given that PMSM systems are inherently nonlinear, the dynamic performance of a drive system employing a linear controller, such as FOC, becomes dependent on the system's operating point.

Researchers have proposed model-based nonlinear control strategies to address the inherent nonlinearity in PMSM drive systems [214–216]. One approach is to introduce differential flatness theory as originally presented in [217]. By using differential flatness, it is possible to estimate the trajectory of a system directly from its trajectory and derivatives, without having to integrate differential equations [218–220].

4.2.1 Model of the PMSM

As mentioned in the previous chapter, the PMSM model in dq-frame as described in (6.2)-(6.4) is employed in the application of the flatness-based control method for PMSM drive.

4.2.2 Flatness-based control theory

Flatness theory is a mathematical framework and control methodology commonly used in control engineering and system theory. The method is particularly useful when it comes to modeling and controlling complex nonlinear systems. An important concept behind flatness theory is the idea of transforming a nonlinear system into a "flat" rep-

resentation, where state variables and control inputs are selected and consequently the system's dynamics become particularly linear-like. The control design can be simplified by using this transformed representation, which makes it easier to achieve desired system behavior.

A system is said to be "differentially flat" if its output trajectory can be expressed as a function of a set of flat outputs and their derivatives without solving differential equations. These flat outputs are carefully selected state variables that fully describe the system's behavior. By determining the desired trajectories for flat outputs, the entire system can be controlled without the need for complex nonlinear equations.

A nonlinear dynamic system x, defined by the equation:

$$\dot{x}(t) = f(x(t), u(t)) \quad x(t) \in \mathbb{R}^n \text{ and } u(t) \in \mathbb{R}^m, \tag{4.1}$$

is characterized as differentially flat when there exists a set of differentially independent variables, equal in number to the inputs. This characteristic enables the representation of all state variables $x(t)$ and control inputs $u(t)$ using output variables $y(t)$ and their time derivatives. This representation is achieved without the need to solve differential equations [221].

$$y(t) = (y_1(t), y_2(t), ..., y_m(t)). \tag{4.2}$$

In other words, the system is flat if:

- Each $y_i,\ i = 1, ..., m$ can be represented as a function of state variables $x_i,\ i = 1, ..., n$ and inputs $u_i,\ i = 1, ..., m$ and a finite number of derivatives ${u_i}^{(k)},\ k = 1, ..., \alpha_i$.
- Each $x_i, i = 1, ..., n$ and inputs $u_i, i = 1, ..., m$ can be represented as a function of flat outputs $y_i,\ i = 1, ..., m$ and a finite number of derivatives ${y_i}^{(k)},\ k = 1, ..., m$.
- Flat outputs $y_i,\ i = 1, ..., m$ are differentially independent.

4.2.3 Flatness property of the system

In this section, we demonstrate that the PMSM drive can be considered a flat system. Hence, it is possible to control its output variables using flatness-based control method.

The PMSM system's state variables comprise both the d- and q-axis currents, as well as the motor's mechanical speed. These variables are represented together as the vector:

$$x = [i_d, i_q, \Omega]^t \tag{4.3}$$

The PMSM system is composed of the following inputs:

$$u = [V_d, V_q]^t \tag{4.4}$$

It is important to note that the flat outputs chosen for the control system design consist of two variables; the d-axis current (i_d) and the mechanical speed of the motor (Ω), which play pivotal roles in the system's overall performance.

$$\begin{cases} y_d = i_d \\ y_\Omega = \Omega \end{cases} \tag{4.5}$$

Hence, it is possible to represent the state variables as functions of flat outputs and their respective derivatives, as illustrated in (4.6).

$$i_q = \frac{1}{p[\psi_f + (L_d - L_q)y_d]}(J\dot{y}_\Omega + f y_\Omega + T_L) = h_{iq}(y_d, \dot{y}_\Omega, y_\Omega) \tag{4.6}$$

Equations (4.5) and (4.6) provide a means to describe the switching voltages, namely V_d and V_q, for the PMSM in terms of the flat outputs and their derivatives.

$$\begin{cases} V_d = R_s y_d + L_d \dot{y}_d - p y_\Omega L_q h_{iq}(y_d, \dot{y}_\Omega, y_\Omega) \\ = h_{V_d}(y_d, \dot{y}_d, y_\Omega, \dot{y}_\Omega) \\ V_q = R_s h_{iq}(y_d, \dot{y}_\Omega, y_\Omega) + L_q \dot{h}_{iq}(y_d, \dot{y}_\Omega, y_\Omega) \\ + p y_\Omega L_d y_d + p\psi_f y_\Omega = h_{V_q}(y_d, \dot{y}_d, y_\Omega, \dot{y}_\Omega, \ddot{y}_\Omega). \end{cases} \tag{4.7}$$

Consequently, the PMSM drive system can be effectively regulated through the utilization of the flatness-based control methodology, due to flatness property of the PMSM system.

4.2.4 Flatness-based control of PMSM considering the saturation effect

As it is previously mentioned the PMSM motor under saturation condition can be expressed as:

$$\begin{cases} \begin{bmatrix} V_d \\ V_q \end{bmatrix} = R_s \begin{bmatrix} i_d \\ i_q \end{bmatrix} + \frac{d}{dt} \begin{bmatrix} \psi_d(i_d, i_q) \\ \psi_q(i_d, i_q) \end{bmatrix} + \dot{\theta} P(\pi/2) \begin{bmatrix} \psi_d(i_d, i_q) \\ \psi_q(i_d, i_q) \end{bmatrix} \\ T_e = p[\psi_d(i_d, i_q) i_q - \psi_q(i_d, i_q) i_d] \end{cases} \tag{4.8}$$

It has been demonstrated in [128] that $\psi_d(i_d, i_q)$ and $\psi_q(i_d, i_q)$ can be modeled as:

$$\begin{cases} \psi_d(i_d, i_q) = \psi_{d0} + A_1 i_d - B_1 i_d^2 - C_1 |i_q| \\ \psi_q(i_d, i_q) = i_q (A_2 - C_2 i_q^2 - D_2 i_d + E_2 i_d^3) \end{cases} \tag{4.9}$$

Considering the flat outputs $y_d = \psi_d(i_d, i_q)$ and $y_\Omega = \Omega$, (4.9) can be rewritten as:

$$y_d - \psi_{d0} - A_1 i_d + B_1 i_d^2 + C_1 |i_q| = 0 \tag{4.10}$$

Therefore,

$$\begin{cases} i_d = \dfrac{A_1 - \sqrt{A_1^2 + 4B_1(\psi_{d0} - C_1|i_q| - y_d)}}{2B_1} = \dfrac{A_1 - \gamma}{2B_1} = f(y_d, i_q) \\ \gamma = \sqrt{A_1^2 + 4B_1(\psi_{d0} - C_1|i_q| - y_d)} \end{cases} \tag{4.11}$$

Similarly, it can be proven that electromagnetic torque of the motor is a function of y_d and i_q as demonstrated in (4.12).

$$\begin{aligned} T_e = p[\psi_d(i_d, i_q) i_q - \psi_q(i_d, i_q) i_d] = p[y_d i_q - i_q (A_2 - C_2 i_q^2 - D_2 i_d + E_2 i_d^3) i_d] \\ = p[y_d i_q - A_2 i_q (\frac{A_1 - \gamma}{2B_1}) + C_2 i_q^3 (\frac{A_1 - \gamma}{2B_1}) + D_2 i_q (\frac{A_1 - \gamma}{2B_1})^2 - E_2 i_q (\frac{A_1 - \gamma}{2B_1})^4] \end{aligned} \tag{4.12}$$

Using (4.11), it has been demonstrated in [128] that i_q can be expressed as follows:

$$|i_q| = \frac{1}{C_1}(\psi_{d0} - \frac{\gamma^2 - A_1^2}{4B_1} - y_d) \tag{4.13}$$

As a result, the electromagnetic torque can be expressed as a function of y_d and γ. Consequently, within the PMSM model, γ becomes a function of y_d, y_Ω, and $\dot{y}_\Omega$. As a consequence, both the control system outputs (V_d and V_q) and the system's state variables (i_d, i_q, and Ω) can be represented as functions of the flat outputs, as depicted in (4.14).

$$\begin{cases} i_d = h'_{i_d}(y_d, \dot{y_\Omega}, y_\Omega) \\ i_q = h'_{i_q}(y_d, \dot{y_\Omega}, y_\Omega) \\ \Omega = y_\Omega \\ V_d = h'_{V_d}(\dot{y_d}, y_d, \ddot{y_\Omega}, \dot{y_\Omega}, y_\Omega) \\ V_q = h'_{V_q}(\dot{y_d}, y_d, \ddot{y_\Omega}, \dot{y_\Omega}, y_\Omega) \end{cases} \tag{4.14}$$

Therefore, as detailed in [128], it has been demonstrated that the PMSM model, accounting for the saturation effect, also exhibits flatness. Consequently, flatness-based control can be employed as an alternative to linear control methods like FOC.

4.3 State of the art

In comparison to classic FOC control, flatness-based control of PMSMs offers several advantages [222, 223].

- Firstly, it eliminates the need for regulators if all parameters are known, allowing for open-loop control.
- Secondly, it can achieve high dynamic performance even in the presence of model errors and external disturbances [224].
- Additionally, the trajectory planning method used in flatness-based control outperforms cascaded linear controllers in both transient and disturbed conditions [223].

- Lastly, it has been demonstrated that flatness-based control consistently delivers competitive performance compared to conventional FOC techniques [225].

4.3.1 Flatness-based control of PMSMs

Researchers have shown that flatness-based control can be used with PMSMs in saturation mode. In addition to addressing manufacturing issues, PMSMs are sometimes engineered to operate efficiently under transient, thermally constrained overload conditions, resulting in magnetic saturation. Also, some industries are trying to design PMSMs in saturation mode to reduce cost, which intensifies the issues regarding nonlinearity of the system controlled with linear controllers. Consequently, several works have outlined innovative flatness-based control strategies utilizing PMSM mathematical models expressed specifically for saturation modes [226–228]. Through these research contributions, flatness-based control has been expanded to include PMSMs in saturation mode. Studying magnetic saturation and incorporating these insights into the control framework aims to enhance the performance of PMSMs under a variety of operating conditions.

The flatness-based control method utilizes a mathematical model to control the behavior of a system. However, the effectiveness of this control strategy is heavily dependent on how accurately the system model represents real-world dynamics. Due to various factors such as system variations, uncertainties, and external disturbances, achieving a highly accurate model can be challenging in practical industrial applications. Recently, research has been dedicated to improving the dynamic performance of the flatness-based control method in order to overcome the limitations caused by model inaccuracies. It is possible to improve the system by incorporating observers. In this case, two types of observers have been explored in recent studies: nonlinear state observer and ELO.

- **State observer**: According to [229], state observers are designed to estimate variables or states that are difficult to measure directly. As part of flatness-based control, they can help estimate parameters such as load torque and voltage drops.

- **Extended Luenberger Observers (ELO)**: As proposed in [230], ELOs are a specific type of observer designed to estimate system states, especially in the pres-

ence of uncertainties and disturbances.

Adding these observers to the flatness-based control framework seeks to mitigate the adverse effects of inaccurate model of the system. The observers provide real-time estimates of critical parameters, which allow the control system to compensate for discrepancies between the model and actual behavior. In this way, flatness-based control becomes more reliable and robust for industrial applications requiring precise and robust performance.

4.3.2 Trajectory planning

Flatness-control method is designed in a way to make sure that its flat outputs always follow the trajectory reference. Therefore, trajectory planning can play a pivotal role in its dynamic performance [231]. Even though trajectory planning is a research topic in the some other fields such as robotics, it has not received significant attention in PMSM drive applications so far.

Second-order transfer functions described in (4.15) are commonly used to limit transient speed and current references in classical trajectory planning designs for PMSM drive applications. In the trajectory planning phase, the desired output, denoted as y_{ref}, is generated by the trajectory planning block. Similarly, the flat output, denoted by y_{inf}, is derived from the reference signal.

$$y_{ref} = \frac{1}{\frac{1}{\omega_f^2}s^2 + \frac{2\zeta_f}{\omega_f}s + 1} y_{inf}, \tag{4.15}$$

where ω_f and ζ_f are the cutoff frequency and damping ratio of the trajectory transfer function, respectively.

However, a simple second-order trajectory function does not provide overcurrent protection for motor drive system. Therefore, a cascaded flatness-based control approaches are often employed in these cases, as shown in Figure 6.5, although this leads to a slower response time of the control system [230, 232]. There is another cascaded flatness-based control scheme proposed in [233] for eliminating static errors in the system's state variables. The transfer functions for the cascaded flatness-control can be expressed as:

$$\begin{cases} \dfrac{y_{q,ref}}{y_{q,inf}} = \dfrac{1}{\frac{1}{\omega_{f1}^2}s^2 + \frac{2\zeta_{f1}}{\omega_{f1}}s + 1} \\ \dfrac{y_{\Omega,ref}}{y_{\Omega,inf}} = \dfrac{1}{\frac{1}{\omega_{f2}^2}s^2 + \frac{2\zeta_{f2}}{\omega_{f2}}s + 1} \end{cases} \tag{4.16}$$

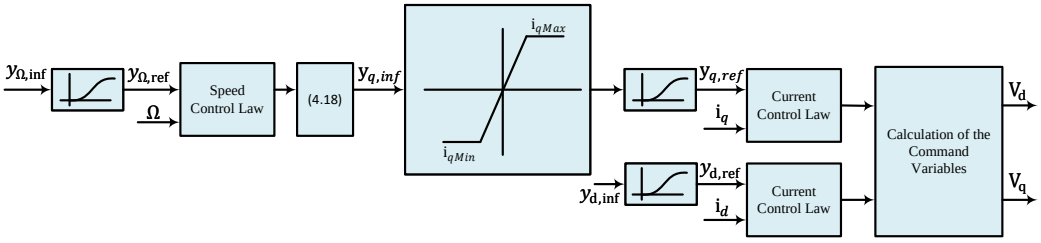

Figure 4.1: Schematic of the cascaded flatness-based control of PMSMs [232].

Signal $y_{q,inf}$ is calculated using (6.14).

$$y_{q,inf} = \frac{J\dot{y}_{\Omega,ref} + f y_{\Omega,ref} + T_L}{p\psi_f} \tag{4.17}$$

Considering the possible interaction between the switching frequency of the inverter (ω_s) and cutoff frequency of the cascade control system, for designing the control system it is assumed that the outer speed control loop operates at a cutoff frequency satisfying $\omega_{n2} \leq \omega_{f1} \leq \omega_{n1} \leq \omega_s$, where ω_{n1} and ω_{n2} are the cutoff frequency of cascaded flatness-controllers. To improve the the speed control response, usually ω_{f2} is chosen to be equal to ω_{n2} [232].

Furthermore, a comprehensive comparison of conventional flatness-based control and FOC method is provided in [223]. The findings indicate that flatness-based control schemes with a one control loop are effective at rapidly regulating motor speed, even in the presence of disturbances and variations in load torque. However using flatness-based control with only one loop results in sacrificing the motor current protection.

To address this challenge of overcurrent protection for one-loop flatness-based control, two approaches have been proposed in [234]. The first method involves dynamic adjustments to the reference trajectory of the mechanical speed to prevent overcurrent conditions. The second approach focuses on system safety by stoping the system opera-

tion when significant disturbances happen, and consequently prevents potential damage.

Moreover, an extended flatness-based control method is introduced in [235]. This method incorporates an event-based mechanism to enhance the system performance. During these events, the trajectory planning and controller parameters are updated based on real-time measurements and estimations of the system parameters.

4.4 Flatness-based control method

In Figure 6.4, the schematic of a flatness-based control framework is presented. As part of this control approach, two state variables, i_d and Ω, are directly controlled, whereas the q-axis current (i_q) is controlled indirectly.

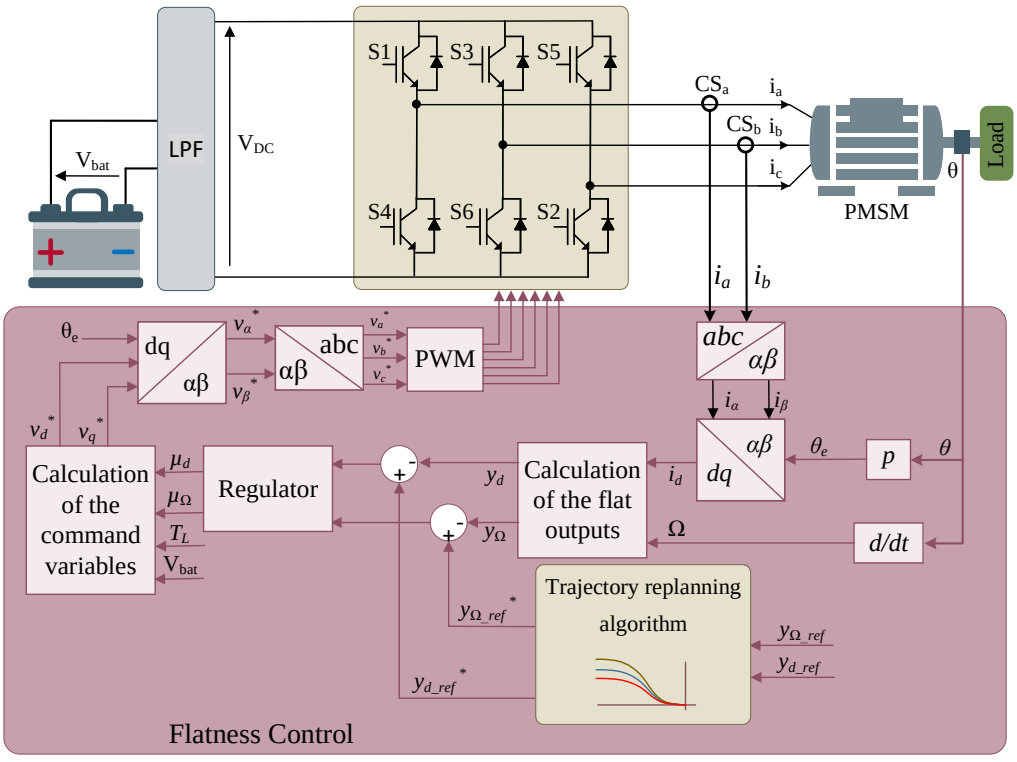

Figure 4.2: Schematic of the flatness-based control of a PMSM.

There are two new variables that need to be introduced for designing the differential

flatness-based controller. These variables are supposed to represent the highest-order derivative components of flat outputs in the equations for V_d and V_q. For instance, for the studied PMSM in this thesis, V_d and V_q can be expressed based on flat output variables as:

$$\begin{cases} V_d = L_d \dot{y_d} + R_s y_d - p L_q \dot{i_q} y_\Omega \\ V_q = L_q \dot{i_q} + R_s i_q + p L_d y_d y_\Omega + p \psi_f y_\Omega \end{cases} \tag{4.18}$$

Considering that q-axis current can be expressed based on flat output variables as $\frac{1}{p\psi_f}(J\dot{y_\Omega} + f y_\Omega + T_L)$, (6.5) is equal to:

$$\begin{cases} V_d = L_d \dot{y_d} + R_s y_d - \dfrac{J L_q}{\psi_f} y_\Omega \dot{y_\Omega} - \dfrac{f L_q}{\psi_f} y_\Omega^2 - \dfrac{L_q}{\psi_f} y_\Omega T_L \\ V_q = \dfrac{J L_q}{p\psi_f} \ddot{y_\Omega} + \dfrac{f L_q + J R_s}{p\psi_f} \dot{y_\Omega} + (p\psi_f + \dfrac{f R_s}{p\psi_f}) y_\Omega + p L_d y_d y_\Omega + \dfrac{R_s}{p\psi_f} T_L \\ + \dfrac{L_q}{p\psi_f} \dot{T_L} \end{cases} \tag{4.19}$$

Therefore,

$$\begin{cases} \mu_d = \dot{y_d} \\ \mu_\Omega = \ddot{y_\Omega} \end{cases} \tag{4.20}$$

In order to address uncertainties in system parameters and deal with disturbances, the one-loop flatness-based control method formulates control laws for regulators as follows:

$$\begin{cases} \dot{y_{d,ref}} - \mu_d + k_{d1}.(y_{d,ref} - y_d) + k_{d2} \cdot \int (y_{d,ref} - y_d)\, d\tau = 0 \\ \ddot{y_{\Omega,ref}} - \mu_\Omega + k_{\Omega 1} \cdot (\dot{y_{\Omega,ref}} - \dot{y_\Omega}) + k_{\Omega 2} \cdot (y_{\Omega,ref} - y_\Omega) \\ + k_{\Omega 3} \cdot \int (y_{\Omega,ref} - y_\Omega)\, d\tau = 0, \end{cases} \tag{4.21}$$

where $k_{\Omega 1}$, $k_{\Omega 2}$, and $k_{\Omega 3}$ are the controller parameters for mechanical speed regulator. Similarly, k_{d1} and k_{d2} are the controller parameters for direct current regulator. The integral term provides robust rejection of both static error and parameter uncertainty.

To determine the controller coefficients, the following characteristic polynomials are

being used.

$$\begin{cases} s + k_{d1} + \dfrac{k_{d2}}{s} = 0 \\ s^2 + k_{\Omega 1} s + k_{\Omega 2} + \dfrac{k_{\Omega 3}}{s} = 0 \end{cases} \tag{4.22}$$

Equation (6.9) can be rewritten as:

$$\begin{cases} s^2 + k_{d1} s + k_{d2} = 0 \\ s^3 + k_{\Omega 1} s^2 + k_{\Omega 2} s + k_{\Omega 3} = 0 \end{cases} \tag{4.23}$$

For tuning the controller parameters, the desired characteristic polynomial is considered as:

$$\begin{cases} Q_d = s^2 + 2\zeta_d \omega_d s + \omega_d^2 \\ Q_\Omega = (s - p_\Omega)(s^2 + 2\zeta_\Omega \omega_\Omega s + \omega_\Omega^2), \end{cases} \tag{4.24}$$

where ω_Ω, ω_d, and ζ_Ω, ζ_d are the cutoff frequency and the damping coefficients, respectively. The controller parameters are calculated using the pole-placement method. The pole p_Ω is considered equal to $-\zeta_\Omega \omega_\Omega$ in this thesis. Therefore, the controller parameters for i_d polynomial are calculated as follows:

$$\begin{cases} k_{d1} = 2\zeta_d \omega_d \\ k_{d2} = \omega_d^2 \end{cases} \tag{4.25}$$

The same method is utilized for calculating the coefficients of mechanical speed controller, as described in (4.26).

$$\begin{cases} k_{\Omega 1} = 3\zeta_\Omega \omega_\Omega \\ k_{\Omega 2} = \omega_\Omega^2 + 2\zeta_\Omega^2 \omega_\Omega^2 \\ k_{\Omega 3} = \zeta_\Omega \omega_\Omega^3 \end{cases} \tag{4.26}$$

4.5 Comparison of flatness-based control with FOC

A closed-loop model of the system is used to evaluate the robustness of the control method against motor parameter variations. The state-space equations for the open-loop PMSM system are derived from (6.2)-(6.4) by considering the motor's d- and q-axis

currents and its mechanical speed as state variables of the system.

Further sections analyze the state-space representation of the closed-loop system for FOC and flatness-based control for PMSMs. These representations provide insight into the performance and adaptability of these control strategies in response to variable motor parameters.

4.5.1 Robustness analysis of FOC method

Each PI regulator introduces an additional state variable into the closed-loop model in a cascade control system. As a consequence, it is essential to take into account the variables outlined in (4.27).

$$\begin{cases} \dot{x_{id}} = k_{ic}(i_{d,ref} - i_d) \\ \dot{x_{iq}} = k_{ic}(i_{q,ref} - i_q) \\ \dot{x_{\Omega}} = k_{i\Omega}(\Omega_{ref} - \Omega), \end{cases} \tag{4.27}$$

where k_{ic} and $k_{i\Omega}$ are integral coefficients in current and speed regulator, respectively.

Equation (4.28) depicts a nonlinear state-space representation of a closed-loop system with FOC. In order to achieve this representation, V_d and V_q are derived from the state variables of the system and subsequently substituted into (6.2)-(6.4):

$$\dot{X}_{FOC} = A(X_{FOC}) \cdot X_{FOC} + B_{FOC} \cdot U_{FOC}, \tag{4.28}$$

where $X_{FOC} = [i_d, i_q, \Omega, x_{id}, x_{iq}, x_{\Omega}]^T$ is the matrix of state variables and $U_{FOC} = [i_{d,ref}, \Omega_{ref}, T_L]^T$ is the matrix of the system inputs. By linearizing the state-space equations of the system around the equilibrium point for the nominal operating point of the system, the Jacobian matrix of the system, $J_{FOC} \in R^{6\times6}$, can be computed [223]. A detailed calculation of J_{FOC} is presented in Appendix A.

Therefore $A(X_{FOC})$ and B_{FOC} can be described as follows:

$$A(X_{FOC}) = \begin{bmatrix} -\frac{(k_{pc}+R_s)}{L_s} & p(1-\frac{L'_s}{L_s})\Omega_0 & p(1-\frac{L'_s}{L_s})i_{q0} & \frac{1}{L_s} & 0 & 0 \\ -p(1-\frac{L'_s}{L_s})\Omega_0 & -\frac{(k_{pc}+R_s)}{L_s} & A_{23} & 0 & \frac{1}{L_s} & \frac{k_{pc}}{L_s} \\ 0 & \frac{p\psi_f}{J} & -\frac{f}{J} & 0 & 0 & 0 \\ -k_{ic} & 0 & 0 & 0 & 0 & 0 \\ 0 & -k_{ic} & -k_{ic}k_{p\Omega} & 0 & 0 & k_{ic} \\ 0 & 0 & -k_{i\Omega} & 0 & 0 & 0 \end{bmatrix} \tag{4.29}$$

$$B_{FOC} = \begin{bmatrix} \frac{k_{pc}}{L_s} & 0 & 0 \\ 0 & \frac{k_{pc}k_{p\Omega}}{L_s} & 0 \\ 0 & 0 & -\frac{1}{J} \\ k_{ic} & 0 & 0 \\ 0 & k_{ic}k_{p\Omega} & 0 \\ 0 & k_{i\Omega} & 0 \end{bmatrix} \tag{4.30}$$

where $A_{23} = -p(1-\frac{L'_s}{L_s})i_{d0} - \frac{p(\psi_f - \psi'_f) + k_{pc}k_{p\Omega}}{L_s}$.

4.5.2 Robustness analysis of flatness-based control method

In flatness-based control, adding each regulator adds an extra state variable to the closed-loop system's state-space representation. Thus, it becomes necessary to account for the state variables described in (4.31).

$$\begin{cases} \dot{x_{id}} = i_{d,ref} - i_d \\ \dot{x_\Omega} = \Omega_{ref} - \Omega. \end{cases} \tag{4.31}$$

A nonlinear state-space representation of a flatness-based control system can be found in (4.32), which is obtained by calculating V_d, V_q, and $\dot{\Omega}$ using the state variables of the system and substituting them into (6.2)-(6.4).

$$\dot{X}_{Flatness} = A(X_{Flatness}) \cdot X_{Flatness} + B_{Flatness} \cdot U_{Flatness} \tag{4.32}$$

where $X_{Flatness} = [i_d, i_q, \Omega, x_{id}, x_\Omega]^T$ is the matrix of state variables and $U_{Flatness} = [i_{d,ref}, \dot{i}_{d,ref}, \Omega_{ref}, \dot{\Omega}_{ref}, \ddot{\Omega}_{ref}, i_{d,ref} \cdot \Omega_{ref}, \Omega^2_{ref}, \Omega_{ref} \cdot \dot{\Omega}_{ref}, T_L]^T$ is the matrix of the system inputs. It is possible to compute the Jacobian matrix of the system, $J_{Flatness} \in R^{5\times5}$, using the state-space equations of the system around their equilibrium points for the nominal operating point of the system [223]. A detailed calculation of $J_{Flatness}$ is presented in Appendix B.

Therefore $A(X_{Flatness})$ and $B_{Flatness}$ can be described as follows:

$$A(X_{Flatness}) = \begin{bmatrix} A_{11} & p\Omega_0 & pi_{q0} & \frac{L'_s}{L_s}k_{d2} & 0 \\ -p\Omega_0 & A_{22} & A_{23} & 0 & A_{25} \\ 0 & \frac{p\psi_f}{J} & -\frac{f}{J} & 0 & 0 \\ -1 & 0 & 0 & 0 & 0 \\ 0 & 0 & -1 & 0 & 0 \end{bmatrix} \tag{4.33}$$

where,

$$\begin{cases} A_{11} = -(\frac{R_s}{L_s} + \frac{L'_s}{L_s}k_{d1}) \\ A_{22} = -(\frac{R_s}{L_s} + \frac{L'_s J' \psi_f}{L_s J \psi'_f}k_{\Omega1}) \\ A_{23} = \frac{L'_s J' f}{L_s J p \psi'_f}k_{\Omega1} - \frac{L'_s J'}{L_s p \psi'_f}k_{\Omega2} - pi_{d0} - \frac{p\psi_f}{L_s} \\ A_{25} = \frac{L'_s J'}{L_s p \psi'_f}k_{\Omega3}. \end{cases} \tag{4.34}$$

$$B_{Flatness} = \begin{bmatrix} B_{11} & \frac{L'_s}{L_s} & 0 & 0 & 0 & 0 & -\frac{L'_s f'}{L_s \psi'_f} & -\frac{L'_s J'}{L_s \psi'_f} & 0 \\ 0 & 0 & B_{23} & B_{24} & \frac{J' L'_s}{L_s p \psi'_f} & \frac{p L'_s}{L_s} & 0 & 0 & B_{29} \\ 0 & 0 & 0 & 0 & 0 & 0 & 0 & 0 & -\frac{1}{J} \\ 1 & 0 & 0 & 0 & 0 & 0 & 0 & 0 & 0 \\ 0 & 0 & 1 & 0 & 0 & 0 & 0 & 0 & 0 \end{bmatrix} \tag{4.35}$$

where,

$$\begin{cases} B_{11} = \dfrac{R_s}{L_s} + \dfrac{L'_s}{L_s} k_{d1} \\ B_{23} = \dfrac{p\psi'_f}{L_s} + \dfrac{R'_s f'}{L_s p\psi'_f} + \dfrac{L'_s J'}{L_s p\psi'_f} k_{\Omega 2} \\ B_{24} = \dfrac{R'_s J'}{L_s p\psi'_f} + \dfrac{L'_s f'}{L_s p\psi'_f} + \dfrac{J' L'_s}{L_s p\psi'_f} k_{\Omega 1} \\ B_{29} = \dfrac{J' L'_s}{J L_s p\psi'_f} k_{\Omega 1}. \end{cases} \tag{4.36}$$

4.5.3 Robustness-based comparison of both methods

The eigenvalues of the Jacobian matrices for FOC and flatness-based control across different motor parameter values are analyzed to assess the robustness of these methods to variations of motor parameters. The parameters of the studied motor are given in Table 4.1. Also ω_f and ω_Ω for these simulation studies are considered 60 rad/s and 600 rad/s, respectively.

Table 4.1: Water pump PMSM parameters for the original testbench.

Nominal speed	3000 rpm
Number of poles	8
Battery voltage	12 V
Nominal power	200 W
Motor equivalent resistance	66.7 $m\Omega$
Motor d- and q-axis inductance	40 μH
Motor inertia	45.5e-6 $kg.m^2$

The system nonlinearity in equations is linked to the motor inductance. Therefore, the system robustness against changes in motor inductance values has been compared for these control methods as an example. Figure 4.3 shows how changing the motor inductance from 0.5 times the nominal value to 12 times that value affects the eigenvalues (J_{FOC}). It also illustrates that if the motor's inductance goes beyond a certain point, the closed-loop system might become unstable.

Figure 4.4 depicts the eigenvalues of the $J_{Flatness}$ matrix as the motor inductance varies from 0.5 times to 7 times the nominal inductance (L_{nom}). Therefore, a single

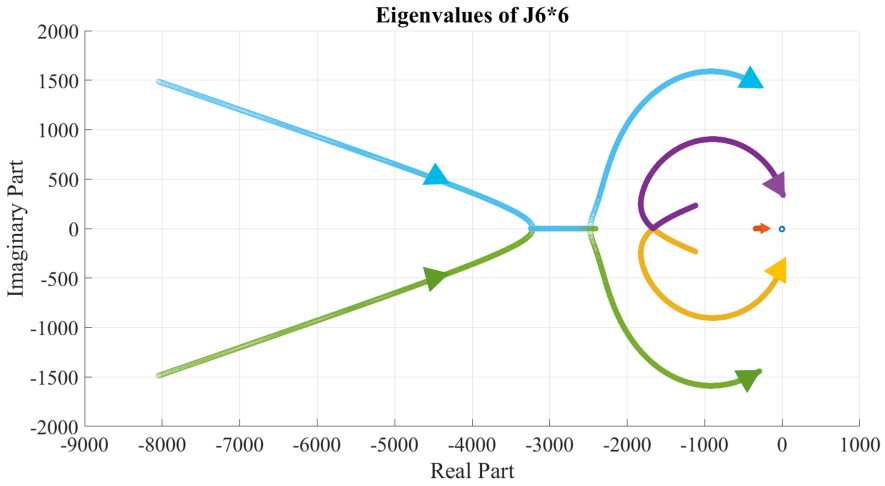

(a)

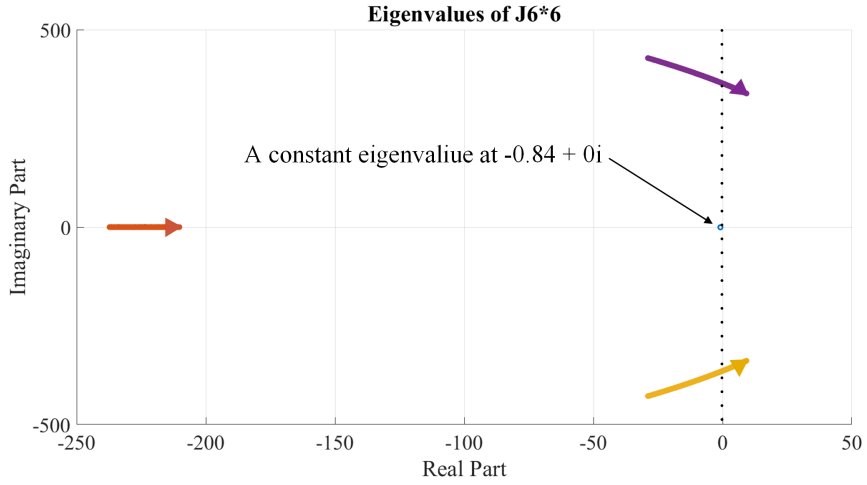

(b)

Figure 4.3: (a) Eigenvalues of J_{FOC} for different motor inductance from $0.5\ L_{nom}$ to $12\ L_{nom}$. (b) Zoom on the eigenvalues that make the system unstable.

control loop in flatness-based methods appears less robust against parameter variations when compared to the FOC method with a cascaded structure.

In practice, however, flatness-based methods have been proven to be robust to parameter variations in industrial range.

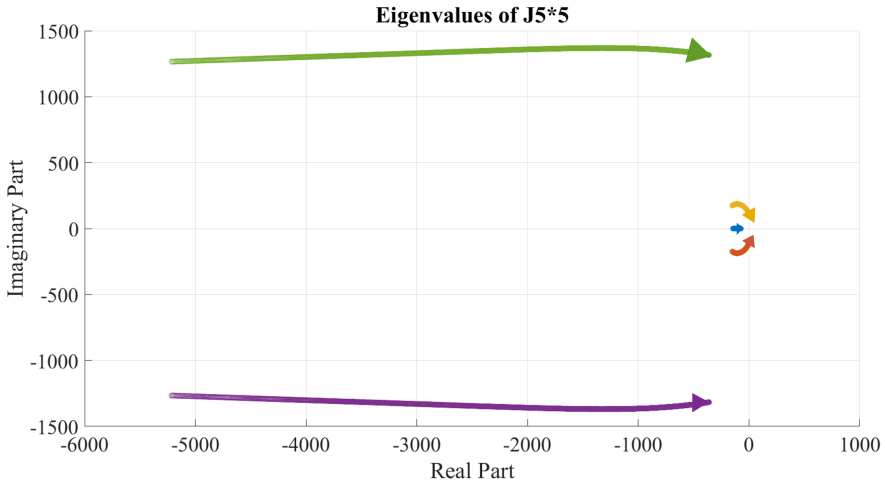

(a)

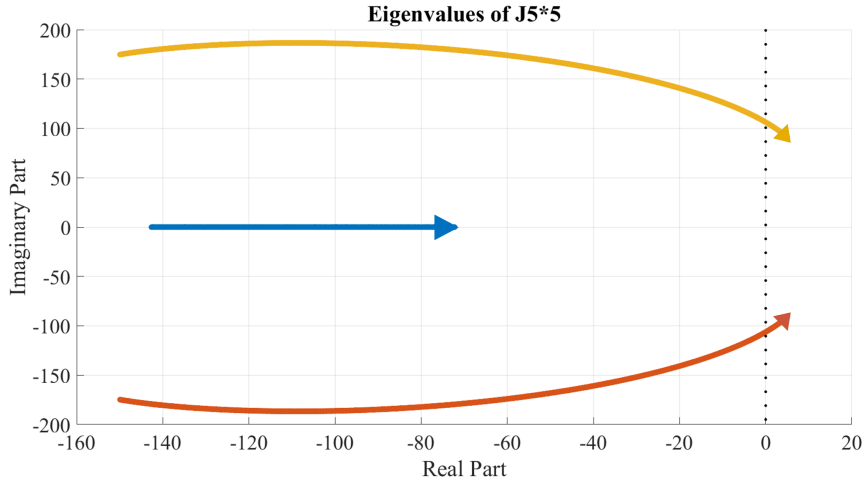

(b)

Figure 4.4: (a) Eigenvalues of $J_{Flatness}$ for different motor inductance from $0.5\ L_{nom}$ to $7\ L_{nom}$. (b) Zoom on the eigenvalues that make the system unstable.

4.6 Proposed trajectory planning

A new trajectory planning method for flatness-based control of PMSMs is proposed in this research.

4.6.1 Idea

Trajectory planning significantly affects the behavior of indirectly controlled state variables of a system. It is particularly notable because of various factors, such as the motor's highest permissible current set by its electrical specifications, as well as the switching voltage constraints. These voltage limitations depend on the DC-bus voltage and, in certain scenarios, the state of charge of the DC battery. Therefore, the system performance without considering the controller limits can be disrupted by these limitations, which could lead to unwanted instability [138].

To deal with controller limits, which have not been addressed properly so far, a novel trajectory planning approach for flatness-based control of PMSM drives is proposed in our research. In this method, a window-based trajectory function is used with an optimization algorithm. The primary goal of this trajectory planning approach is to minimize the response time of the system while ensuring adherence to the constraints imposed by motor current limitations and switching voltage restrictions [138].

In summary, our research aims to optimize trajectory planning for PMSM drives, taking into account the controller limits and electrical limitations of the system. This innovative trajectory planning approach aims to enhance dynamic performance of the system, reduce response time, and lower the risk of system instability, consequently promoting the performance of PMSM drive systems.

4.6.2 Novel trajectory planning

As the maximum motor current in flatness-based control is dependent on the control system trajectory function, the motor current cannot be controlled with classic trajectory planning. A trajectory planning response time that is slow enough should be designed for the worst possible scenario to ensure the current remains in the allowable range for a wide range of motor applications. Additionally, the outputs of the control system, V_d and V_q (as shown in Fig. 6.4), should always satisfy (6.15), which is dependent on DC-bus voltage, and in case of voltage drop, the classical trajectory planning may not function properly. Speed trajectory planning can be used to control both PMSM torque and q-axis current.

$$V_d^2 + V_q^2 < m.V_{dc}^2, \tag{4.37}$$

where $m = \frac{3}{8}$ for sinusoidal pulse width modulation (SPWM) technique and $m = \frac{1}{2}$ for space vector pulse width modulation (SVPWM) technique.

The proposed trajectory planning method uses a window-based function method. Three intervals of equal distribution are included in the window, based on the distribution as shown in Fig. 6.6. These points are calculated using (6.16).

$$\begin{cases} t_1 = t_0 + \dfrac{T_w}{3} \\ t_2 = t_0 + 2\dfrac{T_w}{3}, \end{cases} \tag{4.38}$$

where T_w is the window interval and t_0 is the initial time.

The output of the trajectory planning block (y_{ref}), its first and second derivatives ($\dot{y_{ref}}$ and $\ddot{y_{ref}}$) should be continuous to ensure that the system remains flat. This results in determining the first and second derivatives of each window output from the trajectory planning block. These are y_1, $\dot{y_1}$, $\ddot{y_1}$ y_2, $\dot{y_2}$, $\ddot{y_2}$, y_f, $\dot{y_f}$, and $\ddot{y_f}$. The trajectory function in each of these intervals is a polynomial of degree 5 defined as:

$$y = a_{5,i}t^5 + a_{4,i}t^4 + a_{3,i}t^3 + a_{2,i}t^2 + a_{1,i}t + a_{0,i} \quad i = 1, 2, 3, \tag{4.39}$$

where a_{ki} ($k = 0, 1, ..., 5$ and $i = 1, 2, 3$) are the polynomial coefficients. These coefficients are calculated by solving three sets of similar equations for the intervals of each trajectory window, as described in (6.18)-(6.20). It should be mentioned that y_0, $\dot{y_0}$ and, $\ddot{y_0}$ for each window are given by the last window.

$$\begin{cases} y_1 = a_{5,1}{t_1}^5 + a_{4,1}{t_1}^4 + a_{3,1}{t_1}^3 + a_{2,1}{t_1}^2 + a_{1,1}t_1 + a_{0,1} \\ y_0 = a_{5,1}{t_0}^5 + a_{4,1}{t_0}^4 + a_{3,1}{t_0}^3 + a_{2,1}{t_0}^2 + a_{1,1}t_0 + a_{0,1} \\ \dot{y_1} = 5a_{5,1}{t_1}^4 + 4a_{4,1}{t_1}^3 + 3a_{3,1}{t_1}^2 + 2a_{2,1}t_1 + a_{1,1} \\ \dot{y_0} = 5a_{5,1}{t_0}^4 + 4a_{4,1}{t_0}^3 + 3a_{3,1}{t_0}^2 + 2a_{2,1}t_0 + a_{1,1} \\ \ddot{y_1} = 20a_{5,1}{t_1}^3 + 12a_{4,1}{t_1}^2 + 6a_{3,1}t_1 + 2a_{2,1} \\ \ddot{y_0} = 20a_{5,1}{t_0}^3 + 12a_{4,1}{t_0}^2 + 6a_{3,1}t_0 + 2a_{2,1} \end{cases} \tag{4.40}$$

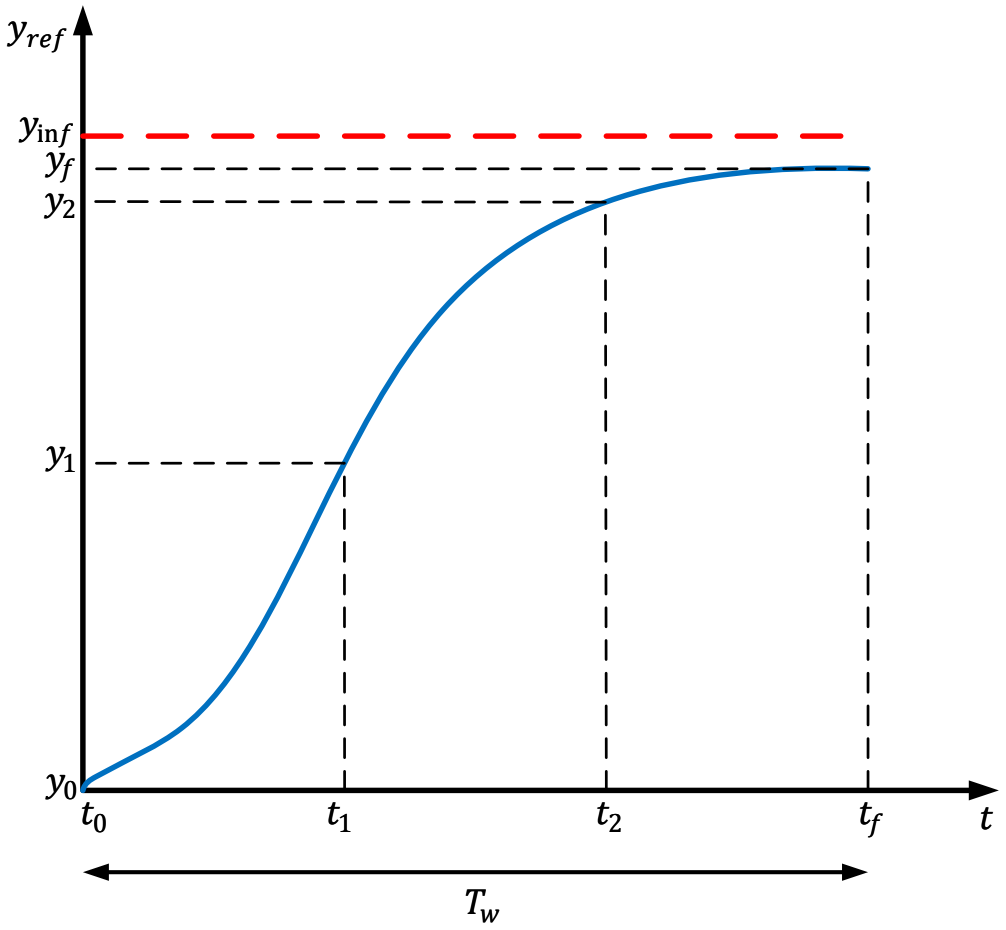

Figure 4.5: Proposed trajectory function for one window.

$$\begin{cases} y_2 = a_{5,2}{t_2}^5 + a_{4,2}{t_2}^4 + a_{3,2}{t_2}^3 + a_{2,2}{t_2}^2 + a_{1,2}t_2 + a_{0,2} \\ y_1 = a_{5,2}{t_1}^5 + a_{4,2}{t_1}^4 + a_{3,2}{t_1}^3 + a_{2,2}{t_1}^2 + a_{1,2}t_1 + a_{0,2} \\ \dot{y_2} = 5a_{5,2}{t_2}^4 + 4a_{4,2}{t_2}^3 + 3a_{3,2}{t_2}^2 + 2a_{2,2}t_2 + a_{1,2} \\ \dot{y_1} = 5a_{5,2}{t_1}^4 + 4a_{4,2}{t_1}^3 + 3a_{3,2}{t_1}^2 + 2a_{2,2}t_1 + a_{1,2} \\ \ddot{y_2} = 20a_{5,2}{t_2}^3 + 12a_{4,2}{t_2}^2 + 6a_{3,2}t_2 + 2a_{2,2} \\ \ddot{y_1} = 20a_{5,2}{t_1}^3 + 12a_{4,2}{t_1}^2 + 6a_{3,2}t_1 + 2a_{2,2} \end{cases} \tag{4.41}$$

$$\begin{cases} y_f = a_{5,3}{t_f}^5 + a_{4,3}{t_f}^4 + a_{3,3}{t_f}^3 + a_{2,3}{t_f}^2 + a_{1,3}t_f + a_{0,3} \\ y_2 = a_{5,3}{t_2}^5 + a_{4,3}{t_2}^4 + a_{3,3}{t_2}^3 + a_{2,3}{t_2}^2 + a_{1,3}t_2 + a_{0,3} \\ \dot{y_f} = 5a_{5,3}{t_f}^4 + 4a_{4,3}{t_f}^3 + 3a_{3,3}{t_f}^2 + 2a_{2,3}t_f + a_{1,3} \\ \dot{y_2} = 5a_{5,3}{t_2}^4 + 4a_{4,3}{t_2}^3 + 3a_{3,3}{t_2}^2 + 2a_{2,3}t_2 + a_{1,3} \\ \ddot{y_f} = 20a_{5,3}{t_f}^3 + 12a_{4,3}{t_f}^2 + 6a_{3,3}t_f + 2a_{2,3} \\ \ddot{y_2} = 20a_{5,3}{t_2}^3 + 12a_{4,3}{t_2}^2 + 6a_{3,3}t_2 + 2a_{2,3} \end{cases} \tag{4.42}$$

The matrix denoted as X_{opt}, as defined in (6.21), represents the optimization variables. It results from the application of an optimization algorithm, while adhering to the constraints described in (6.22).

$$X_{opt} = [y_1, y_2, y_f, \dot{y_1}, \dot{y_2}, \dot{y_f}, \ddot{y_1}, \ddot{y_2}, \ddot{y_f}] \tag{4.43}$$

$$\begin{cases} |i_q(k)| \leq I_{q,max} \\ V_d(k)^2 + V_q(k)^2 \leq \dfrac{3}{8}V_{dc}^2 \\ \text{Less than } 20\% \text{ overshoot in tracking speed reference.} \end{cases} \tag{4.44}$$

Here, $k = 1, 2, \ldots, \frac{T_w}{T_e}$, and T_e represents the virtual sampling interval considered for the points within each window. A trade-off exists between the computational time required for the optimization algorithm and the accuracy of constraint satisfaction. Decreasing the value of T_e increases the computational burden and time required for optimization but enhances robustness and accuracy.

A description of the optimization algorithm's objective function can be found in (6.23), where K_{opt_0}, K_{opt_1}, and K_{opt_2} are the weighting factors for difference between the trajectory function's output and its derivatives at the end of the window and the speed reference.

$$\begin{aligned} f(X_{opt}) = \sum_{k=1}^{\frac{T_w}{T_e}} (y_k - y_{inf})^2 + K_{opt_0}.(y_f - y_{inf})^2 + K_{opt_1}.(\dot{y_f} - 0)^2 \\ + K_{opt_2}.(\ddot{y_f} - 0)^2 \end{aligned} \tag{4.45}$$

Figure 6.7 presents the block diagram depicting the proposed trajectory planning process. Within this diagram, the Trajectory Function Generation (TFG) block generates $y_{\Omega,ref}$ utilizing polynomial coefficients computed by the optimization algorithm. The output of this block is determined as follows:

$$\begin{cases} y_{\Omega,ref} = a_{5,1}t^5 + a_{4,1}t^4 + a_{3,1}t^3 + a_{2,1}t^2 + a_{1,1}t + a_{0,1} & t < t_1 \\ y_{\Omega,ref} = a_{5,2}t^5 + a_{4,2}t^4 + a_{3,2}t^3 + a_{2,2}t^2 + a_{1,2}t + a_{0,2} & t_1 \leq t \leq t_2 \\ y_{\Omega,ref} = a_{5,3}t^5 + a_{4,3}t^4 + a_{3,3}t^3 + a_{2,3}t^2 + a_{1,3}t + a_{0,3} & t_2 < t < t_f \end{cases} \tag{4.46}$$

The optimization algorithm is executed once within each window, guided by equation (6.23), all while ensuring compliance with the constraints outlined in (6.22). Subsequently, the polynomial coefficients are computed based on the output of the optimization algorithm, denoted as X_{opt}. It should be mentioned that the optimization algorithm demands computational resources, and as such, the maximum computation time is calculated in advance and called as T_{cal}. Consequently, the trajectory function uses the same polynomial from the preceding window until the completion of the new optimization process. Therefore,

$$\begin{aligned} y_{\Omega,ref} = a_{5,3,old}\left(t+T_w\right)^5 + a_{4,3,old}\left(t+T_w\right)^4 + a_{3,3,old}\left(t+T_w\right)^3 \\ +a_{2,3,old}\left(t+T_w\right)^2 + a_{1,3,old}\left(t+T_w\right) + a_{0,3,old} \quad t < T_{cal} \end{aligned} \tag{4.47}$$

As a result, it is possible to extend the constraints and optimization function to cover a prediction horizon of T_{cal}. However, it should be noted that this prediction horizon must remain sufficiently small to ensure that the constraints continue to be satisfied considering the transient events and disturbances.

Furthermore, it's essential to notice the trade-off between the amount of computational resources demanded by the optimization algorithm, which represents a significant challenge in this approach, and, consequently, its cost, against the precision and effectiveness of the control system.

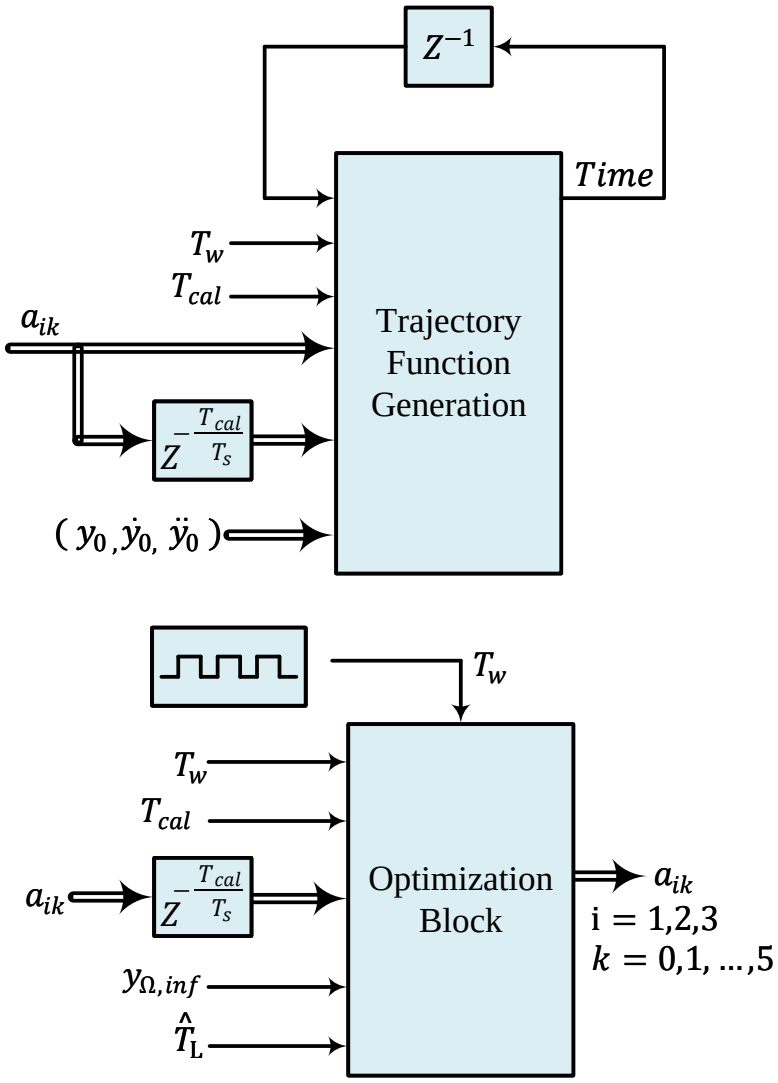

Figure 4.6: Schematic of the proposed trajectory planning method.

4.7 Torque and voltage drop observer

As discussed previously, load torque and voltage drop observers improve the dynamic performance of the control system. In this section, two current methods that have been proposed in the current literature will be reviewed and extended.

4.7.1 Nonlinear state observer

The nonlinear state observer principle can be described as follows:

$$\begin{cases} \dot{\mathbf{X}} = \begin{bmatrix} \dot{\mathbf{x}} \\ \dot{\mathbf{p}} \end{bmatrix} = \begin{bmatrix} f(x,u) + g(x,u).\mathbf{p} \\ 0 \end{bmatrix} \\ \mathbf{Y} = \mathrm{x} \end{cases} \tag{4.48}$$

where $\mathbf{X} \in \mathbb{R}^{n+m}$ is the vector of estimated variables, $\mathbf{x} \in \mathbb{R}^n$ is the vector of system state variables, $\mathbf{p} \in \mathbb{R}^m$ is the vector of unknown parameters that are going to be estimated, and $\mathbf{Y} \in \mathbb{R}^n$ is the vector of measured variables.

Function $f(x,u) \in \mathbb{R}^n$ and $g(x,u) \in \mathbb{R}^{n*m}$ are nonlinear functions of **x** and **u** (the command signal vector). The state-observer is defined in (4.49) where $\mathbf{e}_x = \hat{\mathbf{x}} - \mathbf{x}$ is the estimation error:

$$\begin{bmatrix} \dot{\hat{\mathbf{x}}} \\ \dot{\hat{\mathbf{p}}} \end{bmatrix} = \begin{bmatrix} f(x,u) + g(x,u).\hat{\mathbf{p}} - \mathbf{S}.\mathbf{e}_x \\ \mathbf{K}_p.\dot{\mathbf{e}}_x + \mathbf{K}_i.\mathbf{e}_x - g^t(x,u).\mathbf{e}_x \end{bmatrix}, \tag{4.49}$$

where **S** and **P** is the positive-definitive parameter matrix $\in \mathbb{R}^{n*m}$. Vectors $\mathbf{K}_p$ and $\mathbf{K}_i$ are calculated using

$$\begin{cases} \mathbf{K}_p = -\mathbf{P}.g^{-1}(x,u) \\ \mathbf{K}_i = \mathbf{K}_p.\mathbf{S} \end{cases} \tag{4.50}$$

To illustrate the convergence of the estimation achieved with the state observer, the errors in derivative estimation, $\mathbf{e}_x$ and $\mathbf{e}_p$, are expressed as follows [236]:

$$\begin{cases} \dot{\mathbf{e}}_x = g(x,u).\mathbf{e}_p - \mathbf{S}.\mathbf{e}_x \\ \dot{\mathbf{e}}_p = \mathbf{K}_p.g(x,u).\mathbf{e}_p - \mathbf{K}_p.\mathbf{S}.\mathbf{e}_x + \mathbf{K}_i.\mathbf{e}_x - g^t(x,u).\mathbf{e}_x \end{cases} \tag{4.51}$$

A classical Lyapunov approach can be used to establish the exponential stability of the estimation based on the introduced nonlinear observer. The Lyapunov candidate function, V has the following definition:

$$V = \frac{1}{2} \begin{bmatrix} \mathbf{e}_x & \mathbf{e}_p \end{bmatrix} . \begin{bmatrix} \mathbf{e}_x \\ \mathbf{e}_p \end{bmatrix} \geq 0. \tag{4.52}$$

The derivative of function V is calculated in (4.53).

$$\dot{V} = \mathbf{e}_x^t.\dot{\mathbf{e}}_x + \mathbf{e}_p^t.\dot{\mathbf{e}}_p \tag{4.53}$$

By substituting (4.53) in (4.51), the derivative of function V can be expressed as:

$$\begin{aligned}\dot{V} = \mathbf{e}_x^t.g(x,u).\mathbf{e}_p - \mathbf{e}_x^t.\mathbf{S}.\mathbf{e}_x + \mathbf{e}_p^t.\mathbf{K}_p.g(x,u).\mathbf{e}_p - \mathbf{e}_p^t.\mathbf{K}_p.\mathbf{S}.\mathbf{e}_x + \mathbf{e}_p^t.\mathbf{K}_i.\mathbf{e}_x \\ -\mathbf{e}_p^t.g^t(x,u).\mathbf{e}_x.\end{aligned} \tag{4.54}$$

By combining (4.54) and (4.50), $\dot{V}$ can be expressed as:

$$\dot{V} = \begin{bmatrix}\mathbf{e}_x & \mathbf{e}_p\end{bmatrix} \cdot \begin{bmatrix}-\mathbf{S} & 0 \\ 0 & -\mathbf{P}\end{bmatrix} \cdot \begin{bmatrix}\mathbf{e}_x \\ \mathbf{e}_p\end{bmatrix} \tag{4.55}$$

The estimation can be guaranteed to be exponentially stable as long as **P** and **S** are positive-definite matrices. Furthermore, when tuning the **S** and **P** matrices, it is assumed that the dynamics of the state vector error ε_x must be significantly faster than the dynamics of the parameter vector error ε_p. Thus, the matrix **S** must have eigenvalues with real parts that are substantially larger than those of the matrix **P** [232, 234].

Considering $x(t) = \begin{bmatrix}i_d & i_q & \Omega\end{bmatrix}$, $p(t) = \begin{bmatrix}V_{td} & V_{tq} & T_L\end{bmatrix}$, and $u(t) = \begin{bmatrix}V_q & V_d\end{bmatrix}$ for the PMSM drive system, $f(x,u)$ and $g(x,u)$ can be expressed as follows:

$$f(x,u) = \begin{bmatrix}\frac{1}{L_d}(V_d + p\Omega L_q i_q) \\ \frac{1}{L_q}(V_q - p\Omega L_d i_q - p\Omega\psi_f) \\ \frac{1}{J}(p\psi_f i_q - f\Omega)\end{bmatrix} \tag{4.56}$$

$$g(x,u) = \begin{bmatrix}-\frac{1}{L_d} & 0 & 0 \\ 0 & -\frac{1}{L_q} & 0 \\ 0 & 0 & -\frac{1}{J}\end{bmatrix} \tag{4.57}$$

4.7.2 Extended Luenberger observer

ELO method has been proposed in [230] to enhance the robustness of flatness control against parameter variations and external load disturbances. In [230], a simplified version of Luenberger observer is presented, but it should be noted that it neglects the dynamics of i_d. In this context, an extended version of the observer is considered in this research.

An equivalent circuit for a PMSM drive where the resistance (R_s) is represented by $V_{tq}(= R_s i_q)$ and $V_{td}(= R_s i_d)$. ELO is utilized to estimate T_L, V_{td}, and V_{tq}. In order to use the ELO, the system must be linearized around a specific operating point since Luenberger observers are introduced for linear systems.

It should be mentioned that the very short sampling time of the current loop makes it reasonable to assume that variations in T_L, V_{td} and V_{tq} within one sampling period can be ignored. Therefore,

$$\frac{dT_L}{dt} = \frac{dV_{td}}{dt} = \frac{dV_{tq}}{dt} = 0. \tag{4.58}$$

The Luenberger observer can be expressed as:

$$\begin{cases} \dot{x}(t) = \mathbf{A}x(t) + \mathbf{B}u(t) \\ y(t) = \mathbf{C}x(t), \end{cases} \tag{4.59}$$

where $x(t) = \begin{bmatrix} i_d & i_q & \Omega & V_{td} & V_{tq} & T_L \end{bmatrix}$ are the state variables, $u(t) = \begin{bmatrix} V_q & V_d \end{bmatrix}$ are input variables, and $y(t) = \begin{bmatrix} i_d & i_q & \Omega \end{bmatrix}$ are output variables.

Therefore, the matrices **A**, **B**, **C** can be calculated as follows:

$$\mathbf{A} = \begin{bmatrix} 0 & p\frac{L_q}{L_d}\Omega_0 & p\frac{L_q}{L_d}i_{q0} & -\frac{1}{L_d} & 0 & 0 \\ -p\frac{L_d}{L_q}\Omega_0 & 0 & -\frac{p\psi_f}{L_q} - p\frac{L_d}{L_q}i_{d0} & 0 & -\frac{1}{L_q} & 0 \\ 0 & \frac{p\psi_f}{J} & -\frac{f}{J} & 0 & 0 & \frac{1}{J} \\ 0 & 0 & 0 & 0 & 0 & 0 \\ 0 & 0 & 0 & 0 & 0 & 0 \\ 0 & 0 & 0 & 0 & 0 & 0 \end{bmatrix} \tag{4.60}$$

where Ω_0, i_{q0}, and i_{d0} are the values of mechanical speed, q-axis and d-axis currents at the nominal operating point of the motor.

$$\mathbf{B} = \begin{bmatrix} \frac{1}{L_d} & 0 \\ 0 & \frac{1}{L_q} \\ 0 & 0 \\ 0 & 0 \\ 0 & 0 \\ 0 & 0 \end{bmatrix} \tag{4.61}$$

$$\mathbf{C} = \begin{bmatrix} 1 & 0 & 0 & 0 & 0 & 0 \\ 0 & 1 & 0 & 0 & 0 & 0 \\ 0 & 0 & 1 & 0 & 0 & 0 \end{bmatrix} \tag{4.62}$$

ELO method can be expressed as:

$$\begin{cases} \dot{\hat{x}}(t) = \mathbf{A}\hat{x}(t) + \mathbf{B}u(t) + \mathbf{L}(y(t) - \hat{y}(t)) \\ \hat{y}(t) = \mathbf{C}\hat{x}(t) \end{cases} \tag{4.63}$$

The estimation error using ELO method can be functioned as:

$$\dot{e}(t) = \dot{x}(t) - \dot{\hat{x}}(t) = (\mathbf{A} - \mathbf{LC})e(t) \tag{4.64}$$

In order to achieve convergence, the matrix $(\mathbf{A} - \mathbf{LC})$ should have eigenvalues with negative real parts. Matrix $\mathbf{L}$ can be designed using function "place" in Matlab based on the desired eigenvalues for matrix $(\mathbf{A} - \mathbf{LC})$.

4.8 Simulation and experimental results

This section involves the simulation and validation of both the conventional and proposed flatness-based control methods. Herein, you will find simulation and experimental results for the following methods:

- Conventional flatness-based control with a second-order trajectory function

- Torque and voltage drops observers
- The proposed flatness-based control method

These results will be presented and discussed in this section.

4.8.1 Comparison of flatness-based control with FOC

The inverter operates at a frequency of 10 kHz. The bandwidth of the inner loop (current control) of FOC regulators should be at least 10 times higher than that of the outer loop (speed control) in order to achieve effective tuning. As a result, the current control has a response time of 1 ms and the speed control has a response time of 10 ms. Figure 4.7 illustrates the motor's speed under two distinct conditions: when the speed reference and load torque change. This scenario is evaluated for three different scenarios, including one with precise parameters, one with an inaccurate motor inductance (L_d and L_q equal three times of their nominal value, L_{nom}), and one with an inaccurate motor resistance (R_s equals three times its nominal value, R_{nom}).

The motor's reference speed changes to 3000 rpm at time t = 1 s and the load torque to 0.26 Nm at time t = 2 s. This cascaded control approach exhibits robustness within the range of motor parameter variations discussed previously. However, the system's response to disturbances, load torque changes, and shifts in operating points is not exceptionally rapid, as indicated in Figure 4.7 (a).

The flatness-based control system has only one loop, which means the flatness-based controller cut-off frequency, ω_Ω, is at least 10 times smaller than the switching frequency. It is chosen to be 600 rad/s.

Figure 4.8 provides simulation results under conditions similar to those of FOC. Despite imprecise model parameters, the trajectory planning block output of the flatness-based control method closely tracks the motor speed. Furthermore, when comparing system dynamics, it becomes evident that flatness-based control outperforms FOC, as illustrated in Figure 4.8 (c) compared to Figure 4.7 (c). Based on the simulation results, flatness-based controllers provide superior dynamic performance, especially in scenarios with variable torque loads and disturbances.

Figure 4.9 illustrates the performance of the flatness-based control method under conditions of inaccurate motor parameters. As indicated in Figure 4.9, the system's sta-

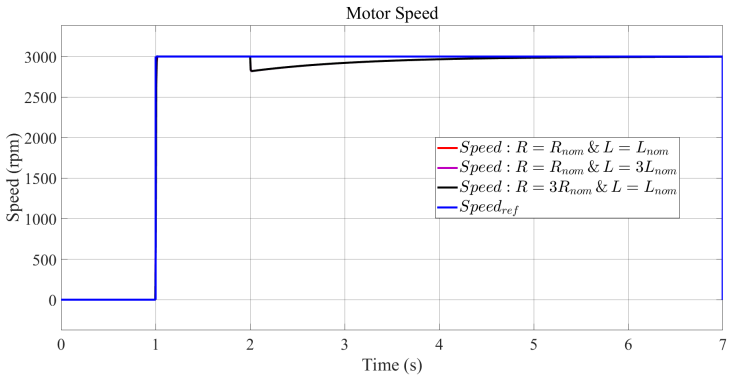

(a)

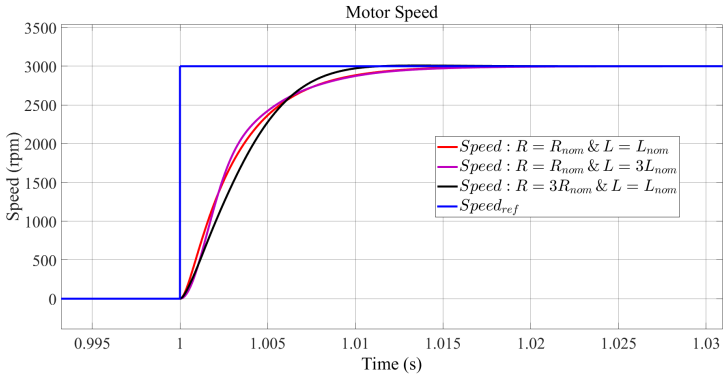

(b)

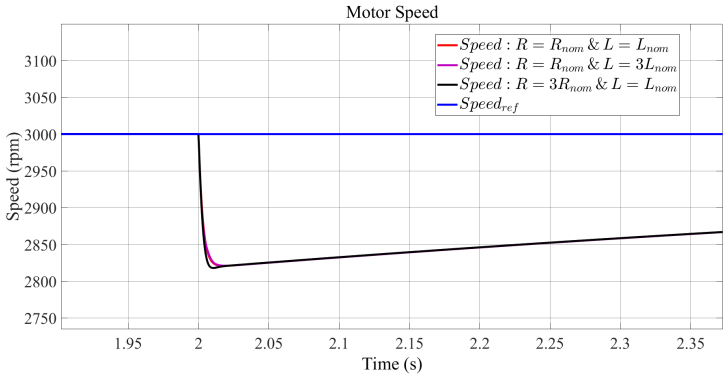

(c)

Figure 4.7: (a) Simulation results of motor speed with FOC method. (b) Comparison of motor performance under change of speed reference considering motor parameter variation. (c) Comparison of motor performance under change of load torque considering motor parameter variation.

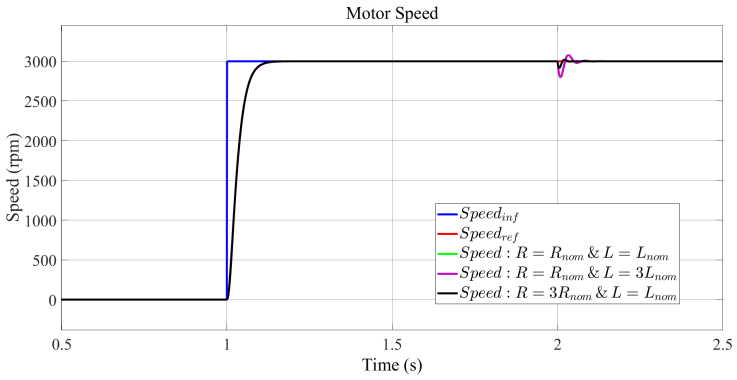

(a)

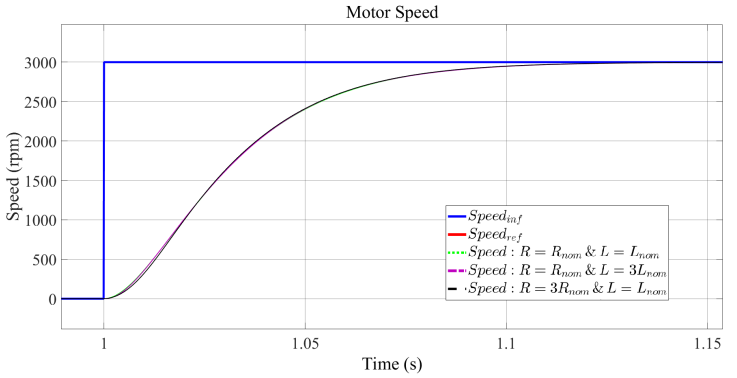

(b)

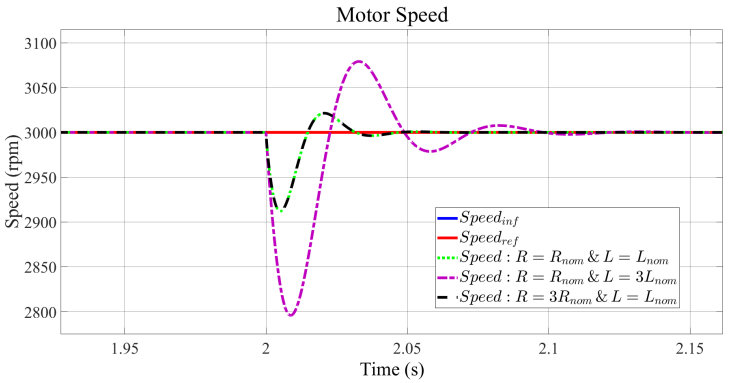

(c)

Figure 4.8: (a) Simulation results of motor speed with flatness-based control method. (b) Comparison of motor performance under change of speed reference considering motor parameter variation. (c) Comparison of motor performance under change of load torque considering motor parameter variation.

bility is maintained when the inductance value is set to $5.5\ L_{nom}$ and becomes unstable when the inductance is increased to $6\ L_{nom}$. This behavior aligns with the results of the robustness analysis, as demonstrated in Figure 4.4.

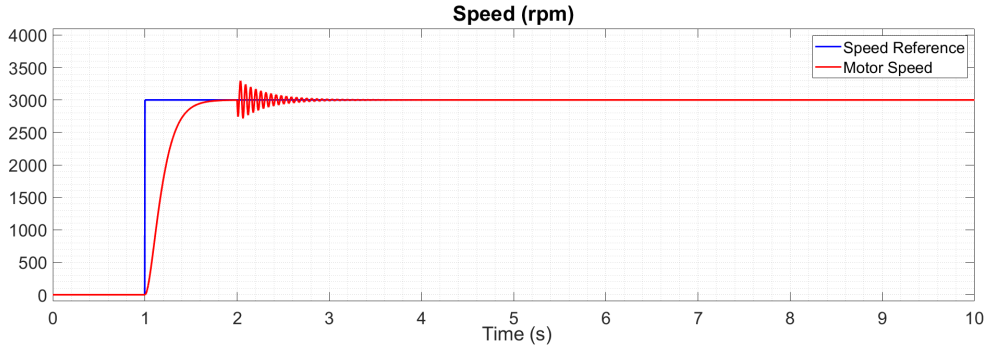

(a)

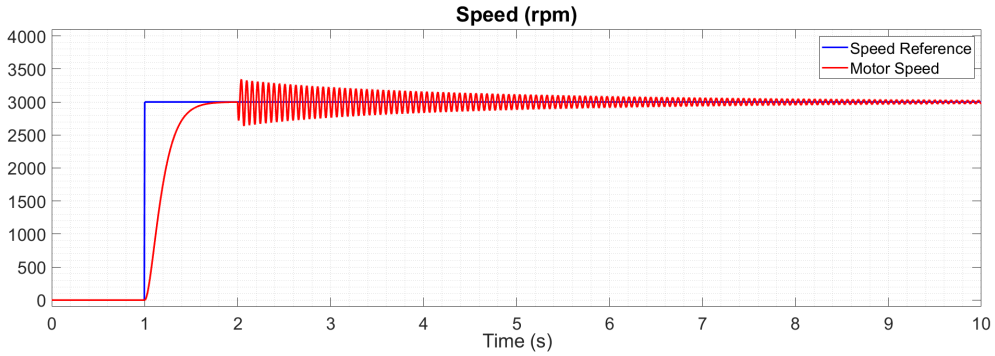

(b)

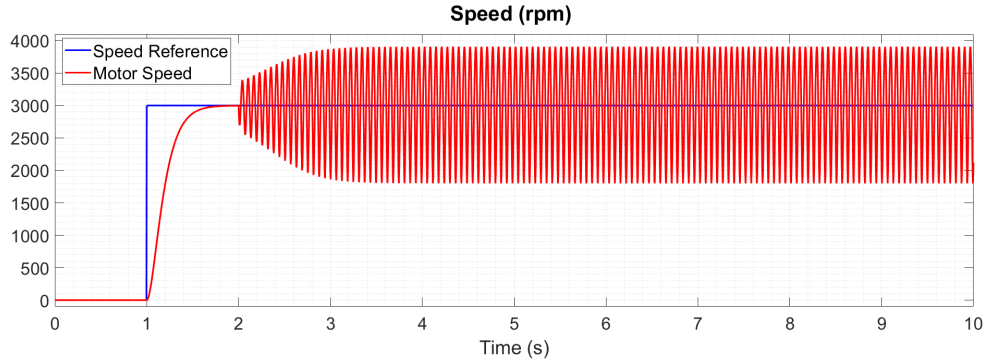

(c)

Figure 4.9: Simulation results of motor speed with flatness-based control method (a) when $L_d = L_q = 5\ L_{nom}$. (b) when $L_d = L_q = 5.5\ L_{nom}$. (c) when $L_d = L_q = 6\ L_{nom}$.

The performance of the system using the FOC method with inaccurate motor parameters is showcased in Figure 4.10. The system exhibits stability when the inductance is set to $10.5\ L_{nom}$, while instability arises when the inductance is increased to $11.5\ L_{nom}$. These observations align with the findings of the robustness analysis presented in Figure 4.3.

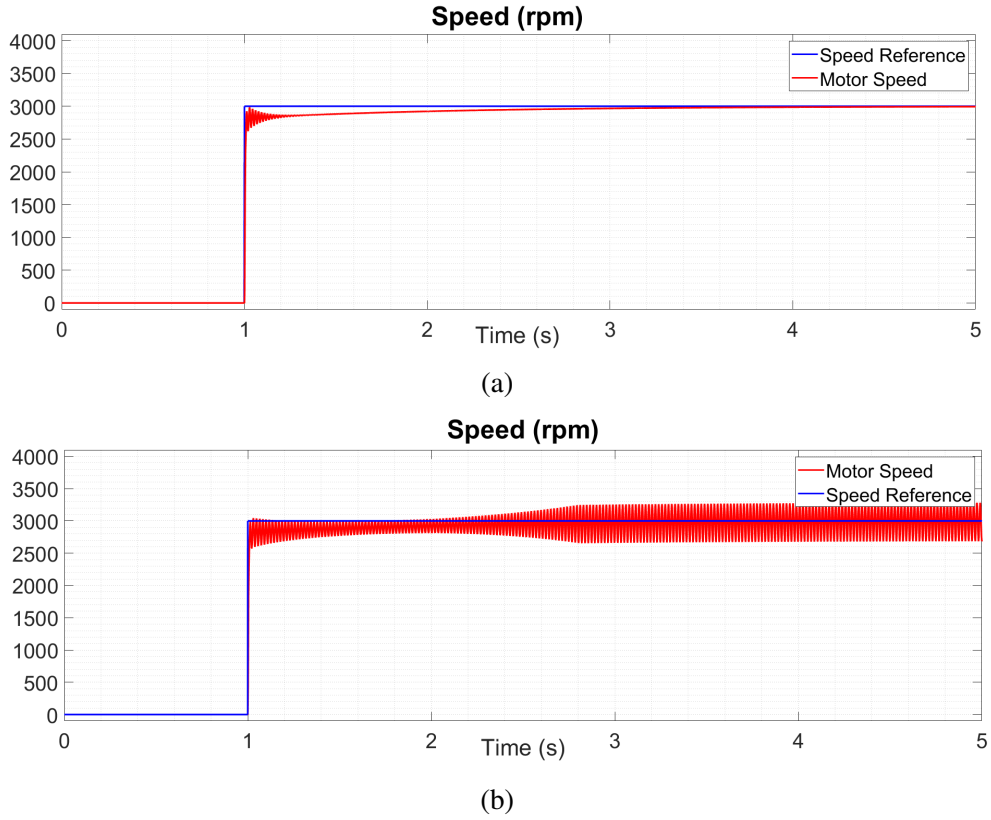

Figure 4.10: Simulation results of motor speed with FOC method (a) Motor speed with FOC method (a) when $L_d = L_q = 10.5\ L_{nom}$. (b) when $L_d = L_q = 11.5\ L_{nom}$.

4.8.2 Load torque and voltage drop observers

To achieve accurate and robust results, the choice of observer for load torque and resistance estimation plays an important role. The performance of the two reviewed observers, ELO and nonlinear state observer, have been explored. The design parameters of these observers have been provided in Appendix C.

Based on the simulation results shown in Figure 4.11, the nonlinear observer outperforms the linear observer for estimating load torques and resistances. The nonlinear observer exhibits remarkable accuracy and robustness, outperforming the ELO across various operating conditions and disturbances. The nonlinear observer's advantages are particularly evident during transient states and rapid load changes, where its performance surpasses the ELO.

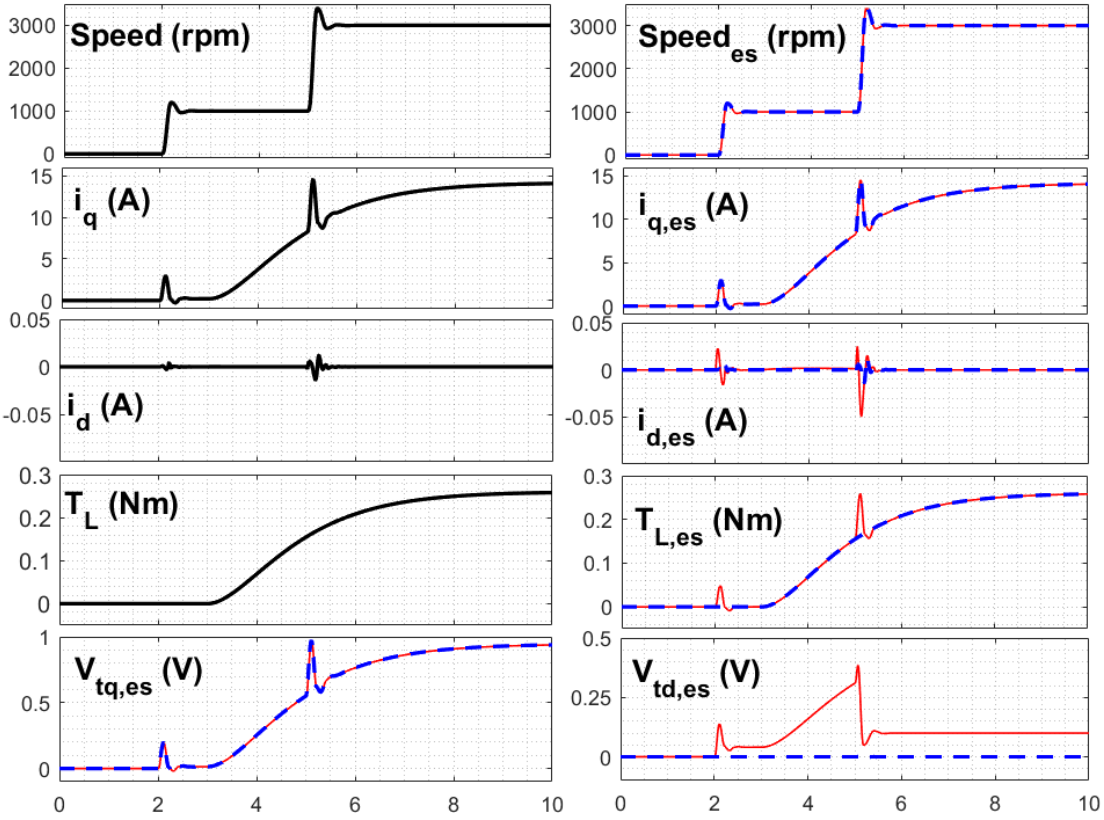

Figure 4.11: Simulation results of the nonlinear state observer (dotted blue curves) and ELO (solid red curves) and their comparison with the measured variables (solid black curves).

It is possible to enhance the ELO method by defining distinct observer matrices for different speed ranges, as the method operates based on the linearized model of the system around the operating point. However, this approach can increase system complexity and computation time. Therefore, the nonlinear state observer was chosen for observing load torque and voltage drop.

Figure 4.12 demonstrates that the selected observer effectively estimates both the system's state variables, such as mechanical speed, d-axis, and q-axis currents, matching their measured values, as well as providing reliable estimations for load torque and voltage drops.

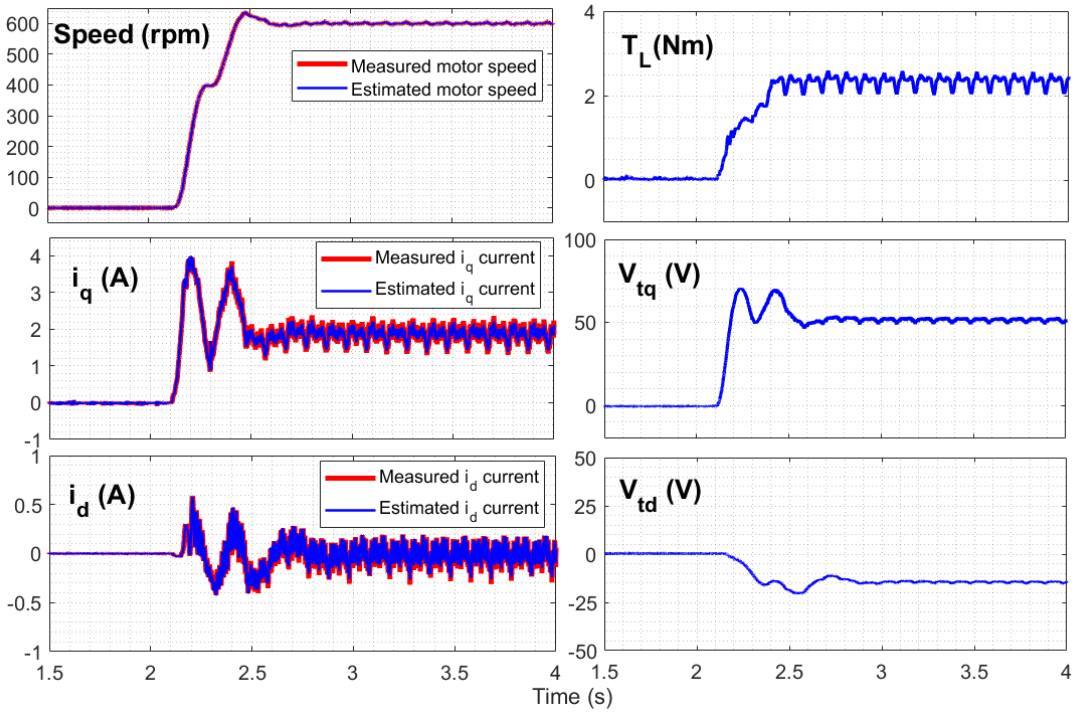

Figure 4.12: Experimental results of the nonlinear state observer (blue curves) and their comparison with the measured variables (red curves).

4.8.3 Comparison of the proposed flatness-Based control method with conventional one

We compare the proposed trajectory planning method with a flatness-based approach with a conventional second-order transfer function using a scenario of the step change of speed reference for the PMSM motor described in Table 4.1. This simulation highlights the differences between the two methods by setting $I_{q,max}$ to 3 and i_d to zero, while the motor runs in no-load mode to emphasize performance comparison.

We fixed the trajectory planning function's time window interval at 100 milliseconds

as part of this study. The motor speed reference ($y_{\Omega,inf}$) changes from 0 to 3000 rpm at t = 0.2 seconds. Figure 4.13 demonstrates how the proposed trajectory method effectively generates a trajectory that adheres to constraints and ultimately attains the desired motor speed in 0.4 seconds (approximately 4 windows).

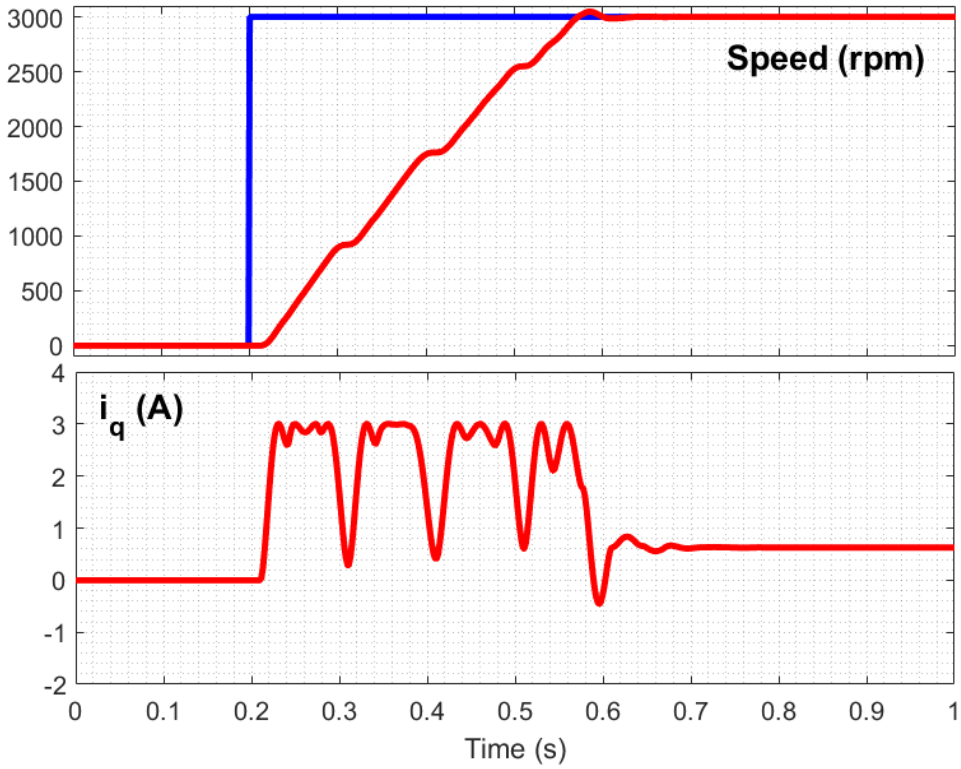

Figure 4.13: Simulation results of input ($y_{\Omega,inf}$) and output ($y_{\Omega,ref}$) of the proposed trajectory planning function satisfying the constraint $I_{q,max}$ = 3 A.

For the conventional trajectory function to produce a response time equivalent to that of the proposed method, the current must exceed the limit $I_{q,max}$. This is illustrated in Figure 4.14.

For the conventional trajectory function to adhere the current constraints, it requires a reduction in ω_f of the trajectory function as a result of the impact of trajectory response time on transient motor currents. The disadvantage of this approach is that it results in slower response times across all scenarios, as shown in Figure 4.15.

Furthermore, a reduction in ω_f does not guarantee current protection, as it does not account for transients, variations in load torques, and parameter discrepancies. For

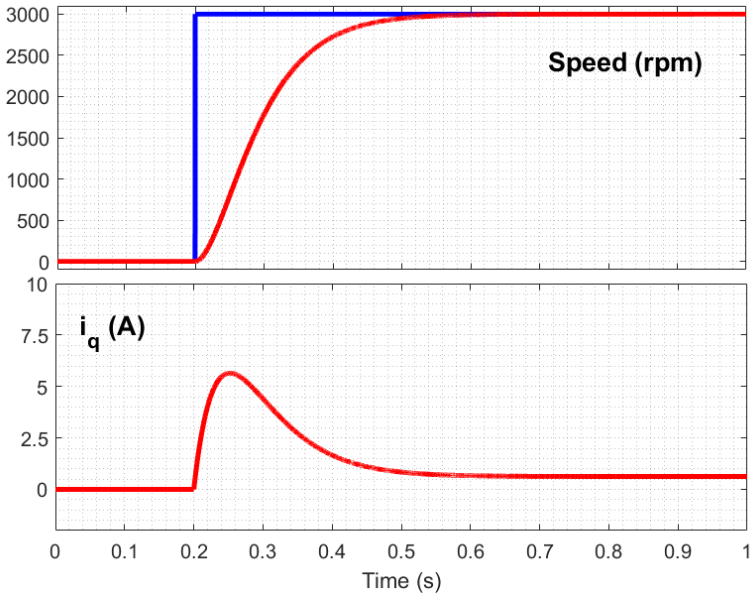

Figure 4.14: Simulation results of input ($y_{\Omega,inf}$) and output ($y_{\Omega,ref}$) of the conventional trajectory planning with same response time to that of proposed method, resulting in not satisfying the constraint $I_{q,max}$ = 3 A.

instance, setting $\omega_f = 60\ rad/s$ leads to substantial current overshoot, as demonstrated in Figure 4.16.

We have examined an additional scenario involving load torque to facilitate the comparison between flatness-based control and the proposed trajectory planning method. In this particular scenario, the motor speed reference transitions from its initial state to 500 rpm at t = 0.2 seconds. Subsequently, the load torque changes to 0.13 Nm at t = 1 second and then to 0.26 Nm (full load) at t = 2 seconds. At t = 3 seconds, the motor speed reference shifts to 3000 rpm. The constraint $I_{q,max} = 15$ A is set for this test to ensure a more highlighted comparison.

The proposed trajectory planning method successfully tracks the reference speed while adhering to the specified constraints, as shown in Figure 4.17. In contrast, the traditional approach, as depicted in Figure 4.18, lacks current protection.

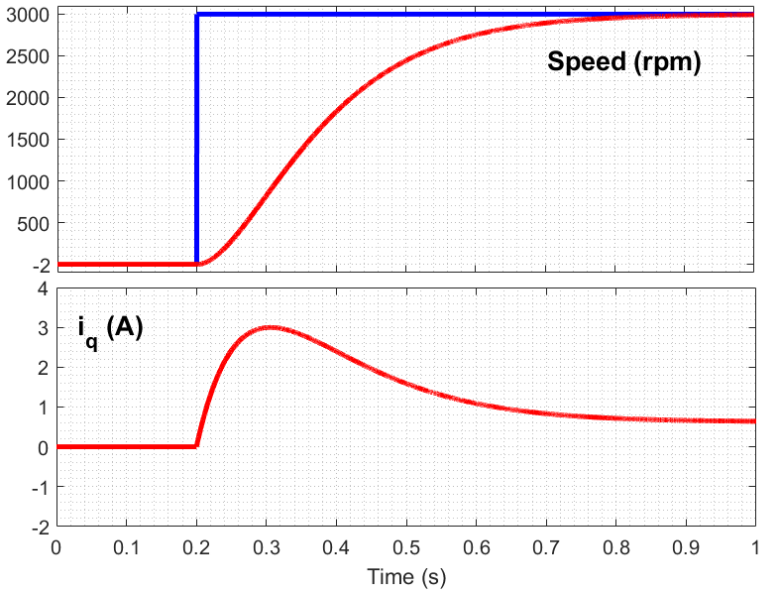

Figure 4.15: Simulation results of input ($y_{\Omega,inf}$) and output ($y_{\Omega,ref}$) of the conventional trajectory planning satisfying the constraint $I_{q,max}$ = 3 A, resulting in longer response time.

4.8.4 Experimental results

As mentioned in Section 3.7.3, a new testbench setup has been provided due to malfunctioning of the original one described in Table 3.2.

4.8.4.1 Flatness-based control with second-order trajectory function

Figures 4.19 and 4.20 illustrate the system's response to a step change in speed reference, based on simulation and experimental data, respectively. The speed reference shifts from 0 to 600 rpm, with both simulation and experimental scenarios.

In another scenario, the motor's speed reference undergoes step-wise changes, as shown in Figure 4.21 for simulation and Figure 4.22 for experimental studies. The speed reference changes at specific time points: from 0 to 150 rpm at t = 2 s, 150 rpm to 300 rpm at t = 7 s, 300 rpm to 450 rpm at t = 12 s, and finally, 450 rpm to 600 rpm at t = 17 s. As the DC motor's speed, linked to the PMSM under study, increases, the load torque is estimated using the nonlinear state observer.

In another scenario, we analyzed the system's response to load variations. With the

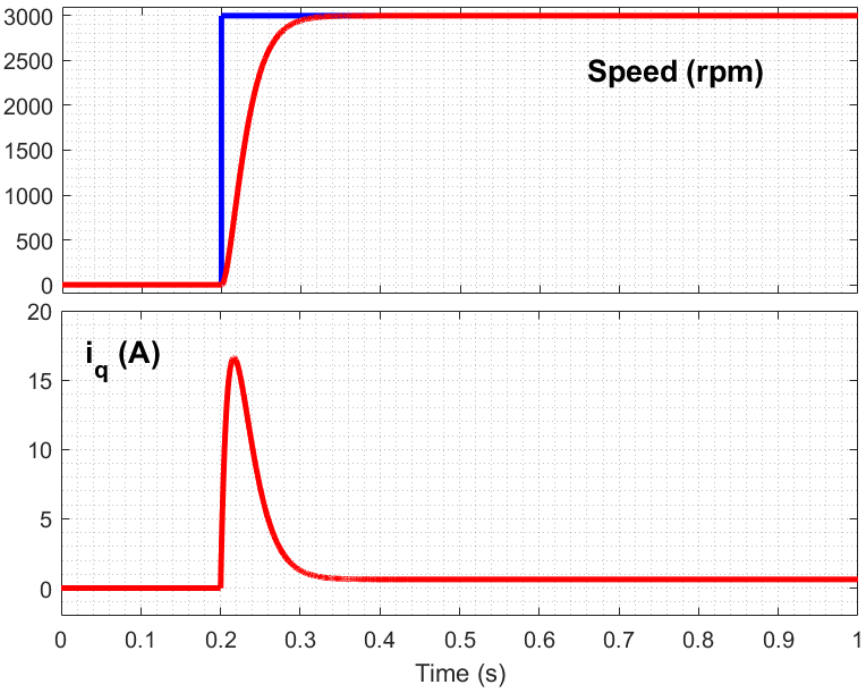

Figure 4.16: Simulation results of input ($y_{\Omega,inf}$) and output ($y_{\Omega,ref}$) of the conventional trajectory planning with $\omega_f = 60$ rad/s, resulting in significant current overshoot.

motor speed set at 600 rpm, we introduced load torque changes by changing the resistive load connected to the DC motor. Figures 4.23 and 4.24 show the results for simulation and experimentation, respectively. The torque load increased from 3 Nm to 5.5 Nm at t = 2 s and returned to 3 Nm at t = 5 s. The control system effectively regulated the motor speed. The control system regulates the speed under variation of load torque much faster than FOC method with cascaded structure.

4.8.4.2 Flatness-based control with proposed trajectory function

To experimentally validate the proposed trajectory planning, a modification was made due to difficulties in implementing the optimization function on the dSPACE MicroLab-Box. To preserve the core concept of trajectory planning while addressing this issue, the approach shifted from considering three polynomial functions within each trajectory window to employing a single polynomial function, as described in (6.26).

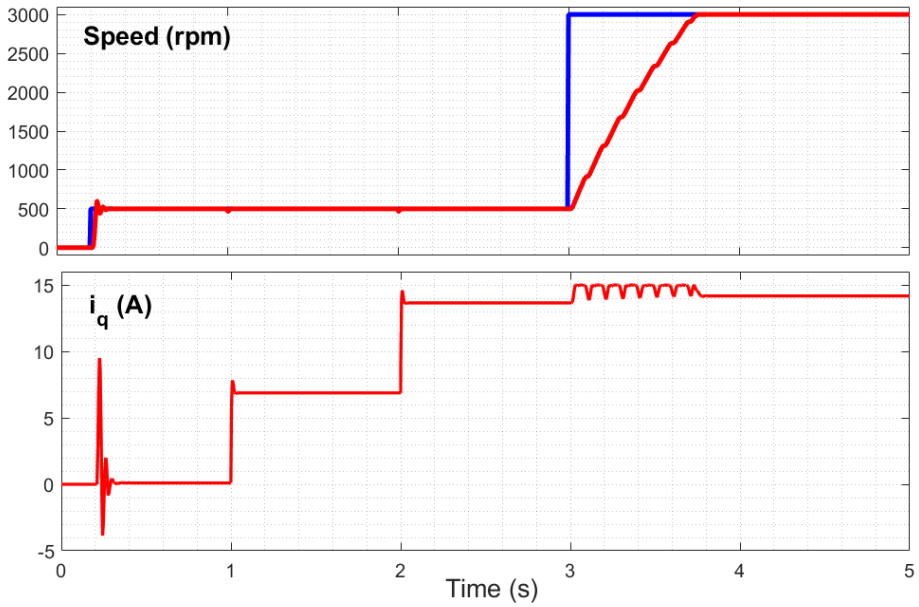

Figure 4.17: Simulation results of input ($y_{\Omega,inf}$) and motor speed using the proposed trajectory planning under heavy load satisfying the constraint $I_{q,max}$ = 15 A.

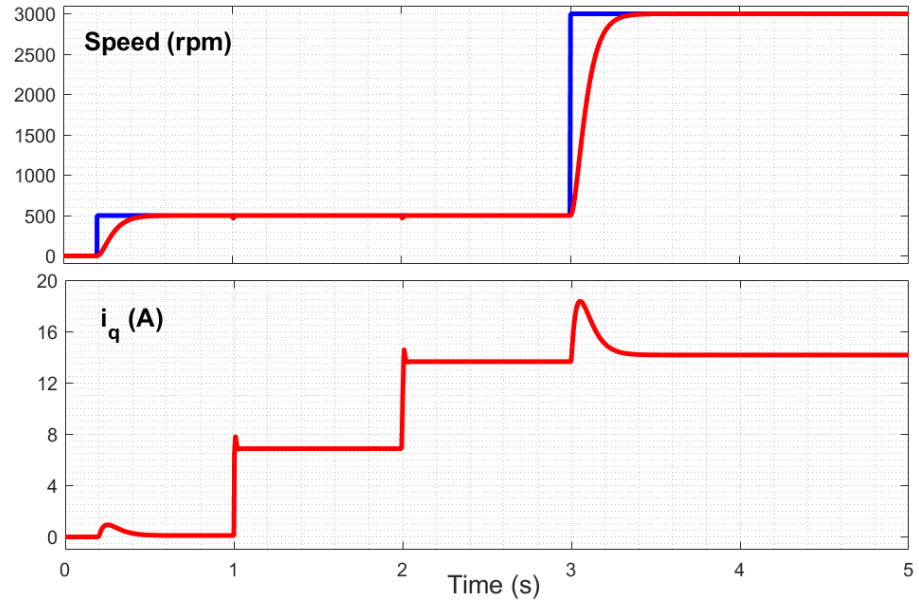

Figure 4.18: Simulation results of input ($y_{\Omega,inf}$) and motor speed using the conventional trajectory planning when the motor speed changes under heavy load.

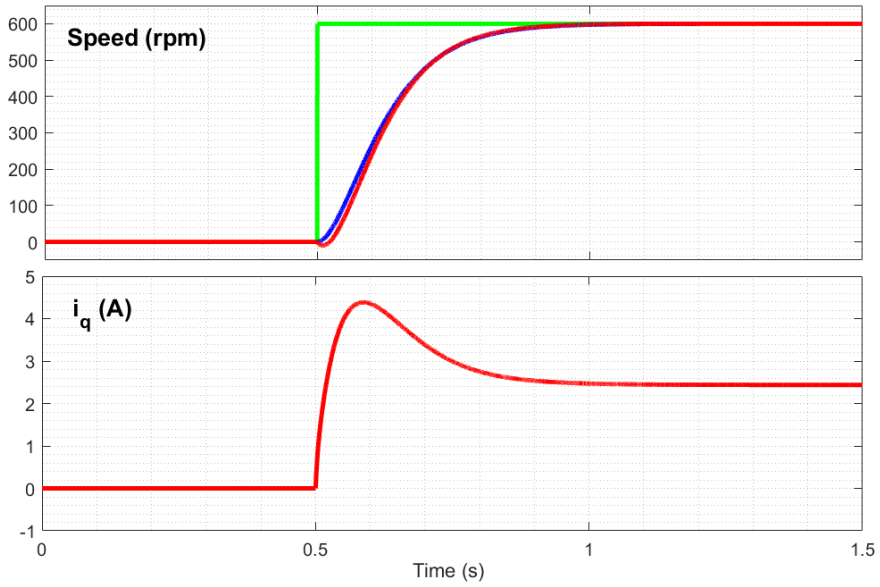

Figure 4.19: Simulation of the responses of motor speed and q-axis current (i_q) to a step change in speed reference. Red curve is motor speed, blue curve is $y_{\Omega,ref}$, and green one is $y_{\Omega,inf}$.

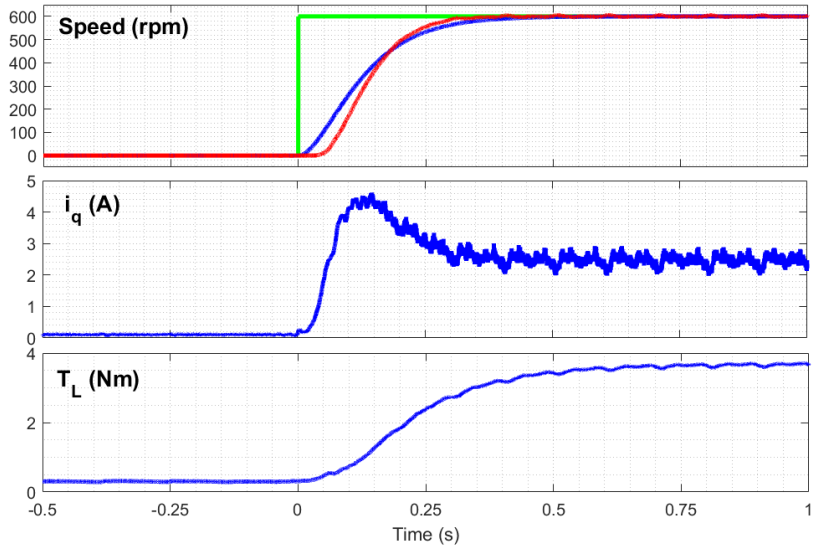

Figure 4.20: Experimental results of the variation of load torque (T_L) and responses of motor speed and q-axis current (i_q) to a step change in speed reference. Red curve is motor speed, blue curve is $y_{\Omega,ref}$, and green one is $y_{\Omega,inf}$.

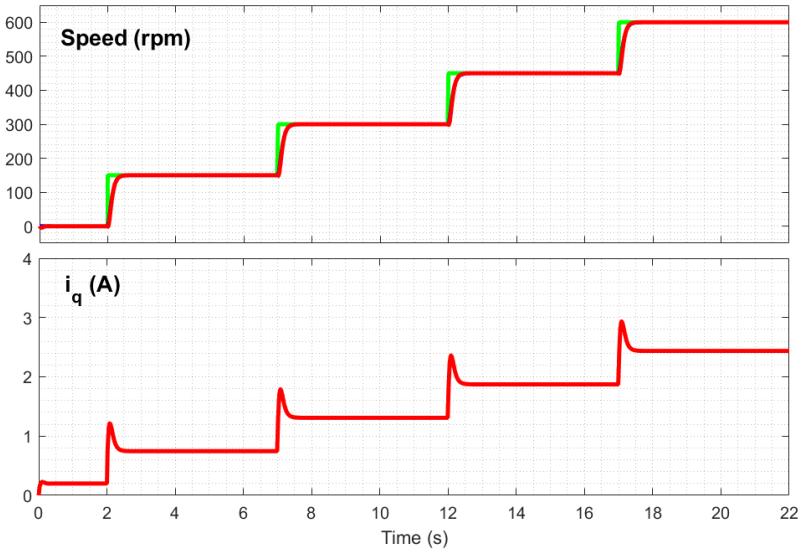

Figure 4.21: Simulation of the responses of motor speed and q-axis current (i_q) to step-wise changes of speed reference using flatness-based control with second-order function trajectory.

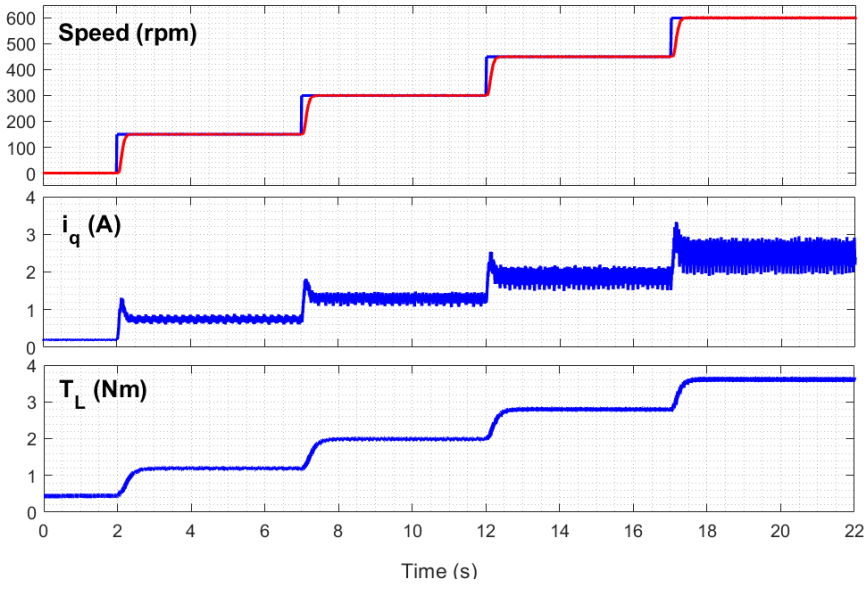

Figure 4.22: Experimental results of the variation of load torque (T_L) and responses of motor speed and q-axis current (i_q) to step-wise changes of speed reference using flatness-based control with second-order function trajectory.

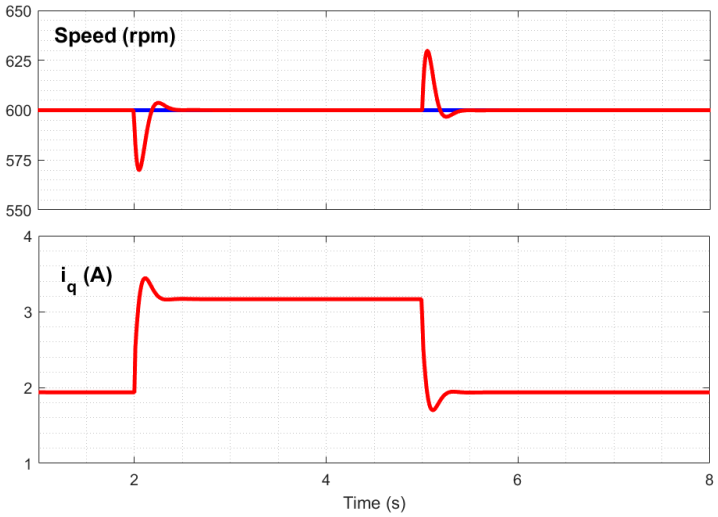

Figure 4.23: Simulation of the responses of motor speed and q-axis current (i_q) to changes of the load torque (T_L) using flatness-based control.

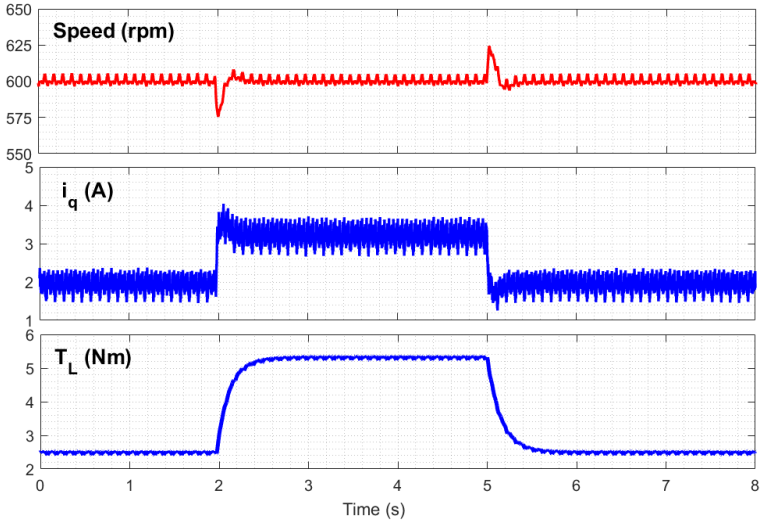

Figure 4.24: Experimental results of the responses of motor speed and q-axis current (i_q) to changes of the load torque (T_L) using flatness-based control.

$$y = a_{5,tr}t^5 + a_{4,tr}t^4 + a_{3,tr}t^3 + a_{2,tr}t^2 + a_{1,tr}t + a_{0,tr} \tag{4.65}$$

where $a_{k,tr}$ ($k = 0, 1, ..., 5$) are the polynomial coefficients. These coefficients are calculated by solving a set of equations of each trajectory window, as described in (4.66).

It should be mentioned that y_0, $\dot{y_0}$ and, $\ddot{y_0}$ for each window are given by the last window.

$$\begin{cases} y_f = a_{5,tr}{t_f}^5 + a_{4,tr}{t_f}^4 + a_{3,tr}{t_f}^3 + a_{2,tr}{t_f}^2 + a_{1,tr}t_f + a_{0,tr} \\ y_0 = a_{5,tr}{t_0}^5 + a_{4,tr}{t_0}^4 + a_{3,tr}{t_0}^3 + a_{2,tr}{t_0}^2 + a_{1,tr}t_0 + a_{0,tr} \\ \dot{y_f} = 5a_{5,tr}{t_f}^4 + 4a_{4,tr}{t_f}^3 + 3a_{3,tr}{t_f}^2 + 2a_{2,tr}t_f + a_{1,tr} \\ \dot{y_0} = 5a_{5,tr}{t_0}^4 + 4a_{4,tr}{t_0}^3 + 3a_{3,tr}{t_0}^2 + 2a_{2,tr}t_0 + a_{1,tr} \\ \ddot{y_f} = 20a_{5,tr}{t_f}^3 + 12a_{4,tr}{t_f}^2 + 6a_{3,tr}t_f + 2a_{2,tr} \\ \ddot{y_0} = 20a_{5,tr}{t_0}^3 + 12a_{4,tr}{t_0}^2 + 6a_{3,tr}t_0 + 2a_{2,tr} \end{cases} \tag{4.66}$$

The number of optimization variables was reduced from 9 to 3, as a result of this adjustment. As a result, the computational burden was reduced and the method was easier to implement on the hardware.

$$X_{opt,tr} = [y_f, \dot{y_f}, \ddot{y_f}] \tag{4.67}$$

The proposed trajectory planning method was validated using Matlab Simulink® simulations with a modification of one polynomial in each window to align it with the experimental study. The simulations employed a 100-millisecond window time (T_w).

In the simulation, we tested the trajectory planning method under various speed reference changes in a no-load condition. The speed reference started at 0 rpm, increased to 600 rpm at t = 2 s, returned to 0 rpm at t = 4 s, then changed to 100 rpm at t = 6 s, followed by increments to 400 rpm at t = 8 s, 300 rpm at t = 10 s, 100 rpm at t = 12 s, and a final increase to 600 rpm at t = 14 s.

Figure 6.8 illustrates the trajectory planning block's performance, showing that it generates the $y_{\Omega,ref}$ signal that closely tracks its reference value while adhering to the $i_{q,max} = 3$ constraint.

A study was conducted to assess the performance of the proposed system under varying torque loads. In this investigation, two different cases were examined.

In the first case, a step load change, equivalent to a rapid increase in load torque from 0 to 5 Nm at t = 6 s, was applied to the system. The load torque reverted to 0 at t = 12 s. This abrupt torque change led to the i_q current exceeding its limit ($i_{q,max}$) even at steady-state. To address this issue, the speed trajectory output adjusted itself to a lower value than its reference to ensure the current remained within the acceptable

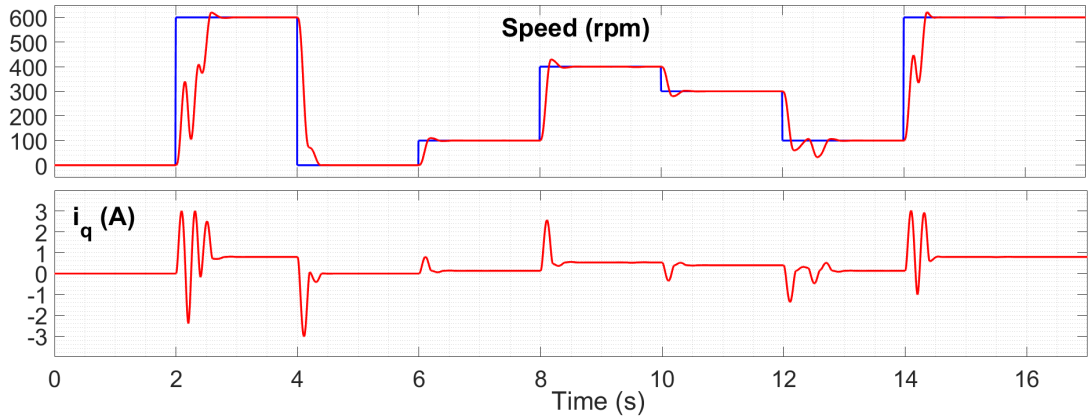

Figure 4.25: Simulation results of the motor speed and q-axis current (i_q) using flatness-based controller with proposed trajectory planning under various speed reference changes.

range, as shown in Figure 6.9. This capability is a potential advantage of the proposed control method. Notably, since the torque change is a step change, the current briefly exceeds its maximum value to allow the trajectory window to detect and adapt to this change. During this period, the flatness control regulator deals with the load torque change, similar to the conventional method.

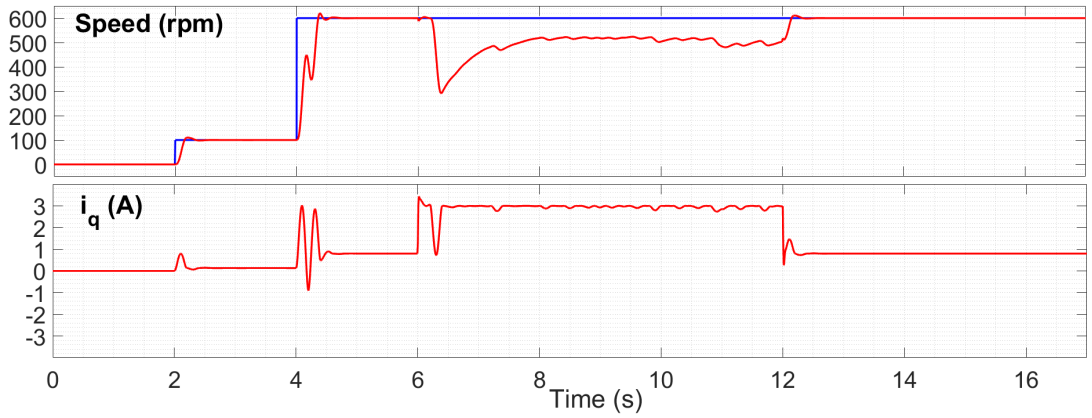

Figure 4.26: Simulation results of the motor speed and q-axis current (i_q) using flatness-based controller with proposed trajectory planning under significant change of load torque (T_L).

The same load change test was applied to the conventional one-loop flatness-based control system. On two occasions, the current exceeded its maximum value, as shown in

Figure 6.10. As previously discussed, the first instance occurred when the motor speed reference reached its maximum value. A second instance occurred when the motor operated under a transient heavy load, which persisted even at steady-state.

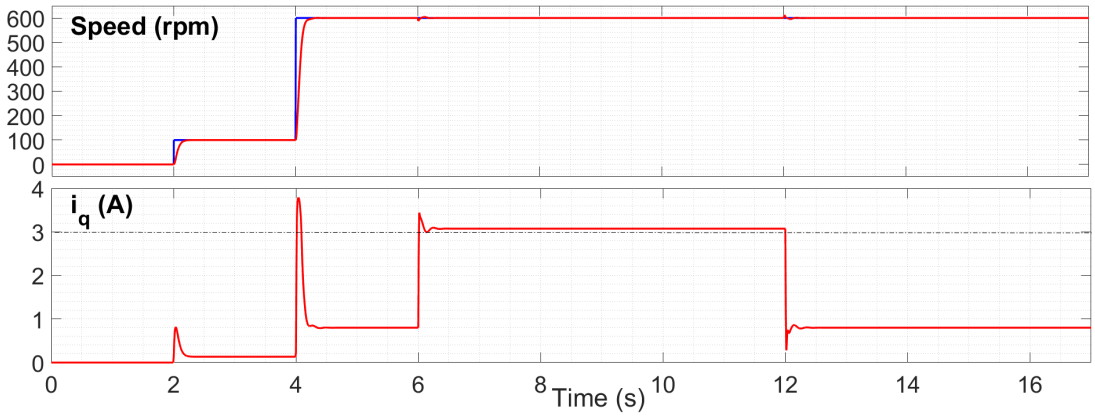

Figure 4.27: Simulation results of the motor speed and q-axis (i_q) current using flatness-based controller with traditional trajectory planning under significant change of load torque (T_L).

In the second test, we introduced a gradual increase and decrease in torque load instead of an abrupt step change. This gradual variation provided the trajectory planning method with more time to detect and adjust its output accordingly. According to Figure 4.28, the proposed method demonstrated successful performance, with the q-axis current remaining within its defined limits throughout the test.

The proposed trajectory planning method was implemented on the dSPACE MicroLabBox, utilizing the fmincon optimization algorithm. To ensure straightforward hardware integration, a fixed time window of the trajectory function (T_w) of 200 milliseconds was selected for subsequent tests.

In the initial test, the motor speed reference transitioned from 0 to 600 rpm at $t = 2$ seconds. Figure 6.11 illustrates how the proposed trajectory planning effectively generates a trajectory signal while adhering to the current constraint ($i_q = 3$). However, the measured motor current exceeds this threshold for a specific reason. The primary factor contributing to this discrepancy is the insufficient value of ω_Ω in the flatness-based controller. Consequently, ω_Ω is not adequate to track the motor speed with its desired trajectory, leading to a significant difference in $\dot{y}_{\Omega,ref}$, which is calculated in the trajectory planning module using equation (4.68) to determine the expected value of the

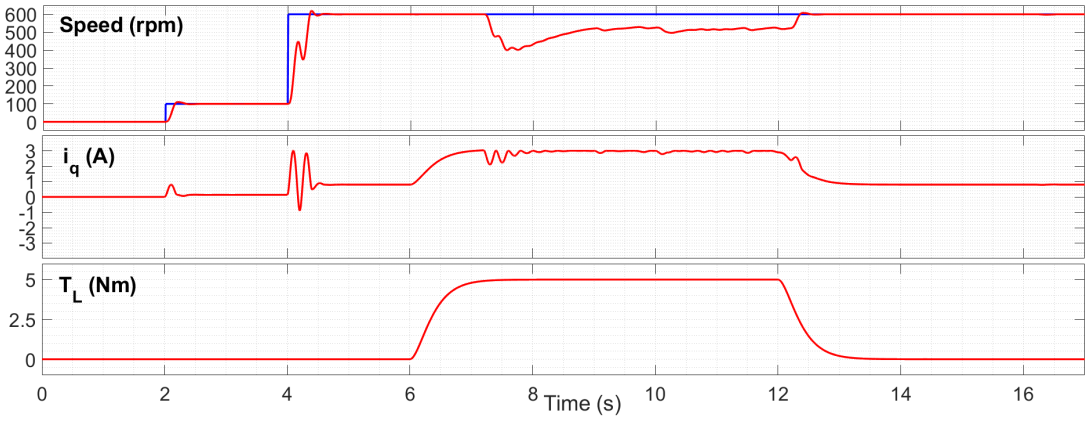

Figure 4.28: Simulation results of the motor speed and q-axis current (i_q) using flatness-based controller with proposed trajectory planning under gradual change of load torque (T_L).

current i_q.

$$i_{q,expected} = \frac{J\dot{y}_{\Omega,ref} + f y_{\Omega,ref} + \hat{T}_L}{p\psi_f} \tag{4.68}$$

A comparison of the measured i_q and its expected value at steady-state condition revealed a fairly accurate motor parameter identification process. It is not a feasible solution to increase ω_Ω significantly for this testbench. Doing so would not only intensify ripple of the switching voltages (V_d and V_q), potentially causing saturation of switching voltages and duty cycles, but it would also induce undesired speed fluctuations in the lower speed ranges. Consequently, striking a balance with respect to the choice of ω_Ω is essential when employing flatness regulators.

In addition, several other factors contribute to the discrepancy between i_q and its expected value. Among them are static friction within the system, particularly during startup, noise in the system, and possible parameter mismatches.

The impact of ω_Ω on the control system's performance was investigated, with various values of ω_Ω being tested. As shown in Figures 4.30 and 4.31, increasing ω_Ω results in a more precise tracking of the motor speed with the trajectory signal, thus achieving a better match between the measured and expected values of i_q.

Two different tests were conducted with ω_Ω = 60 rad/s. In the first test, the motor speed references changed from 100 to 400 rpm at $t = 2$ seconds, as depicted in Figure

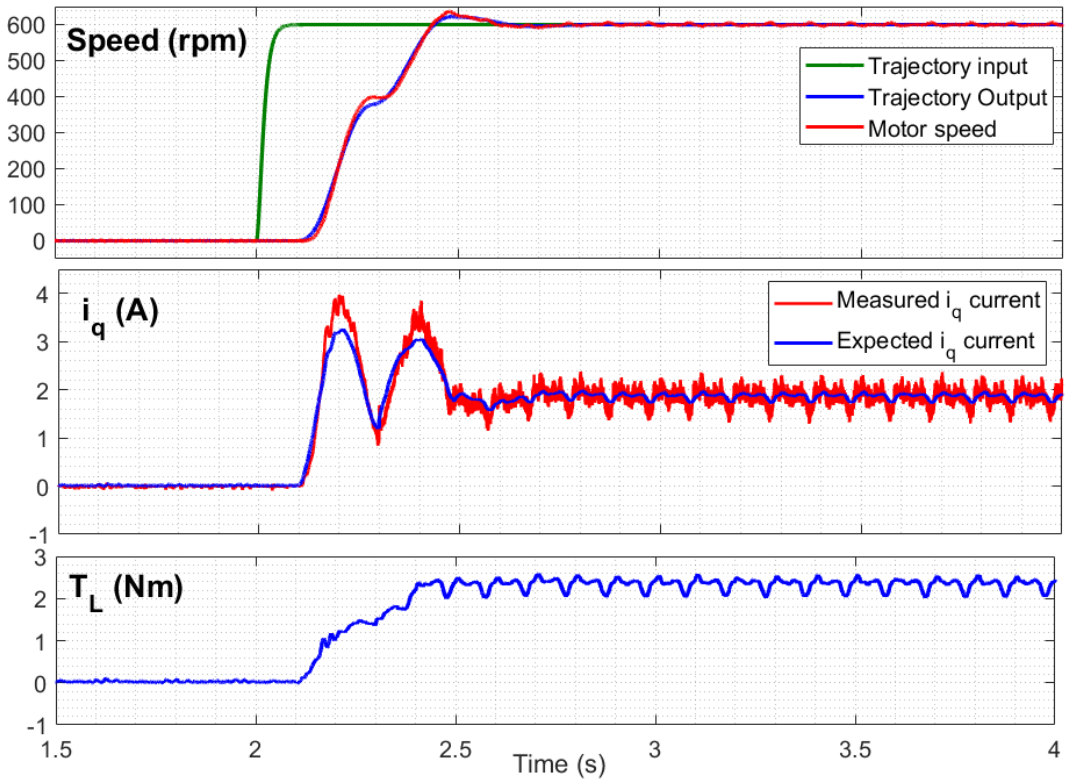

Figure 4.29: Experimental results of the variation of load torque (T_L) and responses of the motor speed and q-axis current (i_q) using flatness-based controller with proposed trajectory planning when the speed reference changes from 0 to 600 rpm.

4.32. In the second test, the motor speed reference changed from 300 to 100 rpm at $t = 2$, as shown in Figure 4.33. These tests were designed to assess the system's response to both speed increase and decrease scenarios, providing valuable insights into its performance under different conditions. The results reveal that the trajectory planning method consistently produces signals that effectively track the speed references while staying within the controller's defined limits.

In another test, a more substantial change in the speed reference was employed. The motor speed reference changed from 100 to 600 rpm. As demonstrated in Figure 4.34, the trajectory function was produced in a way to ensure that the expected current value remained within its permissible limits. As a result of this approach, the motor speed gradually reaches its desired speed over a number of windows.

In another test, the flatness-based control method using the proposed trajectory func-

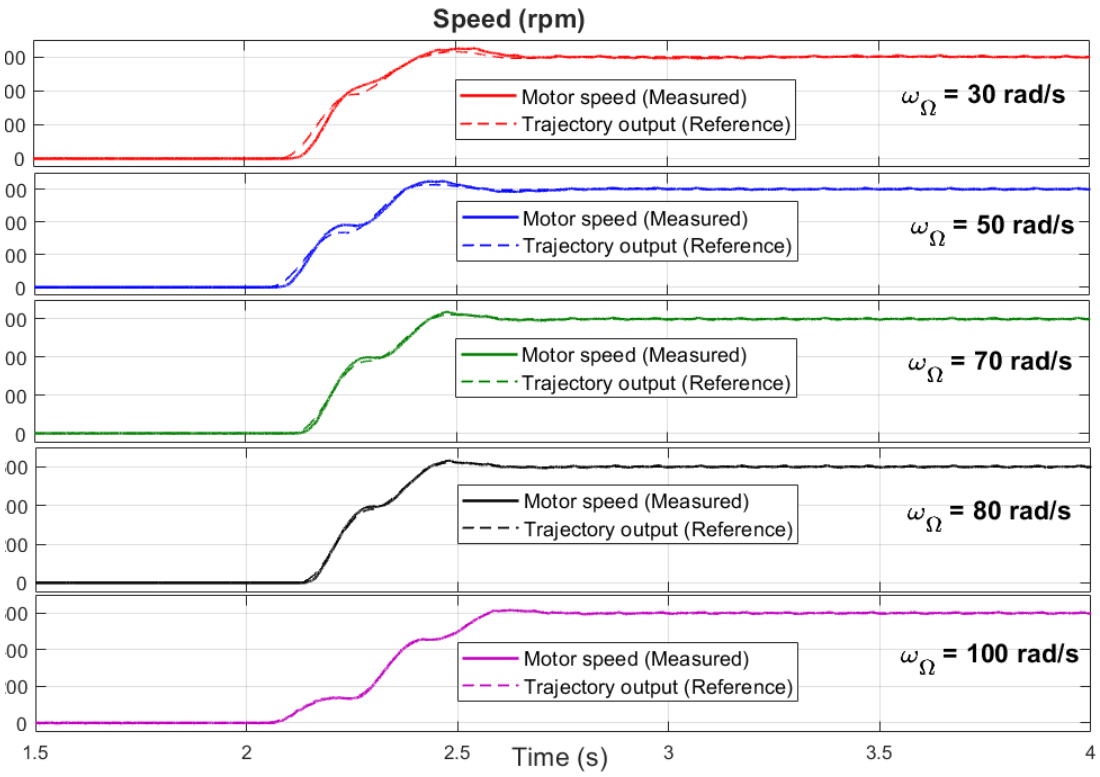

Figure 4.30: Experimental results of trajectory block output and motor speed when the speed references changes from 0 to 600 rpm considering different values of ω_Ω.

tion was compared with traditional control approaches. The test involved a motor speed transition from 0 to 600 rpm, with ω_Ω fixed at 80 rad/s. Figure 6.12 illustrates the motor speed and trajectory function generated by the proposed method, demonstrating that the motor reaches its final value while adhering to current constraints. In contrast, Figure 6.13 highlights that traditional control lacks current protection mechanisms

Another test has been conducted on the system with the proposed control system. During this test, the motor operated at a constant speed of 600 rpm, while the load was gradually increased. This led to a gradual increase in the i_q current. As shown in Figure 4.37, when the i_q current reached its maximum value (in this case, 2.8 A), the system's trajectory output and, consequently, the motor speed decreased to ensure compliance with the current constraint. When the torque decreased, the motor speed returned to its initial value of 600 rpm.

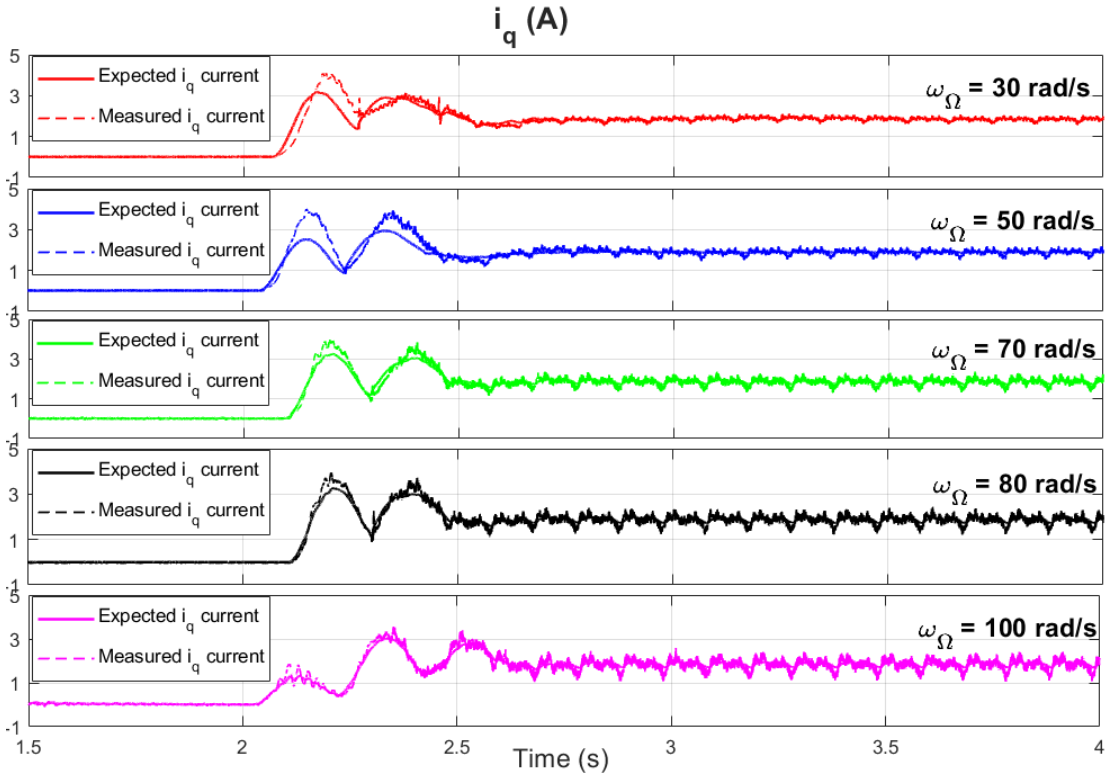

Figure 4.31: Experimental results of the trajectory expected i_q current and its measured value when the speed references changes from 0 to 600 rpm considering different values of ω_Ω.

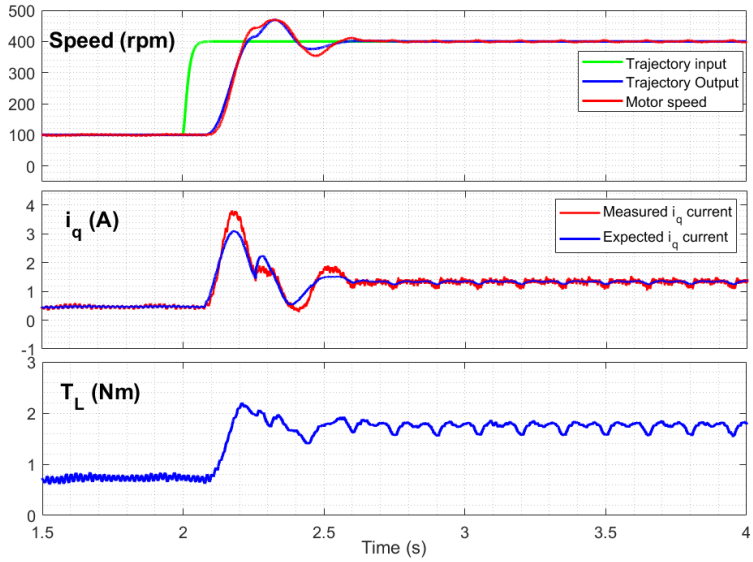

Figure 4.32: Experimental results of the variation of load torque (T_L) and responses of the motor speed and q-axis current (i_q) using flatness-based controller with proposed trajectory planning when the speed reference changes from 100 to 400 rpm.

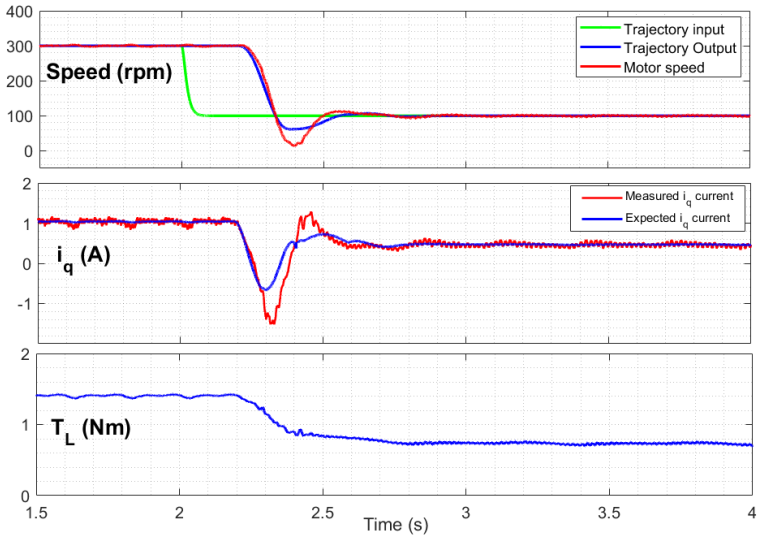

Figure 4.33: Experimental results of the variation of load torque (T_L) and responses of the motor speed and q-axis current (i_q) using flatness-based controller with proposed trajectory planning when the speed reference changes from 300 to 100 rpm.

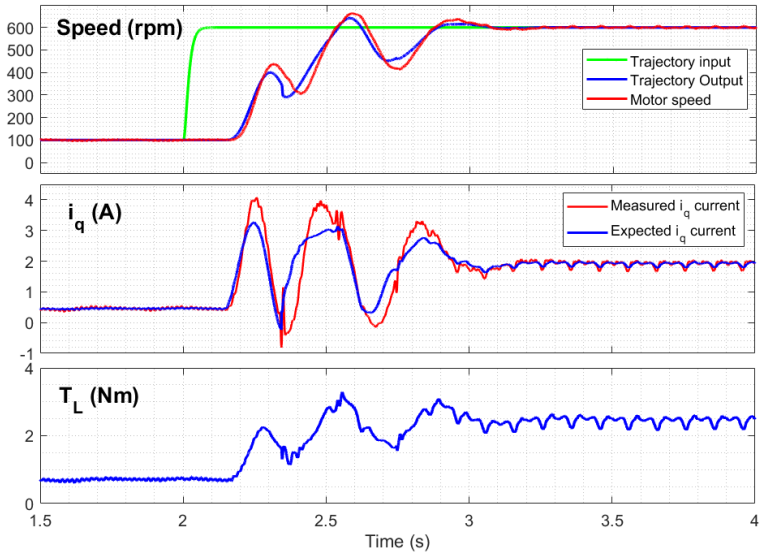

Figure 4.34: Experimental results of the variation of load torque (T_L) and responses of the motor speed and q-axis current (i_q) using flatness-based controller with proposed trajectory planning when the speed reference changes from 100 to 600 rpm.

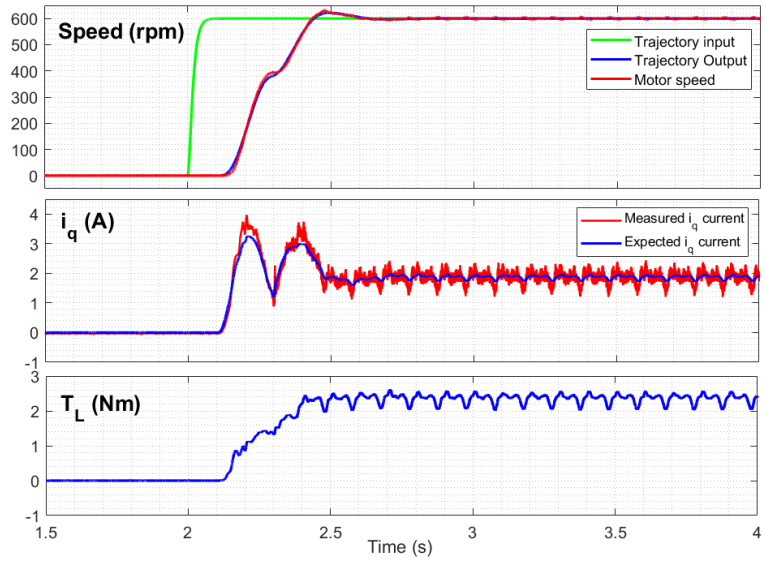

Figure 4.35: Experimental results of the variation of load torque (T_L) and responses of the motor speed and q-axis current (i_q) using flatness-based controller with proposed trajectory planning when the speed reference changes from 0 to 600 rpm considering $\omega_\Omega = 80$ rad/s.

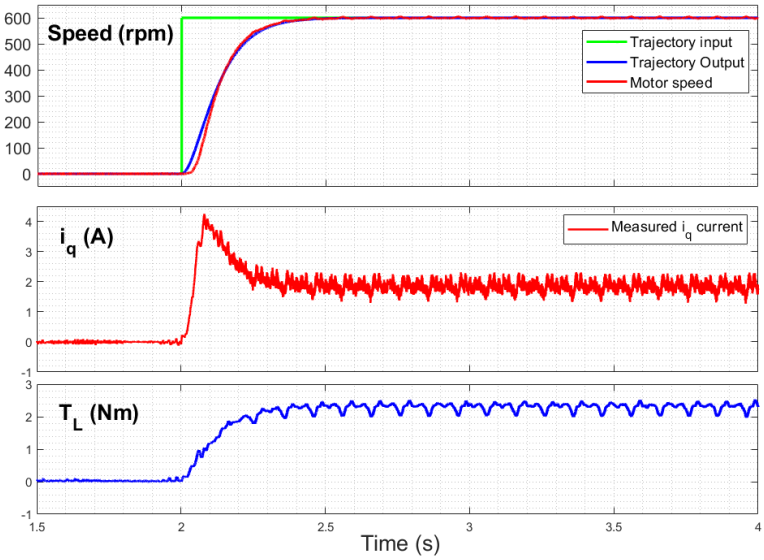

Figure 4.36: Experimental results of the variation of load torque (T_L) and responses of the motor speed and q-axis current (i_q) using flatness-based controller with traditional trajectory planning when the speed reference changes from 0 to 600 rpm considering $\omega_\Omega = 80$ rad/s.

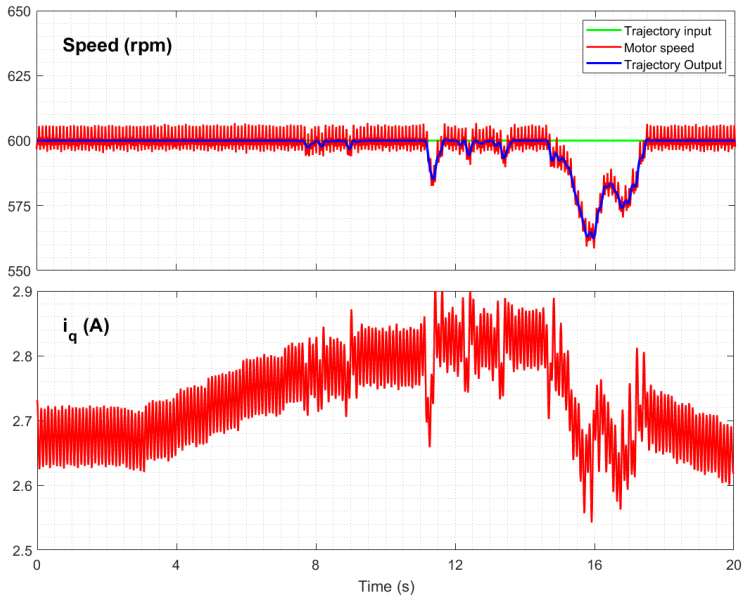

Figure 4.37: Experimental results of responses of the motor speed and q-axis current (i_q) using flatness-based controller with proposed trajectory planning when the load increasing resulting in modification of the trajectory output.

The abovementioned simulation studies and experimental tests have shown the effectiveness and advantages of the proposed method. These comprehensive investigations have demonstrated the potential future works and application of this method for various practical applications in the field.

4.9 Conclusion

This chapter provided a comprehensive analysis of flatness-based control for PMSMs. It began with an analysis of the structure and modeling of three-phase PMSMs, followed by a discussion of flatness-based control principles and the structure and design considerations for them. Additionally, a comprehensive analysis of state-of-the-art approaches to trajectory planning and flatness-based control was provided, along with their advantages and disadvantages.

As part of the chapter, flatness-based control was compared to FOC in terms of robustness and dynamic performance under transient conditions. Although FOC exhibits superior robustness against variations in motor parameters because of its cascaded structure, both methods display robustness in industrial applications. In contrast, flatness-based control offers significantly faster response times and demonstrates superior dynamic performance during transient events and torque fluctuations. The major drawback of single-loop flatness-based control is the absence of overcurrent protection.

Additionally, this chapter introduced a novel trajectory planning approach that takes into consideration the limitations of the controller. By using a window-based online function, this method optimizes system response time while adhering to constraints such as motor current, switching voltage, and speed overshoot. To increase the performance of the control system, the chapter explored the use of load torque and voltage drop observers.

The effectiveness of this approach has been verified through simulation studies and experimental tests, demonstrating its clear advantages over conventional flatness-based control methods.

Chapter 5

Conclusion

Contents

5.1 Conclusion and key points

In this thesis, a control approach for electric motors in water pump applications was developed and examined. Given the superior balance between cost-effectiveness and performance, PM brushless motors were chosen as the prime candidates for this application, with particular emphasis on BLDC motors and PMSMs.

Chapter 2 of this thesis offered a comprehensive overview and evaluation of BLDC motor drives. It delved into the modeling, equations, and fundamental principles of BLDC motors. The drive mechanisms of BLDC motors were examined, with a specific focus on sensorless control techniques, discussing their respective advantages and drawbacks. Furthermore, the chapter discussed the challenges of nonideal and asymmetric back-EMF signals, along with mitigation strategies to address these issues. However, during the course of this research project, a shift to PMSMs took place in a parallel thesis, making PMSMs the central focus of this project.

Chapter 3 explored PMSM drive systems. It provides a detailed description of the system's model and equations. Various control strategies were discussed, including sensorless control methods, Hall-position sensor-based techniques, and flatness-based control. The chapter also introduced the testbench used for experimental purposes and outlines the necessary tests for parameter identification. The FOC method, in particular, is implemented on the testbench, with a controller tuning methodology provided.

In Chapter 4, the thesis discussed flatness-based control in detail. It started by describing the conventional flatness-based control method, incorporating a second-order transfer trajectory function. The chapter highlighted the potential limitations of the cascaded flatness-based control structure, which may affect the system's ability to regulate motor speed during transient and disturbance events. On the other hand, using one-loop flatness-based control results in losing current protection. A one-loop flatness-based control approach was presented to address the issue of current protection, with the introduction of a novel trajectory planning method. This novel approach employs a window-based function combined with an online optimization algorithm to generate trajectory signals for each window, optimizing the system's response time while adhering to critical constraints such as motor current, switching voltages, and speed overshoot.

In comparison to the FOC method, flatness-based control demonstrates superior dynamic response to disturbances and transients. Notably, when dealing with the inherent nonlinearity of PMSM systems and scenarios where saturation effects cannot be disregarded, flatness-based control offers a compelling alternative to linear control methods like FOC.

The proposed trajectory planning method also accounts for current and voltage constraints, thus improving the method's overall performance. Unlike conventional flatness-based control, which may necessitate a slower response time due to controller limitations, this novel approach enhances system robustness, making it more reliable during disturbances. Additionally, the method's robustness and performance can be further elevated by introducing torque and voltage drop observers to the control system, which are also essential for the trajectory planning function.

Ultimately, the effectiveness and viability of this innovative control method are shown through simulation studies and experimental validation on a testbench.

5.2 Future work

The research on window-based trajectory planning for flatness-based control of PMSMs presents several promising avenues for future development:

- **Optimization algorithm enhancement:** It is possible to further refine the optimization algorithm used in trajectory planning to reduce its computational time.

In addition to improving its performance, we can reduce the required window by enhancing the optimization algorithm. This, in turn, will enhance the dynamic performance of the control system, making it more responsive and adaptable.

- **FPGA implementation:** One challenge faced is the deviation of window time from the desired value when employing the fmincon optimization algorithm. This deviation can introduce discontinuities in the trajectory output. To address this issue, an alternative approach is to implement the method on a Field-Programmable Gate Array (FPGA). An FPGA-based implementation has the potential to provide precise control and mitigate the variations in window time, which is particularly important for smaller window time scenarios.

- **Motor constraint integration for load variation:** It is essential to extend the trajectory planning methodology to take into account motor constraints during load variation. It is possible to address this challenge in two different ways. In the first place, it is possible to decrease the window time, allowing more frequent updates of the trajectory planning during continuous changes in load. Another option would be to design an event-detection algorithm that can identify torque variations and trigger the initiation of a new trajectory window.

- **Experimental validation on a PCB:** Experimental validation of the developed method on a Printed Circuit Board (PCB) is a potential future step. In order to confirm whether the proposed approach is practical and effective, real-world experiments are essential. Experimental results will contribute to the validation of theoretical predictions.

These avenues of research will help us refine and advance the window-based trajectory planning approach for flatness-based control of PMSMs, resulting in improved performance, robustness, and practical applicability.

Chapter 6

Résumé long

6.1 Introduction

Récemment, de nombreux efforts ont été déployés pour remplacer les véhicules conventionnels à moteur thermiques par des véhicules électriques (VE). Quel que soit le type de motorisation (moteur à combustion interne, électrique ou hybride), le système de refroidissement joue un rôle essentiel dans le fonctionnement du véhicule. Les exigences en matière de refroidissement pour les véhicules utilitaires et de tourisme sont restées inchangées au cours du siècle dernier. Dans un véhicule conventionnel équipé d'un moteur thermique, une pompe à liquide de refroidissement mécanique reliée à une vanne capable de réguler le débit suffit généralement à contrôler grossièrement la température de fonctionnement du moteur.

Aujourd'hui, en raison de la prise de conscience croissante de la pollution environnementale et de l'épuisement des ressources énergétiques dans le monde, cette solution traditionnelle doit être remplacée par des solutions plus efficaces, comme un moteur électrique dédié à la pompe à eau. Cette solution est également privilégiée pour les véhicules électriques, car ils comportent de nombreux composants thermorégulés (moteurs, batteries, convertisseurs électroniques de puissance) qui nécessitent des circuits de refroidissement dédiés. Pour répondre à ces besoins, la pompe de refroidissement mécanique sera remplacée par une pompe à moteur électrique dans cette thèse. Les moteurs des véhicules électriques doivent généralement fonctionner dans des environnements difficiles, avec des températures élevées et des vibrations. L'objectif de cette

thèse est de concevoir et de mettre en œuvre une nouvelle commande compatible avec un moteur électrique (développé dans le cadre d'une autre thèse liée à ce projet) de la pompe à eau véhicules électriques.

L'industrie automobile a connu une augmentation rapide des variateurs de vitesse basés sur des entraînements hybrides. Cette croissance influe également sur la demande de variateurs de vitesse de moteurs a aimant permanent (PM). Par conséquent, les moteurs synchrones à aimant permanent (PMSM) et les moteurs à courant continu sans balais (BLDC) sont devenus un choix populaire pour les applications automobiles, y compris les véhicules électriques (VE) et les véhicules électriques hybrides (VEH), au cours des dernières décennies, en raison de plusieurs caractéristiques, notamment une densité de couple élevée, un rendement élevé et une densité de puissance élevée.

Traditionnellement, les variateurs PMSM sont commandés par un contrôle orienté champ (FOC) utilisant des contrôleurs proportionnels et intégraux (PI) pour la régulation de la vitesse et du couple. La détermination des paramètres du contrôleur basée sur des méthodes linéaires nécessite une approximation linéaire qui dépend du point de fonctionnement du système. Des stratégies de contrôle non linéaire basées sur des modèles, y compris le contrôle différentiel de la platitude, ont été proposées comme solution à la nature non linéaire du système d'entraînement PMSM. Dans cette approche alternative, la conception de contrôleurs non linéaires et la planification de trajectoires sont clairement abordées. En utilisant la platitude différentielle, il est possible d'estimer la trajectoire du système directement à partir de la trajectoire d'une sortie plane et de ses dérivées sans intégrer d'équations différentielles.

Par rapport à la commande FOC classique, la commande des PMSM basée sur la platitude offre plusieurs avantages. Tout d'abord, elle élimine le besoin de régulateurs si tous les paramètres sont connus, ce qui permet un contrôle en boucle ouverte. Deuxièmement, elle permet d'obtenir des performances dynamiques élevées même en présence d'erreurs de modélisation et de perturbations externes. En plus, la méthode de planification de trajectoire utilisée dans le contrôle basé sur la platitude surpasse les contrôleurs linéaires en cascade dans les conditions transitoires et perturbées. Enfin, il a été démontré que le contrôle basé sur la platitude offre systématiquement des performances compétitives par rapport aux techniques de contrôle conventionnelles axées sur le champ.

La planification de la trajectoire affecte la réponse des états contrôlés indirectement.

Étant donné que les courants maximaux admissibles du moteur sont déterminés par les caractéristiques électriques du moteur et du pilote, et que les tensions de commutation dépendent de la tension du bus continu (et, dans certains cas, de l'état de charge de la batterie à courant continu), la condition de platitude du système peut s'avérer insuffisante et entraîner l'instabilité du système. Cette thèse propose une méthode de planification de trajectoire pour le contrôle basé sur la platitude des entraînements PMSM pour les pompes à eau des véhicules électriques. Cette approche vise principalement à garantir que le courant du moteur PMSM reste dans les limites permises grâce à un contrôle indirect basé sur la platitude, tout en conservant les avantages du contrôle en boucle unique. En outre, la contrainte de la tension de commutation a été prise en compte dans la méthode de planification de trajectoire proposée pour maintenir le bon fonctionnement du système d'entraînement du PMSM en régime permanent ainsi que pendant les phases transitoires. Une fonction de planification de trajectoire basée sur une fenêtre est utilisée pour l'entraînement PMSM dans cette méthode. La fonction de trajectoire est calculée à l'aide d'un algorithme d'optimisation prenant en compte les contraintes de dépassement de vitesse, de courant moteur et de tension de commutation. Contrairement à la planification conventionnelle de la trajectoire, qui est une fonction de second ordre, cette méthode prend en compte les limites du contrôleur tout en utilisant un contrôle basé sur la platitude en boucle unique.

6.2 Structure des moteurs à aimant permanent

Une machine électrique tournante est un système électromécanique bidirectionnel qui peut convertir l'énergie électrique en énergie mécanique (comme un moteur) et convertir l'énergie mécanique en énergie électrique (comme un générateur). Ces machines électriques sont composées de deux éléments principaux: la partie fixe appelée stator et la partie tournante appelée rotor. Ces deux parties sont séparées par un petit espace, l'entrefer. En général, les machines électriques peuvent être classées en fonction de trois facteurs clés:

- Source d'énergie du stator: courant continu (CC) ou courant alternatif (CA).
- Structure du rotor: utilisation d'aimants permanents, enroulement court-circuité ou enroulement excité, entre autres possibilités.

- Structure de l'entrefer.

La figure 6.1 présente le modèle 3D et la structure d'un moteur à aimant permanent. Ces moteurs ont un enroulement statorique triphasé, dont la construction est similaire à celle d'un moteur à induction à courant alternatif. Un enroulement statorique triphasé est bobiné pour produire une distribution trapézoïdale ou sinusoïdale du flux d'entrefer, selon qu'il s'agit d'un moteur BLDC ou d'un moteur PMSM. Le rotor de ces moteurs est constitué d'aimants permanents à haute performance solidement fixés au noyau. Il est possible d'obtenir diverses caractéristiques de moteur en ajustant la disposition, la forme et le positionnement de ces aimants [10].

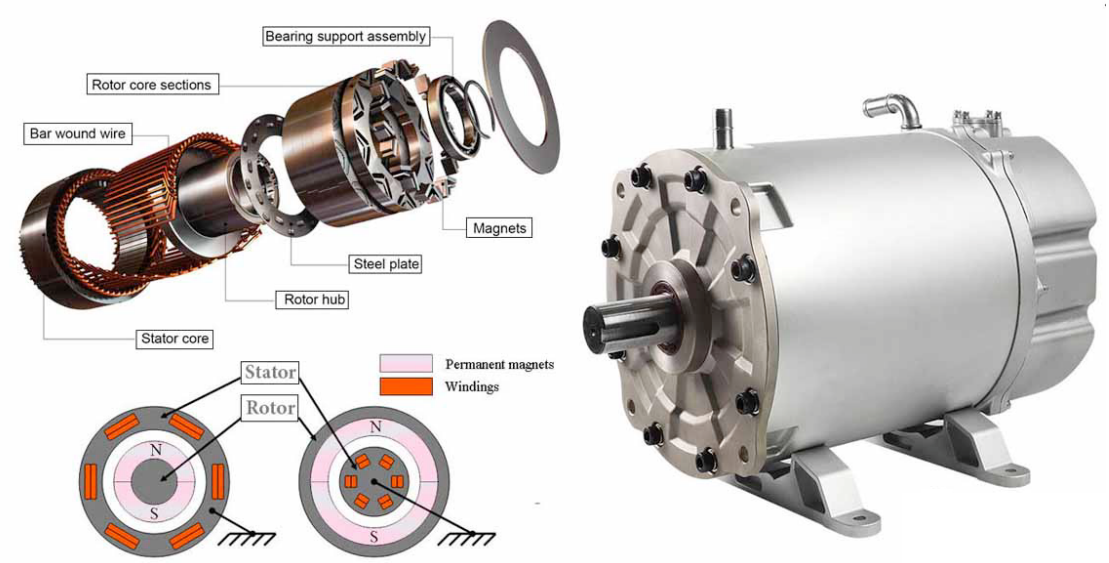

Figure 6.1: Construction d'un moteur à aimant permanent [11].

6.3 Modèle du PMSM

Le modèle électrique des moteurs sans balais, y compris les PMSM, peut être exprimé comme suit:

$$\begin{bmatrix} V_a \\ V_b \\ V_c \end{bmatrix} = \begin{bmatrix} R_s & 0 & 0 \\ 0 & R_s & 0 \\ 0 & 0 & R_s \end{bmatrix} \begin{bmatrix} i_a \\ i_b \\ i_c \end{bmatrix} + \begin{bmatrix} L & 0 & 0 \\ 0 & L & 0 \\ 0 & 0 & L \end{bmatrix} \frac{d}{dt} \begin{bmatrix} i_a \\ i_b \\ i_c \end{bmatrix} + \begin{bmatrix} e_a \\ e_b \\ e_c \end{bmatrix} \tag{6.1}$$

où R_s et L représentent l'impédance et l'inductance du stator; i_a, i_b et i_c sont les courants de phase; V_a, V_b et V_c sont les tensions de phase; et e_a, e_b et e_c sont les forces contre-électromotrice de phase.

Il est assez difficile d'analyser le comportement du moteur avec les équations sinusoïdales variant dans le temps, en particulier pendant le fonctionnement transitoire, malgré les hypothèses de simplification concernant le modèle du système. Afin de simplifier cette analyse, la transformation de Park est utilisée pour exprimer les variables dans un cadre dq tournant. De plus, pour assurer cette condition de somme nulle pour les courants statoriques, il est possible d'exprimer les variables statoriques (courant, tension et flux) dans un cadre de référence $\alpha\beta$. Dans ce cadre, le vecteur de courant se situe dans le cadre $\alpha\beta$, et la composante homopolaire du courant, proportionnelle à la somme des courants de phase, serait nulle. Ainsi, une composante homopolaire de tension ou de flux total ne joue pas de rôle dans la conversion d'énergie électromécanique, en particulier lors de l'expression du couple électromagnétique. En conséquence, le comportement du Moteur Synchrone à Aimants Permanents peut être représenté par les composantes $\alpha\beta$ des variables statoriques. La transformation peut être divisée en deux étapes:

- Transformation de Concordia: Transformation de trois phases (abc) en deux phases dans le cadre stationnaire ($\alpha\beta$).
- Transformation de Park: Transformation du cadre stationnaire ($\alpha\beta$) au cadre tournant (dq).

La figure 6.2 illustre le modèle de PMSM dans le cadre dq. Ses enroulements sont décalés électriquement de 90 degrés et l'enroulement du rotor est positionné à un angle de θ par rapport à l'enroulement de l'axe d du stator. On suppose que l'axe q précède l'axe d, ce qui entraîne la rotation du rotor dans le sens inverse des aiguilles d'une montre. Pour les PMSM ayant plus de pôles, il est possible de calculer l'angle électrique du rotor en multipliant la position mécanique du rotor par le nombre de paires de pôles.

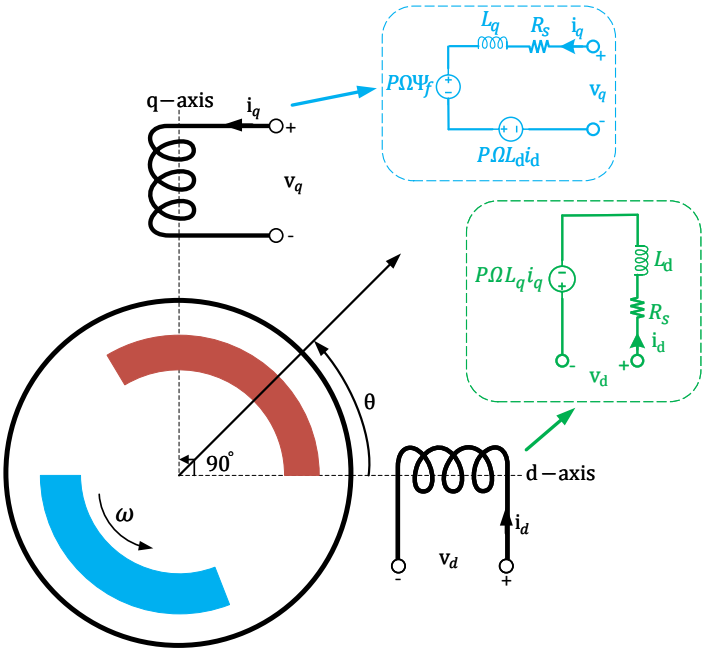

Figure 6.2: Modèle PMSM biphasé dans le cadre dq [127].

Par conséquent, le modèle du système d'entraînement du PMSM dans le cadre dq peut être décrit comme suit:

$$\begin{cases} V_d = Ri_d + L_d \dfrac{di_d}{dt} - p\Omega L_q i_q \\ V_q = Ri_q + L_q \dfrac{di_q}{dt} + p\Omega L_d i_d + p\psi_f \Omega \end{cases} \tag{6.2}$$

où V_d, V_q, i_d et i_q sont respectivement la tension aux bornes et le courant du stator dans le cadre dq. Le paramètre ψ_f est le flux magnétique constant du moteur. En outre, L_d et L_q désignent respectivement l'inductance de l'axe d et l'inductance de l'axe q. Le paramètre p est le nombre de paires de pôles et Ω correspond à la vitesse mécanique du moteur.

Lorsque les flux du stator et du rotor interagissent, ils génèrent un couple électromagnétique dans l'entrefer. Si ce couple atteint une magnitude suffisante, il déclenche la rotation du rotor. Pour une machine électrique tournante, l'équation du couple est

définie comme suit:

$$J\frac{d\Omega}{dt} = T_e - f\Omega - T_L. \tag{6.3}$$

où J est le moment d'inertie du rotor, T_L et T_e désignent respectivement le couple de charge et le couple électromagnétique. Le paramètre f indique le coefficient de frottement. Le couple électromagnétique développé par les machines synchrones avec une FEM sinusoïdale peut être exprimé comme suit:

$$T_e = p[\psi_f + (L_d - L_q)i_d]i_q. \tag{6.4}$$

Par conséquent, le modèle PMSM peut être décrit à l'aide de (6.2) et (6.4).

6.4 Commande par orientation du champ (FOC)

Le contrôle séparé du courant d'excitation et du courant d'armature dans les PMSM est une tâche difficile. Dans le découplage mathématique, le courant statorique est divisé en deux composantes, la composante directe (i_d), qui crée le champ du moteur, et la composante en quadrature (i_q), qui génère le couple du moteur à l'intérieur d'un cadre dq en rotation. La figure 6.3 illustre le concept de la méthode FOC. Les PMSM peuvent être contrôlés de la même manière que les moteurs à courant continu à l'aide de régulateurs de courant PI et d'onduleurs PWM. Dans cette approche, les courants et les tensions du stator sont convertis en cadre dq à l'aide de la transformée de Park, ce qui permet un contrôle indépendant du flux et du couple du moteur. Le contrôle individuel du courant de l'axe d (i_d) et du courant de l'axe q (i_q) est réalisé par la mise en œuvre d'une compensation découplée par anticipation dans les axes d et q. Cette technique est utilisée pour rendre le contrôle plus efficace. Cette technique est utilisée pour simplifier la conception de la commande et pour améliorer les performances globales de l'entraînement du moteur. Dans le cadre de la FOC, un capteur de position du rotor, tel qu'un codeur, ou une méthode d'estimation de la position sans capteur doit être utilisé pour déterminer la position du rotor pour le contrôle de la vitesse. La position du rotor est nécessaire non seulement pour le contrôle de la vitesse, mais aussi pour la transformation de Park. Le système FOC offre plusieurs avantages, notamment la capacité de convertir un système CA double complexe en un système linéaire général, un couple élevé à faible courant

pendant le démarrage et un rendement élevé [130].

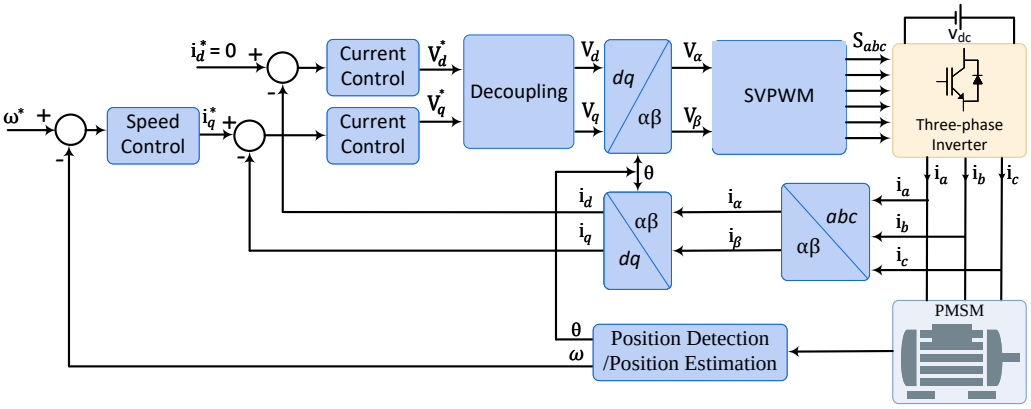

Figure 6.3: Schéma de la commande FOC du PMSM.

6.5 Méthode de contrôle basée sur la platitude

Traditionnellement, les variateurs PMSM sont commandés par un contrôle orienté champ (FOC) utilisant des contrôleurs proportionnels et intégraux (PI) pour la régulation de la vitesse et du couple. La détermination des paramètres du contrôleur basée sur des méthodes linéaires nécessite une approximation linéaire qui dépend du point de fonctionnement du système. Des stratégies de contrôle non linéaire basées sur des modèles ont été proposées comme solution à la nature non linéaire du système d'entraînement PMSM.

La théorie de la platitude différentielle a été introduite par Fliess et al [217]. Dans cette approche alternative, la conception de contrôleurs non linéaires et la planification de trajectoires sont clairement abordées. En utilisant la platitude différentielle, il est possible d'estimer la trajectoire du système directement à partir de la trajectoire d'une sortie plane et de ses dérivées sans intégrer d'équations différentielles.

Par rapport à la commande FOC classique, la commande des PMSM basée sur la platitude offre plusieurs avantages [222]. Tout d'abord, elle élimine le besoin de régulateurs si tous les paramètres sont connus, ce qui permet un contrôle en boucle ouverte. Deuxièmement, elle permet d'obtenir des performances dynamiques élevées même en

présence d'erreurs de modélisation et de perturbations externes. En plus, la méthode de planification de trajectoire utilisée dans le contrôle basé sur la platitude surpasse les contrôleurs linéaires en cascade dans les conditions transitoires et perturbées. Enfin, il a été démontré que le contrôle basé sur la platitude offre systématiquement des performances compétitives par rapport aux techniques de contrôle conventionnelles axées sur le champ.

La littérature récente fait état de travaux visant à améliorer la commande basée sur la platitude pour les applications d'entraînement PMSM. L'estimation de la platitude différentielle étant une approche basée sur un modèle, des observateurs tels que les observateurs d'état ou les observateurs de Luenburger sont proposés pour estimer la perturbation du couple de charge et la résistance du stator (représentant les pertes dans l'onduleur et le PMSM) au moyen de sa chute de tension [232]. Il a été démontré que cette méthode peut contribuer à améliorer le système d'entraînement du PMSM et son efficacité. En plus, une commande de platitude en cascade a été proposée pour éliminer les erreurs statiques dans les variables d'état. Dans l'approche dite dq, l'angle du système de coordonnées et les courants de stator de l'axe dq sont considérés comme des composants de sortie plats [233].

Des recherches ont été menées sur l'extension de la commande des PMSM basée sur la platitude au mode de saturation. Outre les considérations de fabrication, les PMSM sont souvent conçus pour un fonctionnement à court terme, limité thermiquement, dans des plages de surcharge. Certains articles ont proposé des méthodes de contrôle basées sur la platitude qui utilisent le modèle mathématique du PMSM pour le mode de saturation [226]. Une méthode étendue de commande d'entraînement de PMSM basée sur la platitude a été proposée dans [235] par l'ajout d'un mécanisme basé sur les événements. Dans ce cas, la planification de la trajectoire et les paramètres du contrôleur sont mis à jour sur la base de mesures et d'estimations des états du système.

La planification de la trajectoire affecte la réponse des états contrôlés indirectement. Étant donné que les courants maximaux admissibles du moteur sont déterminés par les caractéristiques électriques du moteur et du pilote, et que les tensions de commutation dépendent de la tension du bus continu (et, dans certains cas, de l'état de charge de la batterie à courant continu), la condition de platitude du système peut s'avérer insuffisante et entraîner l'instabilité du système. Pour traiter les limites du contrôleur, qui n'ont pas été abordées correctement jusqu'à présent, une approche de planification

de trajectoire pour le contrôle basé sur la platitude des entraînements PMSM est proposée dans notre recherche. Dans cette méthode, une fonction de trajectoire basée sur une fenêtre est utilisée avec un algorithme d'optimisation pour minimiser le temps de réponse de la fonction de trajectoire tout en satisfaisant les contraintes de courant du moteur et de tension de commutation.

La figure 6.4 présente le schéma d'un cadre de contrôle basé sur la planéité. Dans le cadre de cette approche de contrôle, deux variables d'état, i_d et Ω, sont directement contrôlées, tandis que le courant de l'axe q (i_q) est contrôlé indirectement.

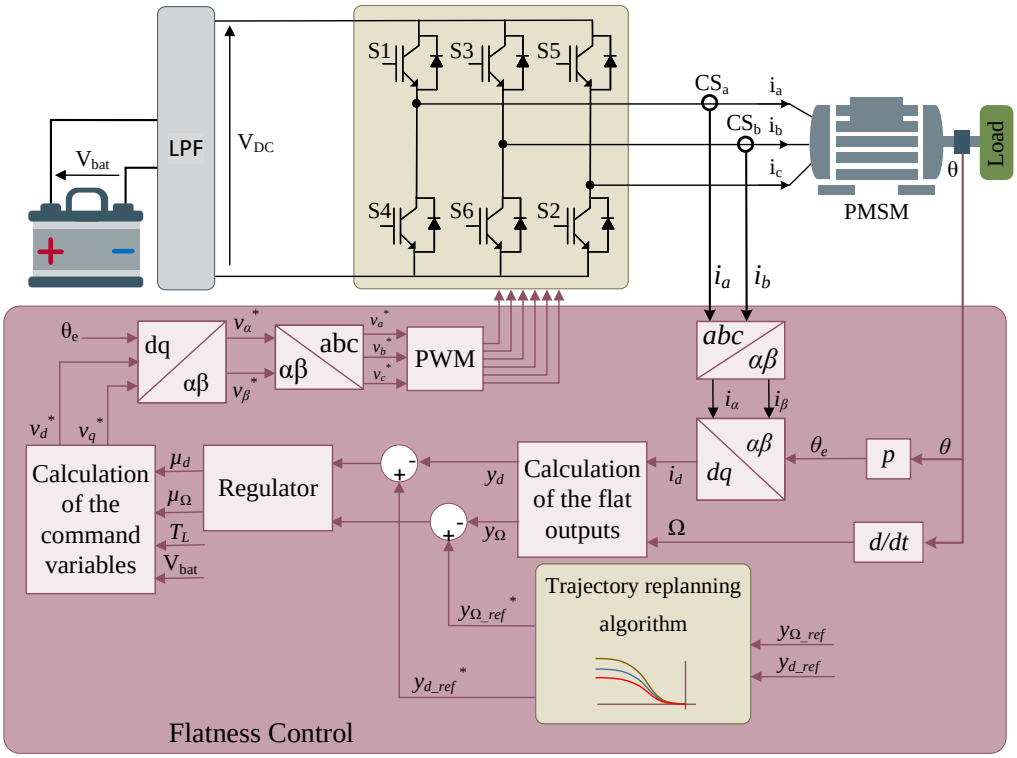

Figure 6.4: Schéma de la commande d'un PMSM basée sur la planéité.

Deux nouvelles variables doivent être introduites pour concevoir le régulateur différentiel basé sur la planéité. Ces variables sont censées représenter les composantes dérivées d'ordre supérieur des sorties plates dans les équations pour V_d et V_q. Par exemple, pour le PMSM étudié dans cette thèse, V_d et V_q peuvent être exprimés sur la base

des variables de sortie plates comme suit:

$$\begin{cases} V_d = L_d \dot{y_d} + R_s y_d - p L_q i_q y_\Omega \\ V_q = L_q \dot{i_q} + R_s i_q + p L_d y_d y_\Omega + p \psi_f y_\Omega \end{cases} \tag{6.5}$$

Si l'on considère que le courant de l'axe q peut être exprimé sur la base de variables de sortie planes comme $\frac{1}{p\psi_f}(J\dot{y_\Omega} + f y_\Omega + T_L)$, (6.5) est égal à:

$$\begin{cases} V_d = L_d \dot{y_d} + R_s y_d - \frac{J L_q}{\psi_f} y_\Omega \dot{y_\Omega} - \frac{f L_q}{\psi_f} y_\Omega^2 - \frac{L_q}{\psi_f} y_\Omega T_L \\ V_q = \frac{J L_q}{p\psi_f} \ddot{y_\Omega} + \frac{f L_q + J R_s}{p\psi_f} \dot{y_\Omega} + (p\psi_f + \frac{f R_s}{p\psi_f}) y_\Omega + p L_d y_d y_\Omega + \frac{R_s}{p\psi_f} T_L \\ + \frac{L_q}{p\psi_f} \dot{T_L} \end{cases} \tag{6.6}$$

En conséquence,

$$\begin{cases} \mu_d = \dot{y_d} \\ \mu_\Omega = \ddot{y_\Omega} \end{cases} \tag{6.7}$$

Afin de tenir compte des incertitudes des paramètres du système et de gérer les perturbations, la méthode de contrôle à boucle unique basée sur la planéité formule des lois de contrôle pour les régulateurs comme suit:

$$\begin{cases} \dot{y_{d,ref}} - \mu_d + k_{d1}.(y_{d,ref} - y_d) + k_{d2} \cdot \int (y_{d,ref} - y_d)\, d\tau = 0 \\ \ddot{y_{\Omega,ref}} - \mu_\Omega + k_{\Omega 1} \cdot (\dot{y_{\Omega,ref}} - \dot{y_\Omega}) + k_{\Omega 2} \cdot (y_{\Omega,ref} - y_\Omega) \\ + k_{\Omega 3} \cdot \int (y_{\Omega,ref} - y_\Omega)\, d\tau = 0, \end{cases} \tag{6.8}$$

où $k_{\Omega 1}$, $k_{\Omega 2}$ et $k_{\Omega 3}$ sont les paramètres du régulateur de vitesse mécanique. De même, k_{d1} et k_{d2} sont les paramètres du régulateur de courant continu. Le terme intégral permet un rejet robuste de l'erreur statique et de l'incertitude des paramètres.

Pour déterminer les coefficients du régulateur, les polynômes caractéristiques suiv-

ants sont utilisés.

$$\begin{cases} s + k_{d1} + \dfrac{k_{d2}}{s} = 0 \\ s^2 + k_{\Omega 1} s + k_{\Omega 2} + \dfrac{k_{\Omega 3}}{s} = 0 \end{cases} \tag{6.9}$$

L'équation (6.9) peut être réécrite comme suit:

$$\begin{cases} s^2 + k_{d1} s + k_{d2} = 0 \\ s^3 + k_{\Omega 1} s^2 + k_{\Omega 2} s + k_{\Omega 3} = 0 \end{cases} \tag{6.10}$$

Pour régler les paramètres du régulateur, le polynôme caractéristique souhaité est considéré comme suit:

$$\begin{cases} Q_d = s^2 + 2\zeta_d \omega_d s + \omega_d^2 \\ Q_\Omega = (s - p_\Omega)(s^2 + 2\zeta_\Omega \omega_\Omega s + \omega_\Omega^2), \end{cases} \tag{6.11}$$

où ω_Ω, ω_d, et ζ_Ω, ζ_d sont respectivement la fréquence de coupure et les coefficients d'amortissement. Les paramètres du contrôleur sont calculés à l'aide de la méthode de placement des pôles. Le pôle p_Ω est considéré comme égal à $-\zeta_\Omega \omega_\Omega$ dans cette thèse.

Les chercheurs ont montré que le contrôle basé sur la planéité peut être utilisé avec des PMSM en mode de saturation. Outre les problèmes de fabrication, les PMSM sont parfois conçus pour fonctionner efficacement dans des conditions de surcharge transitoires et thermiquement contraignantes, ce qui entraîne une saturation magnétique. En outre, certaines industries essaient de concevoir des PMSM en mode saturation pour réduire les coûts, ce qui intensifie les problèmes de non-linéarité du système contrôlé par des contrôleurs linéaires. Par conséquent, plusieurs travaux ont décrit des stratégies de contrôle innovantes basées sur la planéité utilisant des modèles mathématiques de PMSM exprimés spécifiquement pour les modes de saturation [226–228]. Grâce à ces contributions à la recherche, la commande basée sur la planéité a été élargie pour inclure les PMSM en mode de saturation. L'étude de la saturation magnétique et l'intégration de ces connaissances dans le cadre de contrôle visent à améliorer les performances des PMSM dans diverses conditions de fonctionnement.

La méthode de contrôle basée sur la planéité utilise un modèle mathématique pour contrôler le comportement d'un système. Cependant, l'efficacité de cette stratégie de contrôle dépend fortement de la précision avec laquelle le modèle du système représente

la dynamique du monde réel. En raison de divers facteurs tels que les variations du système, les incertitudes et les perturbations externes, l'obtention d'un modèle très précis peut s'avérer difficile dans les applications industrielles pratiques. Récemment, des recherches ont été consacrées à l'amélioration des performances dynamiques de la méthode de contrôle basée sur la planéité afin de surmonter les limitations causées par les imprécisions du modèle. Il est possible d'améliorer le système en incorporant des observateurs. Dans ce cas, deux types d'observateurs ont été explorés dans des études récentes : l'observateur d'état non linéaire et l'ELO.

- **Observateur d'état** : Selon [229], les observateurs d'état sont conçus pour estimer les variables ou les états qui sont difficiles à mesurer directement. Dans le cadre d'un contrôle basé sur la planéité, ils peuvent aider à estimer des paramètres tels que le couple de charge et les chutes de tension.

- **Observateurs de Luenberger étendus (ELO)** : Comme proposé dans [230], les ELO sont un type spécifique d'observateur conçu pour estimer les états du système, en particulier en présence d'incertitudes et de perturbations.

L'ajout de ces observateurs au cadre de contrôle basé sur la planéité vise à atténuer les effets négatifs d'un modèle inexact du système. Les observateurs fournissent des estimations en temps réel des paramètres critiques, ce qui permet au système de contrôle de compenser les écarts entre le modèle et le comportement réel. De cette manière, le contrôle basé sur la planéité devient plus fiable et plus robuste pour les applications industrielles nécessitant des performances précises et solides.

6.6 Planification de la trajectoire

La méthode de contrôle de la planéité est conçue de manière à s'assurer que ses sorties planes suivent toujours la référence de la trajectoire. Par conséquent, la planification de la trajectoire peut jouer un rôle essentiel dans ses performances dynamiques [231]. Bien que la planification de la trajectoire soit un sujet de recherche dans d'autres domaines tels que la robotique, elle n'a pas encore fait l'objet d'une attention particulière dans les applications d'entraînement PMSM.

Les fonctions de transfert du second ordre décrites dans (6.12) sont couramment utilisées pour limiter les références transitoires de vitesse et de courant dans les conceptions classiques de planification de trajectoire pour les applications d'entraînement PMSM. Dans la phase de planification de la trajectoire, la sortie souhaitée, désignée par y_{ref}, est générée par le bloc de planification de la trajectoire. De même, la sortie plate, désignée par y_{inf}, est dérivée du signal de référence.

$$y_{ref} = \frac{1}{\frac{1}{\omega_f^2}s^2 + \frac{2\zeta_f}{\omega_f}s + 1} y_{inf}, \tag{6.12}$$

où ω_f et ζ_f sont respectivement la fréquence de coupure et le rapport d'amortissement de la fonction de transfert de la trajectoire.

Cependant, une simple fonction de trajectoire du second ordre ne permet pas de protéger le système d'entraînement du moteur contre les surintensités. Par conséquent, les approches de contrôle en cascade basées sur la planéité sont souvent employées dans ces cas, comme le montre la figure 6.5, bien que cela entraîne un temps de réponse plus lent du système de contrôle [230, 232]. Un autre schéma de contrôle cascadé basé sur la planéité a été proposé dans [233] pour éliminer les erreurs statiques dans les variables d'état du système. Les fonctions de transfert de la commande de planéité en cascade peuvent être exprimées comme suit:

$$\begin{cases} \dfrac{y_{q,ref}}{y_{q,inf}} = \dfrac{1}{\frac{1}{\omega_{f1}^2}s^2 + \frac{2\zeta_{f1}}{\omega_{f1}}s + 1} \\ \dfrac{y_{\Omega,ref}}{y_{\Omega,inf}} = \dfrac{1}{\frac{1}{\omega_{f2}^2}s^2 + \frac{2\zeta_{f2}}{\omega_{f2}}s + 1} \end{cases} \tag{6.13}$$

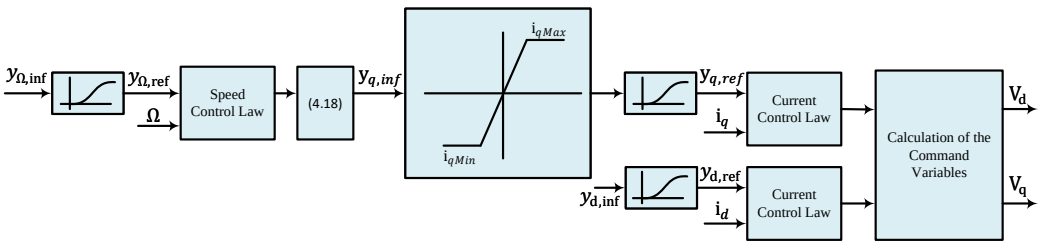

Figure 6.5: Schéma de la commande en cascade des PMSM basée sur la planéité [232].

Le signal $y_{q,inf}$ est calculé en utilisant (6.14).

$$y_{q,inf} = \frac{J\dot{y}_{\Omega,ref} + f y_{\Omega,ref} + T_L}{p\psi_f} \tag{6.14}$$

Compte tenu de l'interaction possible entre la fréquence de commutation de l'onduleur (ω_s) et la fréquence de coupure du système de commande en cascade, on suppose, pour la conception du système de commande, que la boucle extérieure de commande de la vitesse fonctionne à une fréquence de coupure satisfaisant $\omega_{n2} \leq \omega_{f1} \leq \omega_{n1} \leq \omega_s$, où ω_{n1} et ω_{n2} sont la fréquence de coupure des contrôleurs de planéité en cascade. Pour améliorer la réponse du contrôle de la vitesse, ω_{f2} est généralement choisi pour être égal à ω_{n2} [232].

En outre, une comparaison complète du contrôle conventionnel basé sur la planéité et de la méthode FOC est fournie dans [223]. Les résultats indiquent que les schémas de contrôle basés sur la planéité avec une boucle de contrôle unique sont efficaces pour réguler rapidement la vitesse du moteur, même en présence de perturbations et de variations du couple de charge. Cependant, l'utilisation d'une commande basée sur la planéité avec une seule boucle entraîne le sacrifice de la protection contre les surintensités du moteur.

Pour relever ce défi de la protection contre les surintensités pour le contrôle basé sur la planéité à une boucle, deux approches ont été proposées dans [234]. La première méthode implique des ajustements dynamiques de la trajectoire de référence de la vitesse mécanique pour prévenir les conditions de surintensité. La deuxième approche se concentre sur la sécurité du système en arrêtant son fonctionnement lorsque des perturbations importantes se produisent et, par conséquent, évite les dommages potentiels. En outre, une méthode de contrôle étendue basée sur la planéité est introduite dans [235]. Cette méthode intègre un mécanisme basé sur les événements pour améliorer les performances du système. Au cours de ces événements, la planification de la trajectoire et les paramètres du contrôleur sont mis à jour sur la base de mesures et d'estimations en temps réel des paramètres du système.

6.7 Méthode de planification de trajectoire proposée

La planification de la trajectoire affecte de manière significative le comportement des variables d'état indirectement contrôlées d'un système. Elle est particulièrement remarquable en raison de divers facteurs, tels que le courant maximal admissible du moteur fixé par ses spécifications électriques, ainsi que les contraintes de tension de commutation. Ces limitations de tension dépendent de la tension du bus CC et, dans certains scénarios, de l'état de charge de la batterie CC. Par conséquent, les performances du système sans tenir compte des limites du contrôleur peuvent être perturbées par ces limites, ce qui pourrait conduire à une instabilité indésirable [138].

Pour faire face aux limites du contrôleur, qui n'ont pas été traitées correctement jusqu'à présent, une nouvelle approche de planification de trajectoire pour le contrôle basé sur la planéité des entraînements PMSM est proposée dans notre recherche. Dans cette méthode, une fonction de trajectoire basée sur une fenêtre est utilisée avec un algorithme d'optimisation. L'objectif principal de cette approche de planification de trajectoire est de minimiser le temps de réponse du système tout en garantissant le respect des contraintes imposées par les limitations de courant du moteur et les restrictions de tension de commutation [138].

Comme le courant maximal du moteur dépend de la fonction de trajectoire du système de commande, le courant du moteur ne peut pas être contrôlé avec une planification classique de la trajectoire. Un temps de réponse de la planification de la trajectoire suffisamment lent doit être conçu pour le pire scénario possible afin de garantir que le courant reste dans la plage autorisée pour une large gamme d'applications du moteur. En plus, les sorties du système de contrôle, V_d et V_q (comme l'illustre la figure 6.4.), doivent toujours satisfaire à la condition (6.15), qui dépend de la tension du bus CC, et en cas de chute de tension, la planification classique de la trajectoire risque de ne pas fonctionner correctement. La planification de la trajectoire de vitesse peut être utilisée pour contrôler à la fois le couple du PMSM et le courant de l'axe q.

$$v_d^2 + v_q^2 < mV_{dc}^2 \tag{6.15}$$

où $m = \frac{3}{8}$ pour la modulation de largeur d'impulsion sinusoïdale (MLI-S) et $m = \frac{1}{2}$ pour la modulation de largeur d'impulsion à vecteur spatial (MLI-VS).

La méthode de planification de trajectoire proposée utilise une méthode de fonction basée sur une fenêtre. Trois intervalles de distribution égale sont inclus dans la fenêtre sur la base de la distribution illustrée à la figure 6.6. Ces points sont calculés à l'aide de (6.16).

$$\begin{cases} t_1 = t_0 + \dfrac{T_w}{3} \\ t_2 = t_0 + 2\dfrac{T_w}{3}, \end{cases} \tag{6.16}$$

où T_p est l'intervalle de la fenêtre et t_0 le temps initial.

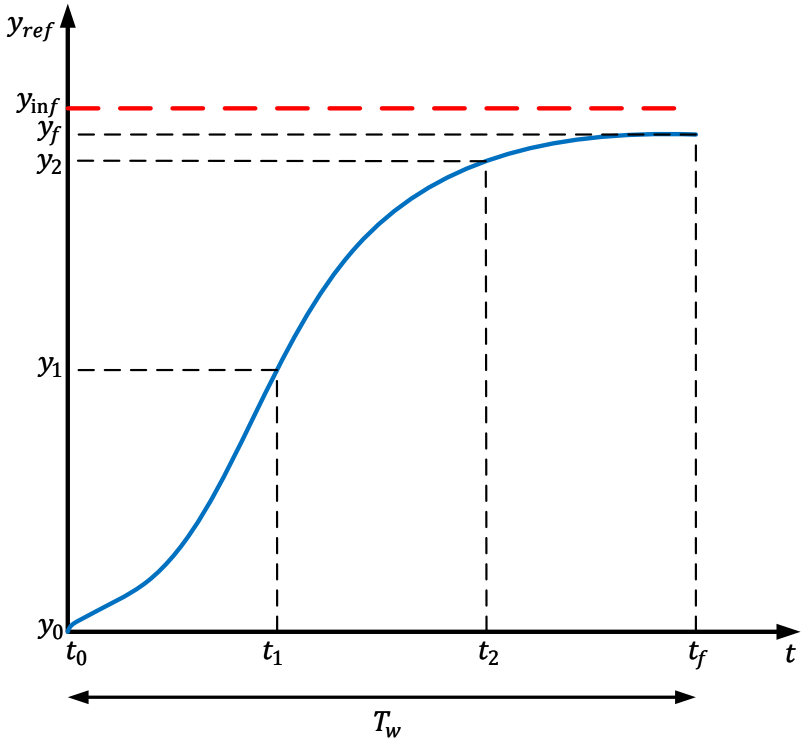

Figure 6.6: Fonction de trajectoire proposée pour une fenêtre.

La sortie du bloc de planification de la trajectoire (y_{ref}), ses dérivées première et seconde ($\dot{y_{ref}}$ et $\ddot{y_{ref}}$) doivent être continues pour garantir que le système reste plat. Il en résulte la détermination des dérivées première et seconde de chaque sortie de fenêtre du bloc de planification de la trajectoire. Il s'agit de y_1, $\dot{y}_1$, $\ddot{y}_1$ y_2, $\dot{y}_2$, $\ddot{y}_2$, y_p, $\dot{y}_p$, et $\ddot{y}_p$. La

fonction de trajectoire dans chacun de ces intervalles est un polynôme de degré 5 défini comme:

$$y = a_{5,i}t^5 + a_{4,i}t^4 + a_{3,i}t^3 + a_{2,i}t^2 + a_{1,i}t + a_{0,i} \quad i = 1, 2, 3, \tag{6.17}$$

où a_{ki} ($k = 0, 1, ..., 5$ et $i = 1, 2, 3$) sont les coefficients polynomiaux. Ces coefficients sont calculés en résolvant trois séries d'équations similaires pour les intervalles de chaque fenêtre de trajectoire, comme décrit dans (6.18)-(6.20). Il convient de mentionner que y_0, $\dot{y_0}$ et $\ddot{y_0}$ pour chaque fenêtre sont donnés par la dernière fenêtre.

$$\begin{cases} y_1 = a_{5,1}{t_1}^5 + a_{4,1}{t_1}^4 + a_{3,1}{t_1}^3 + a_{2,1}{t_1}^2 + a_{1,1}t_1 + a_{0,1} \\ y_0 = a_{5,1}{t_0}^5 + a_{4,1}{t_0}^4 + a_{3,1}{t_0}^3 + a_{2,1}{t_0}^2 + a_{1,1}t_0 + a_{0,1} \\ \dot{y_1} = 5a_{5,1}{t_1}^4 + 4a_{4,1}{t_1}^3 + 3a_{3,1}{t_1}^2 + 2a_{2,1}t_1 + a_{1,1} \\ \dot{y_0} = 5a_{5,1}{t_0}^4 + 4a_{4,1}{t_0}^3 + 3a_{3,1}{t_0}^2 + 2a_{2,1}t_0 + a_{1,1} \\ \ddot{y_1} = 20a_{5,1}{t_1}^3 + 12a_{4,1}{t_1}^2 + 6a_{3,1}t_1 + 2a_{2,1} \\ \ddot{y_0} = 20a_{5,1}{t_0}^3 + 12a_{4,1}{t_0}^2 + 6a_{3,1}t_0 + 2a_{2,1} \end{cases} \tag{6.18}$$

$$\begin{cases} y_2 = a_{5,2}{t_2}^5 + a_{4,2}{t_2}^4 + a_{3,2}{t_2}^3 + a_{2,2}{t_2}^2 + a_{1,2}t_2 + a_{0,2} \\ y_1 = a_{5,2}{t_1}^5 + a_{4,2}{t_1}^4 + a_{3,2}{t_1}^3 + a_{2,2}{t_1}^2 + a_{1,2}t_1 + a_{0,2} \\ \dot{y_2} = 5a_{5,2}{t_2}^4 + 4a_{4,2}{t_2}^3 + 3a_{3,2}{t_2}^2 + 2a_{2,2}t_2 + a_{1,2} \\ \dot{y_1} = 5a_{5,2}{t_1}^4 + 4a_{4,2}{t_1}^3 + 3a_{3,2}{t_1}^2 + 2a_{2,2}t_1 + a_{1,2} \\ \ddot{y_2} = 20a_{5,2}{t_2}^3 + 12a_{4,2}{t_2}^2 + 6a_{3,2}t_2 + 2a_{2,2} \\ \ddot{y_1} = 20a_{5,2}{t_1}^3 + 12a_{4,2}{t_1}^2 + 6a_{3,2}t_1 + 2a_{2,2} \end{cases} \tag{6.19}$$

$$\begin{cases} y_f = a_{5,3}{t_f}^5 + a_{4,3}{t_f}^4 + a_{3,3}{t_f}^3 + a_{2,3}{t_f}^2 + a_{1,3}t_f + a_{0,3} \\ y_2 = a_{5,3}{t_2}^5 + a_{4,3}{t_2}^4 + a_{3,3}{t_2}^3 + a_{2,3}{t_2}^2 + a_{1,3}t_2 + a_{0,3} \\ \dot{y_f} = 5a_{5,3}{t_f}^4 + 4a_{4,3}{t_f}^3 + 3a_{3,3}{t_f}^2 + 2a_{2,3}t_f + a_{1,3} \\ \dot{y_2} = 5a_{5,3}{t_2}^4 + 4a_{4,3}{t_2}^3 + 3a_{3,3}{t_2}^2 + 2a_{2,3}t_2 + a_{1,3} \\ \ddot{y_f} = 20a_{5,3}{t_f}^3 + 12a_{4,3}{t_f}^2 + 6a_{3,3}t_f + 2a_{2,3} \\ \ddot{y_2} = 20a_{5,3}{t_2}^3 + 12a_{4,3}{t_2}^2 + 6a_{3,3}t_2 + 2a_{2,3} \end{cases} \tag{6.20}$$

La matrice X_{opt}, telle que définie dans (6.21), représente les variables d'optimisation. Elle résulte de l'application d'un algorithme d'optimisation, tout en

respectant les contraintes décrites dans (6.22).

$$X_{opt} = [y_1, y_2, y_f, \dot{y_1}, \dot{y_2}, \dot{y_f}, \ddot{y_1}, \ddot{y_2}, \ddot{y_f}] \tag{6.21}$$

$$\begin{cases} |i_q(k)| \leq I_{q,max} \\ V_d(k)^2 + V_q(k)^2 \leq \dfrac{3}{8} V_{dc}^2 \\ \text{Less than } 20\% \text{ overshoot in tracking speed reference.} \end{cases} \tag{6.22}$$

Ici, $k = 1, 2, \ldots, \frac{T_w}{T_e}$, et T_e représente l'intervalle d'échantillonnage virtuel considéré pour les points dans chaque fenêtre. Il existe un compromis entre le temps de calcul requis pour l'algorithme d'optimisation et la précision de la satisfaction des contraintes. Diminuer la valeur de T_e augmente la charge de calcul et le temps nécessaire à l'optimisation, mais améliore la robustesse et la précision.

Une description de la fonction objective de l'algorithme d'optimisation figure dans (6.23), où K_{opt_0}, K_{opt_1} et K_{opt_2} sont les facteurs de pondération de la différence entre la sortie de la fonction de trajectoire et ses dérivées à la fin de la fenêtre et la référence de vitesse.

$$\begin{aligned} f(X_{opt}) = \sum_{k=1}^{\frac{T_w}{T_e}} (y_k - y_{inf})^2 + K_{opt_0}.(y_f - y_{inf})^2 + K_{opt_1}.(\dot{y_f} - 0)^2 \\ + K_{opt_2}.(\ddot{y_f} - 0)^2 \end{aligned} \tag{6.23}$$

La figure 6.7 présente le schéma fonctionnel décrivant le processus de planification de la trajectoire proposé. Dans ce diagramme, le bloc de génération de la fonction de trajectoire (TFG) génère $y_{\Omega,ref}$ en utilisant les coefficients polynomiaux calculés par l'algorithme d'optimisation. La sortie de ce bloc est déterminée comme suit:

$$\begin{cases} y_{\Omega,ref} = a_{5,1}t^5 + a_{4,1}t^4 + a_{3,1}t^3 + a_{2,1}t^2 + a_{1,1}t + a_{0,1} & t < t_1 \\ y_{\Omega,ref} = a_{5,2}t^5 + a_{4,2}t^4 + a_{3,2}t^3 + a_{2,2}t^2 + a_{1,2}t + a_{0,2} & t_1 \leq t \leq t_2 \\ y_{\Omega,ref} = a_{5,3}t^5 + a_{4,3}t^4 + a_{3,3}t^3 + a_{2,3}t^2 + a_{1,3}t + a_{0,3} & t_2 < t < t_f \end{cases} \tag{6.24}$$

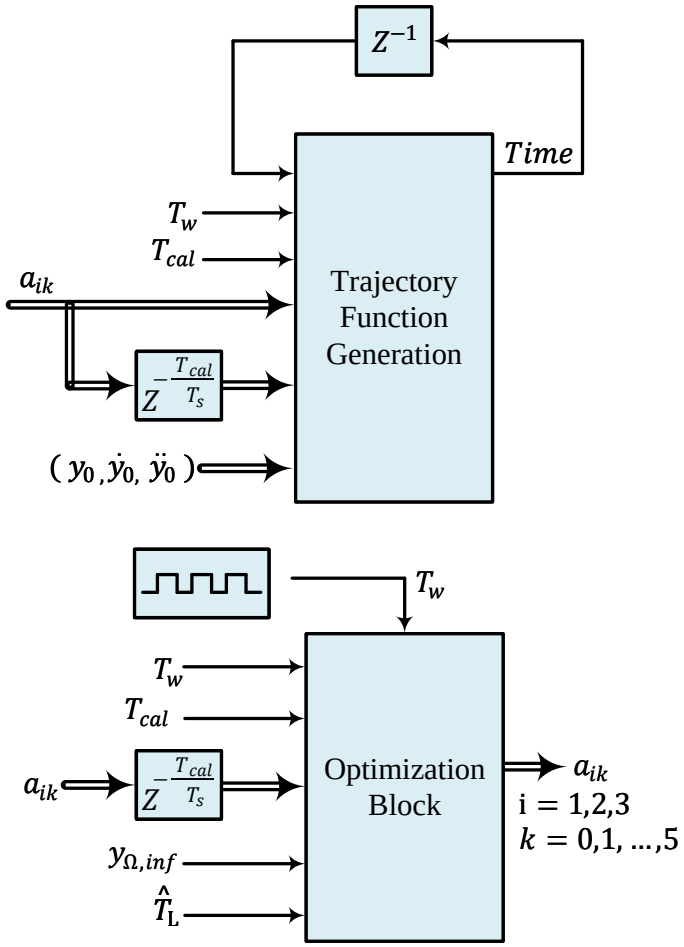

Figure 6.7: Schéma de la méthode de planification de trajectoire proposée.

L'algorithme d'optimisation est exécuté une fois dans chaque fenêtre, guidé par l'équation (6.23), tout en veillant à respecter les contraintes décrites dans (6.22). Ensuite, les coefficients polynomiaux sont calculés sur la base de la sortie de l'algorithme d'optimisation, désignée par X_{opt}. Il convient de mentionner que l'algorithme d'optimisation exige des ressources informatiques et que, par conséquent, le temps de calcul maximal est calculé à l'avance et appelé T_{cal}. Dans ce cas, la fonction de trajectoire utilise le même polynôme depuis la fenêtre précédente jusqu'à l'achèvement du

nouveau processus d'optimisation. De ce fait,

$$\begin{aligned} y_{\Omega,ref} = a_{5,3,old}\left(t+T_w\right)^5 + a_{4,3,old}\left(t+T_w\right)^4 + a_{3,3,old}\left(t+T_w\right)^3 \\ +a_{2,3,old}\left(t+T_w\right)^2 + a_{1,3,old}\left(t+T_w\right) + a_{0,3,old} \quad t < T_{cal} \end{aligned} \tag{6.25}$$

Par conséquent, il est possible d'étendre les contraintes et la fonction d'optimisation pour couvrir un horizon de prédiction de T_{cal}. Toutefois, il convient de noter que cet horizon de prédiction doit rester suffisamment petit pour garantir que les contraintes continuent d'être satisfaites compte tenu des événements transitoires et des perturbations.

De plus, il est essentiel de noter le compromis entre la quantité de ressources informatiques requises par l'algorithme d'optimisation, qui représente un défi important dans cette approche, et, par conséquent, son coût, par rapport à la précision et à l'efficacité du système de contrôle.

6.8 Résultats de simulation et résultats expérimentaux

Pour valider expérimentalement la planification de trajectoire proposée, une modification a été apportée en raison des difficultés d'implémentation de la fonction d'optimisation sur la MicroLabBox de dSPACE. Pour préserver le concept central de la planification de trajectoire tout en traitant ce problème, l'approche est passée de la prise en compte de trois fonctions polynomiales dans chaque fenêtre de trajectoire à l'utilisation d'une seule fonction polynomiale, comme décrit dans (6.26).

$$y = a_{5,tr}t^5 + a_{4,tr}t^4 + a_{3,tr}t^3 + a_{2,tr}t^2 + a_{1,tr}t + a_{0,tr} \tag{6.26}$$

où $a_{k,tr}$ $(k = 0, 1, ..., 5)$ sont les coefficients polynomiaux.

Le nombre de variables d'optimisation a été réduit de 9 à 3, à la suite de cet ajustement. En conséquence, la charge de calcul a été réduite et la méthode a été plus facile à mettre en œuvre sur le matériel.

$$X_{opt,tr} = [y_f, \dot{y_f}, \ddot{y_f}] \tag{6.27}$$

La méthode de planification de trajectoire proposée a été validée à l'aide de sim-

ulations Matlab Simulink® avec une modification d'un polynôme dans chaque fenêtre pour l'aligner sur l'étude expérimentale. Les simulations ont utilisé une fenêtre de 100 millisecondes (T_w).

Dans la simulation, nous avons testé la méthode de planification de trajectoire sous différents changements de référence de vitesse dans une condition sans charge. La référence de vitesse a commencé à 0 tr/min, a augmenté à 600 tr/min à t = 2 s, est revenue à 0 tr/min à t = 4 s, puis est passée à 100 tr/min à t = 6 s, suivie par des augmentations à 400 tr/min à t = 8 s, 300 tr/min à t = 10 s, 100 tr/min à t = 12 s, et une augmentation finale à 600 tr/min à t = 14 s.

La figure 6.8 illustre les performances du bloc de planification de trajectoire, montrant qu'il génère le signal $y_{\Omega,ref}$ qui suit de près sa valeur de référence tout en respectant la contrainte $i_{q,max} = 3$.

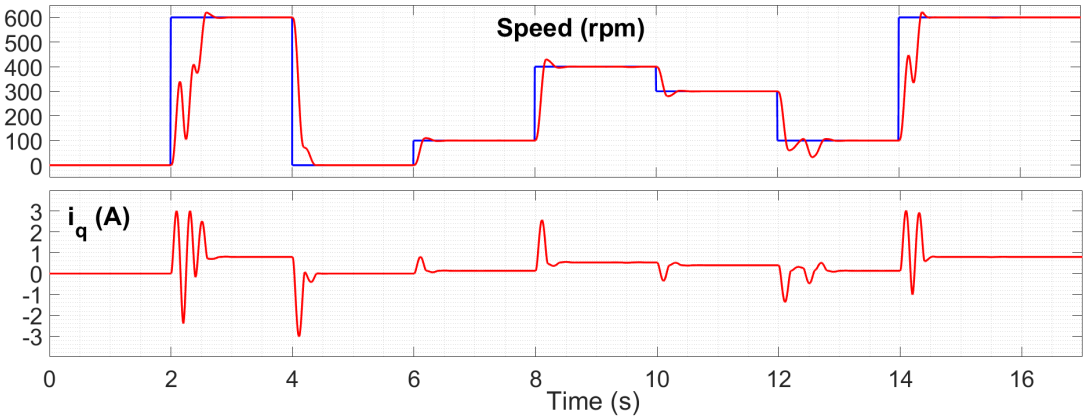

Figure 6.8: Résultats de simulation de la vitesse du moteur et du courant de l'axe q (i_q) à l'aide d'un contrôleur basé sur la planéité avec la planification de trajectoire proposée pour différentes consignes de vitesse.

Une étude a été menée pour évaluer les performances du système proposé sous des charges de couple variables. Deux cas différents ont été examinés.

Dans le premier cas, une variation de charge par paliers, équivalente à une augmentation rapide du couple de charge de 0 à 5 Nm à t = 6 s, a été appliquée au système, le couple de charge revenant à 0 à t = 12 s. Cette variation brutale de couple a conduit à une baisse de la performance du système. Le couple de charge est revenu à 0 à t = 12 s. Cette brusque variation de couple a conduit le courant i_q à dépasser sa limite ($i_{q,max}$) même en régime permanent. Pour résoudre ce problème, la sortie de la trajectoire de

vitesse s'est ajustée à une valeur inférieure à sa référence pour garantir que le courant reste dans la plage acceptable, comme le montre la figure 6.9. Cette capacité est un avantage potentiel de la méthode de contrôle proposée. Notamment, étant donné que le changement de couple est un changement par paliers, le courant dépasse brièvement sa valeur maximale pour permettre à la fenêtre de trajectoire de détecter ce changement et de s'y adapter. Pendant cette période, le régulateur de contrôle de la planéité traite la variation du couple de charge, comme dans la méthode conventionnelle.

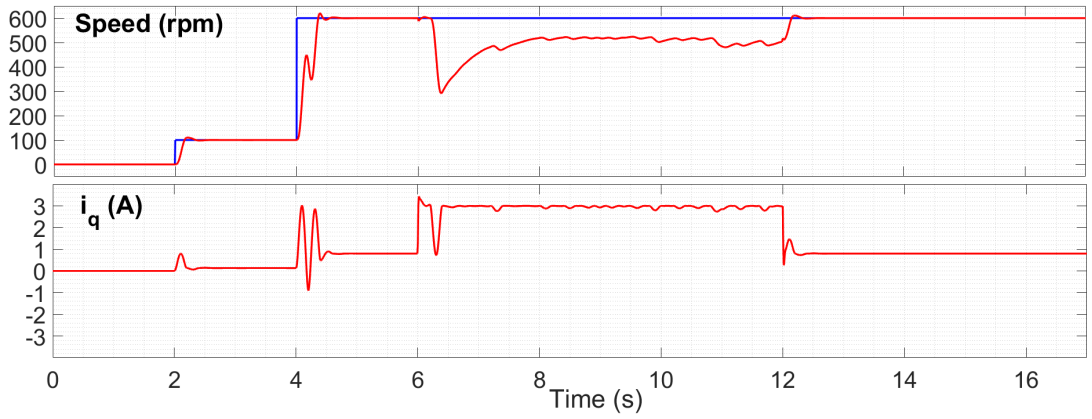

Figure 6.9: Résultats de simulation de la vitesse du moteur et du courant de l'axe q (i_q) à l'aide d'un contrôleur basé sur l'aplatissement avec la planification de trajectoire proposée en cas de changement important du couple de charge (T_L).

Le même essai de changement de charge a été appliqué au système de commande conventionnel à boucle unique basé sur la planéité. À deux reprises, le courant a dépassé sa valeur maximale, comme le montre la figure 6.10. Comme nous l'avons vu précédemment, le premier cas s'est produit lorsque la référence de vitesse du moteur a atteint sa valeur maximale. Le deuxième cas s'est produit lorsque le moteur a fonctionné sous une forte charge transitoire, qui a persisté même à l'état stable.

La méthode de planification de trajectoire proposée a été mise en œuvre sur la MicroLabBox de dSPACE, en utilisant l'algorithme d'optimisation fmincon. Pour assurer une intégration matérielle directe, une fenêtre temporelle fixe de la fonction de trajectoire (T_w) de 200 millisecondes a été sélectionnée pour les tests ultérieurs.

Dans le test initial, la référence de vitesse du moteur est passée de 0 à 600 tr/min à $t = 2$ secondes. La figure 6.11 illustre comment la planification de trajectoire proposée génère efficacement un signal de trajectoire tout en respectant la contrainte actuelle

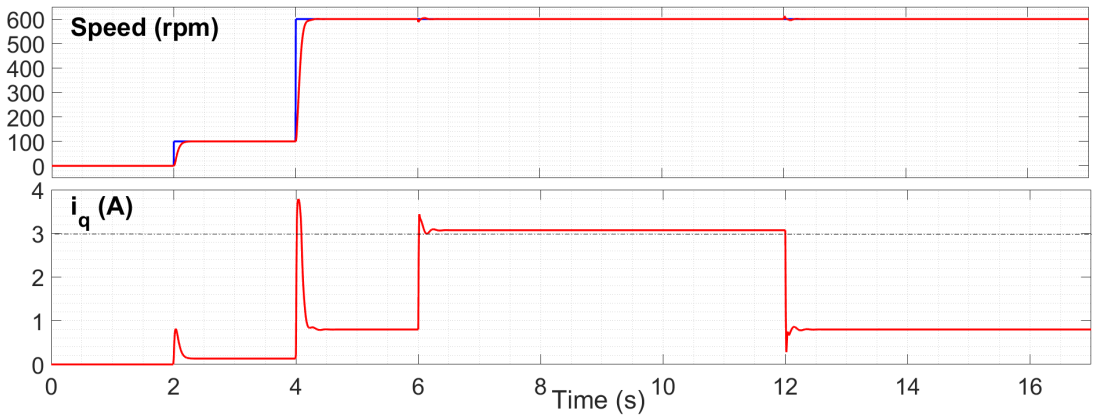

Figure 6.10: Résultats de simulation de la vitesse du moteur et du courant de l'axe q (i_q) à l'aide d'un contrôleur basé sur la planéité avec une planification de trajectoire traditionnelle en cas de changement important du couple de charge (T_L).

($i_q = 3$).

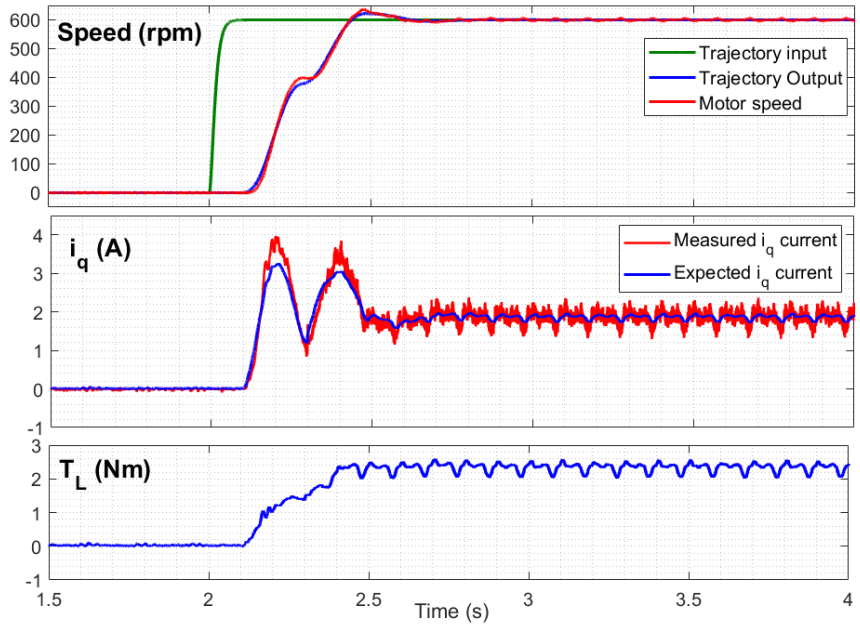

Figure 6.11: Résultats expérimentaux de la variation du couple de charge (T_L) et des réponses de la vitesse du moteur et du courant de l'axe q (i_q) en utilisant un contrôleur basé sur la planéité avec la planification de trajectoire proposée lorsque la référence de vitesse passe de 0 à 600 tr/min.

Dans un autre test, la méthode de contrôle basée sur la planéité utilisant la fonction de trajectoire proposée a été comparée aux approches de contrôle traditionnelles. Le test comprenait une transition de la vitesse du moteur de 0 à 600 tr/min, avec ω_Ω fixé à 80 rad/s. La figure 6.12 illustre la vitesse du moteur et la fonction de trajectoire générée par la méthode proposée, démontrant que le moteur atteint sa valeur finale tout en respectant les contraintes de courant. En revanche, la figure 6.13 montre que la commande traditionnelle ne dispose pas de mécanismes de protection contre le courant.

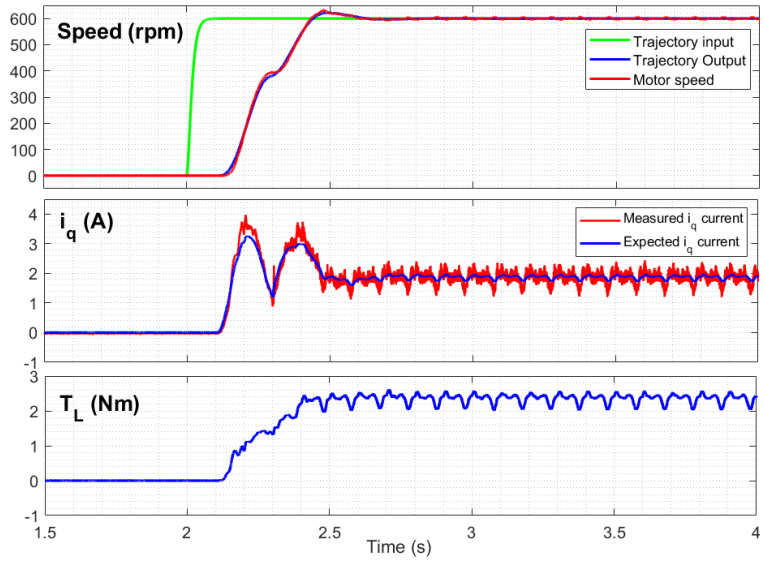

Figure 6.12: Résultats expérimentaux de la variation du couple de charge (T_L) et des réponses de la vitesse du moteur et du courant de l'axe q (i_q) en utilisant un contrôleur basé sur la planéité avec la planification de trajectoire proposée lorsque la référence de vitesse change de 0 à 600 tr/min en considérant $\omega_\Omega = 80$ rad/s.

Les études de simulation et les tests expérimentaux susmentionnés ont montré l'efficacité et les avantages de la méthode proposée. Ces recherches approfondies ont démontré le potentiel des travaux futurs et de l'application de cette méthode pour diverses applications pratiques dans le domaine.

6.9 Conclusion

Dans cette thèse, une approche de contrôle pour les moteurs électriques dans les applications de pompes à eau a été développée et examinée. Compte tenu de l'équilibre

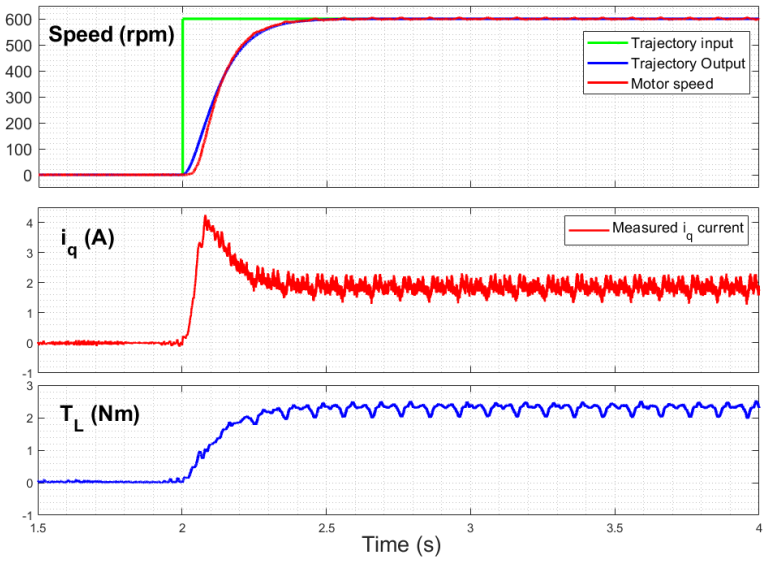

Figure 6.13: Résultats expérimentaux de la variation du couple de charge (T_L) et des réponses de la vitesse du moteur et du courant de l'axe q (i_q) en utilisant un contrôleur basé sur la planéité avec une planification de trajectoire traditionnelle lorsque la référence de vitesse change de 0 à 600 tr/min en considérant $\omega_\Omega = 80$ rad/s.

supérieur entre la rentabilité et la performance, les moteurs sans balais à PM ont été choisis comme candidats principaux pour cette application, avec un accent particulier sur les moteurs BLDC et les PMSM.

Le chapitre 2 de cette thèse présente une vue d'ensemble et une évaluation des entraînements par moteur BLDC. Il a approfondi la modélisation, les équations et les principes fondamentaux des moteurs BLDC. Les mécanismes d'entraînement des moteurs BLDC ont été examinés, avec un accent particulier sur les techniques de contrôle sans capteur, en discutant de leurs avantages et inconvénients respectifs. En outre, le chapitre a abordé les défis posés par les signaux non idéaux et asymétriques de la FEM rétroactive, ainsi que les stratégies d'atténuation de ces problèmes. Cependant, au cours de ce projet de recherche, une thèse parallèle a été consacrée aux PMSM, ce qui a fait des PMSM le point central de ce projet.

Le chapitre 3 a exploré les systèmes d'entraînement PMSM. Il fournit une description détaillée du modèle et des équations du système. Différentes stratégies de contrôle ont été discutées, y compris les méthodes de contrôle sans capteur, les techniques basées sur le capteur de position Hall et le contrôle basé sur la planéité. Le chapitre présente

également le banc d'essai utilisé à des fins expérimentales et décrit les tests nécessaires à l'identification des paramètres. La méthode FOC, en particulier, est mise en œuvre sur le banc d'essai, avec une méthodologie de réglage du contrôleur.

Au chapitre 4, la thèse aborde en détail la commande basée sur la planéité. Elle a commencé par décrire la méthode de commande conventionnelle basée sur la planéité, qui incorpore une fonction de trajectoire de transfert du second ordre. Le chapitre a mis en évidence les limites potentielles de la structure de commande en cascade basée sur la planéité, qui peut affecter la capacité du système à réguler la vitesse du moteur pendant les événements transitoires et les perturbations. D'autre part, l'utilisation d'une commande basée sur la planéité à une boucle entraîne une perte de la protection du courant. Une approche de contrôle basée sur la planéité à une boucle a été présentée pour résoudre le problème de la protection du courant, avec l'introduction d'une nouvelle méthode de planification de la trajectoire. Cette nouvelle approche utilise une fonction basée sur les fenêtres combinée à un algorithme d'optimisation en ligne pour générer des signaux de trajectoire pour chaque fenêtre, optimisant le temps de réponse du système tout en respectant les contraintes critiques telles que le courant du moteur, les tensions de commutation et le dépassement de la vitesse.

Par rapport à la méthode FOC, la commande basée sur la planéité présente une réponse dynamique supérieure aux perturbations et aux transitoires. Notamment, lorsqu'il s'agit de traiter la non-linéarité inhérente aux systèmes PMSM et les scénarios où les effets de saturation ne peuvent être négligés, la commande basée sur la planéité offre une alternative convaincante aux méthodes de commande linéaire telles que FOC.

La méthode de planification de trajectoire proposée tient également compte des contraintes de courant et de tension, ce qui améliore les performances globales de la méthode. Contrairement au contrôle conventionnel basé sur la planéité, qui peut nécessiter un temps de réponse plus lent en raison des limitations du contrôleur, cette nouvelle approche améliore la robustesse du système, le rendant plus fiable en cas de perturbations. En outre, la robustesse et les performances de la méthode peuvent être encore améliorées en introduisant des observateurs de couple et de chute de tension dans le système de contrôle, qui sont également essentiels pour la fonction de planification de la trajectoire.

Enfin, l'efficacité et la viabilité de cette méthode de contrôle innovante sont démontrées par des études de simulation et une validation expérimentale sur un banc d'essai.

Bibliography

[1] Z. Q. Zhu and D. Howe, "Electrical machines and drives for electric, hybrid, and fuel cell vehicles," *Proceedings of the IEEE*, vol. 95, no. 4, pp. 746–765, 2007.

[2] J. Shao, "An improved microcontroller-based sensorless brushless dc (bldc) motor drive for automotive applications," in *Fourtieth IAS Annual Meeting. Conference Record of the 2005 Industry Applications Conference, 2005.*, vol. 4, pp. 2512–2517 Vol. 4, 2005.

[3] J. S. Park, B.-G. Gu, J.-H. Choi, and I.-S. Jung, "Development of bldc motor drive for automotive water pump systems," *Journal of International Council on Electrical Engineering*, vol. 1, no. 4, pp. 395–399, 2011.

[4] G.-C. Lee and T.-U. Jung, "Design comparisons of bldc motors for electric water pump," in *2012 IEEE Vehicle Power and Propulsion Conference*, pp. 48–50, 2012.

[5] A. Arias, E. Ibarra, E. Trancho, R. Griñó, I. Kortabarria, and J. Caum, "Comprehensive high speed automotive sm-pmsm torque control stability analysis including novel control approach," *International Journal of Electrical Power & Energy Systems*, vol. 109, pp. 423–433, 07 2019.

[6] A. Abdelrahman, M. Hamouda, and M. Youssef, "A cost effective bldc drive for the water pump application: Analysis, design, and experimentation," in *2016 IEEE Transportation Electrification Conference and Expo, Asia-Pacific (ITEC Asia-Pacific)*, pp. 240–245, 2016.

[7] A. S. Abdelrahman and M. Z. Youssef, "A cost effective magnetic/electronic design for the water pump application drive: Analysis, design, and experimentation," in *2017 IEEE Applied Power Electronics Conference and Exposition (APEC)*, pp. 2329–2335, 2017.

[8] K. Algarny, A. S. Abdelrahman, and M. Z. Youssef, "Performance comparison between induction and permanent magnet synchronous electric machines in water pump application," in *2018 2nd European Conference on Electrical Engineering and Computer Science (EECS)*, pp. 165–169, 2018.

[9] M. Ehsani, K. V. Singh, H. O. Bansal, and R. T. Mehrjardi, "State of the art and trends in electric and hybrid electric vehicles," *Proceedings of the IEEE*, vol. 109, no. 6, pp. 967–984, 2021.

[10] R. M. Crowder, *Electric drives and electromechanical systems: Applications and Control*. Butterworth-Heinemann, 2020.

[11] "Permanent magnet synchronous motor construction." `https://innovationdiscoveries.space/permanent-magnet-synchronous-motor\-construction/`. Accessed on November 4, 2023.

[12] M. Z. Youssef, "Design and performance of a cost-effective bldc drive for water pump application," *IEEE Transactions on Industrial Electronics*, vol. 62, no. 5, pp. 3277–3284, 2015.

[13] A.-M. Nicorici, L. Szabo, and C. Martis, "Design and analysis of a permanent magnet synchronous machine used in automotive applications," in *2019 IEEE International Conference on Environment and Electrical Engineering and 2019 IEEE Industrial and Commercial Power Systems Europe (EEEIC / I&CPS Europe)*, pp. 1–6, 2019.

[14] A. Mattern, D. Flieller, J. B. Kammerer, F. Depasse, L. Roch, and J. Peuch, "Study of the use of an axial flux permanent magnet motor for electric coolant pumps," in *2022 International Conference on Electrical Machines (ICEM)*, pp. 1054–1060, 2022.

[15] G. xu Zhou, H. jun Wang, D.-H. Lee, and J.-W. Ahn, "Study on efficiency optimizing of pmsm for pump applications," in *2007 7th Internatonal Conference on Power Electronics*, pp. 912–915, 2007.

[16] S. Bolognani, R. Oboe, and M. Zigliotto, "Sensorless full-digital pmsm drive with ekf estimation of speed and rotor position," *IEEE Transactions on Industrial Electronics*, vol. 46, no. 1, pp. 184–191, 1999.

[17] O. C. Kivanc and S. B. Ozturk, "Sensorless pmsm drive based on stator feedforward voltage estimation improved with mras multiparameter estimation," *IEEE/ASME Transactions on Mechatronics*, vol. 23, no. 3, pp. 1326–1337, 2018.

[18] H. Kim, J. Son, and J. Lee, "A high-speed sliding-mode observer for the sensorless speed control of a pmsm," *IEEE Transactions on Industrial Electronics*, vol. 58, no. 9, pp. 4069–4077, 2011.

[19] L. V. Gera, G. Botto, L. D. Suarez Cabrera, and M. Chiaberge, "Advanced sensorless control system for pmsm-based automotive application," in *2014 16th European Conference on Power Electronics and Applications*, pp. 1–8, 2014.

[20] W. Xu, Y. Jiang, C. Mu, and F. Blaabjerg, "Improved nonlinear flux observer-based second-order soifo for pmsm sensorless control," *IEEE Transactions on Power Electronics*, vol. 34, no. 1, pp. 565–579, 2019.

[21] C. liang Xia, *PERMANENT MAGNET BRUSHLESS DC MOTOR DRIVES AND CONTROLS*. Wiley, 1st ed., April 2012.

[22] J. S. Park, J.-H. Choi, B.-G. Gu, and I.-S. Jung, "Bldc drive control of electric water pump for automotive application," in *2010 IEEE Vehicle Power and Propulsion Conference*, pp. 1–5, 2010.

[23] M. Shafiei, S. Niapour, G. Garjan, M. R. Feyzi, S. Danyali, and M. Bahrami Kouhshahi, "Review of permanent-magnet brushless dc motor basic drives based on analysis and simulation study," 07 2015.

[24] N. Samoylenko, Q. Han, and J. Jatskevich, "Dynamic performance of brushless dc motors with unbalanced hall sensors," *IEEE Transactions on Energy Conversion*, vol. 23, no. 3, pp. 752–763, 2008.

[25] C. Xia, Y. Xiao, W. Chen, and T. Shi, "Torque ripple reduction in brushless dc drives based on reference current optimization using integral variable structure control," *IEEE Transactions on Industrial Electronics*, vol. 61, no. 2, pp. 738–752, 2014.

[26] Q. Lu, X. Zhu, L. Quan, Y. Zuo, and S. Du, "Rotor position estimation scheme with harmonic ripple attenuation for sensorless controlled permanent magnet synchronous motors," *IET Electric Power Applications*, vol. 12, 05 2018.

[27] Y. Li, H. Wu, X. Xu, X. Sun, and J. Zhao, "Rotor position estimation approaches for sensorless control of permanent magnet traction motor in electric vehicles: A review," *World Electric Vehicle Journal*, vol. 12, p. 9, 01 2021.

[28] W.-J. Lee and S.-K. Sul, "A new starting method of bldc motors without position sensor," *IEEE Transactions on Industry Applications*, vol. 42, no. 6, pp. 1532–1538, 2006.

[29] C.-H. Chen and M.-Y. Cheng, "A new cost effective sensorless commutation method for brushless dc motors without phase shift circuit and neutral voltage," *IEEE Transactions on Power Electronics*, vol. 22, no. 2, pp. 644–653, 2007.

[30] K.-Y. Cheng, Y.-T. Lin, C.-H. Tso, and Y.-Y. Tzou, "Design of a sensorless commutation ic for bldc motors," in *2002 IEEE 33rd Annual IEEE Power Electronics Specialists Conference. Proceedings (Cat. No.02CH37289)*, vol. 1, pp. 295–300 vol.1, 2002.

[31] G.-J. Su and J. McKeever, "Low-cost sensorless control of brushless dc motors with improved speed range," *IEEE Transactions on Power Electronics*, vol. 19, no. 2, pp. 296–302, 2004.

[32] Y.-S. Lai and Y.-K. Lin, "Novel back-emf detection technique of brushless dc motor drives for wide range control without using current and position sensors," *IEEE Transactions on Power Electronics*, vol. 23, no. 2, pp. 934–940, 2008.

[33] Y. Wu, Z. Deng, X. Wang, X. Ling, and X. Cao, "Position sensorless control based on coordinate transformation for brushless dc motor drives," *IEEE Transactions on Power Electronics*, vol. 25, no. 9, pp. 2365–2371, 2010.

[34] D. Mohanraj, R. Aruldavid, R. Verma, K. Sathiyasekar, A. B. Barnawi, B. Chokkalingam, and L. Mihet-Popa, "A review of bldc motor: State of art, advanced control techniques, and applications," *IEEE Access*, vol. 10, pp. 54833–54869, 2022.

[35] J.-C. Gamazo-Real, E. Vázquez-Sánchez, and J. Gomez-Gil, "Position and speed control of brushless dc motors using sensorless techniques and application trends," *Sensors*, vol. 10, 07 2010.

[36] J. Shen and K. Tseng, "Analyses and compensation of rotor position detection error in sensorless pm brushless dc motor drives," *IEEE Transactions on Energy Conversion*, vol. 18, no. 1, pp. 87–93, 2003.

[37] A. Halvaei Niasar, A. Vahedi, and H. Moghbelli, "A novel position sensorless control of a four-switch, brushless dc motor drive without phase shifter," *IEEE Transactions on Power Electronics*, vol. 23, no. 6, pp. 3079–3087, 2008.

[38] R. W. Hejny and R. D. Lorenz, "Evaluating the practical low-speed limits for back-emf tracking-based sensorless speed control using drive stiffness as a key metric," *IEEE Transactions on Industry Applications*, vol. 47, no. 3, pp. 1337–1343, 2011.

[39] J. Shao, D. Nolan, and T. Hopkins, "A novel direct back emf detection for sensorless brushless dc (bldc) motor drives," in *APEC. Seventeenth Annual IEEE Applied Power Electronics Conference and Exposition (Cat. No.02CH37335)*, vol. 1, pp. 33–37 vol.1, 2002.

[40] J. Shao, D. Nolan, M. Teissier, and D. Swanson, "A novel microcontroller-based sensorless brushless dc (bldc) motor drive for automotive fuel pumps," in *Conference Record of the 2002 IEEE Industry Applications Conference. 37th IAS Annual Meeting (Cat. No.02CH37344)*, vol. 4, pp. 2386–2392 vol.4, 2002.

[41] K. Iizuka, H. Uzuhashi, M. Kano, T. Endo, and K. Mohri, "Microcomputer control for sensorless brushless motor," *IEEE Transactions on Industry Applications*, vol. IA-21, no. 3, pp. 595–601, 1985.

[42] C.-K. Lai, W.-T. Lin, and G.-Y. Chen, "An improved position sensorless drive system design of brushless dc motor by terminal voltage difference," in *2019 8th International Conference on Innovation, Communication and Engineering (ICICE)*, pp. 66–69, 2019.

[43] S. Ogasawara and H. Akagi, "An approach to position sensorless drive for brushless dc motors," in *Conference Record of the 1990 IEEE Industry Applications Society Annual Meeting*, pp. 443–447 vol.1, 1990.

[44] M. Abbes and S. Chebbi, "Sensorless trapezoidal control of a brushless dc motor based on a three-phase pll," in *2020 4th International Conference on Advanced Systems and Emergent Technologies (IC_ASET)*, pp. 377–382, 2020.

[45] G. Jang and M. Kim, "Optimal commutation of a bldc motor by utilizing the symmetric terminal voltage," *IEEE Transactions on Magnetics*, vol. 42, no. 10, pp. 3473–3475, 2006.

[46] C.-T. Lin, C.-W. Hung, and C.-W. Liu, "Position sensorless control for four-switch three-phase brushless dc motor drives," *IEEE Transactions on Power Electronics*, vol. 23, no. 1, pp. 438–444, 2008.

[47] L. Yang, Z. Q. Zhu, H. Bin, Z. Zhang, and L. Gong, "Safety operation area of zero-crossing detection-based sensorless high-speed bldc motor drives," *IEEE Transactions on Industry Applications*, vol. 56, no. 6, pp. 6456–6466, 2020.

[48] B. Asaei and A. Rostami, "A novel starting method for bldc motors without the position sensors," Nov 2008.

[49] X. Song, B. Han, and K. Wang, "Sensorless drive of high-speed bldc motors based on virtual third-harmonic back emf and high-precision compensation," *IEEE Transactions on Power Electronics*, vol. 34, no. 9, pp. 8787–8796, 2019.

[50] T. Li and J. Zhou, "High-stability position-sensorless control method for brushless dc motors at low speed," *IEEE Transactions on Power Electronics*, vol. 34, no. 5, pp. 4895–4903, 2019.

[51] G. Liu, C. Cui, K. Wang, B. Han, and S. Zheng, "Sensorless control for high-speed brushless dc motor based on the line-to-line back emf," *IEEE Transactions on Power Electronics*, vol. 31, no. 7, pp. 4669–4683, 2016.

[52] D. Arifiyan and S. Riyadi, "Hardware implementation of sensorless bldc motor control to expand speed range," in *2019 International Seminar on Application for Technology of Information and Communication (iSemantic)*, pp. 476–481, 2019.

[53] P. Damodharan and K. Vasudevan, "Sensorless brushless dc motor drive based on the zero-crossing detection of back electromotive force (emf) from the line voltage difference," *IEEE Transactions on Energy Conversion*, vol. 25, no. 3, pp. 661–668, 2010.

[54] S. Tsotoulidis and A. Safacas, "A sensorless commutation technique of a brushless dc motor drive system using two terminal voltages in respect to a virtual neutral potential," in *2012 XXth International Conference on Electrical Machines*, pp. 830–836, 2012.

[55] C. Cui, G. Liu, K. Wang, and X. Song, "Sensorless drive for high-speed brushless dc motor based on the virtual neutral voltage," *IEEE Transactions on Power Electronics*, vol. 30, no. 6, pp. 3275–3285, 2015.

[56] D.-k. Kim, K.-w. Lee, and B.-i. Kwon, "Commutation torque ripple reduction in a position sensorless brushless dc motor drive," *IEEE Transactions on Power Electronics*, vol. 21, no. 6, pp. 1762–1768, 2006.

[57] R. Kumar and B. Singh, "Position sensorless bldc motor drive for single stage pv based water pumping," in *2020 IEEE 5th International Conference on Computing Communication and Automation (ICCCA)*, pp. 634–639, 2020.

[58] R. Kumar and B. Singh, "Solar pv powered-sensorless bldc motor driven water pump," *IET Renewable Power Generation*, vol. 13, 11 2018.

[59] T.-W. Chun, Q.-V. Tran, H.-H. Lee, and H.-G. Kim, "Sensorless control of bldc motor drive for an automotive fuel pump using a hysteresis comparator," *IEEE Transactions on Power Electronics*, vol. 29, no. 3, pp. 1382–1391, 2014.

[60] M. Lee and K. Kong, "Fourier-series-based phase delay compensation of brushless dc motor systems," *IEEE Transactions on Power Electronics*, vol. 33, no. 1, pp. 525–534, 2018.

[61] J. Moreira, "Indirect sensing for rotor flux position of permanent magnet ac motors operating in a wide speed range," in *Proceedings of 1994 IEEE Industry Applications Society Annual Meeting*, vol. 1, pp. 401–407 vol.1, 1994.

[62] J. Shen, Z. Zhu, and D. Howe, "Sensorless flux-weakening control of permanent-magnet brushless machines using third harmonic back emf," *IEEE Transactions on Industry Applications*, vol. 40, no. 6, pp. 1629–1636, 2004.

[63] J. Shen and S. Iwasaki, "Sensorless control of ultrahigh-speed pm brushless motor using pll and third harmonic back emf," *IEEE Transactions on Industrial Electronics*, vol. 53, no. 2, pp. 421–428, 2006.

[64] C. Gu, X. Wang, X. Shi, and Z. Deng, "A pll-based novel commutation correction strategy for a high-speed brushless dc motor sensorless drive system," *IEEE Transactions on Industrial Electronics*, vol. 65, no. 5, pp. 3752–3762, 2018.

[65] J. Shen, Z. Zhu, and D. Howe, "Sensorless flux-weakening control of permanent magnet brushless machines using third-harmonic back-emf," in *IEEE International Electric Machines and Drives Conference, 2003. IEMDC'03.*, vol. 2, pp. 1229–1235 vol.2, 2003.

[66] X. Song, B. Han, S. Zheng, and J. Fang, "High-precision sensorless drive for high-speed bldc motors based on the virtual third harmonic back-emf," *IEEE Transactions on Power Electronics*, vol. 33, no. 2, pp. 1528–1540, 2018.

[67] D. A. Papathanasopoulos and E. D. Mitronikas, "Evaluation of the virtual third harmonic back-emf in identifying misaligned hall-effect position sensors in brushless dc motor drives," in *2019 IEEE 12th International Symposium on Diagnostics for Electrical Machines, Power Electronics and Drives (SDEMPED)*, pp. 181–187, 2019.

[68] J. M. Liu and Z. Q. Zhu, "Improved sensorless control of permanent-magnet synchronous machine based on third-harmonic back emf," *IEEE Transactions on Industry Applications*, vol. 50, no. 3, pp. 1861–1870, 2014.

[69] T. Jahns, R. Becerra, and M. Ehsani, "Integrated current regulation for a brushless ecm drive," *IEEE Transactions on Power Electronics*, vol. 6, no. 1, pp. 118–126, 1991.

[70] R. Becerra, T. Jahns, and M. Ehsani, "Four-quadrant sensorless brushless ecm drive," in *[Proceedings] APEC '91: Sixth Annual Applied Power Electronics Conference and Exhibition*, pp. 202–209, 1991.

[71] A. Attar, B. Jamal, and K. Grari, "Control of brushless dc motors using sensorless back-emf integration method," *Materials Today: Proceedings*, vol. 45, 03 2021.

[72] H. Jin, G. Liu, and S. Zheng, "Commutation error closed-loop correction method for sensorless bldc motor using hardware-based floating phase back-emf integration," *IEEE Transactions on Industrial Informatics*, vol. 18, no. 6, pp. 3978–3986, 2022.

[73] D. S. Sawant, Y. S. Rao, and R. R. Sawant, "Sensorless control of a bldc motor using back-emf detection method," in *2023 International Conference for Advancement in Technology (ICONAT)*, pp. 1–5, 2023.

[74] Y. Li, X. Song, X. Zhou, Z. Huang, and S. Zheng, "A sensorless commutation error correction method for high-speed bldc motors based on phase current integration," *IEEE Transactions on Industrial Informatics*, vol. 16, no. 1, pp. 328–338, 2020.

[75] H. Zhang, H. Wu, H. Jin, and H. Li, "High-dynamic and low-cost sensorless control method of high-speed brushless dc motor," *IEEE Transactions on Industrial Informatics*, vol. 19, no. 4, pp. 5576–5584, 2023.

[76] J. Joy and S. Ushakumari, "Performance comparison of a sensorless pmbldc motor drive system with conventional and fuzzy logic controllers," *Procedia Technology*, vol. 25, pp. 643–651, 12 2016.

[77] M. Ebadpour and J. T. Oujghaz, "Improved electric differential system for independent speed control of brushless dc motors driven electric vehicles," in *2021 7th International Conference on Control, Instrumentation and Automation (ICCIA)*, pp. 1–5, 2021.

[78] S. Ogasawara and H. Akagi, "An approach to position sensorless drive for brushless dc motors," *IEEE Transactions on Industry Applications*, vol. 27, no. 5, pp. 928–933, 1991.

[79] N. Kasa and H. Watanabe, "A mechanical sensorless control system for salient-pole brushless dc motor with autocalibration of estimated position angles," *IEEE Transactions on Industrial Electronics*, vol. 47, no. 2, pp. 389–395, 2000.

[80] U. Soni and R. Tripathi, "Sensorless control of high-speed bldc motor using equal area criterion based precise commutation scheme with fuzzy based phase delay compensation," *International Transactions on Electrical Energy Systems*, 07 2021.

[81] F. Huang and D. Tien, "A neural network approach to position sensorless control of brushless dc motors," in *Proceedings of the 1996 IEEE IECON. 22nd International Conference on Industrial Electronics, Control, and Instrumentation*, vol. 2, pp. 1167–1170 vol.2, 1996.

[82] A. Del Pizzo, C. Olivieri, F. Ciancetta, M. Tursini, and N. Rotondale, "Development issues of a neural observer-based and fault-adaptive sensorless strategy for a multiphase bldc motor," in *2014 International Symposium on Power Electronics, Electrical Drives, Automation and Motion*, pp. 1166–1173, 2014.

[83] G. R, S. Seetharaman, and S. Sivaraju, "Anfis based multi-sector space vector pwm scheme for sensorless bldc motor drive," *Microprocessors and Microsystems*, vol. 76, p. 103091, 03 2020.

[84] X. Zhou, X. Chen, C. Peng, and Y. Zhou, "High performance nonsalient sensorless bldc motor control strategy from standstill to high speed," *IEEE Transactions on Industrial Informatics*, vol. 14, no. 10, pp. 4365–4375, 2018.

[85] H. Yanzhao, S. Zheng, and F. Jiancheng, "Start-up current adaptive control for sensorless high-speed brushless dc motors based on inverse system method and internal mode controller," *Chinese Journal of Aeronautics*, vol. 30, 12 2016.

[86] R. Wu and G. Slemon, "A permanent magnet motor drive without a shaft sensor," *IEEE Transactions on Industry Applications*, vol. 27, no. 5, pp. 1005–1011, 1991.

[87] N. Ertugrul and P. Acarnley, "A new algorithm for sensorless operation of permanent magnet motors," *IEEE Transactions on Industry Applications*, vol. 30, no. 1, pp. 126–133, 1994.

[88] J. Gao and Y. Hu, "Direct self-control for bldc motor drives based on three-dimensional coordinate system," *IEEE Transactions on Industrial Electronics*, vol. 57, no. 8, pp. 2836–2844, 2010.

[89] W. Chen, Z. Liu, Y. Cao, X. Li, T. Shi, and C. Xia, "A position sensorless control strategy for the bldcm based on a flux-linkage function," *IEEE Transactions on Industrial Electronics*, vol. 66, no. 4, pp. 2570–2579, 2019.

[90] T.-H. Kim and M. Ehsani, "Sensorless control of the bldc motors from near-zero to high speeds," *IEEE Transactions on Power Electronics*, vol. 19, no. 6, pp. 1635–1645, 2004.

[91] R. R. Chladny and C. R. Koch, "Flatness-based tracking of an electromechanical variable valve timing actuator with disturbance observer feedforward compensation," *IEEE Transactions on Control Systems Technology*, vol. 16, no. 4, pp. 652–663, 2008.

[92] S. K. Chung, C. R. Koch, and A. F. Lynch, "Flatness-based feedback control of an automotive solenoid valve," *IEEE Transactions on Control Systems Technology*, vol. 15, no. 2, pp. 394–401, 2007.

[93] M. Tawadros, J. Rizk, and M. Nagrial, "Estimation of commutation instances using back emf mapping for sensorless control of brushless permanent magnet motors," *IET Electric Power Applications*, vol. 7, no. 4, p. 270–277, 2013.

[94] J.-W. Park, S.-H. Hwang, and J.-M. Kim, "Sensorless control of brushless dc motors with torque constant estimation for home appliances," *IEEE Transactions on Industry Applications*, vol. 48, no. 2, pp. 677–684, 2012.

[95] Z. Qiao, T. Shi, Y. Wang, Y. Yan, C. Xia, and X. He, "New sliding-mode observer for position sensorless control of permanent-magnet synchronous motor," *IEEE Transactions on Industrial Electronics*, vol. 60, no. 2, pp. 710–719, 2013.

[96] Y. Zhao, W. Qiao, and L. Wu, "An adaptive quasi-sliding-mode rotor position observer-based sensorless control for interior permanent magnet synchronous machines," *IEEE Transactions on Power Electronics*, vol. 28, no. 12, pp. 5618–5629, 2013.

[97] F. Alonge, F. D'Ippolito, and A. Sferlazza, "Sensorless control of induction-motor drive based on robust kalman filter and adaptive speed estimation," *IEEE Transactions on Industrial Electronics*, vol. 61, no. 3, pp. 1444–1453, 2014.

[98] I. Bahri, L. Idkhajine, E. Monmasson, and M. El Amine Benkhelifa, "Hardware/software codesign guidelines for system on chip fpga-based sensorless ac drive applications," *IEEE Transactions on Industrial Informatics*, vol. 9, no. 4, pp. 2165–2176, 2013.

[99] P. Mercorelli, "A Hysteresis Hybrid Extended Kalman Filter as an Observer for Sensorless Valve Control in Camless Internal Combustion Engines," *IEEE Transactions on Industry Applications*, vol. 48, no. 6, pp. 1940–1949, 2012.

[100] P. Mercorelli, "A two-stage augmented extended kalman filter as an observer for sensorless valve control in camless internal combustion engines," *IEEE Transactions on Industrial Electronics*, vol. 59, no. 11, pp. 4236–4247, 2012.

[101] M. Kashif, S. Murshid, and B. Singh, "Solar pv array fed self-sensing control of pmsm drive with robust adaptive hybrid sogi based flux observer for water pumping," *IEEE Transactions on Industrial Electronics*, vol. 68, no. 8, pp. 6962–6972, 2021.

[102] R. Sreejith and B. Singh, "Sensorless predictive current control of pmsm ev drive using dsogi-fll based sliding mode observer," *IEEE Transactions on Industrial Electronics*, vol. 68, no. 7, pp. 5537–5547, 2021.

[103] Z. Li, S. Zhou, Y. Xiao, and L. Wang, "Sensorless vector control of permanent magnet synchronous linear motor based on self-adaptive super-twisting sliding mode controller," *IEEE Access*, vol. 7, pp. 44998–45011, 2019.

[104] S. R and B. Singh, "Sensorless predictive control of spmsm-driven light ev drive using modified speed adaptive super twisting sliding mode observer with maf-pll," *IEEE Journal of Emerging and Selected Topics in Industrial Electronics*, vol. 2, no. 1, pp. 42–52, 2021.

[105] B. Saha and B. Singh, "Smo based position sensorless bldc motor drive employing canonical switching cell converter for light electric vehicle," in *2021 IEEE International Power and Renewable Energy Conference (IPRECON)*, pp. 1–6, 2021.

[106] D. Liang, J. Li, R. Qu, and W. Kong, "Adaptive second-order sliding-mode observer for pmsm sensorless control considering vsi nonlinearity," *IEEE Transactions on Power Electronics*, vol. 33, no. 10, pp. 8994–9004, 2018.

[107] Z. Chen, A. A. Dawara, X. Zhang, H. Zhang, C. Liu, and G. Luo, "Adaptive sliding mode observer-based sensorless control for spmsm employing a dual-pll," *IEEE Transactions on Transportation Electrification*, vol. 8, no. 1, pp. 1267–1277, 2022.

[108] D. S. Nair, G. Jagadanand, and S. George, "Sensorless direct torque controlled bldc motor drive with kalman filter algorithm," in *IECON 2017 - 43rd Annual Conference of the IEEE Industrial Electronics Society*, pp. 2160–2165, 2017.

[109] A. Ejlali and J. Soleimani, "Sensorless vector control of 3-phase bldc motor using a novel extended kalman," in *2012 International Conference on Advances in Power Conversion and Energy Technologies (APCET)*, pp. 1–6, 2012.

[110] L. Y, B. N.P.G, N. Ramesh, and K. Sujatha, "Sensorless vector control of bldc using extended kalman filter," *Signal & Image Processing : An International Journal*, vol. 6, pp. 103–114, 06 2015.

[111] H. Lv, G. Wei, Z. Ding, and X. Ding, "Sensorless control for the brushless dc motor: an unscented kalman filter algorithm," *Systems Science & Control Engineering*, vol. 3, pp. 8–13, 12 2014.

[112] H. Arasaratnam, K. P. Chandra, M. Devendra, S. Ch, K. Mary, and D.-W. Gu, "Derivative-free square-root cubature kalman filter for non-linear brushless dc motors," *IET Electric Power Applications*, vol. 10, 04 2016.

[113] P. Ubare, D. Ingole, and D. Sonawane, "Nonlinear model predictive control of bldc motor with state estimation," *IFAC-PapersOnLine*, vol. 54, pp. 107–112, 01 2021.

[114] T.-S. Kim, B.-G. Park, D.-M. Lee, J.-S. Ryu, and D.-S. Hyun, "A new approach to sensorless control method for brushless dc motors," *International Journal of Control, Automation and Systems*, vol. 6(4), 08 2008.

[115] W. Li, J. Fang, H. Li, and J. Tang, "Position sensorless control without phase shifter for high-speed bldc motors with low inductance and nonideal back emf," *IEEE Transactions on Power Electronics*, vol. 31, no. 2, pp. 1354–1366, 2016.

[116] P. Kshirsagar and R. Krishnan, "High-efficiency current excitation strategy for variable-speed non-sinusoidal back-emf pmsm machines," *IEEE Transactions on Industry Applications*, vol. 48, no. 6, pp. 1875–1889, 2012.

[117] H. Li, S. Zheng, and H. Ren, "Self-correction of commutation point for high-speed sensorless bldc motor with low inductance and nonideal back emf," *IEEE Transactions on Power Electronics*, vol. 32, no. 1, pp. 642–651, 2017.

[118] J. Fang, W. Li, and H. Li, "Self-compensation of the commutation angle based on dc-link current for high-speed brushless dc motors with low inductance," *IEEE Transactions on Power Electronics*, vol. 29, no. 1, pp. 428–439, 2014.

[119] H. Zhang and H. Li, "Fast commutation error compensation method of sensorless control for mscmg bldc motor with nonideal back emf," *IEEE Transactions on Power Electronics*, vol. 36, no. 7, pp. 8044–8054, 2021.

[120] L. Yang, Z. Q. Zhu, H. Bin, Z. Zhang, and L. Gong, "Virtual third harmonic back emf-based sensorless drive for high-speed bldc motors considering machine parameter asymmetries," *IEEE Transactions on Industry Applications*, vol. 57, no. 1, pp. 306–315, 2021.

[121] J. S. Park, K.-D. Lee, S. G. Lee, and W.-H. Kim, "Unbalanced ZCP Compensation Method for Position Sensorless BLDC Motor," *IEEE Transactions on Power Electronics*, vol. 34, no. 4, pp. 3020–3024, 2019.

[122] X. Chen and G. Liu, "Sensorless optimal commutation steady speed control method for a nonideal back-emf bldc motor drive system including buck converter," *IEEE Transactions on Industrial Electronics*, vol. 67, no. 7, pp. 6147–6157, 2020.

[123] G. Liu, X. Chen, X. Zhou, and S. Zheng, "Sensorless commutation deviation correction of brushless dc motor with three-phase asymmetric back-emf," *IEEE Transactions on Industrial Electronics*, vol. 67, no. 7, pp. 6158–6167, 2020.

[124] H. Zhang, G. Liu, X. Zhou, and S. Zheng, "High-precision sensorless optimal commutation deviation correction strategy of bldc motor with asymmetric back emf," *IEEE Transactions on Industrial Informatics*, vol. 17, no. 8, pp. 5250–5259, 2021.

[125] A.-C. Lee, C.-J. Fan, and G.-H. Chen, "Current integral method for fine commutation tuning of sensorless brushless dc motor," *IEEE Transactions on Power Electronics*, vol. 32, no. 12, pp. 9249–9266, 2017.

[126] M. Akrami, E. Jamshidpour, and V. Frick, "Application of hall position sensor in control and position estimation of pmsm - a review," in *2023 IEEE International Conference on Environment and Electrical Engineering and 2023 IEEE Industrial and Commercial Power Systems Europe (EEEIC / I&CPS Europe)*, pp. 1–6, 2023.

[127] R. Krishnan, *Permanent magnet synchronous and brushless DC motor drives*. CRC Press, 2017.

[128] J. Cuenot, *Architectures d'alimentation et de commande des actionneurs haute-vitesse connectés aux réseaux avioniques à tension variable*. PhD thesis, Université de Lorraine, 2017.

[129] M. Abassi, A. Khlaief, O. Saadaoui, A. Chaari, and M. Boussak, "Performance analysis of foc and dtc for pmsm drives using svpwm technique," in *2015 16th International Conference on Sciences and Techniques of Automatic Control and Computer Engineering (STA)*, pp. 228–233, 2015.

[130] S. Sakunthala, R. Kiranmayi, and P. N. Mandadi, "A review on speed control of permanent magnet synchronous motor drive using different control techniques," in *2018 International Conference on Power, Energy, Control and Transmission Systems (ICPECTS)*, pp. 97–102, 2018.

[131] B. Bossoufi, M. Karim, A. Lagrioui, and S. Ionitţă, "Performance analysis of direct torque control (dtc) for synchronous machine permanent magnet (pmsm)," in *2010 IEEE 16th International Symposium for Design and Technology in Electronic Packaging (SIITME)*, pp. 237–242, 2010.

[132] Q. Liu and K. Hameyer, "Torque ripple minimization for direct torque control of pmsm with modified fcsmpc," *IEEE Transactions on Industry Applications*, vol. 52, no. 6, pp. 4855–4864, 2016.

[133] N. Ozturk and E. Çelik, "Speed control of permanent magnet synchronous motors using fuzzy controller based on genetic algorithms," *International Journal of Electrical Power & Energy Systems*, vol. 43, pp. 889–898, 12 2012.

[134] R. Du, Y. Wu, W. Chen, and Q. Chen, "Adaptive fuzzy speed control for permanent magnet synchronous motor servo systems," *Electric Power Components and Systems*, vol. 42, 06 2014.

[135] A. Haldar and R. Khatua, "Speed control of permanent magnet synchronous machine using genetic and fuzzy algorithm," in *2022 International Conference on Innovative Trends in Information Technology (ICITIIT)*, pp. 1–6, 2022.

[136] Y. Yi, D. Vilathgamuwa, and M. Rahman, "Implementation of an artificial-neural-network-based real-time adaptive controller for an interior permanent-magnet motor drive," *Industry Applications, IEEE Transactions on*, vol. 39, pp. 96–104, 02 2003.

[137] B. K. Bose, "Neural network applications in power electronics and motor drives—an introduction and perspective," *IEEE Transactions on Industrial Electronics*, vol. 54, no. 1, pp. 14–33, 2007.

[138] M. Akrami, E. Jamshidpour, S. Pierfederici, and V. Frick, "Flatness-based trajectory planning/replanning for a permanent magnet synchronous machine control," in *2023 IEEE Transportation Electrification Conference & Expo (ITEC)*, pp. 1–5, 2023.

[139] S. Singh and A. N. Tiwari, "Various techniques of sensorless speed control of pmsm: A review," in *2017 Second International Conference on Electrical, Computer and Communication Technologies (ICECCT)*, pp. 1–6, 2017.

[140] D. Xu, B. Wang, G. Zhang, G. Wang, and Y. Yu, "A review of sensorless control methods for ac motor drives," *CES Transactions on Electrical Machines and Systems*, vol. 2, pp. 104–115, 03 2018.

[141] G. Wang, M. Valla, and J. Solsona, "Position sensorless permanent magnet synchronous machine drives—a review," *IEEE Transactions on Industrial Electronics*, vol. 67, no. 7, pp. 5830–5842, 2020.

[142] S.-I. Kim, J.-H. Im, E.-Y. Song, and R.-Y. Kim, "A new rotor position estimation method of ipmsm using all-pass filter on high-frequency rotating voltage signal injection," *IEEE Transactions on Industrial Electronics*, vol. 63, no. 10, pp. 6499–6509, 2016.

[143] R. Hosooka, S. Shinnaka, and N. Nakamura, "New sensorless vector control of pmsm by discrete-time voltage injection of pwm carrier frequency — sine- and cosine-form amplitudes extraction method," in *IECON 2016 - 42nd Annual Conference of the IEEE Industrial Electronics Society*, pp. 2862–2867, 2016.

[144] S. Medjmadj, D. Diallo, M. Mostefai, C. Delpha, and A. Arias, "Pmsm drive position estimation: Contribution to the high-frequency injection voltage selection issue," *IEEE Transactions on Energy Conversion*, vol. 30, no. 1, pp. 349–358, 2015.

[145] D. Raca, P. Garcia, D. Reigosa, F. Briz, and R. D. Lorenz, "Carrier signal selection for sensorless control of pm synchronous machines at zero and very low speeds," in *2008 IEEE Industry Applications Society Annual Meeting*, pp. 1–8, 2008.

[146] M. Corley and R. Lorenz, "Rotor position and velocity estimation for a salient-pole permanent magnet synchronous machine at standstill and high speeds," *IEEE Transactions on Industry Applications*, vol. 34, no. 4, pp. 784–789, 1998.

[147] P. L. Xu and Z. Q. Zhu, "Novel square-wave signal injection method using zero-sequence voltage for sensorless control of pmsm drives," *IEEE Transactions on Industrial Electronics*, vol. 63, no. 12, pp. 7444–7454, 2016.

[148] X. Zhang, H. Li, S. Yang, and M. Ma, "Improved initial rotor position estimation for pmsm drives based on hf pulsating voltage signal injection," *IEEE Transactions on Industrial Electronics*, vol. 65, no. 6, pp. 4702–4713, 2018.

[149] J.-H. Jang, J.-I. Ha, M. Ohto, K. Ide, and S.-K. Sul, "Analysis of permanent-magnet machine for sensorless control based on high-frequency signal injection," *IEEE Transactions on Industry Applications*, vol. 40, no. 6, pp. 1595–1604, 2004.

[150] N.-C. Park and S.-H. Kim, "Simple sensorless algorithm for interior permanent magnet synchronous motors based on high-frequency voltage injection method," *Electric Power Applications, IET*, vol. 8, pp. 68–75, 02 2014.

[151] R. Ni, D. Xu, F. Blaabjerg, K. Lu, G. Wang, and G. Zhang, "Square-wave voltage injection algorithm for pmsm position sensorless control with high robustness to voltage errors," *IEEE Transactions on Power Electronics*, vol. 32, no. 7, pp. 5425–5437, 2017.

[152] F. Gabriel, F. De Belie, X. Neyt, and P. Lataire, "High-frequency issues using rotating voltage injections intended for position self-sensing," *IEEE Transactions on Industrial Electronics*, vol. 60, no. 12, pp. 5447–5457, 2013.

[153] P. L. Xu and Z. Q. Zhu, "Novel carrier signal injection method using zero-sequence voltage for sensorless control of pmsm drives," *IEEE Transactions on Industrial Electronics*, vol. 63, no. 4, pp. 2053–2061, 2016.

[154] D. Raca, P. Garcia, D. Reigosa, F. Briz, and R. Lorenz, "A comparative analysis of pulsating vs. rotating vector carrier signal injection-based sensorless control," in *2008 Twenty-Third Annual IEEE Applied Power Electronics Conference and Exposition*, pp. 879–885, 2008.

[155] M. Schrodl and M. Lambeck, "Statistic properties of the inform method for highly dynamic sensorless control of pm motors down to standstill," in *IECON'03. 29th Annual Conference of the IEEE Industrial Electronics Society (IEEE Cat. No.03CH37468)*, vol. 2, pp. 1479–1486 Vol.2, 2003.

[156] E. Robeischl and M. Schroedl, "Optimized inform measurement sequence for sensorless pm synchronous motor drives with respect to minimum current distortion," *IEEE Transactions on Industry Applications*, vol. 40, no. 2, pp. 591–598, 2004.

[157] D. Q. Guan, M. X. Bui, D. Xiao, and M. F. Rahman, "Performance comparison of two fpe sensorless control methods on a direct torque controlled interior permanent magnet synchronous motor drive," in *2016 19th International Conference on Electrical Machines and Systems (ICEMS)*, pp. 1–6, 2016.

[158] G. Wang, J. Kuang, N. Zhao, G. Zhang, and D. Xu, "Rotor position estimation of pmsm in low-speed region and standstill using zero-voltage vector injection," *IEEE Transactions on Power Electronics*, vol. 33, no. 9, pp. 7948–7958, 2018.

[159] D. Q. Guan, M. X. Bui, D. Xiao, and M. F. Rahman, "Evaluation of an fpga current derivative measurement system for the fundamental pwm excitation sensorless method for ipmsm," in *2016 IEEE 2nd Annual Southern Power Electronics Conference (SPEC)*, pp. 1–6, 2016.

[160] G. Zhang, G. Wang, and D. Xu, "Saliency-based position sensorless control methods for pmsm drives - a review," *Chinese Journal of Electrical Engineering*, vol. 3, no. 2, pp. 14–23, 2017.

[161] M. H. Bierhoff, "A general pll-type algorithm for speed sensorless control of electrical drives," *IEEE Transactions on Industrial Electronics*, vol. 64, no. 12, pp. 9253–9260, 2017.

[162] Y. Lee and S.-K. Sul, "Model-based sensorless control of ipmsm enhancing robustness based on the estimation of speed error," in *2016 IEEE Symposium on Sensorless Control for Electrical Drives (SLED)*, pp. 1–8, 2016.

[163] S. Chenxing and W. Chen, "Sensorless vector control of three-phase permanent magnet synchronous motor based on model reference adaptive system," in *2018 IEEE 4th International Conference on Control Science and Systems Engineering (ICCSSE)*, pp. 178–182, 2018.

[164] Hoque and Rahman, "Speed and position sensorless permanent magnet synchronous motor drives," in *1994 Proceedings of Canadian Conference on Electrical and Computer Engineering*, pp. 689–692 vol.2, 1994.

[165] A. Kulkarni and M. Ehsani, "A novel position sensor elimination technique for the interior permanent-magnet synchronous motor drive," *IEEE Transactions on Industry Applications*, vol. 28, no. 1, pp. 144–150, 1992.

[166] M. Naidu and B. Bose, "Rotor position estimation scheme of a permanent magnet synchronous machine for high performance variable speed drive," in *Conference Record of the 1992 IEEE Industry Applications Society Annual Meeting*, pp. 48–53 vol.1, 1992.

[167] S. Bolognani, L. Tubiana, and M. Zigliotto, "Extended kalman filter tuning in sensorless pmsm drives," *IEEE Transactions on Industry Applications*, vol. 39, no. 6, pp. 1741–1747, 2003.

[168] Z. Zhang and J. Feng, "Sensorless control of salient pmsm with ekf of speed and rotor position," in *2008 International Conference on Electrical Machines and Systems*, pp. 1625–1628, 2008.

[169] C. Li and M. Elbuluk, "A sliding mode observer for sensorless control of permanent magnet synchronous motors," in *Conference Record of the 2001 IEEE Industry Applications Conference. 36th IAS Annual Meeting (Cat. No.01CH37248)*, vol. 2, pp. 1273–1278 vol.2, 2001.

[170] Y. Zhang, Y. Jin, R. Cao, and K. Wang, "An adaptive sliding mode observer for sensorless vector control of surface-mounted pmsm," *2016 19th International Conference on Electrical Machines and Systems (ICEMS)*, pp. 1–5, 2016.

[171] H. Kojabadi and M. Ghribi, "Mras-based adaptive speed estimator in pmsm drives," in *9th IEEE International Workshop on Advanced Motion Control, 2006.*, pp. 569–572, 2006.

[172] J. Kang, X. Zeng, Y. Wu, and D. Hu, "Study of position sensorless control of pmsm based on mras," in *2009 IEEE International Conference on Industrial Technology*, pp. 1–4, 2009.

[173] C. J. V. Filho, D. Xiao, R. P. Vieira, and A. Emadi, "Observers for high-speed sensorless pmsm drives: Design methods, tuning challenges and future trends," *IEEE Access*, vol. 9, pp. 56397–56415, 2021.

[174] K.-W. Lee and J.-I. Ha, "Evaluation of back-emf estimators for sensorless control of permanent magnet synchronous motors," *Journal of Power Electronics*, vol. 12, 07 2012.

[175] Y. Lee, Y.-C. Kwon, and S.-K. Sul, "Comparison of rotor position estimation performance in fundamental-model-based sensorless control of pmsm," in *2015 IEEE Energy Conversion Congress and Exposition (ECCE)*, pp. 5624–5633, 2015.

[176] J. Hu and B. Wu, "New integration algorithms for estimating motor flux over a wide speed range," *IEEE Transactions on Power Electronics*, vol. 13, no. 5, pp. 969–977, 1998.

[177] J. Solsona, M. Valla, and C. Muravchik, "Nonlinear control of a permanent magnet synchronous motor with disturbance torque estimation," *IEEE Transactions on Energy Conversion*, vol. 15, no. 2, pp. 163–168, 2000.

[178] G. Zhu, A. Kaddouri, L. Dessaint, and O. Akhrif, "A nonlinear state observer for the sensorless control of a permanent-magnet ac machine," *IEEE Transactions on Industrial Electronics*, vol. 48, no. 6, pp. 1098–1108, 2001.

[179] Y. Yao, F. Peng, and Y. Huang, "Position and capacitor voltage sensorless control of high-speed surface-mounted pmsm drive with output filter," in *2018 IEEE Energy Conversion Congress and Exposition (ECCE)*, pp. 2374–2381, 2018.

[180] A. M. EL-Refaie, "Fractional-slot concentrated-windings synchronous permanent magnet machines: Opportunities and challenges," *IEEE Transactions on Industrial Electronics*, vol. 57, no. 1, pp. 107–121, 2010.

[181] N. Muley, A. Saxena, and P. Chaudhary, "Comparative Evaluation of Methods for Continuous Rotor Position Estimation using Low Resolution Hall Sensors," in *2021 National Power Electronics Conference (NPEC)*, pp. 1–6, 2021.

[182] S. Jung, B. Lee, and K. Nam, "Pmsm control based on edge field measurements by hall sensors," in *2010 Twenty-Fifth Annual IEEE Applied Power Electronics Conference and Exposition (APEC)*, pp. 2002–2006, 2010.

[183] S. Zaim, J. P. Martin, B. Nahid-Mobarakeh, and F. Meibody-Tabar, "High performance low cost control of a permanent magnet wheel motor using a hall effect position sensor," in *2011 IEEE Vehicle Power and Propulsion Conference*, pp. 1–6, 2011.

[184] Z. Yu, M. Qin, X. Chen, L. Meng, Q. Huang, and C. Fu, "Computationally Efficient Coordinate Transformation for Field-Oriented Control Using Phase Shift of Linear Hall-Effect Sensor Signals," *IEEE Transactions on Industrial Electronics*, vol. 67, no. 5, pp. 3442–3451, 2020.

[185] J. Wang, Q. Jiang, and D. Xiong, "Review of rotor position and speed estimation method of pmsm with hall sensor," in *2021 IEEE 16th Conference on Industrial Electronics and Applications (ICIEA)*, pp. 1832–1837, 2021.

[186] Q. An, C. Chen, M. Zhao, T. Ma, and K. Ge, "Research on Rotor Position Estimation of PMSM Based on Hall Position Sensor," in *2021 IEEE 16th Conference on Industrial Electronics and Applications (ICIEA)*, pp. 2088–2094, 2021.

[187] B.-H. Bae, S.-K. Sul, J.-H. Kwon, and J.-S. Byeon, "Implementation of sensorless vector control for super-high-speed PMSM of turbo-compressor," *IEEE Transactions on Industry Applications*, vol. 39, no. 3, pp. 811–818, 2003.

[188] A. Yoo, S.-K. Sul, D.-C. Lee, and C.-S. Jun, "Novel speed and rotor position estimation strategy using a dual observer for low-resolution position sensors," *IEEE Transactions on Power Electronics*, vol. 24, no. 12, pp. 2897–2906, 2009.

[189] Y. Zhao, W. Huang, J. Yang, F. Bu, and S. Liu, "A PMSM rotor position estimation with low-cost Hall-effect sensors using improved PLL," in *2016 IEEE Transportation Electrification Conference and Expo, Asia-Pacific (ITEC Asia-Pacific)*, pp. 804–807, 2016.

[190] X. Zheng, L. Tiecai, L. Yongping, and G. Bingyi, "Position-measuring error analysis and solution of hall sensor in pseudo-sensorless pmsm driving system," in *IECON'03. 29th Annual Conference of the IEEE Industrial Electronics Society (IEEE Cat. No.03CH37468)*, vol. 2, pp. 1337–1342 Vol.2, 2003.

[191] Q. Ni, M. Yang, S. A. Odhano, M. Tang, P. Zanchetta, X. Liu, and D. Xu, "A new position and speed estimation scheme for position control of pmsm drives using low-resolution position sensors," *IEEE Transactions on Industry Applications*, vol. 55, no. 4, pp. 3747–3758, 2019.

[192] A.-Y. Ko, D.-Y. Kim, I.-K. Won, Y.-R. Kim, and C.-Y. Won, "Interpolation error compensation method for look-up table based ipmsm drive," in *2014 IEEE Conference and Expo Transportation Electrification Asia-Pacific (ITEC Asia-Pacific)*, pp. 1–5, 2014.

[193] F. Giulii Capponi, G. De Donato, L. Del Ferraro, O. Honorati, M. Harke, and R. Lorenz, "AC brushless drive with low-resolution Hall-effect sensors for surface-mounted PM Machines," *IEEE Transactions on Industry Applications*, vol. 42, no. 2, pp. 526–535, 2006.

[194] L. Kreindler, I. Iacob, G. Casaru, A. Sarca, R. Olteanu, and D. Matianu, "PMSM drive using digital hall position sensors for light EV applications," in *2015 9th International Symposium on Advanced Topics in Electrical Engineering (ATEE)*, pp. 199–204, 2015.

[195] H. Kim, M. Harke, and R. Lorenz, "Sensorless control of interior permanent magnet machine drives with zero-phase-lag position estimation," in *Conference Record of the 2002 IEEE Industry Applications Conference. 37th IAS Annual Meeting (Cat. No.02CH37344)*, vol. 3, pp. 1661–1667 vol.3, 2002.

[196] R. Brown, S. Schneider, and M. Mulligan, "Analysis of algorithms for velocity estimation from discrete position versus time data," *IEEE Transactions on Industrial Electronics*, vol. 39, no. 1, pp. 11–19, 1992.

[197] X. Zhang and W. Zhang, "An improved rotor position estimation in PMSM with low-resolution hall-effect sensors," in *2014 17th International Conference on Electrical Machines and Systems (ICEMS)*, pp. 2722–2727, 2014.

[198] H. Dan, S. Zeng, Y. Liu, Y. Sun, and M. Su, "An Improved Position and Speed Estimation Scheme for Permanent Magnet Synchronous Motor with Low-cost Hall Sensors," in *2022 IEEE 5th International Electrical and Energy Conference (CIEEC)*, pp. 1831–1836, 2022.

[199] L. Kovudhikulrungsri and T. Koseki, "Precise speed estimation from a low-resolution encoder by dual-sampling-rate observer," *IEEE/ASME Transactions on Mechatronics*, vol. 11, no. 6, pp. 661–670, 2006.

[200] G. Scelba, G. De Donato, G. Scarcella, F. Giulii Capponi, and F. Bonaccorso, "Fault-tolerant rotor position and velocity estimation using binary hall-effect sensors for low-cost vector control drives," *IEEE Transactions on Industry Applications*, vol. 50, no. 5, pp. 3403–3413, 2014.

[201] G. Liu, B. Chen, and X. Song, "High-Precision Speed and Position Estimation Based on Hall Vector Frequency Tracking for PMSM With Bipolar Hall-Effect Sensors," *IEEE Sensors Journal*, vol. 19, no. 6, pp. 2347–2355, 2019.

[202] G. De Donato, G. Scelba, M. Pulvirenti, G. Scarcella, and F. Giulii Capponi, "Low-cost, high-resolution, fault-robust position and speed estimation for pmsm drives operating in safety-critical systems," *IEEE Transactions on Power Electronics*, vol. 34, no. 1, pp. 550–564, 2019.

[203] T. Shi, Z. Wang, and C. Xia, "Speed measurement error suppression for pmsm control system using self-adaption kalman observer," *IEEE Transactions on Industrial Electronics*, vol. 62, no. 5, pp. 2753–2763, 2015.

[204] T. Batzel and K. Lee, "Commutation torque ripple minimization for permanent magnet synchronous machines with Hall effect position feedback," *IEEE Transactions on Energy Conversion*, vol. 13, no. 3, pp. 257–262, 1998.

[205] Y. Liu, J. Zhao, M. Xia, and H. Luo, "Model reference adaptive control-based speed control of brushless dc motors with low-resolution hall-effect sensors," *IEEE Transactions on Power Electronics*, vol. 29, no. 3, pp. 1514–1522, 2014.

[206] M. C. Harke, G. D. Donato, F. G. Capponi, T. Tesch, and R. Lorenz, "Implementation Issues and Performance Evaluation of Surface-Mounted PM Machine Drives with Hall-Effect Position Sensors and a Vector-Tracking Observer," in *Conference Record of the 2006 IEEE Industry Applications Conference Forty-First IAS Annual Meeting*, vol. 4, pp. 1621–1628, 2006.

[207] M. C. Harke, G. De Donato, F. Giulii Capponi, T. R. Tesch, and R. D. Lorenz, "Implementation issues and performance evaluation of sinusoidal, surface-mounted pm machine drives with hall-effect position sensors and a vector-tracking observer," *IEEE Transactions on Industry Applications*, vol. 44, no. 1, pp. 161–173, 2008.

[208] G. Scelba, G. De Donato, M. Pulvirenti, F. Giulii Capponi, and G. Scarcella, "Hall-Effect Sensor Fault Detection, Identification, and Compensation in Brushless DC Drives," *IEEE Transactions on Industry Applications*, vol. 52, no. 2, pp. 1542–1554, 2016.

[209] M. Comanescu, "Speed, rotor position and load torque estimation of the pmsm using an extended dynamic model and cascaded sliding mode observers," in *2016 International Symposium on Power Electronics, Electrical Drives, Automation and Motion (SPEEDAM)*, pp. 98–103, 2016.

[210] A. Yoo, S.-K. Sul, D. C. Lee, and C. Seung, "Novel speed and rotor position estimation strategy using a dual observer for low resolution position sensors," in *2008 IEEE Power Electronics Specialists Conference*, pp. 647–653, 2008.

[211] T. Ahmed-Ali, E. Cherrier, and M. M'Saad, "Cascade high gain observers for nonlinear systems with delayed output measurement," in *Proceedings of the 48h IEEE Conference on Decision and Control (CDC) held jointly with 2009 28th Chinese Control Conference*, pp. 8226–8231, 2009.

[212] Q. Ni, M. Yang, X. Dong, X. Liu, and D. Xu, "State Estimation Error Suppression for PMSM Speed Observer Based on Hall Position Sensor," *Diangong Jishu Xuebao/Transactions of China Electrotechnical Society*, vol. 32, pp. 189–198, 09 2017.

[213] S. Chaithongsuk, B. Nahid-Mobarakeh, J.-P. Caron, N. Takorabet, and F. Meibody-Tabar, "Optimal design of permanent magnet motors to improve field-weakening performances in variable speed drives," *IEEE Transactions on Industrial Electronics*, vol. 59, no. 6, pp. 2484–2494, 2012.

[214] E. Delaleau and A. Stankovic, "Flatness-based hierarchical control of the pm synchronous motor," in *Proceedings of the 2004 American Control Conference*, vol. 1, pp. 65–70 vol.1, 2004.

[215] A. Battiston, E.-H. Miliani, J.-P. Martin, B. Nahid-Mobarakeh, S. Pierfederici, and F. Meibody-Tabar, "A control strategy for electric traction systems using a pm-motor fed by a bidirectional z-source inverter," *IEEE Transactions on Vehicular Technology*, vol. 63, no. 9, pp. 4178–4191, 2014.

[216] A. Fezzani, S. Drid, A. Makouf, and L. Chrifi Alaoui, "Speed sensorless flatness-based control of pmsm using a second order sliding mode observer," in *2013 Eighth International Conference and Exhibition on Ecological Vehicles and Renewable Energies (EVER)*, pp. 1–9, 2013.

[217] M. Fliess, J. Levine, P. Martin, and P. Rouchon, "A lie-backlund approach to equivalence and flatness of nonlinear systems," *IEEE Transactions on Automatic Control*, vol. 44, no. 5, pp. 922–937, 1999.

[218] V. Hagenmeyer, A. Ranftl, and E. Delaleau, *Flatness-based control of the induction drive minimising energy dissipation*, pp. 149–160. 10 2003.

[219] V. Hagenmeyer and E. Delaleau, "Continuous-time non-linear flatness-based predictive control: An exact feedforward linearisation setting with an induction drive example," *International Journal of Control - INT J CONTR*, vol. 81, pp. 1645–1663, 10 2008.

[220] P. Thounthong, S. Sikkabut, N. Poonnoy, P. Mungporn, B. Yodwong, P. Kumam, N. Bizon, B. Nahid-Mobarakeh, and S. Pierfederici, "Differential flatness based speed/torque control with state-observers of permanent magnet synchronous motor drives," in *2016 IEEE Industry Applications Society Annual Meeting*, pp. 1–8, 2016.

[221] M. Fliess, J. Lévine, P. Martin, and P. Rouchon, "Flatness and defect of non-linear systems: introductory theory and examples," *International Journal of Control*, vol. 61, pp. 13–27, 06 1995.

[222] A. Battiston, J.-P. Martin, E.-H. Miliani, B. Nahid-Mobarakeh, S. Pierfederici, and F. Meibody-Tabar, "Control of a pmsm fed by a quasi z-source inverter based on flatness properties and saturation schemes," in *2013 15th European Conference on Power Electronics and Applications (EPE)*, 2013.

[223] M. Akrami, E. Jamshidpour, S. Pierfederici, and V. Frick, "Comparison of flatness-based control and field-oriented control for pmsms in automotive water pump application," in *2023 IEEE International Conference on Environment and Electrical Engineering and 2023 IEEE Industrial and Commercial Power Systems Europe (EEEIC / I&CPS Europe)*, pp. 1–6, 2023.

[224] A. Payman, S. Pierfederici, and F. Meibody-Tabar, "Energy management in a fuel cell/supercapacitor multisource/multiload electrical hybrid system," *IEEE Transactions on Power Electronics*, vol. 24, no. 12, pp. 2681–2691, 2009.

[225] J. Dannehl and F. W. Fuchs, "Flatness-based control of an induction machine fed via voltage source inverter - concept, control design and performance analysis," in *IECON 2006 - 32nd Annual Conference on IEEE Industrial Electronics*, pp. 5125–5130, 2006.

[226] D. Faustner, W. Kemmetmüller, and A. Kugi, "Flatness-based torque control of saturated surface-mounted permanent magnet synchronous machines," *IEEE Transactions on Control Systems Technology*, vol. 24, no. 4, pp. 1201–1213, 2016.

[227] J. Cuenot, S. Zaim, S. Pierfederici, E. Monmasson, B. Nahid-Mobarakeh, R. Meuret, and F. Meibody-Tabar, "Flatness based control of a high-speed saturable permanent magnet synchronous machine," in *2016 IEEE Transportation Electrification Conference and Expo (ITEC)*, pp. 1–6, 2016.

[228] D. Faustner, W. Kemmetmüller, and A. Kugi, "Field weakening in flatness-based torque control of saturated surface-mounted permanent magnet synchronous machines," in *2015 IEEE Conference on Control Applications (CCA)*, pp. 858–863, 2015.

[229] S. Sriprang, B. Nahid-Mobarakeh, S. Pierfederici, N. Takorabet, N. Bizon, P. Kumam, P. Mungporn, and P. Thounthong, "Robust flatness-based control with state observer-based parameter estimation for pmsm drive," in *2018 IEEE International Conference on Electrical Systems for Aircraft, Railway, Ship Propulsion and Road Vehicles & International Transportation Electrification Conference (ESARS-ITEC)*, pp. 1–6, 2018.

[230] S. Sriprang, B. Nahid-Mobarakeh, S. Pierfederici, N. Takorabet, N. Bizon, P. Kumam, P. Mungporn, and P. Thounthong, "Robust flatness control with extended luenberger observer for pmsm drive," in *2018 IEEE Transportation Electrification Conference and Expo, Asia-Pacific (ITEC Asia-Pacific)*, pp. 1–8, 2018.

[231] A. Chamseddine, Y. Zhang, C. A. Rabbath, C. Join, and D. Theilliol, "Flatness-based trajectory planning/replanning for a quadrotor unmanned aerial vehicle," *IEEE Transactions on Aerospace and Electronic Systems*, vol. 48, no. 4, pp. 2832–2848, 2012.

[232] P. Thounthong, S. Sikkabut, N. Poonnoy, P. Mungporn, B. Yodwong, P. Kumam, N. Bizon, B. Nahid-Mobarakeh, and S. Pierfederici, "Nonlinear differential flatness-based speed/torque control with state-observers of permanent magnet synchronous motor drives," *IEEE Transactions on Industry Applications*, 2018.

[233] P. T. Thanh and N. D. That, "Nonlinear flatness-based controller for permanent magnet-excited synchronous motor," in *Proceedings of the 31st International Symposium on Automation and Robotics in Construction and Mining (ISARC)* (Q. Ha, X. Shen, and A. Akbarnezhad, eds.), (Sydney, Australia), pp. 120–125, International Association for Automation and Robotics in Construction (IAARC), July 2014.

[234] S. Sriprang, B. Nahid-Mobarakeh, P. Mungporn, N. Takorabet, S. Pierfederici, N. Bizon, P. Kumam, and P. Thounthong, "Modeling of one-loop flatness-based control with state observer-based parameter estimation for pmsm drive," in *2018 2nd European Conference on Electrical Engineering and Computer Science (EECS)*, pp. 105–111, 2018.

[235] J. Belikov, A. Kaldmäe, and Y. Levron, "An extended flatness-based controller for permanent magnet synchronous machines incorporating an event-based mechanism," in *2019 27th Mediterranean Conference on Control and Automation (MED)*, pp. 416–421, 2019.

[236] H. Renaudineau, J.-P. Martin, B. Nahid-Mobarakeh, and S. Pierfederici, "Dc–dc converters dynamic modeling with state observer-based parameter estimation," *IEEE Transactions on Power Electronics*, vol. 30, no. 6, pp. 3356–3363, 2015.

Appendix A

Closed-loop model of system with FOC method

As has previously been discussed, the open-loop state equations of the system can be expressed as follows:

$$\begin{cases} V_d = R_s i_d + L_s \dfrac{di_d}{dt} - p\Omega L_s i_q \\ V_q = R_s i_q + L_s \dfrac{di_q}{dt} + p\Omega L_s i_d + p\psi_f \Omega \\ J\dfrac{d\Omega}{dt} = p\psi_f i_q - f\Omega - T_L, \end{cases} \tag{A.1}$$

For the closed-loop model of the system, each PI controller adds one state variable, which are defined in (A.2) and illustrated in Figure A.1.

$$\begin{cases} \dot{x_{id}} = k_{ic}(i_{d,ref} - i_d) \\ \dot{x_{iq}} = k_{ic}(i_{q,ref} - i_q) \\ \dot{x_{\Omega}} = k_{i\Omega}(\Omega_{ref} - \Omega), \end{cases} \tag{A.2}$$

Considering the cascaded structure of the control system, $i_{q,ref}$ is calculated as follows:

$$i_{q,ref} = k_{p\Omega}(\Omega_{ref} - \Omega) + x_{\Omega} \tag{A.3}$$

Assuming the equality of the inverter's output and input, and the incorporation of

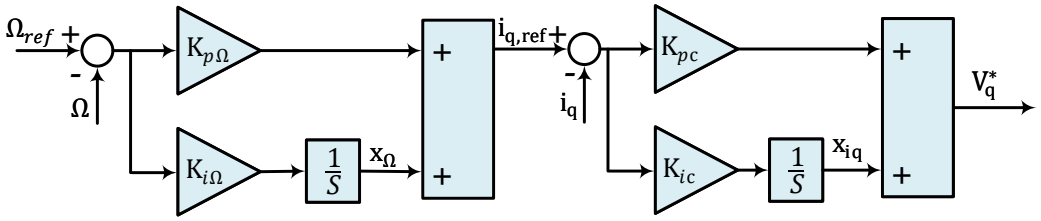

(a)

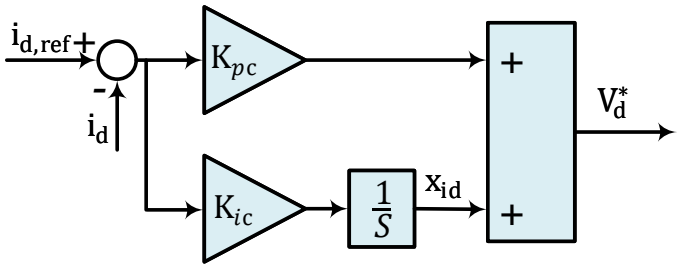

(b)

Figure A.1: (a) Structure of the cascaded speed and q-axis current controller. (b) Structure of d-axis current controller

the feed-forward decoupling term within the current-control loop, the expressions for the switching voltages can be derived as presented in (A.4) and (A.5).

$$\begin{cases} V_d^* = k_{pc}(i_{d,ref} - i_d) + x_{id} \\ V_d = V_d^* - p\Omega L_s' i_q \end{cases} \tag{A.4}$$

$$\begin{cases} V_q^* = k_{p\Omega}(i_{q,ref} - i_q) + x_{iq} \\ V_q = V_q^* + p\Omega L_s' i_d + p\psi_f' \Omega \end{cases} \tag{A.5}$$

Where L_s' and ψ_f' are the nominal values of the stator inductance and constant magnet flux. Therefore the state equations of the closed-loop system with FOC method can be

expressed as:

$$\begin{cases} \dfrac{di_d}{dt} = (x_{id} - R_s i_d - i_d k_{pc} + i_{d,ref} k_{pc} + L_s i_q p\Omega - L'_s i_q p\Omega)/L_s \\ \dfrac{di_q}{dt} = (x_{iq} - R_s i_q - i_q k_{pc} + k_{pc} x_\Omega - \psi_f p\Omega + \psi'_f p\Omega - k_{pc} k_{p\Omega}\Omega \\ +k_{pc} k_{p\Omega}\Omega_{ref} - L_s i_d p\Omega + L'_s i_d p\Omega)/L \\ \dfrac{d\Omega}{dt} = -(T_L + f\Omega - p\psi_f i_q)/J \\ \dfrac{dx_{id}}{dt} = k_{ic} i_{d,ref} - k_{ic} i_d \\ \dfrac{dx_{iq}}{dt} = k_{ic} x_\Omega - k_{ic} i_q - k_{ic} k_{p\Omega}\Omega + k_{ic} k_{p\Omega}\Omega_{ref} \\ \dfrac{dx_\Omega}{dt} = k_{i\Omega}\Omega_{ref} - k_{i\Omega}\Omega \end{cases} \tag{A.6}$$

Using the closed-loop model of the system, the $J_{FOC} \in R^{6\times 6}$ is equal to:

$$\begin{bmatrix} -\dfrac{(k_{pc}+R_s)}{L_s} & p(1-\dfrac{L'_s}{L_s})\Omega_0 & p(1-\dfrac{L'_s}{L_s})i_{q0} & \dfrac{1}{L_s} & 0 & 0 \\ -p(1-\dfrac{L'_s}{L_s})\Omega_0 & -\dfrac{(k_{pc}+R_s)}{L_s} & -p(1-\dfrac{L'_s}{L_s})i_{d0} - \dfrac{p(\psi_f-\psi'_f)+k_{pc}k_{p\Omega}}{L_s} & 0 & \dfrac{1}{L_s} & \dfrac{k_{pc}}{L_s} \\ 0 & \dfrac{p\psi_f}{J} & -\dfrac{f}{J} & 0 & 0 & 0 \\ -k_{ic} & 0 & 0 & 0 & 0 & 0 \\ 0 & -k_{ic} & -k_{ic}k_{p\Omega} & 0 & 0 & k_{ic} \\ 0 & 0 & -k_{i\Omega} & 0 & 0 & 0 \end{bmatrix} \tag{A.7}$$

Appendix B

Closed-loop model of system with flatness-based method

As discussed in Chapter 4, the control laws for the flatness-based control can be expressed as:

$$\begin{cases} \mu_d = \dot{i}_{d,ref} + k_{d1}.(i_{d,ref} - i_d) + k_{d2} \cdot \int (y_{d,ref} - y_d)\, d\tau \\ \mu_\Omega = \ddot{\Omega}_{ref} + k_{\Omega 1} \cdot (\dot{\Omega}_{ref} - \dot{\Omega}) + k_{\Omega 2} \cdot (\Omega_{ref} - \Omega) + k_{\Omega 3} \cdot \int (\Omega_{ref} - \Omega)\, d\tau \end{cases} \tag{B.1}$$

The switching voltages are calculated based on (B.2), where L'_s, R'_s, f' and J' are the nominal values of the corresponding parameters of the motor.

$$\begin{cases} V_d = L'_s \mu_d + R'_s i_{d,ref} - pL'_s \Omega_{ref} i'_q \\ V_q = L'_s \dfrac{J'\mu_\Omega + f'\dot{\Omega}_{ref}}{p\psi'_f} + R'_s i'_q + p\Omega_{ref}(L'_s + i_{d,ref}\psi'_f) \end{cases} \tag{B.2}$$

It should be mentioned that i'_q is the theoretical value of the q-axis current based on the trajectory reference and can be expressed as:

$$i'_q = \frac{J\dot{\Omega}_{ref} + f'\Omega_{ref} + T'_L}{p\psi'_f} \tag{B.3}$$

Each of the the flatness-based control laws adds one extra state variables, which are

defined in (B.4).

$$\begin{cases} \dot{x}_{id} = i_{d,ref} - i_d \\ \dot{x}_{\Omega} = i_{\Omega,ref} - \Omega \end{cases} \tag{B.4}$$

The derivative of the mechanical speed of the motor can be expressed as:

$$\dot{\Omega} = \frac{p\psi_f}{J} i_q - \frac{f}{J}\Omega - \frac{1}{J} T_L \tag{B.5}$$

As a result, the switching voltages (V_d and V_q) can be described based on state variables of the system.

Therefore, the state equations of the closed-loop flatness-based control system for steady-state situation can be expressed as:

$$\begin{cases} \frac{di_d}{dt} = -(\frac{R_s}{L_s} + \frac{L'_s}{L_s} k_{d1}) i_d + p\Omega i_q + \frac{L'_s}{L_s} k_{d2} x_{id} + (\frac{R'_s}{L_s} + \frac{L'_s}{L_s} k_{d1}) i_{d,ref} - \frac{L'_s f'}{L_s \psi'_f} \Omega^2_{ref} \\ -\frac{L'_s J'}{L_s \psi'_f} \dot{\Omega}_{ref} \Omega_{ref} + \frac{L'_s}{L_s} \dot{i}_{d,ref} \\ \frac{di_q}{dt} = -p\Omega i_d - (\frac{R_s}{L_s} + \frac{L'_s J' \psi_f}{L_s J \psi'_f} k_{\Omega 1}) i_q + (\frac{L'_s J' f}{L_s J p \psi'_f} k_{\Omega 1} - \frac{L'_s J'}{L_s p \psi'_f} k_{\Omega 2} - \frac{p\psi_f}{L_s}) \Omega \\ + \frac{L'_s J'}{L_s p \psi'_f} k_{\Omega 3} x_{\Omega} + (\frac{p\psi'_f}{L_s} + \frac{R'_s f'}{L_s p \psi'_f} + \frac{L'_s J'}{L_s p \psi'_f} k_{\Omega 2}) \Omega_{ref} + (\frac{R'_s J'}{L_s p \psi'_f} + \frac{L'_s f'}{L_s p \psi'_f} \\ + \frac{J' L'_s}{L_s p \psi'_f} k_{\Omega 1}) \dot{\Omega}_{ref} + \frac{p L'_s}{L_s} \Omega_{ref} i_{d,ref} + \frac{J' L'_s}{L_s p \psi'_f} \ddot{\Omega}_{ref} + \frac{J' L'_s}{J L_s p \psi'_f} k_{\Omega 1} T_L \\ \frac{d\Omega}{dt} = \frac{p\psi_f}{J} i_q - \frac{f}{J}\Omega - \frac{1}{J} T_L \\ \frac{dx_{id}}{dt} = i_{d,ref} - i_d \\ \frac{dx_{\Omega}}{dt} = \Omega_{ref} - \Omega \end{cases} \tag{B.6}$$

As the robustness analysis is conducted for flatness-based control without torque and resistance observer, $T'_L = 0$. Also, the analysis is performed using the Jacobean matrix of the closed-loop system around the equilibrium point. Therefore,

$$\begin{cases} \dot{\Omega}_{ref} = 0 \\ \ddot{\Omega}_{ref} = 0 \end{cases} \tag{B.7}$$

Using the closed-loop model of the system, the $J_{Flatness} \in R^{5\times5}$ is equal to:

$$\begin{bmatrix} J_{11} & p\Omega_0 & pi_{q0} & \frac{L'_s}{L_s}k_{d2} & 0 \\ -p\Omega_0 & J_{22} & J_{23} & 0 & J_{25} \\ 0 & \frac{p\psi_f}{J} & -\frac{f}{J} & 0 & 0 \\ -1 & 0 & 0 & 0 & 0 \\ 0 & 0 & -1 & 0 & 0 \end{bmatrix} \tag{B.8}$$

where,

$$\begin{cases} J_{11} = -(\frac{R_s}{L_s} + \frac{L'_s}{L_s}k_{d1}) \\ J_{22} = -(\frac{R_s}{L_s} + \frac{L'_s J'\psi_f}{L_s J\psi'_f}k_{\Omega1}) \\ J_{23} = \frac{L'_s J' f}{L_s Jp\psi'_f}k_{\Omega1} - \frac{L'_s J'}{L_s p\psi'_f}k_{\Omega2} - pi_{d0} - \frac{p\psi_f}{L_s} \\ J_{25} = \frac{L'_s J'}{L_s p\psi'_f}k_{\Omega3}. \end{cases} \tag{B.9}$$

Appendix C

Design parameters for the observers

The parameters for the nonlinear state observer, as discussed in Section 4.7.1, are determined by considering the constraints involving the eigenvalues of matrix **S**, the eigenvalues of matrix **P**, and the switching frequency of the inverter. Consequently, matrices **S** and **P** are designed as follows:

$$\begin{cases} \mathbf{S} = \begin{bmatrix} 5000 & 0 & 0 \\ 0 & 5000 & 0 \\ 0 & 0 & 5000 \end{bmatrix} \\ \mathbf{P} = \begin{bmatrix} 500 & 0 & 0 \\ 0 & 500 & 0 \\ 0 & 0 & 500 \end{bmatrix} \end{cases} \tag{C.1}$$

Additionally, as discussed in Section 4.7.2, the pole placement method, implemented through Matlab®, is employed to determine the matrix **L**. Consequently, considering the specific motor parameters under study, **L** is designed as follows:

$$\mathbf{L} = \begin{bmatrix} 9995 & 1256.6 & 7.9 \\ -1256.6 & 10001 & -480 \\ 0 & 422 & 10000.2 \\ -9.9 & 0 & 0 \\ 0 & -10.02 & 0 \\ 0 & 0 & -11.4 \end{bmatrix} \tag{C.2}$$

List of Publications

- M. Akrami, E. Jamshidpour, S. Pierfederici and V. Frick, "Flatness-Based Trajectory Planning/Replanning for a Permanent Magnet Synchronous Machine Control," 2023 IEEE Transportation Electrification Conference & Expo (ITEC), Detroit, MI, USA, 2023, pp. 1-5, doi: 10.1109/ITEC55900.2023.10186976.

- M. Akrami, E. Jamshidpour, S. Pierfederici and V. Frick, "Comparison of Flatness-based Control and Field-Oriented Control for PMSMs in Automotive Water Pump Application," 2023 IEEE International Conference on Environment and Electrical Engineering and 2023 IEEE Industrial and Commercial Power Systems Europe (EEEIC / I&CPS Europe), Madrid, Spain, 2023, pp. 1-6, doi: 10.1109/EEEIC/ICPSEurope57605.2023.10194821.

- M. Akrami, E. Jamshidpour and V. Frick, "Application of Hall Position Sensor in Control and Position Estimation of PMSM - A Review," 2023 IEEE International Conference on Environment and Electrical Engineering and 2023 IEEE Industrial and Commercial Power Systems Europe (EEEIC / I&CPS Europe), Madrid, Spain, 2023, pp. 1-6, doi: 10.1109/EEEIC/ICPSEurope57605.2023.10194763.

- M. Akrami, E. Jamshidpour, B. Nahid-mobarakh, S. Pierfederici and V. Frick, "Sensorless Control Methods for BLDC Motor Drives: A Review," IEEE Transactions on Transportation Electrification, Under Review, submitted in October 2023.

- M. Akrami, E. Jamshidpour and V. Frick, "Application of Hall Position Sensor in Control and Position Estimation of PMSM: A Comprehensive Review," IEEE Transactions on Industry Applications, Under Review, submitted in November 2023.

- M. Akrami, E. Jamshidpour, S. Pierfederici and V. Frick, "A Novel Trajectory Planning for One-loop Flatness-based Control of PMSMs," IEEE Transactions on Transportation Electrification, Under Review, submitted in November 2023.

Université de Strasbourg iCUBE Milad AKRAMI Groupe de Recherche en Energie Electrique de Nancy Green UNIVERSITÉ DE LORRAINE

Design and Implementation of Electric Motor Drive for Automotive Cooling Water Pump

Résumé

L'industrie automobile a connu une augmentation rapide des variateurs de vitesse basés sur des entraînements hybrides. Cette croissance influe également sur la demande de variateurs de vitesse à aimant permanent (PM). Par conséquent, les moteurs synchrones à aimant permanent (PMSM) et les moteurs à courant continu sans balais (BLDC) sont devenus un choix populaire pour les applications automobiles, y compris les véhicules électriques (VE) et les véhicules électriques hybrides (VEH), au cours des dernières décennies, en raison de plusieurs caractéristiques, notamment une densité de couple élevée, un rendement élevé et une densité de puissance élevée. Traditionnellement, les variateurs PMSM sont commandés par un contrôle orienté champ (FOC) utilisant des contrôleurs proportionnels et intégraux (PI) pour la régulation de la vitesse et du couple. La détermination des paramètres du contrôleur basée sur des méthodes linéaires nécessite une approximation linéaire qui dépend du point de fonctionnement du système. Des stratégies de contrôle non linéaire basées sur des modèles, y compris le contrôle différentiel de la platitude, ont été proposées comme solution à la nature non linéaire du système d'entraînement PMSM. Cette thèse propose une méthode de planification de trajectoire pour le contrôle basé sur la platitude des entraînements PMSM pour les pompes à eau des véhicules électriques. Cette approche vise principalement à garantir que le courant du moteur PMSM reste dans les limites permises grâce à un contrôle indirect basé sur la platitude, tout en conservant les avantages du contrôle en boucle unique. En outre, la contrainte de la tension de commutation a été prise en compte dans la méthode de planification de trajectoire proposée pour maintenir le bon fonctionnement du système d'entraînement du PMSM en régime permanent ainsi que pendant les phases transitoires. Une fonction de planification de trajectoire basée sur une fenêtre est utilisée pour l'entraînement PMSM dans cette méthode. La fonction de trajectoire est calculée à l'aide d'un algorithme d'optimisation prenant en compte les contraintes de dépassement de vitesse, de courant moteur et de tension de commutation. Contrairement à la planification conventionnelle de la trajectoire, qui est une fonction de second ordre, cette méthode prend en compte les limites du contrôleur tout en utilisant un contrôle basé sur la platitude en boucle unique.

Mots clés: Contrôle basée sur la platitude, Planification de la trajectoire, Optimisation, Commande de moteur, Machine synchrone à aimants permanents, Moteur sans balais

Abstract

There has been a rapid increase of variable-speed drives based on hybrid drives in the automotive industry. This growth is also influencing the industry demand for variable-speed permanent magnet (PM) drives. Therefore, permanent magnet synchronous motors (PMSMs) and brushless DC (BLDC) motors have become a popular choice for automotive applications including EVs and hybrid electric vehicles (HEVs) over the past decades due to several features including high torque density, high efficiency, and high power density. Traditionally, PMSM drives are controlled by field-oriented control (FOC) using Proportional-Integral (PI) controllers for speed and torque regulation. Designing controller parameters based on linear methods requires linear approximation, which is dependent on the operating point of the system. Model-based nonlinear control strategies such as flatness-based control have been proposed as a solution to the nonlinear nature of the PMSM drive system. A trajectory planning method for flatness-based control of PMSM drives for EV water pump application is proposed in this thesis. This approach is primarily intended to ensure PMSM motor current remains within permissible limits through indirect flatness-based control while still having the advantages of one-loop control. Furthermore, the constraint on switching voltage has been taken into account in the proposed trajectory planning method to maintain the proper operation of the PMSM drive system in steady-state mode as well as during transients. A window-based trajectory planning function is used for the PMSM drive in this method. The trajectory function is generated using an optimization algorithm considering the speed overshoot, motor current, and switching voltage constraints. Unlike conventional trajectory planning, which is a second-order function, this method takes controller limits into account while using one-loop flatness-based control.

Keywords: Flatness-based control, Trajectory planning, Optimization, Motor drive, Permanent magnet synchronous motors, BLDC motors